MATERIALS CHALLENGES OF TWO-DIMENSIONAL MATERIALS FOR FLEXIBLE SENSING APPLICATIONS

A Dissertation
Presented to
The Academic Faculty

by

Meng-Yen Tsai

In Partial Fulfillment
of the Requirements for the Degree
Doctor of Philosophy in the
School of Materials Science and Engineering

Georgia Institute of Technology
December, 2017

MATERIALS CHALLENGES OF TWO-DIMENSIONAL MATERIALS FOR FLEXIBLE SENSING APPLICATIONS

Approved by:

Dr. Eric M. Vogel, Advisor
School of Materials Science and Engineering
Georgia Institute of Technology

Dr. Samuel Graham
School of Materials Science and Engineering
Georgia Institute of Technology

Dr. Vladimir Tsukruk
School of Materials Science and Engineering
Georgia Institute of Technology

Dr. Oliver Brand
School of Electrical and Computer Engineering
Georgia Institute of Technology

Dr. Valeria Milam
School of Materials Science and Engineering
Georgia Institute of Technology

Date Approved: August 21, 2017

To my family

ACKNOWLEDGEMENTS

I would like to express my sincere gratitude to my advisor Dr. Eric Vogel for the guidance and support of my studies at Georgia Tech with his patience and knowledge. I am especially thankful that I was granted many opportunities to gain academic and industrial experiences under his mentoring. His encouragement has had a big impact on me.

I would like to thank my thesis committee, Dr. Oliver Brand, Dr. Samuel Graham, Dr. Valeria Milam and Dr. Vladimir Tsukruk, for their insightful comments and discussion.

I would like to thank members of Vogel group who have lent their help and support: Dr. Alexey Tarasov for mentoring and exploring research directions together; Dr. Philip Campbell for developing our materials synthesis with me; Dr. Tania Roy for training and guidance; Dr. Zohreh Razavi-Hesabi for sharing experiences and ideas; Dr. Corey Joiner for the advice and input; Eleanor Brightbill and Dr. Spyridon Pavlidis for working together and discovering the beauty of science. I would like to recognize Brian Beatty, Chris Perini, Katie Townsend, Erin Flynn, Janine Feirer, Noah Ellis, Dr. Akira Fujimoto, Dr. Bhaswar Chakrabarti and Robert Taylor for their help and collaboration. I would also like to thank Georgia Tech IEN for the process and tool support.

I am especially thankful for my collaborators for enlightening and supporting me: Dr. Siyuan Zhang, Dr. Stephen Barlow, Dr. Seth Marder, Hossein Taghinejad, Dr.

Billyde Brown, Niamh Creedon, Dr. Armelle Montrose, Dr. Pierre Lovera, Dr. Alan O'Riordan, Dr. Darren Gray, Niall Shields and Dr. Mark Mooney.

My sincere thank goes to Dr. Jen-Sue Chen, my advisor at National Cheng Kung University in Taiwan, who equipped me with the necessary knowledge and skills so I can embrace the challenges throughout my studies. I would like to recognize Dr. Tak-Wah Wong, who taught me that scientific researches should be always for a good cause.

Finally, I would like to express my greatest gratitude to my family. Without their support and love, I would not have made it this far.

TABLE OF CONTENTS

ACKNOWLEDGEMENTS **iv**

LIST OF TABLES **viii**

LIST OF FIGURES **ix**

LIST OF SYMBOLS AND ABBREVIATIONS **xxvi**

SUMMARY **xxix**

CHAPTER 1. Introduction **1**
1.1 Smart systems beyond Silicon **1**
1.2 Layout of this thesis **3**
1.3 Challenges for devices on flexible substrates **4**
1.4 Properties of 2D TMDs **7**
1.5 Synthesis of TMDs **16**
1.6 Doping of TMD semiconductors **31**
1.6.1 Volatile doping 33
1.6.2 Non-volatile doping 34
1.7 Strain-band structure relationship of TMDs **40**
1.8 Chemical and biological sensing using ISFETs and EGFETs **51**
1.8.1 Working principles of ISFET and EGFET 51
1.8.2 Binding events at the sensing surface 56
1.9 TMD-based Sensors **61**
1.9.1 Gas sensors 62
1.9.2 Chemical sensors 64
1.9.3 Biological sensors 65
1.9.4 Mechanical sensors 71
1.10 Summary of background **71**

CHAPTER 2. Charge transfer Doping of 2D TMD semiconductors **73**
2.1 Introduction **73**
2.2 Experimental methods **75**
2.2.1 Device fabrication 75
2.2.2 Doping treatment 76
2.2.3 Electrical characterization 77
2.2.4 Physical characterization 78
2.3 Doping of MoS_2 **79**
2.4 Doping of WSe_2 **93**
2.5 Conclusion **108**

CHAPTER 3. Flexible MoS_2 FET-based piezoresistive mechanical strain sensor **110**
3.1 Introduction **110**

3.2 Experimental methods 111
3.2.1 Fabrication of flexible MoS_2 FETs 111
3.2.2 Electrical characterization of MoS_2 under bending condition 113
3.2.3 Optical band gap measurement 114
3.3 Gate-tunable flexible MoS_2 piezoresistive strain sensors 115
3.4 Conclusion 130

CHAPTER 4. FET-based Potentiometric sensors for the detection of biochemical species 132
4.1 Introduction 133
4.1.1 Nanoelectronic ISFET and Simplified EGFET 133
4.1.2 On-site detection of animal diseases 134
4.2 Fabrication of potentiometric biochemical sensors 136
4.2.1 Fabrication of graphene ISFET and electrical measurement 136
4.2.2 Fabrication of EGFET and electrical measurement 137
4.2.3 Functionalization of sensing surface 138
4.3 Comparison between graphene ISFET and EGFET potentiometric sensors for chemical and biological sensing 140
4.4 Animal disease diagnosis using potentiometric EGFET biosensors 150
4.5 Conclusion 160

CHAPTER 5. Integrated potentiometric and impedimetric biosensing system 162
5.1 Introduction 163
5.2 Fabrication of integrated biosensors and electrical characterization 166
5.3 Direct correlation between potentiometric and impedance biosensors of antibody-antigen interactions using an integrated system 167
5.4 Conclusion 177

CHAPTER 6. Summary and Future Work 178
6.1 Future work 182
6.1.1 Optimization of the growth of TMDs 182
6.1.2 Strain-engineering of large-area TMDs 183
6.1.3 Interface engineering of TMD-based devices 184
6.1.4 Reliability and stability of potentiometric biosensors 185
6.1.5 Surface blocking in practical biosensors 185

REFERENCES 187

LIST OF TABLES

Table 1-1	Maximum process temperatures for different plastic flexible substrates	6
Table 1-2	Mechanical properties of strong engineering materials, including 2D materials[184, 186-187]	41
Table 2-1	Summary of the Fermi level shift after p-doping using P1 and P2 relative to the pristine sample. The values of the Fermi level shift were obtained from three different approaches: (1) estimated value using I_d-V_{ds} relationship from the change of I_d upon doping, denoted as I_d-V_{ds}; (2) estimated value using room-temperature thermionic emission model by monitoring the change of Schottky barrier height induced by the Fermi level shift, denoted as TE; and (3) measured values from UPS analysis, denoted as UPS. The calculated values are smaller than the UPS-measured values.	105

LIST OF FIGURES

Figure 1-1 Comparisons of electrical mobility (a) and strain limit (b) between various semiconductors. Graphene and TMDs have comparable or higher mobility to single-crystalline silicon. In addition, 2D materials have much higher strain limit than bulk materials and are promising for flexible electronic applications.[25] Reprinted by permission from Macmillan Publishers Ltd: Nature Communications 5, 5678 (2014) 7

Figure 1-2 (a) MoS_2 crystal (collection of The Natural History Museum of Los Angeles County) (b) A scheme of TMD layered structure. Each TMD layer is around 6 – 7 Å thick.[49] (c) Polytypes of TMDs.[27] 2H, 3R and 1T lattice of TMD, from left to right, respectively. (d) The graphical depiction of *d*-orbitals in TMDs.[50] 2H TMD gives primarily semiconducting nature because of the completely filled d_{Z^2} and empty d_{xy} and $d_{x^2-y^2}$ orbitals; the 1T form is metallic because of the partially filled t_{2g} band (d_{xy}, d_{xz}, d_{yz}). (b) Reprinted with permission from Radisavljevic et al., Single-Layer MoS_2 Transistors. *Nat. Nanotechnol.* 2011, *6*, 147-150. Copyright 2011 Nature Publishing Group. (c) Reprinted with permission from Wang et al., Electronics and Optoelectronics of Two-Dimensional Transition Metal Dichalcogenides. *Nat. Nanotechnol.* 2012, *7*, 699-712. Copyright 2012 Nature Publishing Group. (d) Reprinted with permission from Schmidt, H.; Giustiniano, F.; Eda, G., Electronic transport properties of transition metal dichalcogenide field-effect devices: surface and interface effects. *Chem. Soc. Rev.* 2015, *44*, 7715-7736. Copyright 2015 Royal Society of Chemistry. 10

Figure 1-3 Energy dipersion versus wavevector of MoS_2. The E-k diagram of bulk, 4-layer, bilayer and monolayer MoS_2 (from left to right). The dashed line indicates the energy of of the band maximum at K point. The red and blue lines represent the conduction band and valence band, respectively. The solid arrows indicate the lowest energy transition. The direct (vertical) energy transition between conduction and valence band, i.e. direct bandgap, is only observed in monolayer MoS_2.[52] Reprinted with permission from Splendiani et al., Emerging Photoluminescence in Monolayer MoS_2. *Nano Lett.* 2010, *10*, 1271-1275. Copyright 11

2010 American Chemical Society.

Figure 1-4 Lattice phonon properties of TMDs. (a) Two phonon vibrational modes in MX_2 layers. (b) The thickness-dependent Raman spectra of MoS_2.[56] (c) Summary of thickness-dependent evolution of the peak position and the peak separation of MoS_2.[56] Reprinted with permission from Lee et al., Anomalous Lattice Vibrations of Single- and Few-Layer MoS_2. *ACS Nano* 2010, *4*, 2695-2700. Copyright 2010 American Chemical Society. 13

Figure 1-5 Mechanically exfoliated single- and multilayer MoS_2 films on Si/SiO_2. Optical microscope images of single-layer (1L), bilayer (2L), trilayer (3L), and quadrilayer (4L) MoS_2 films (A–D). Panels E–H show the corresponding AFM images of the 1L (thickness: ≈ 0.8 nm), 2L (thickness: ≈1.5 nm), 3L (thickness: ≈ 2.1 nm), and 4L (thickness: ≈ 2.9 nm) MoS_2 films shown in (A–D).[89] Reprinted with permission from Li et al., Fabrication of Single- and Multilayer MoS_2 Film-Based Field-Effect Transistors for Sensing NO at Room Temperature. *Small* 2012, *8*, 63-67. Copyright 2012 John Wiley & Sons. 18

Figure 1-6 Schematic description of the main liquid exfoliation mechanisms.[91] (A) Ion intercalation. Ions (yellow spheres) are intercalated between the layers in a liquid environment, swelling the crystal and weakening the interlayer attraction. Then, agitation (such as shear, ultrasonication, or thermal) can completely separate the layers, resulting in an exfoliated dispersion. (B) Ion exchange. (C) Sonication-assisted exfoliation. The layered crystal is sonicated in a solvent, resulting in exfoliation and nanosheet formation. Reprinted with permission from Nicolosi et al., Liquid Exfoliation of Layered Materials. *Science* 2013, *340*. Copyright 2013 The American Association for the Advancement of Science. 19

Figure 1-7 Summary of primary growth techniques for the formation of monolayers of transition metal dichalcogenides.[101] These methods include chemical vapor deposition, powder vaporization, metal transformation, chemical vapor transport, chemical exfoliation, pulsed laser deposition, molecular beam epitaxy, spray pyrolysis, and electrochemical synthesis. Reprinted with permission from Das et al., Beyond Graphene: Progress in Novel Two-Dimensional Materials and van der Waals Solids. *Annual Review of Materials Research* 2015, *45*, 1-27. Copyright 2015 Annual Reviews. 21

Figure 1-8 Ternary phase diagram of Mo-O-S system.[109] Reprinted with permission from Feldman et al., High-Rate, Gas-Phase Growth of MoS_2 Nested Inorganic Fullerenes and Nanotubes. *Science* 1995, *267*, 222-225. Copyright 1995 The American Association for the Advancement of Science. 24

Figure 1-9 Optical image of MoS_2 film showing the coalescence of individual triangular grains into a continuous film using CVD growth. 25

Figure 1-10 (a) An optical image of a fabricated MoS_2 FET. (b) A representative Raman spectrum of trilayer MoS_2 synthesized by direct sulfurization of Mo film. (c) The cross-sectional TEM image of Au/Ti/MoS_2/SiO_2 stacking from MoS_2 FET device. The TEM sample was prepared using focused ion-beam (FIB) (d)-(e) Enlarged TEM images under bright and dark field trilayer MoS_2 sample. A trilayer structure is clearly shown. 27

Figure 1-11 (a) A photography of as-grown MoS_2 on SiO_2/Si substrates grown with Mo seed layer of 20, 15, 10, 7, 5, 2, and 0.3 nm, respectively (from left to right). (b–e) TEM characterizations of MoS_2 grown with (b) 10 nm Mo, (c) 4 nm Mo, (d) 1 nm Mo, and (e) 0.3 nm Mo.[130] Reprinted with permission from Jung et al., Metal Seed Layer Thickness-Induced Transition From Vertical to Horizontal Growth of MoS_2 and WS_2. *Nano Lett.* 2014, *14*, 6842-6849. Copyright 2014 American Chemical Society. 28

Figure 1-12 PL properties of $WS_{2x}Se_{(2-2x)}$ and $MoS_{2x}Se_{(2-2x)}$.[131-132] (a) The evolution of PL peak of $MoS_{2x}Se_{(2-2x)}$ from pure MoS_2 to pure $MoSe_2$. (b) The evolution of PL peak of $WS_{2x}Se_{(2-2x)}$ from pure WS_2 to pure WSe_2. (c) The optical band gap of $MoS_{2x}Se_{(2-2x)}$ measured from PL peak position. The band gap decreases as S content decreases. (d) The transition of electrical transport behaviors from n-type WS_2 to p-type WSe_2 transistors. (a) and (c): Reprinted with permission from Li et al., Growth of Alloy $MoS_{2x}Se_{2(1–x)}$ Nanosheets with Fully Tunable Chemical Compositions and Optical Properties. *J. Am. Chem. Soc.* **2014,** *136*, 3756-3759. Copyright 2014 American Chemical Society. (b) and (d): Reprinted with permission from Duan et al., Synthesis of $WS_{2x}Se_{2–2x}$ Alloy Nanosheets with Composition-Tunable Electronic Properties. *Nano Lett.* **2016,** *16*, 264-269. Copyright 2016 American Chemical Society. 30

Figure 1-13 The comparative mechanisms of classical substitutional doping and surface charge transfer doping of semiconductors.[145] Reprinted with permission from Ristein, J., Surface Transfer Doping of Semiconductors. *Science* **2006,** *313*, 1057-1058. 33

Copyright 2006 The American Association for the Advancement of Science.

Figure 1-14 Standard reduction potentials of chemicals used for charge-transfer doping of TMDs and the energy level of the valence and conduction band edges of monolayer MoS_2.[50] BV, benzyl viologen; NADH, nicotinamide adenine dinucleotide; TCNQ, 7,7,8,8-tetracyanoquinodimethane; F_4TCNQ, 2,3,5,6-tetrafluoro-7,7,8,8-tetracyanoquinodimethane. Reprinted with permission from Schmidt et al., Electronic transport properties of transition metal dichalcogenide field-effect devices: surface and interface effects. *Chem. Soc. Rev.* **2015,** *44*, 7715-7736. Copyright 2015 The Royal Society of Chemistry. 37

Figure 1-15 Doping mechanisms by which dimeric n-dopants (D_2) can react with acceptors (A).[173] Reprinted with permission from Zhang et al., n-Dopants Based on Dimers of Benzimidazoline Radicals: Structures and Mechanism of Redox Reactions. *Chem. Eur. J.* **2015,** *21*, 10878-10885. Copyright 2015 John Wiley & Sons. 38

Figure 1-16 Chemical doping of graphene using redox molecules. The carrier concentration in the material is changed due to the electron transfer between dopants and graphene. Extra electron filling above conduction band of graphene after n-doping with electron-donating molecules, untreated graphene (middle) and decreased number of electrons in valence band after p-doping with electron-accepting molecules (right) are shown.[174] Schematic representation of n- and p-doping of graphene by 1_2 (in equilibrium with 1, 10 min dip) and 2 (overnight dip), with associated energy levels. IP, EA and WF (ϕ) values were estimated from electrochemical and UPS data. The pristine graphene ϕ depended on the batch (4.1 eV for the sample before n-doping and 3.9 eV before p-doping). After treatment, the ϕ is affected by electron transfer (ET) between dopant and graphene, shifting the Fermi level (E_F) relative to the Dirac point (E_D), and the induced surface dipoles (SD) from the resulting charges, which change the local vacuum level (VL). Reprinted with permission from Paniagua et al., Production of heavily n- and p-doped CVD graphene with solution-processed redox-active metal-organic species. *Mater. Horiz.* **2014,** *1*, 111-115. Copyright 2014 The Royal Society of Chemistry. 39

Figure 1-17 Brillouin zone of MX_2. Under symmetrical strain, M' is reduced to M and the irreducible path is ΓKML. ΓKMLM'L enclosure represents the asymmetrical strain conditions. 42

Figure 1-18 (a) Strain dependence of band gap energies of 1L-MoS_2 (a=3.160 Å). The representative band structures for the (b) compressive and (c), (d) tensile stresses are displayed, respectively. Inset indicates the hexagonal structure consisting of Mo (red/gray balls) and S (yellow/light gray balls) from the top views.[195] Reprinted with permission from Yun et al., Thickness and strain effects on electronic structures of transition metal dichalcogenides: 2H-MX_2 semiconductors (M = Mo, W; X = S, Se, Te). *Phys. Rev. B* **2012,** *85*, 033305. Copyright 2012 American Physical Society. 43

Figure 1-19 Band gap of monolayer TMDs with respect to strain, ε, which varies from 0 to 10%. Strain is applied to the optimized structures (ε = 0) through various approaches, such as uniaxial expansion in x-direction (xx), y-direction (yy), homogeneous expansion in both x- and y-directions (xx+yy), expansion in x-direction and compression in y-direction (xx–yy), and compression in x-direction and expansion in y-direction (yy–xx) with same magnitude of strain. The first three strain profiles correspond to tensile strain, while the latter two represent pure shear strain. The top (left, middle, and right) panels of Figure 2 depict the graphs corresponding to MoX_2 (WX_2), while the bottom panels show the same for MS_2, MSe_2, and MTe_2, respectively, where M denotes Mo or W.[192] Reprinted with permission from Johari et al., Tuning the Electronic Properties of Semiconducting Transition Metal Dichalcogenides by Applying Mechanical Strains. *ACS Nano* **2012,** *6*, 5449-5456. Copyright 2012 American Chemical Society. 45

Figure 1-20 Absorbance and PL spectrum for a bilayer MoS_2 sample under tensile strain. (a) Absorption (left panel) and PL (right panel) spectrum of a monolayer MoS_2 sample under tensile strains up to 0.52% along the zigzag direction. The dashed blue and red lines are guide to the eye of the redshift of the peaks. Strain dependence of the A and B peak energies determined from absorption and of the A and I peak energies determined from PL is summarized in (b) and (c), respectively.[189] Reprinted with permission from He et al., Experimental Demonstration of Continuous Electronic Structure Tuning via Strain in Atomically Thin MoS_2. *Nano Lett.* **2013,** *13*, 2931-2936. Copyright 2013 American Chemical Society. 47

Figure 1-21 Photoluminescence property of trilayer MoS_2 under compressive strain.[198] (a) PL spectra of the MoS_2 under various strains. (b) PL peak energy as a function of compressive strain. The inset shows PL spectra of the sample under 0.0% and 0.2% strain. Reprinted with permission from Hui et al., Exceptional Tunability of Band 48

Energy in a Compressively Strained Trilayer MoS_2 Sheet. *ACS Nano* **2013,** *7*, 7126-7131. Copyright 2013 American Chemical Society.

Figure 1-22 Strain-induced Raman shifts in MoS_2.[206] Position of the (a) A_{1g} and (b) E^1_{2g} Raman peaks from monolayer (open circles) and few-layer (filled squares) MoS_2. Dashed lines are linear fits to the data discussed in the text. Error bars indicate the spectrometer resolution. Reprinted with permission from Rice et al., Raman-scattering measurements and first-principles calculations of strain-induced phonon shifts in monolayer MoS_2. *Phys. Rev. B* **2013,** *87*, 081307. Copyright 2013 American Physical Society. 49

Figure 1-23 Strain-induced band gap tuning in mono and few-layer MoS_2 flakes and modulation of the device resistance due to mechanical deformation of the MoS_2 membrane. (a) Measurements and the corresponding simulation results for a monolayer MoS_2 indicating a reduction of the band gap $\partial E_g/\partial \varepsilon$ with a rate of −73 meV/%. (b) Bilayer MoS_2 with $|\partial E_g/\partial \varepsilon| = -120$ meV/% and (c) trilayer MoS_2 with $|\partial E_g/\partial \varepsilon| = -21$ meV/%. (d) Extracted rate of band gap change $|\partial E_g/\partial \varepsilon|$ and piezoresistive gauge factor for six monolayers, three bilayers, and three trilayers.[205] Reprinted with permission from Manzeli et al., Piezoresistivity and Strain-induced Band Gap Tuning in Atomically Thin MoS_2. *Nano Lett.* **2015,** *15*, 5330-5335. Copyright 2015 American Chemical Society. 50

Figure 1-24 A representative scheme of ISFET. The gate of the MOFET serves as the active sensing surface of the ISFET sensors and is immersed in the electrolyte. When the charged species attach to the sensing surface, the change of the surface potential will change the gate voltage to the MOSFET, which generates the sensing signal. 54

Figure 1-25 A schematic structure of EGFET. The extended gate (i.e. the active sensing surface) is separated from a MOSFET (i.e. a readout transducer) with electrical interconnection and is immersed in the electrolyte, while the MOSFET is operated in a dry environment. The change of surface potential due to the attachment of charged species onto the sensing chip (extended gap) is transmitted to the MOSFET. 55

Figure 1-26 Protonation and deprotonation of surface hydroxyl groups of a pH sensor. The −OH groups will be protonated to become $-OH_2^+$, and the surface becomes positively charged when decreasing the pH of the electrolyte. The −OH groups will be 59

deprotonated to become $-O^-$, and the surface becomes negatively charged when increasing the pH of the electrolyte.

Figure 1-27 The scheme and the results of MoS_2 sensor in response to different chemical vapors. (a) A single monolayer of MoS_2 is supported on a SiO_2/Si substrate and contacted with Au contact pads. Transient physisorption of molecules induces temporary changes in the conductivity of the monolayer channel. (b) An optical image of the processed devices showing the monolayer MoS_2 flakes electrically contacted by multiple Au leads. (c) Histogram of MoS_2 and CNT-network sensor responses to various analytes. A qualitative summary of the response of the sensors to the analytes tested. The responses are broadly categorized as high, low, or null. The MoS_2 sensor exhibits a much higher selectivity and a complementary response to the CNT-network sensor. The analytes from left to right are triethylamine (TEA), tetrahydrofuran (THF), acetone, methanol, nitrotoluene (NT), 1,5-dichloropentane (DCP), and 1,4-dichlorobenzene (DCB). Ball-and-stick models of the analyte molecules are shown, in which nitrogen atoms are blue, oxygen atoms are red, carbon atoms are black, chlorine atoms are green, and hydrogen atoms are light gray.[77] Reprinted with permission from Perkins *et al.*, Chemical Vapor Sensing with Monolayer MoS_2. *Nano Lett*. 2013, 13, 668-673. Copyright 2013 American Chemical Society. 64

Figure 1-28 MoS_2-based FET biochemical sensor for pH and streptavidin detection. The structure of MoS2 FET sensor is shown in the middle panel. HfO_2 top-dielectric was deposited on MoS_2 channel as sensing surface. For pH sensing, HfO_2 is used as sensing surface (right panel). For biotin-streptavidin sensing, the N-hydroxysulfosuccinimide (sulfo-NHS)-biotin was immobilized onto silane-modified HfO_2 sensing surface. Reprinted with permission from Sarkar *et al.*, MoS_2 Field-Effect Transistor for Next-Generation Label-Free Biosensors. *ACS Nano* 2014, 8, 3992-4003.[228] Copyright 2014 American Chemical Society. 67

Figure 1-29 Schematic illustration of the Fluorimetric DNA Assay using MoS_2. Reprinted with permission from Zhu *et al.*, Single-Layer MoS_2-Based Nanoprobes for Homogeneous Detection of Biomolecules. *J. Am. Chem. Soc.* 2013, 135, 5998-6001.[259] Copyright 2013 American Chemical Society. 68

Figure 1-30 Graphical representations of various modes of MoS_2 functionalization with small molecules. The attachment using S-atom vacancies filling (left) and metal-sulfur dative bonds 70

formation (right). Reprinted with permission from Chen *et al.*, Functionalization of Two-Dimensional Transition-Metal Dichalcogenides. *Adv. Mater.* 2016, 28, 5738-5746.[263] Copyright 2016 John Wiley and Sons.

Figure 1-31 Some organic compounds for the functionalization of TMDs. Reprinted with permission from Chen *et al.*, Functionalization of Two-Dimensional Transition-Metal Dichalcogenides. *Adv. Mater.* 2016, 28, 5738-5746.[263] Copyright 2016 John Wiley and Sons. 70

Figure 2-1 (a) Schematics of a back-gated trilayer MoS_2 transistor. The drain-source voltage V_{ds} is applied to the Ti/Au contacts on top of MoS_2. The back-gate voltage V_{bg} is applied to the highly doped Si wafer (resistivity: 0.001-0.01 Ωcm). (b) Optical image of the MoS_2 transistor. (c) Drain current I_d through the MoS_2 channel as a function of the applied back-gate voltage V_{bg} (transfer curve) at constant drain-source voltage V_{ds} = 1V for two different channel widths (50 µm and 13 µm). The channel length is 100 µm. The maximum currents are limited by extrinsic resistance associated with the contacts; the intrinsic mobility after subtracting these contributions is around ~7 $cm^2V^{-1}s^{-1}$. (d) Output curves I_d vs. V_{ds} at different back-gate voltages V_{bg}. (e) Molecules used in this study. N1, N2 are n-dopants, P1 is a p-dopant. The cation 2-Fc-DMBI$^+$ is also shown and is the expected product of doping with both N1 and N2; in the case of N2/MoS_2 doping, the fate of the H atom is unknown. Treatment with P1 is expected to form neutral tri(4-bromophenyl)amine and leave $SbCl_6^-$ anions on the surface. 80

Figure 2-2 (a) Representative transfer characteristics of a MoS_2 FET before and after doping with N1. Treating the transistor with N1 shifts the threshold voltage V_{th} to more negative values, indicating n-doping (arrow). The drain current I_d at a given back-gate voltage V_{bg} is increased by one order of magnitude. (b) In contrast, the P1 treatment shifts the transfer curves to more positive gate values and decreases the overall current. (c) Effects of different n-dopants (N1, N2) and p-dopants (P1) on the threshold voltage V_{th}. Several transistors were measured in each case. Threshold voltage shifts ΔV_{th} are shown relative to the pristine sample (i.e. $V_{th,\ pristine}$ = 0 V). Dark bars show the mean ΔV_{th} values after a short dip, whereas light bars represent a 10 min treatment. Error bars indicate the standard deviation from averaging the results obtained with different devices. (d) Effect of molecular surface doping on the band structure of an n-type semiconductor. In the pristine case (center), E_F is closer to the conduction band (CB) than to the valence band (VB). The work function of the pristine 82

material ϕ (center), which is the difference between the vacuum level E_{vac} and the Fermi level E_F, decreases upon treatment with an n-dopant (left) and increases for the p-dopant (right). The total ϕ change consists of two different contributions. Firstly, filling (emptying) of semiconductor states ($\Delta \phi_{SF}$) due to electron transfer between the n-(p-)dopants and the channel shifts the Fermi level E_F relative to the valence band maximum E_{VBM}. Secondly, the negatively (positively) charged semiconductor and the positively (negatively) charged dopant ions result in a surface dipole that leads to a shift in the local vacuum level E_{vac} across the surface ($\Delta \phi_{SD}$).

Figure 2-3 UPS and XPS spectra of MoS_2 before and after treatment with N1 (a-d) and P1 (e-h). In a-h, the bottom curves ("bare") are the pristine MoS_2 spectra, middle curves ("dip") are for samples following a short dip in 2.5 mM (N1) or 5 mM (N2 and P1) dopant solution, and the top curves ("10 min") are obtained following a 10 min treatment in the same solution. (a, e) Secondary electron edge shifts (SEE) of MoS_2 after various treatment times. (b, f) Low binding energy region (near the Fermi energy E_F = 0 eV). The onset of ionization of filled states relative to zero binding energy is used to track the shifts of E_F relative to VBM. (c, g) XPS core level spectra of Mo 3d. (d, h) XPS core level ionizations characteristic of N1 (Fe 2p) and P1 treatment (Cl 2p), respectively. (i) Summary of total work function shifts $\Delta\phi$ (black squares) and the contribution to the WF change from state filling/emptying $\Delta\phi_{SF}$ (red circles) for different dopants and treatment times, shown relative to the pristine value (energy = 0 eV, dashed line). The contribution from the surface dipole is the difference $\Delta\phi_{SD} = \Delta\phi - \Delta\phi_{SF}$. 87

Figure 2-4 (a) Raman spectra of trilayer MoS_2 before and after different treatments with N1. The peak separation is A_{1g}-$E_{2g}^1 \approx 23.5$ cm^{-1}, confirming that the MoS_2 film consists of three layers.[56, 297] (b-d) E_{2g}^1 and A_{1g} peak position shifts upon doping with different compounds. 90

Figure 2-5 Full width at half maximum (FWHM) of A_{1g} and E_{2g}^1 peaks before and after successive dopants treatment. A_{1g} peak broadening is observed after n-doping of MoS_2, with N1 causing a stronger effect than N2. The E_{2g}^1 peak width is barely affected. After P1 treatment, both peaks become slightly narrower. 91

Figure 2-6 The redox potentials of dopants used in this study. On reaction with WSe_2, **P1** is expected to form neutral tris(4-bromophenyl)amine and leave $(SbCl_6)^-$ anions on the surface, **P2** is expected to form the corresponding $[Ni(mnt)_2]^{2-}$ dianion, 94

which may or not be accompanied by $(NBu_4)^+$ cations on the surface (see discussion in the SI), and **N1** is expected to form monomeric $(RhCp^*Cp)^+$.

Figure 2-7 UPS spectra of WSe_2 before and after treatment with **P1**, **P2** and **N1** (5×10^{-3} and 2.5×10^{-3} M p- and n-dopant solutions, respectively). In (a) the subsequent treatments from top to bottom are pristine WSe_2 spectra, dip, 1 min dip, 10 min and 1 h dipping using **P1**. The values given in the left and right panels correspond to the WFs and to the position of the Fermi level relative to the VBM. (b) Summary of total WF shifts, $\Delta\phi$ (squares), and the contribution to the WF change from state emptying/ filling $\Delta\phi_{SF}$ (circles) for different dopants and treatment times, shown relative to the pristine value (energy = 0 eV, dashed line). The contribution to the WF shift from the surface dipole is given by $\Delta\phi_{SD} = \Delta\phi - \Delta\phi_{SF}$. 96

Figure 2-8 (a) XPS core-level W 4f spectra before and after doping with **P1** (the pair of peaks at higher binding energy are attributed to the presence of WO_x). XPS core-level peaks indicating the presence of doping products on WSe_2: (b) Cl 2p from the anion of **P1** "Magic Blue", (c) Ni 2p attributed to $[Ni(mnt)_2]^{n-}$ (n = 1 and/or 2) anions from **P2** and (d) Rh 3d from **N1**, attributed primarily to the $(RhCp^*Cp)^+$ cation, with the low-BE shoulders likely attributable to unreacted $(RhCp^*Cp)_2$.[174, 303] 98

Figure 2-9 Raman spectra of trilayer WSe_2 used in this research. (a) Deconvolution of the overlapping $E_{2g}{}^1$ and A_{1g} peaks in WSe_2. (b)-(d) Summary of $E_{2g}{}^1$ and A_{1g} peak position shifts upon doping with **P1**, **P2** and **N1** dopants, respectively. 99

Figure 2-10 Representative I_d-V_{bg} characteristics of WSe_2 transistors treated with (a) **P1** and (b) **P2** dopants. After treatment with p-dopants, the transfer curves shift to the more positive bias side, indicating p-doping. The doping strength can be controlled by the treatment time. (c) The evolution of the change of V_{th} (ΔV_{th}) after p-doping. **P1** dopant is more effective than **P2** and can shift V_{th} up to 80 V after 10 min treatment. (d) The evolution of I_{min} (i.e. off state current) of treated WSe_2 devices. 102

Figure 2-11 Summary of WSe_2 devices treated with **N1** n-dopants. Two types of source and drain contacts were deposited to investigate the impact of contact metals on the n-doping efficiency: Au (100 nm thick) or Ti/Au stacking (30 nm/70 nm thick). Representative I_d-V_{bg} characteristics of WSe_2 transistors treated with **N1** with (a) Au contacts and (b) Ti/Au contacts. (c) The evolution of the change of V_{th} (ΔV_{th}) after n-doping using **N1** 107

dopants solution. The Ti/Au devices show a larger response ton-doping and the shift of the V_{th} is up to -200 V after 14 h treatment. (d) The evolution of I_{min} of treated WSe_2 devices, relative to pristine case $I_{min,0}$, using two types of metal contacts.

Figure 3-1 Fabrication of flexible MoS_2 field-effect transistors using a device transfer technique. (a) MoS_2 field-effect transistors are fabricated on a SiO_2/Si wafer and coated with a layer of PMMA. (b) The SiO_2 layer is chemically etched in a BOE bath to release the devices from the substrate. (c) Floating devices are held together by the PMMA layer and are transferred from a DI water bath onto a new substrate, which, in principle, can be any water-stable material. A flexible PET substrate with a conductive ITO back-gate electrode and ALD-grown Al_2O_3 dielectric is chosen here (d). (e) The PMMA layer is then removed in an acetone bath. 113

Figure 3-2 The schematic description of the bending of MoS_2 devices. 114

Figure 3-3 Optical images of as-fabricated and flexible MoS_2 devices. (a) A top view optical image of MoS_2 FETs after fabrication on a SiO_2/Si wafer. (b) A typical transistor with 100 μm MoS_2 channel length from the die in (a). (c) The released MoS_2 FETs held with the PMMA layer floating on water (the inset shows higher magnification of the same floating sample). (d) A flexible transistor on the Al_2O_3/ITO/PET substrate with probes touching the source and drain contacts during electrical measurements. (e) Flexible MoS_2 FETs on a transparent and flexible PET substrate covered with an ITO back-gate electrode and an 80 nm Al_2O_3 dielectric layer. 115

Figure 3-4 Drain current (I_d) as a function of applied back-gate voltage (V_{bg}) of a MoS_2 FET before and after transfer to a new SiO_2/Si substrate on (a) linear and (b) semi-logarithmic scale at a constant drain-source voltage of V_{ds} = 10 V. (c) Threshold voltage ($V_{th,}$ left axis) extracted from forward (closed circles) and backward sweeping (open circles), and I_{max}/I_{min} ratio of 7 measured FET devices (right axis, squares). 117

Figure 3-5 Transistor behavior of MoS_2 FETs transferred to flexible PET/ITO/Al_2O_3 (80 nm) substrate. (a) Drain current (I_d) flowing through the MoS_2 channel as a function of the applied back-gate voltage (V_{bg}) on a linear (right vertical axis) and semi-logarithmic scale (left vertical axis) at a constant drain-source voltage of V_{ds} = 10 V. (b) Drain current (I_d) as a function of drain voltage (V_d) at different applied back-gate voltage ranging between 0 V and 26.25 V. (c) Threshold voltage (V_{th}) extracted 119

from forward (solid circles) and backward sweeping (open circles), and I_{max}/I_{min} ratio of 7 measured FET devices (squares). Dashed lines represent the average V_{th} and I_{max}/I_{min} values of 7 devices.

Figure 3-6 The I_d-V_{ds} characteristics of MoS_2 FETs transferred to a (a) new SiO_2/Si substrate and (b) flexible Al_2O_3/ITO/PET substrate. The response of channel conductance increase is observed for both types of devices. 120

Figure 3-7 (a) Drain current (I_d) as a function of applied back-gate voltage (V_{bg}) of an as-fabricated MoS_2 FET (W/L = 13μm/100μm) on a Si substrate with 265 nm thick SiO_2 gate dielectric, plotted on semi-logarithmic scale (solid) and linear scale (dashed) at a constant drain-source voltage of V_{ds} = 10 V. All results shown are from the backward voltage sweeps (from high to low V_{bg}). (b) The I_d-V_{bg} curves of an as-fabricated device on a SiO_2/Si wafer (squares), and a transferred device on an Al_2O_3/ITO/PET substrate (circles) on semi-logarithmic scale (solid symbols) and linear scale (open symbols). Since the capacitances of both dielectrics are not the same (265 nm SiO_2 vs. 80 nm Al_2O_3), the samples require different gate voltage to achieve the same drain current. Therefore, the horizontal axis is normalized by their capacitance ratio: $C_{Al2O3,\ 80\ nm}/C_{SiO2,\ 265\ nm}$ ~6.6 for a better comparison. (c) A representative flexible MoS_2 FET on the Al_2O_3/ITO/PET substrate measured after 20, 60 and 80 bending cycles in vacuum (~10^{-5} Torr). All curves align well on top of each other. (d) The threshold voltage (V_{th}) evolution of flexible MoS_2 FETs as a function of total bending cycles. The error bars represent the results obtained with different devices. The observed device-to-device variations are small. No significant change of V_{th} is seen even after 180 bending cycles. The samples were bent around surfaces with different curvature (bending radii r = 7 (square), 2.5 (circle) and 0.9 cm (triangle), which correspond to strain ε = ~0.07, ~0.2 and ~0.54%, respectively). All devices were measured sequentially in the flat state after a given number of bending cycles. 121

Figure 3-8 (a) A representative transfer curve (I_d-V_{bg}) of a flexible MoS_2 transistor measured in the flat state (solid line) and the stretched state (dashed line; applied strain ε = 0.07%). A shift of the transfer curve is observed under strain. Several devices were measured with all showing similar behavior. (b) Output characteristic (I_d-V_{ds}) of the same device at different back gate voltages V_{bg} on a semi-log scale. (W/L = 13μm/100μm) 124

Figure 3-9 (a) Optical reflection spectra of trilayer MoS_2 under different applied strain. The position of the reflection minimum shifts to higher wavelength with increasing strain, as indicated by the arrows. The spectra are shown vertically offset for clarity. (b) Band gap E_g vs. applied strain $\Delta\varepsilon$, estimated from the minimum position in (a). The band gap linearly decreases with increasing strain. The slope is -0.3eV/% strain, in agreement with previous reports on exfoliated MoS_2. 126

Figure 3-10 The change of the Fermi level relative to the conduction band edge ($\Delta\varphi_n$) and the gauge factor (GF) were estimated from electrical measurements. (a) The plots of strain dependence of $\Delta\varphi_n$ at different back gate voltages. The right vertical axis is scaled to $\Delta\varphi_n$ per percent strain applied. (b) The relationship between $\Delta\varphi_n$ and V_{bg} of a representative device. (c) The plots of the strain dependence of $-(\Delta I)/I$ at different back gate voltages. The slope of the linear fit in (c) is the gauge factor (GF) by definition. (d) The relationship between GF and V_{bg} of the same device as shown in (b). Similar back gate dependence is observed for both (b) and (d), while both (a) and (c) show a linear relationship with increasing strain. Solid bands in (b) and (d) are guides to the eye. 128

Figure 4-1 (a) A schematic of a gold-coated graphene FET, which acts as both the sensing surface and the readout transducer. (b) Transfer curves of a graphene sensor, coated with Al_2O_3 and gold, measured vs. voltage applied to the reference electrode V_{ref} in different pH solutions. (c) Sensor response to pH for bare graphene (black squares), coated with Al_2O_3 only (blue triangles); and with Al_2O_3 plus gold (red circles). The response of the gold-coated sample is smaller than that of alumina because much less surface hydroxyl (-OH) groups are available that can interact with protons. In the case of the bare graphene, a very small amount of hydroxyl groups exists at defect sites, leading to a small pH response. The intrinsic response of ideal graphene is zero since no binding sites are available for protons. 141

Figure 4-2 pH sensing with two different extended gate readout configurations. The sensing surface is the same in both cases, i.e. 100 nm thick gold strips evaporated on a Si/SiO_2 substrate. (a) Here, a commercial MOSFET is used to convert potential changes to current changes. The extended gate gold surface is connected to the gate terminal of the transistor. (b) The transistor drain current I_d is measured vs. V_{ref} in different pH buffer solutions. A shift of the transfer curve to the right is observed with increasing pH. This shift is the pH response of the sensor and is plotted in (c) for two different measurements. (d) The 143

potential changes at the gold surface can also be directly monitored by a voltmeter. (e) The measured voltage is shown vs. time for different pH values. (f) The resulting pH response is very similar to the data presented in (c).

Figure 4-3 Study of the BSA/anti-BSA interaction using a gold-coated graphene sensor (a-b) and an extended gate MOSFET sensor (c-d). The interaction is sketched in the inset of part (a). The protein BSA is immobilized on the gold surface of both sensors. The BSA-coated surface is then exposed to different concentrations of BSA antibody in 10 mM PBS buffer (pH=7.4). (a, c) For both sensors, a shift of the transfer curve to the right is observed, because anti-BSA is negatively charged at pH=7.4 (the isoelectric point is ≈4.8-5.2[360]). (b, d) Potential changes (ΔV) are shown vs. anti-BSA concentration in PBS buffer relative to the value measured in buffer without antibodies (i.e. $\Delta V=0$ *at* $c_{\text{anti-BSA}}=0$). Both sensor systems exhibit a similar response, which can be fitted using Langmuir adsorption model (dashed lines). The dissociation constant K_D can be estimated from these fits. The values are in good agreement with the SPR data (~4.4 ±0.2 nM, Figure S1). Insets in (b) and (d) show the data on a semi-log scale (solid symbols), as well as the results obtained with control samples (open circles). The control samples did not have BSA immobilized on the gold surface. The control measurements do not show a clear trend, suggesting that the non-specific binding to the gold surface is small. 146

Figure 4-4 Surface plasmon resonance (SPR) results, showing refractive index units change (RU) vs. time. (a) Immobilization of BSA via amine coupling. A 1:1 EDC:NHS mixture was used to activate the carboxyl groups of the mercaptohexadecanoic acid (MHA) on gold surface. A 1% BSA solution in 10 mM PBS buffer (pH=7.4) was injected to immobilize the protein on the active sample. Plain buffer without the protein was injected on the control sample. Both chip surfaces were deactivated with injection of ethanolamine-HCl (pH 8.5). (b) To demonstrate the binding of anti-BSA, a 100 µg/ml anti-BSA solution was injected on both samples. A clear difference between active and control is observed, which is plotted in (c). 148

Figure 4-5 Fabrication of EGFET sensor. (a) Schematic of the potentiometric sensing device, consisting of two parts: a sensor part for signal generation and a transducer part for signal amplification and readout. The active sensing surface is a thin gold film (Au) evaporated on a Si/SiO_2 substrate. The gold film is contact with the electrolyte and its surface potential depends on the amount of charged molecules attached to the surface. The 152

gold surface can be chemically modified to achieve specific adsorption of certain biomolecules. To read out the potential changes on the gold surface, a commercial MOSFET is used as the readout transducer. The gold film acts as the so-called "extended gate" of the MOSFET, and is electrically connected to the gate terminal. An Ag/AgCl reference electrode is immersed in the solution to gate the transistor through the liquid. Different solutions are delivered to the surface using microfluidics. (b) A typical transistor transfer curve showing that the drain current I_d can be modulated by sweeping the voltage at the reference electrode V_{ref}. This measurement was recorded in 10 mM PBS buffer. The same curve is shown on linear scale (left axis) and semi-log scale (right axis). (c) Image of a disposable sensing chip used in this study. Four 100 nm thick gold strips were e-beam evaporated through a shadow mask. Using a liquid cell shown in (d), two gold strips were functionalized with the protein gE (active), and the other two were functionalized with protein Hp (control). To read out the potential changes generated on the sensor surface, the individual gold strips were connected using a test clip shown in (d) to the gate of the transducer.

Figure 4-6 Evaluation of EGFET and SPR performance for anti-BHV-1 antibody detection in serum. Two gold strips were functionalized differently and used as the active sensor (a-b) and the control (c-d). Both surfaces were measured in the same dilutions of antiserum. (a-b) The BHV-1 glycoprotein E (gE) was immobilized on the active gold strip using amine coupling, and acts as a capture antigen for anti-gE antibody present in antiserum (inset in b). (a) The transistor curves measured with the active gE-coated device shift to the left with increasing serum dilution in 10 mM HPS-EP buffer. (b) The calibration curve in different antiserum dilutions. The FET response is defined as the voltage shift at I_d=10 nA (along the arrow in (a)). The results are in excellent agreement with surface plasmon resonance (SPR) measurements (SAM chip, right axis). (c,d) The control sample was coated with the protein Haptoglobin (Hp) as a control for possible non-specific binding. (c) The Hp-coated control does not show a clear trend with changing antiserum dilution. (d) The observed response due to non-specific binding is small compared to the specific response shown in (b). 154

Figure 4-7 Selectivity control of EGFET and SPR sensors immobilized with gE. (a) The active gE-coated sensor was measured in different concentrations of the haptoglobin antibody (anti-Hp) in 10 mM HBS-EP buffer. At higher concentrations, a small shift to more positive values is observed, opposite to the response direction to 155

anti-gE. The FET and SPR responses (CM5 chip) are compared in (b). The results suggest high selectivity of the gE-coated sensor toward anti-gE in solution.

Figure 4-8 Measurements of Hp-coated control sample in different anti-Hp dilutions. (a) Transfer curves shift significantly to the right. (b) FET (squares) and SPR (CM5 chip, circles) response vs. anti-Hp dilution and concentration. Both sensors show similar behavior, suggesting that anti-Hp binds strongly to the Hp-coated surface (inset). 155

Figure 4-9 Comparison of EGFET and ELISA for anti-BHV-1 antibody detection in serum. The response of a gE-coated FET sensor from Figure 4-6b is plotted together with IDEXX gE blocking ELISA (1/absorbance) vs. the dilution of anti-BHV-1 antiserum. Comparable results (sensitivity and assay linearity) were obtained for both diagnostic platforms. 156

Figure 4-10 Assessment of EGFET and SAM SPR performance for anti-BHV-1 detection in serum from BHV-1 infected animals. Sample 1 was from a BHV-1 negative animal, whereas samples 2 and 3 originated from BHV-1 positive animals. The measurements were performed in different dilutions of the same 3 blood samples. (a) The FET response is shown vs. the dilution of the 3 samples. The sensor response increases in higher dilutions, because more antibodies can bind to the surface. (b) SPR results, obtained with the same blood samples, show very similar behavior validating the FET response. In general, the response to sample 2 > sample 3 > sample 1, indicating different levels of antibodies in the serum. 157

Figure 4-11 Regeneration of an FET sensor. (a) The blood serum was diluted 1:100 in 10 mM HPS-EP buffer and injected on the sensor surface. No shift was observed upon addition of sample 1. Significant response was observed with samples 2 and 3. After each measurement with a blood sample, the surface was regenerated using a short injection of glycine (pH 2.0), and flushed with HPS-EP buffer. The measurements performed in buffer after the regeneration steps align very well on top of each other (black lines), indicating that the sensor is reusable. This regeneration step had been previously tested on SPR. The sensor response in the 1:100 serum dilution is plotted in (b). The red, blue and green arrows indicate injections of different blood samples, while the black arrows represent a regeneration step with glycine and buffer. 158

Figure 5-1 The scheme and the optical image of the integrated FET/EIS biosensor system. (a) The experimental setup of the integrated system. (b) The equivalent circuit model for the impedance spectroscopy. (c) - (d) The optical images of the biosensor chip and the enlarged view of the Au micro-strip working electrode. 169

Figure 5-2 The responses of FET potentiometric and EIS impedance biosensors to anti-BSA concentrations. (a) The shift of I_d-V_{ref} curve measured with FET and (b) the FET signal (surface potential) in response to anti-BSA concentrations in linear scale and logarithmic scale (inset). (c) Nyquist plots of impedance spectra measured with EIS and (d) the R_{ct} change in response to anti-BSA concentrations in linear scale and logarithmic scale (inset). 171

Figure 5-3 The values of circuit elements from the fitting of measured impedance spectra versus different anti-BSA concentrations. (a) The plot of R_{ct} versus different anti-BSA concentrations. (b) The plot of $C_{surface}$ versus different anti-BSA concentrations. 172

Figure 5-4 The relationship between the exponentiation of change of surface potential ($\exp(\alpha q \Delta V / k_B T)$) and the charge transfer resistance (R_{ct}), measured with potentiometric and impedemetric biosensors, respectively. The linear relationship fits well into Butler-Volmer equation and confirms that both potentiometric and impedance biosensors are charge sensitive. 174

Figure 5-5 The sensing response of HN vs. BPIV3 using integrated biosensor system (a) The Nyquist plot of impedance spectra after the sensing surface exposed to different BPIV3 antibody dilutions. (b) The relationship between exponentiation of ΔV and the R_{ct}. A linear relationship is observed and agrees with the prediction of Butler-Volmer theory. 175

Figure 5-6 The comparison between EGFET biosensors using large area Au sensing surface (black square) and Au micro-strip (red circle). The BSA/anti-BSA sensitivities using either approach are comparable. 176

LIST OF SYMBOLS AND ABBREVIATIONS

2D	Two-dimensional
AFM	Atomic force microscopy
ALD	Atomic layer deposition
APTES	(3-Aminopropyl)triethoxysilane
BHV	Bovine herpes virus
BRD	Bovine respiratory disease
BSA	Bovine serum albumin
CB	Conduction band
CBM	Conduction band minimum
CE	Counter electrode
CMOS	Complementary metal–oxide–semiconductor
CNT	Carbon nanotube
CPE	Constant phase element
CVD	Chemical vapor deposition
DCM	Dichloromethane
DFT	Density functional theory
DIVA	Differentiation of infected from vaccinated animals
DNA	Deoxyribonucleic acid
EDC	*N*-(3-Dimethylaminopropyl)-*N′*-ethylcarbodiimide hydrochloride
EGFET	Extended gate field-effect transistor
EIS	Electrochemical impedance spectroscopy
ELISA	Enzyme-linked immunosorbent assay

FET	Field-effect transistor
FWHM	Full width at half maximum
gE	Glycoprotein E
GF	Gauge factor
GIAXRD	Grazing incident angle x-ray diffraction
HN	Hemagglutinin neuraminidase
Hp	Haptoglobin
ISFET	Ion-sensitive field-effect transistor
ITO	Indium tin oxide
LUMO	Lowest unoccupied molecular orbital
MHA	16-Mercaptohexadecanoic acid
MOCVD	Metalorganic chemical vapor deposition
MOFET	Metal–oxide–semiconductor field-effect transistor
NHS	N-Hydroxysuccinimide
NSB	Non-specific binding
NW	Nanowire
PBS	Phosphate buffered saline
PDMS	Polydimethylsiloxane
PECVD	Plasma-enhanced chemical vapor deposition
PEIE	Poly(ethylenimine) ethoxylated
PET	Polyethylene terephthalate
PL	Photoluminescence
PMMA	Poly(methyl methacrylate)
POC	Point-of-care
RE	Reference electrode

SAM	Self-assembly monolayer
SPR	Surface plasmon resonance
TE	Thermionic emission
TMD	Transition metal dichalcogenide
UPS	Ultraviolet photoelectron spectroscopy
UV	Ultraviolet
VBM	Valence band maximum
WE	Working electrode
XPS	X-ray photoelectron spectroscopy

SUMMARY

Sensors are playing an increasingly important role in our lives because they enable the detection of environmental changes and, therefore, initiate a response accordingly. Sensors convert detected physical or chemical changes, for example, motion, radiation, heat, acidity, chemicals, etc., to useful and readable signals. Field-effect transistors (FETs), a class of semiconductor device in which the electrical current is controlled through an applied gate voltage, are promising for many sensing applications. Even though FETs-based sensors have been well-developed, flexible version of such sensors remains a big challenge and requires new materials and new sensing designs. Two-dimensional (2D) materials such as graphene and transition metal dichalcogenides (TMDs) are promising candidates for FET-based sensors due to their flexibility, transparency and potential for high electrical performance. Because of the atomically thin nature of 2D materials, their electrical properties are extremely sensitive to their atomic-scale structure as well as to their surfaces and interfaces with other materials. Specifically, defects, dopants, attached molecules or change in the band structure due to strain can shift the Fermi level resulting in a measured change in current. The goal of this work is to meet the challenges faced by the 2D TMD-based electronics in sensor applications by developing a fundamental understanding of the impact of materials processing, structure, interfaces and surfaces on resultant electronic properties. Furthermore, a simplified strategy for chemical and biological electrical sensors is developed to bridge the current sensing technology to the use of next generation flexible 2D transducers.

To improve 2D TMD-based electronics, this work demonstrates a solution-processed molecular doping technique to control the electronic band structure and the electrical performances of TMD-based devices. Charge transfer doping due to the electron transfer between TMD semiconductors and the redox-active molecular dopants is demonstrated to be a promising tool to control the carrier concentration as well as the Fermi level of MoS_2 and WSe_2.

Understanding the impact of external strain on the flexible devices is crucial toward their practical application. This work investigates the electronic properties and stability of flexible TMD FETs under mechanical strain. The interesting mechano-electric properties of TMDs provide a new opportunity for transparent and flexible mechanical strain sensors. Furthermore, the fundamental physics and the controllability of this strain sensitivity are studied.

FET-based potentiometric sensors provide a promising technique for the detection of chemical and biological species without the use of secondary bio-labels. This work first focuses on the comparison between two commonly used potentiometric sensing platforms – ion-sensitive field-effect transistor (ISFET) based on nano-materials, and a similar, but simplified, extended-gate FET (EGFET) in which the sensor surface is separated from the transducer. It is then demonstrated that the sensor sensitivity depends on the sensing surface instead of sensor platform. As a result, the following demonstration of biochemical sensing is based on EGFETs. In addition, EGFETs provide a more reliable operation and ready compatibility with any commercialized transistors currently as well as 2D TMD-based transistors in the future. Finally, EGFET is proved a

promising candidate for practical sensing application by a direct comparison between EGFET potentiometric biosensors with impedimetric biosensors.

The work presented in this thesis demonstrates initial first steps toward the sensing applications using 2D TMD semiconductors. Despite the current challenges faced by 2D TMD-based FETs in biochemical sensing applications, the proposed EGFET configuration provides a readily available biosensing technique for current technologies and the future compatibility to 2D TMD-based transducers.

CHAPTER 1. INTRODUCTION

1.1 Smart systems beyond Silicon

Modern electronics aim to provide new functionalities and to improve user experiences. Since the initial development of integrated circuits (ICs) technologies in early 1950s, silicon-based semiconductor devices soon replaced germanium-based transistors developed by Kilby (2000 Nobel Prize in Physics) and have dominated the information technology industry.[1-2] Silicon remains the most commonly used semiconductor material due to several main reasons: (1) Silicon is one of the most abundant elements in Earth's surface and therefore available for cheap acquisition. (2) The advancement in purification of silicon and the doping techniques developed at Bell Lab in the 1950s provides high quality materials and yield the ease of fabrication.[3-5] (3) Controllable oxidation of silicon to produce silicon dioxide provides a reliable dielectric layer with high quality interface to silicon and low concentration of interfacial traps. (4) The development of silicon technologies over the past several decades enabled highly complex integrated circuits.

The driving force of ever increasing development of silicon technology is the demand of the miniaturization of the chip size and the increase of computing power. As suggested by Gordon Moore in 1965, the co-founder of Intel, based on his observation of integrated circuit industry, Moore's Law states that the number of transistors in a dense integrated circuit doubles every 18 months.[6-7] The pursuit of Moore's law has propelled the semiconductor industry ever since. As a result, numerous endeavors have been taken to scale the devices and to use the space on the chip more efficiently including the

exploration of new materials, reduction of the channel length of transistors, adoption of new chip designs, etc.[8-9] In addition, the development of low-cost fabrication is also important.

However, the pursuit of Moore's law represents only one of the directions on the semiconductor technology roadmap.[10] Despite the fast and high computing power, conventional silicon devices are rigid and planar, and are fabricated on wafers. Recently, there has been interest in new applications for smart systems including flexible circuits, wearable electronics, wearable sensors for health monitoring, flexible display, biomedical devices, human-machine interfaces and other non-planar devices.[11-12] In 2017, the global market value for flexible electronics has reached $29.28 billion and is projected to grow into $73.43 billion in 2027.[13] These applications beyond conventional wafer-based silicon electronics is a critical new direction of semiconductor technology.

Two-dimensional materials, including graphene, transition metal dichacogenides (TMDs), etc., are promising for above new applications. These atomically thin materials provide comparable electrical properties to conventional bulk semiconductors and can offer extra advantages including flexibility, transparency, controllable electrical and optical properties through layer thickness and strain engineering. [11, 14-16] Therefore, this work focuses on the modification and applications of TMDs toward next-generation electronics.

1.2 Layout of this thesis

In this work, we first focus on two-dimensional transition metal dichalcogenides (2D TMDs) semiconductors, which fulfill the requirements for flexible electronics including transparency, light-weight, flexibility, stretchability, etc.[11, 14-16] Chapter 1 includes some fundamental background for flexible substrates and devices; the properties and fabrication of 2D TMDs; modification of carriers in TMD semiconductors through doping; the influence of external strain on TMDs; operation principles of chemical and biological sensors using ion-sensitive field-effect transistors (ISFET) and extended-gate FETs (EGFET); and, finally, a brief review of TMDs-based sensors from literature. Similar to conventional semiconductors, techniques are required to dope 2D TMDs. Chapter 2 demonstrates that charge transfer doping is a promising tool to tune the Fermi level of the TMD semiconductors. Taking advantage of the flexible nature of the TMDs, Chapter 3 explores the strain-induced mechano-electric properties of 2D TMDs. The strain-induced Fermi level change in flexible TMDs was investigated. Next, Chapter 4 reports potentiometric chemical and biological sensors using different electrical sensing platforms, including 2D materials-based graphene ISFET and commercial MOSFET-based EGFET. Although 2D materials provide some additional functionality, it remains challenging and costly to use 2D materials-based devices for practical sensing applications in liquid phase chemical and biological detection. For example, a large gate bias is needed to operate TMDs-based FETs, which is incompatible with the maximum allowable voltage to the liquid gate for biosensors. Alternatively, EGFET is a simplified design for chemical and biological sensors and is compatible with any appropriate transducers, including commercial MOSFET, nano-electronics and 2D materials-based

FETs in the future. Chapter 4 further presents animal disease diagnosis using EGFET-based biosensors. To further expand the electrical label-free biosensors, an integrated system that combines two of the most common sensing techniques, potentiometric FET-based biosensors and electrochemical impedance spectroscopy (EIS)-based biosensor, will be discussed in Chapter 5. The fundamental correlation between potentiometric and impedimetric biosensors was investigated. Finally, Chapter 6 summarizes this work and provides insight into future studies about 2D TMDs-based electronics and general electrical biosensor applications.

1.3 Challenges for devices on flexible substrates

Flexible electronics are typically built on non-conventional substrates such as plastics and papers, and promise more light-weighted, portable and cheaper design and manufacturing. Unlike the highly-standardized materials and fabrication processes developed for the silicon industry, the manufacturing of flexible electronics is limited by the process temperature, which should not exceed the glass transition temperature of the flexible substrates.[14, 17-18] The maximum allowed process temperatures for several plastic substrates are summarized in Table 1-1.[14]

Although polyimide (Kapton™) provides one of the best thermal tolerances in flexible substrates, the highest available process temperature is limited to around 250°C. As a result, the choice of alternative active materials and fabrication techniques are crucial in order to comply with the temperature limit. In addition, the solvents, photoresists and other chemicals used in standard CMOS fabrication are incompatible

with many flexible plastic and paper substrates, and may damage the substrate.[18] In the past several decades, different classes of semiconductor materials have been utilized in flexible electronics, including organic semiconductors,[18-21] amorphous silicon (a-Si),[11, 17, 22] nano-crystalline silicon (nc-Si), metal oxide semiconductors,[17] carbon nanotubes (CNTs),[23] and the emerging 2D materials.[24-26] Several material challenges including electrical mobility, strain limit, and stability, are yet to be overcome. Organic semiconductors, such as pentacene small molecules or polythiophene polymers, suffer from low mobility and poor ambient stability. Amorphous silicon deposited using chemical vapor deposition (CVD) generally gives carrier mobility less than 1 $cm^2V^{-1}s^{-1}$.[17] Nano-crystalline silicon films deposited by plasma-enhanced CVD (PECVD) with grain size less than 100 nm can provide a higher mobility up to 50 $cm^2V^{-1}s^{-1}$ but requires higher growth temperature.[17] Oxides of transition metals, for example, ZnO, have mobility values typically range from 1 to 70 $cm^2V^{-1}s^{-1}$ depending on the gas phase deposition or solution processes.[17] Electron mobility in single-walled CNTs has been reported to reach 10^5 $cm^2V^{-1}s^{-1}$ but has been deemed impractical for commercial applications because of the difficulties associated with placing an individual CNT along the desired channel direction and the need for expensive e-beam lithography.[23] None of these aforementioned materials provides comparable electrical properties to the state-of-the-art silicon semiconductors.

Table 1-1 Maximum process temperatures for different plastic flexible substrates

Material	Max Process Temp. (°C)
Polyimide (Kapton)	250
Polyether ether ketone (PEEK)	240
Polyethersulphone (PES)	190
Polyetherimide (PEI)	180
Polyethylene Naphthalate (PEN)	160
Polyethylene terephthalate (PET)	120

Figure 1-1 summarizes the mobility and strain limit for several reported materials available for flexible electronics.[25] Two-dimensional (2D) materials including graphene and transition metal dichalcogenides (TMDs) provides higher or comparable mobility to single-crystal silicon and superior strain limit making them promising candidates for flexible electronics. The classifications and properties of 2D materials will be discussed in detail in the following sections.

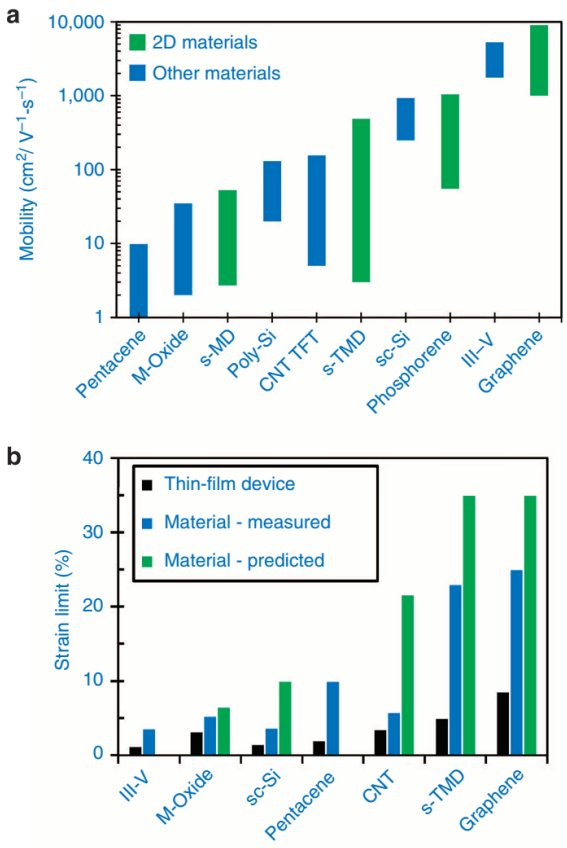

Figure 1-1 Comparisons of electrical mobility (a) and strain limit (b) between various semiconductors. Graphene and TMDs have comparable or higher mobility to single-crystalline silicon. In addition, 2D materials have much higher strain limit than bulk materials and are promising for flexible electronic applications.[25] Reprinted by permission from Macmillan Publishers Ltd: Nature Communications 5, 5678 (2014)

1.4 Properties of 2D TMDs

Two-dimensional (2D) materials cover a full spectrum of functionalities including insulators (hexagonal boron nitride, h-BN), semiconductors (TMD semiconductors: MoS_2, WSe_2, WS_2, etc.), semi-metals (graphene, $TiSe_2$) and superconductors ($NbSe_2$).[27-33] 2D materials are covalent layered crystals that are bonded by only weak van der Waal forces between layers, and are free from out-of-plane covalent bonding.[28] Due to the

weak interlayer force, 2D materials can achieve atomic layer thickness. These atomically thin 2D layers have attracted much attention because they provide numerous unique properties which are not achievable using bulk materials. In addition, devices using hetero-structure by stacking different 2D materials, for example, h-BN dielectrics, MoS_2 semiconductors and graphene contacts, offer many exciting applications including all-2D flexible electronics, tunneling transistors and other vertical devices.[34-36]

Graphene, one of the most prominent 2D materials, is comprised of carbon atoms arranged in a sp^2 hybridized hexagonal lattice.[33, 37] The electronic structure of graphene can be described as a linear dispersion near the K point in the Brillouin zone with massless Dirac fermions,[38-39] leading to some attractive properties including ballistic charge transport and extremely high carrier mobility up to 10,000 $cm^2V^{-1}s^{-1}$ on SiO_2,[40] and 200,000 $cm^2V^{-1}s^{-1}$ for suspended film.[41-42] In addition, pristine graphene lacks a band gap. The Fermi level of graphene can be adjusted into the conduction band or valence band by gate biasing, which results in the ambipolar field-effect characteristics in graphene devices.[43] However, the lack of a bandgap means that graphene transistors cannot be effectively switched off and the ratio of on-current to off-current is less than 10, which is not suitable for low-power and digital switch applications. For digital electronic applications, it is crucial to use other 2D semiconductors beyond graphene.

Transition metal dichalcolgenides (TMDs) is another group of 2D materials. Unlike graphene, several 2D TMDs are semiconductors with tunable bandgaps from 1 – 2 eV, which is promising for digital devices.[44-47] TMDs have the chemical formula MX_2, where M is a transition metal element from group IV (Ti, Hf, etc.), group V (Ta, V, etc.) of group VI (Mo, W, etc.), and X is chalcogen (S, Se or Te). The lattice structure of the

TMDs is generally an X-M-X "sandwich" structure, where metal atoms sit in between top and bottom hexagonally ordered chalcogen atoms, and the oxidation states of M and X are +4 and -2, respectively. The lone-pair electrons of the chalcogen atoms self-terminate the surfaces and eliminate dangling bonds.[48] The lattice and electronic structure of TMDs are shown in Figure 1-2. Figure 1-2(a) shows a picture of MoS_2 natural crystal. Figure 1-2(b) shows the schematic of TMDs and each TMD layer is around 6 – 7 Å thick.[49] There are several stacking polytypes of TMDs including 1T, 2H, and 3R, where the former digits indicate the number of layers in the stacking sequence and the latter alphabets represent trigonal, hexagonal and rhombohedral, respectively. Figure 1-2c depicts the polytypes of TMDs.[27] The electronic structure of TMDs highly depends on the polytypes due to the partially-filled d-orbitals of the transition metals. For example, in group VI TMDs (M = Mo, W), the 2H form gives primarily semiconducting nature because of the completely filled d_Z^2 and empty d_{xy} and $d_{x^2-y^2}$ orbitals; the 1T form is metallic because of the partially filled t_{2g} band (d_{xy}, d_{xz}, d_{yz}) as shown in Figure 1-2(d).[50] Furthermore, the band gap of 2D semiconductors is thickness dependent; for example, monolayer MoS_2 has a direct band gap of 1.8 eV while bulk MoS_2 has an indirect bandgap of 1.3 eV,[51] as shown in Figure 1-3.[52] This indirect-to-direct bandgap transition results from the interaction between p-orbitals of chalcogen atoms.[52] Overall, the bandgap decreases as the number chalcogen atoms increases, i.e. increasing thickness. This thickness-dependent electronic structure is especially attractive and useful in electrical and optical applications.

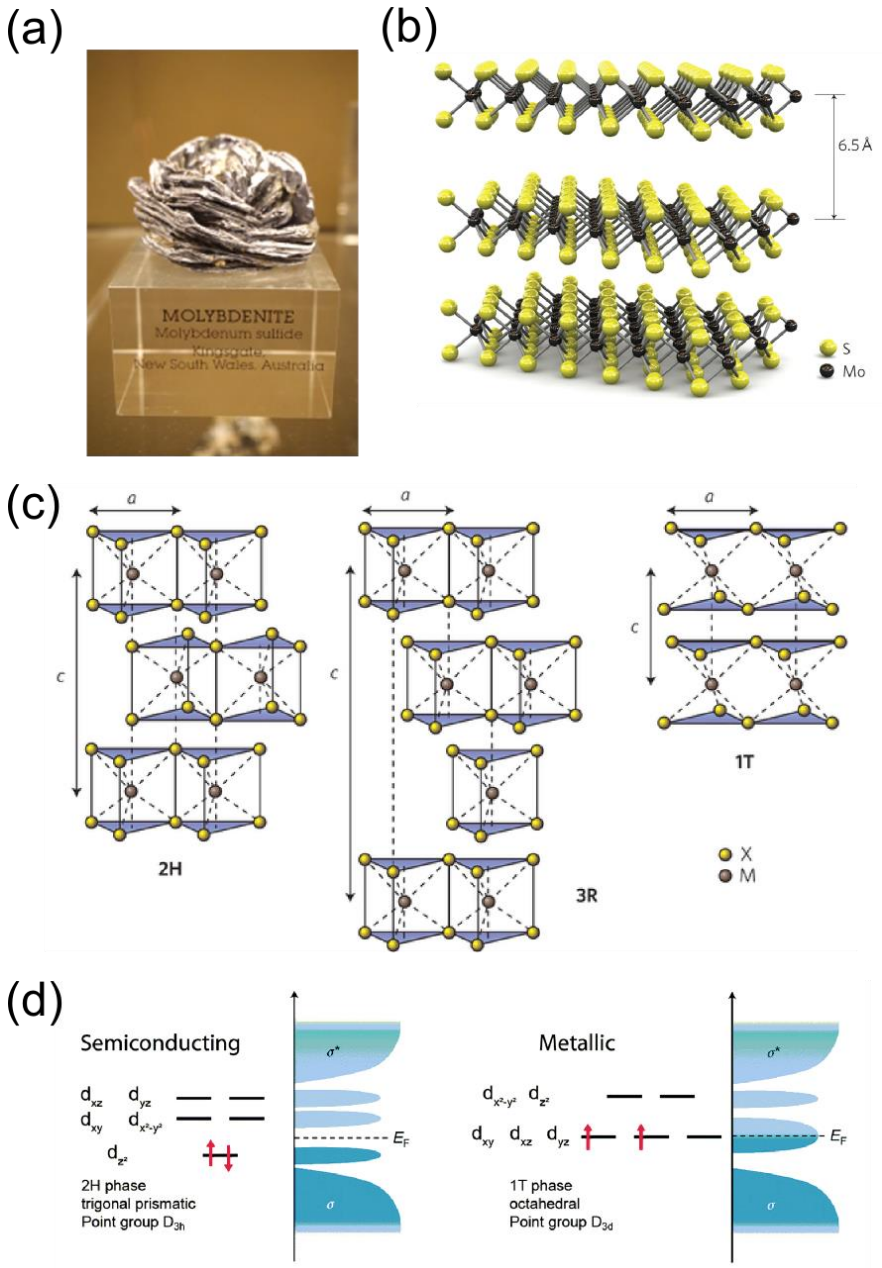

Figure 1-2 (a) MoS_2 crystal (collection of The Natural History Museum of Los Angeles County) (b) A scheme of TMD layered structure. Each TMD layer is around 6 – 7 Å thick.[49] (c) Polytypes of TMDs.[27] 2H, 3R and 1T lattice of TMD, from left to right, respectively. (d) The graphical depiction of *d*-orbitals in TMDs.[50] 2H TMD gives primarily semiconducting nature because of the completely filled d_Z^2 and empty d_{xy} and $d_{x^2-y^2}$ orbitals; the 1T form is metallic because of the partially filled t_{2g} band (d_{xy}, d_{xz}, d_{yz}). (b) Reprinted with permission from Radisavljevic et al., Single-Layer MoS_2 Transistors. *Nat. Nanotechnol.* 2011, *6*, 147-150. Copyright 2011 Nature Publishing Group. (c) Reprinted with permission from Wang et al., Electronics and Optoelectronics of Two-Dimensional Transition Metal Dichalcogenides. *Nat. Nanotechnol.* 2012, *7*, 699-712.

Copyright 2012 Nature Publishing Group. (d) Reprinted with permission from Schmidt, H.; Giustiniano, F.; Eda, G., Electronic transport properties of transition metal dichalcogenide field-effect devices: surface and interface effects. *Chem. Soc. Rev.* 2015, *44*, 7715-7736. Copyright 2015 Royal Society of Chemistry.

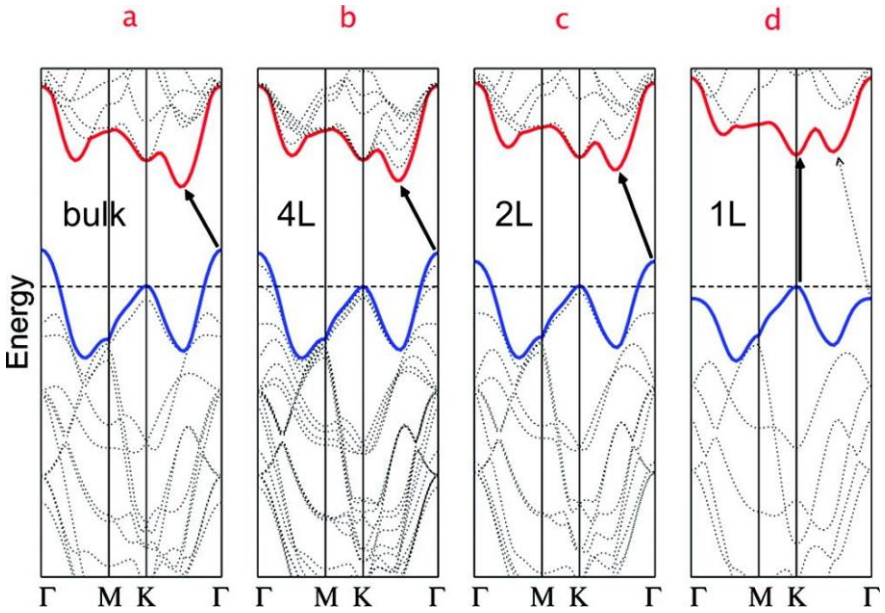

Figure 1-3 Energy dipersion versus wavevector of MoS_2. The E-k diagram of bulk, 4-layer, bilayer and monolayer MoS_2 (from left to right). The dashed line indicates the energy of of the band maximum at K point. The red and blue lines represent the conduction band and valence band, respectively. The solid arrows indicate the lowest energy transition. The direct (vertical) energy transition between conduction and valence band, i.e. direct bandgap, is only observed in monolayer MoS_2.[52] Reprinted with permission from Splendiani et al., Emerging Photoluminescence in Monolayer MoS_2. *Nano Lett.* 2010, *10*, 1271-1275. Copyright 2010 American Chemical Society.

Phonon modes corresponding to the lattice vibration of TMD crystals offer abundant information about both intra- and inter-layer interactions. Raman spectroscopy is a powerful tool to probe the phonon modes and investigate the thickness, film quality, and other phonon related properties of TMD films. Two main Raman peaks correspond to

the in-plane E^1_{2g} phonon mode and the out-of-plane A_{1g} mode in MX_2.[53-54] The schemes of vibrational modes in MX_2 layers are shown in Figure 1-4(a). For MoS_2, the E^1_{2g} and A_{1g} peaks are located at around 383 and 406 cm^{-1}, respectively. When the layer thickness increases, the A_{1g} peak stiffens (upward shift toward higher wavenumbers) and the E^1_{2g} peak softens (downward shift toward lower wavenumbers).[55-56] The separation between the peaks has shown to be related to the thickness of the TMD layer in MoS_2, WS_2, WSe_2, etc. The Raman spectra of MoS_2 with different layer thickness are shown in Figure 1-4(b) and the thickness-dependent evolution of the peak position and the peak separation is summarized in Figure 1-4(c).[56] The stiffening of the A_{1g} peak with increasing thickness can be explained by the hindrance of the out-of-plane vibration due to the van der Waals force; the softening of E^1_{2g} in-plane mode can be attributed to the increase of the dielectric tensor related to the long-range Coulomb interactions.[57] Similarly, this thickness-dependent Raman trend is also observed in WSe_2, but and peaks move closer to each other and degenerate in monolayer samples.[58-59]

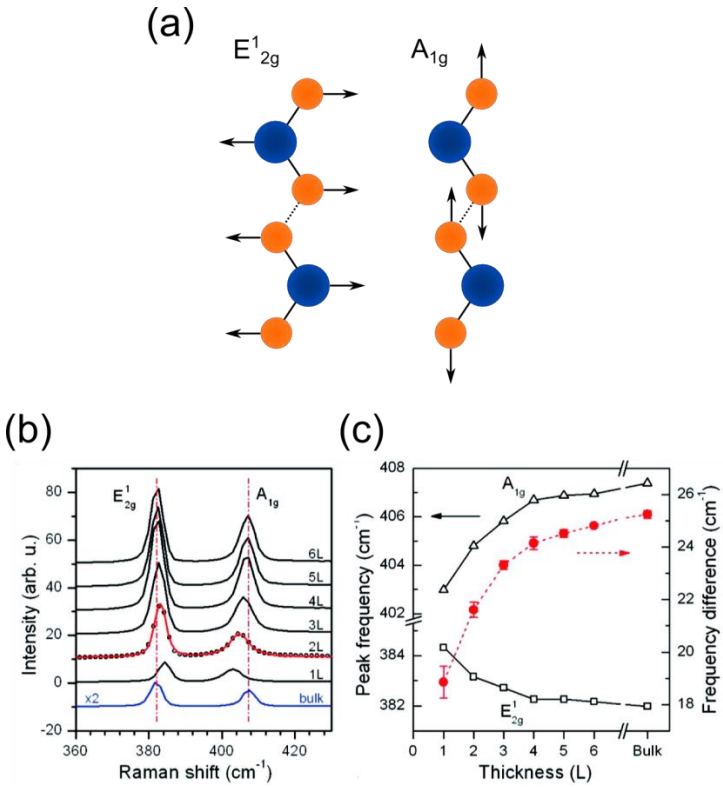

Figure 1-4 Lattice phonon properties of TMDs. (a) Two phonon vibrational modes in MX_2 layers. (b) The thickness-dependent Raman spectra of MoS_2.[56] (c) Summary of thickness-dependent evolution of the peak position and the peak separation of MoS_2.[56] Reprinted with permission from Lee et al., Anomalous Lattice Vibrations of Single- and Few-Layer MoS_2. *ACS Nano* 2010, *4*, 2695-2700. Copyright 2010 American Chemical Society.

The carrier concentration in the TMD semiconductor will also affect the phonon frequencies due to the carrier-phonon interaction. In n-type MoS_2 devices, the increase of electron concentration due to gate modulation or doping will significantly soften the A_{1g} peak but have little impact on E^1_{2g}.[60-61] This phenomenon was explained by the electron-phonon coupling at the K point when the electrons occupy the bottom of the conduction band.[61] A similar Raman peak softening due to hole-phonon coupling was also observed

in p-type WSe_2 devices.[62] As a result, Raman spectroscopy can be used to quantify the carrier concentrations in the TMD semiconductors.

Digital electronics requires transistor devices that can achieve true "1" and false "0", on and off state, respectively. To achieve a high ratio of the on-to-off current of the device (I_{on}/I_{off}) at room temperature, it generally requires a semiconductor material that has > 1 eV bandgap. Theoretical studies predicted the intrinsic mobility can reach ~400 $cm^2V^{-1}s^{-1}$ at room temperature, which is moderate compared to graphene due to a larger effective mass of the carriers.[63-64] Among all TMDs, the most prominent examples are molybdenum- and tungsten-based layered semiconductors, for example, MoS_2 and WSe_2, respectively. Field-effect transistor (FET) devices using single-layer MoS_2 have reported high I_{on}/I_{off} ratios (~10^8), moderate mobilities (~60 - 70 $cm^2V^{-1}s^{-1}$) and low subthreshold swings (74 mV/dec).[49] Monolayer WSe_2 flake-based p-type transistors also exhibited ~250 $cm^2V^{-1}s^{-1}$ mobility, 10^6 I_{on}/I_{off} ratio and ~60 mV subthreshold swing.[65-66] In addition, theoretical simulations of TMD-based transistors predict the alleviation of short-channel effect due to the atomic thickness.[67-68] Experimental studies also suggested the channel length of MoS_2-based transistors can be scaled down to sub-10 nm using high-k dielectrics.[69]

However, due to the atomically thin nature and the extremely large surface to volume ratio of TMD semiconductors, the charge carriers in the 2D TMD channels are poorly shielded, and are sensitive to the environment and the interfaces on both sides of the 2D layer. The mobility of carriers is influenced by several main scattering mechanisms:[70-72] (1) phonon scattering due to temperature; (2) Coulomb scattering at charged species; (3) phonon scattering at surfaces and interfaces; and (4) roughness

scattering. Phonon scattering affect the carrier mobility due to more active phonon vibrations with increasing temperature. Coulomb scattering is a result of the existence of charged impurities in the 2D layer or the fixed charges at the 2D/dielectric interface. As a result, the local dielectric environment plays an important role in the electronic transport properties of 2D TMD devices. Mobility is therefore highly dependent on the thickness of TMD thickness due to the screening of charged impurities and the resulting channel thickness. Carrier mobility is typically higher in few-layer samples.[73] Moreover, the measurement environment also affects the charge transport if the surface of the TMD channel is not protected. This phenomenon can be observed from the comparison of ambient versus vacuum measurement due to the physical absorption of, for example, water and O_2.[74-75] Unlike the irreversible performance degradation in organic semiconductors due to oxidation, the physisorption is reversible and can be removed by reinserting the samples into vacuum condition or by thermal annealing.

Although the nature of high sensitivity of 2D TMD devices to the surfaces, interfaces and local environments can bring challenges, this also provides some new opportunities for surface engineering and sensors. For example, the doping of 2D TMD can be achieved using surface charge transfer doping.[50] TMD-based gas sensing has also been demonstrated by detecting absorbents on the 2D surface.[76-77] The applications using surface sensitivity of 2D materials will be discussed in the following sections.

Finally, the design of metal-semiconductor interfaces is important for the operation of TMD devices. Au is commonly used as source and drain contacts in MoS_2 devices. Despite the fact that Au has a high work function of 5.1 eV while n-type MoS_2 has electron affinity of ~ 4.0 eV, the Au-MoS_2 contact is suggested to be ohmic.[49, 74, 78] This

counterintuitive observation can be explained by the very narrow Schottky barrier between the metal and the atomically TMD film, where the carrier transport is facilitated by tunneling.[79] However, it has been shown that metals with low work function, for example, scandium and titanium, can form a more ohmic (less resistive) contact to MoS_2 than those with high work function.[79] On the other hand, the transport behavior can be controlled by the choice of contact metals in ambipolar WSe_2 because the Fermi level in pristine WSe_2 is located very close to the mid-gap. High work function Pd/Au or Au metals are commonly used for p-type transport in WSe_2 devices,[80] while using low work function In or Ti/Au metals are pervasive to achieve n-type transport.[81] Furthermore, semiconducting interfacial layers including, TiO_2 and MoO_x, are used to facilitate n-type and p-type transports, respectively.[82-83]

1.5 Synthesis of TMDs

Transition metal dichalcogenides and graphite are historically known as tribological materials and lubricants due to their layered structures. Instead of using these layered materials in their bulk form, Richard P. Feynman proposed another possibility of using two-dimensional layers in his famous lecture in 1959, *"There's Plenty of Room at the Bottom"*:[84] Several early works have attempted to create the atomically thin MoS_2 layers using adhesive tape in 1966 and Li intercalation in 1986.[85-86] However, the true realization of 2D materials for modern electronic and optical applications was first demonstrated by Manchester group using mechanical exfoliated graphene flakes.[32, 87] Exfoliation of TMDs provides a convenient yet effective way to produce high-quality

TMD nanoflakes. There are two commonly used exfoliation techniques: mechanical exfoliation using "Scotch-tape" method and liquid exfoliation. "Scotch-tape" methods use adhesive tape to transfer TMD layers from the bulk crystal to a desired substrate.[32, 88] Exfoliated flakes can provide good crystallinity and quality depending on the source of natural crystals. Typical optical and atomic force microscopy images of TMD flakes from monolayer to 4 layers on SiO_2 obtained from mechanical exfoliation are shown in Figure 1-5.[89] However, this method is not practical for scalable manufacturing because the difficulties to control the size, layer thickness and yield. Typically, the fabrication of electronics with exfoliated flakes involves electron-beam lithography, which is costly and not compatible with high throughput and reproducible manufacturing. As a result, mechanically exfoliated TMD flakes are only suitable for fundamental researches and proof-of-concept devices.[49, 51, 56]

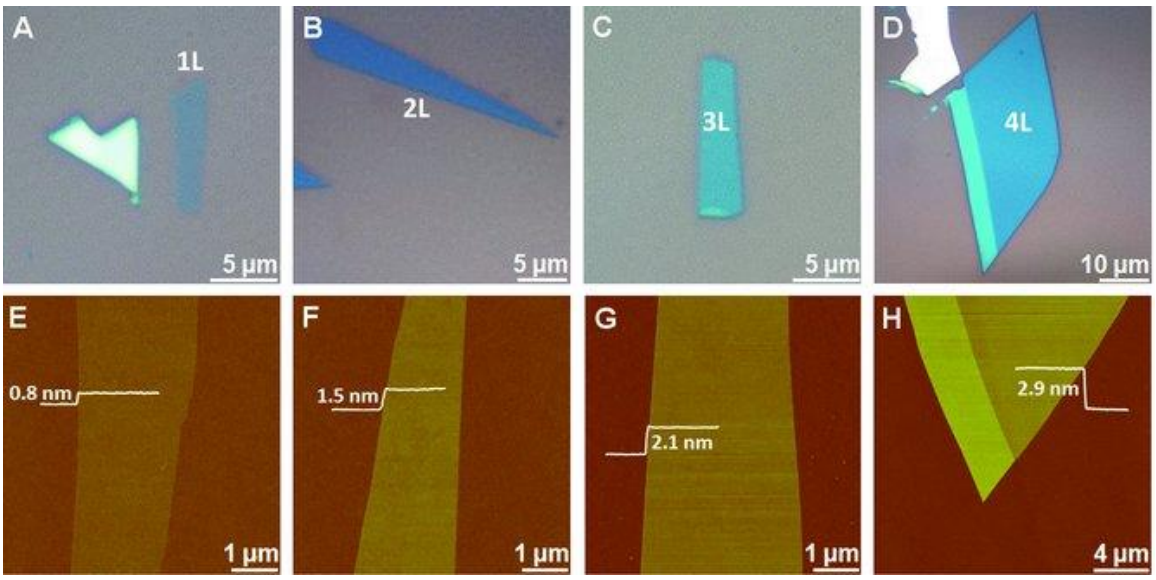

Figure 1-5 Mechanically exfoliated single- and multilayer MoS_2 films on Si/SiO_2. Optical microscope images of single-layer (1L), bilayer (2L), trilayer (3L), and quadrilayer (4L) MoS_2 films (A–D). Panels E–H show the corresponding AFM images of the 1L (thickness: ≈ 0.8 nm), 2L (thickness: ≈1.5 nm), 3L (thickness: ≈ 2.1 nm), and 4L (thickness: ≈ 2.9 nm) MoS_2 films shown in (A–D).[89] Reprinted with permission from Li et al., Fabrication of Single- and Multilayer MoS_2 Film-Based Field-Effect Transistors for Sensing NO at Room Temperature. *Small* 2012, *8*, 63-67. Copyright 2012 John Wiley & Sons.

Liquid-phase exfoliation provides a possible route for producing TMD nanoflakes in large quantity.[90-91] A schematic description of main liquid exfoliation mechanisms is shown in Figure 1-6.[91] By agitating the TMD crystals in ultrasonic bath with appropriate solvents and surfactants, the layered crystal can be exfoliated into crystalline monolayer or few-layer flakes in the size of a few hundred nanometers and further dispersed in the solution.[90, 92] In addition, the bubbles produced by sonication can move in between the layers and cause the separation of monolayers.[93] However, the yields of this method is typically low (1% or less).[94] Another liquid phase exfoliation method involves the intercalation of lithium in between TMD layers was demonstrated in 1970s, and the

concept was recently readopted.[95-96] When lithium containing compounds, for example, n-butyllithium, intercalate into atomic layers in aqueous environment, the vigorous reaction between lithium and the water will produce H_2 and therefore separate the layers.[97-98] Liquid-phase exfoliation may provide a facile way to produce TMD flake suspension solution, and permit additional applications including composites, catalysis, inkjet printing, etc. However, it is not suitable for scalable electronic applications due to the lack of uniformity.

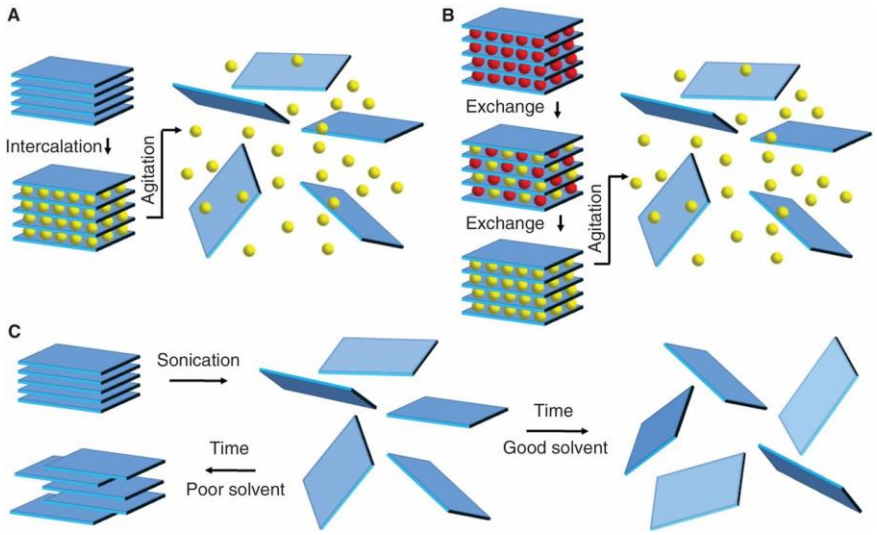

Figure 1-6 Schematic description of the main liquid exfoliation mechanisms.[91] (A) Ion intercalation. Ions (yellow spheres) are intercalated between the layers in a liquid environment, swelling the crystal and weakening the interlayer attraction. Then, agitation (such as shear, ultrasonication, or thermal) can completely separate the layers, resulting in an exfoliated dispersion. (B) Ion exchange. (C) Sonication-assisted exfoliation. The layered crystal is sonicated in a solvent, resulting in exfoliation and nanosheet formation. Reprinted with permission from Nicolosi et al., Liquid Exfoliation of Layered Materials. *Science* 2013, *340*. Copyright 2013 The American Association for the Advancement of Science.

In order to achieve large scale manufacturing of TMD-based electronic devices using state-of-the-art IC technology, it is crucial to obtain large-area TMD films with good control in uniformity, thickness, crystal quality and scalability. Bottom-up approaches using vapor phase techniques are promising for the synthesis of TMDs on the desired substrates in a controllable and scalable fashion.[99] To date, chemical vapor deposition (CVD) and other similar vapor-based methods are the most successful method to deposit both large-area graphene[100] and TMDs. Most of the proposed vapor-based synthesis processes require the TMD constituent elements (metal and sulfur/selenium) in vapor phase reaching the substrate surface placed downstream of carrier gases at elevated temperature. The reaction that forms MX_2 can occur either on the substrate or in the vapor phase. It is important to control the flow dynamics and temperature in the synthesis furnace to achieve scalability, uniformity and thickness control. Vapor phase synthesis of TMDs can be categorized into two main methods based on the source of the metal precursors: (1) deposition of MX_2 produced in vapor-phase reaction of metal (-containing) gas and chalcogen (-containing) gas onto the substrate, and (b) the conversion of metal (-containing species) coated substrate by chalcogen gas. A summary of primary growth techniques of TMD is shown in Figure 1-7.[101]

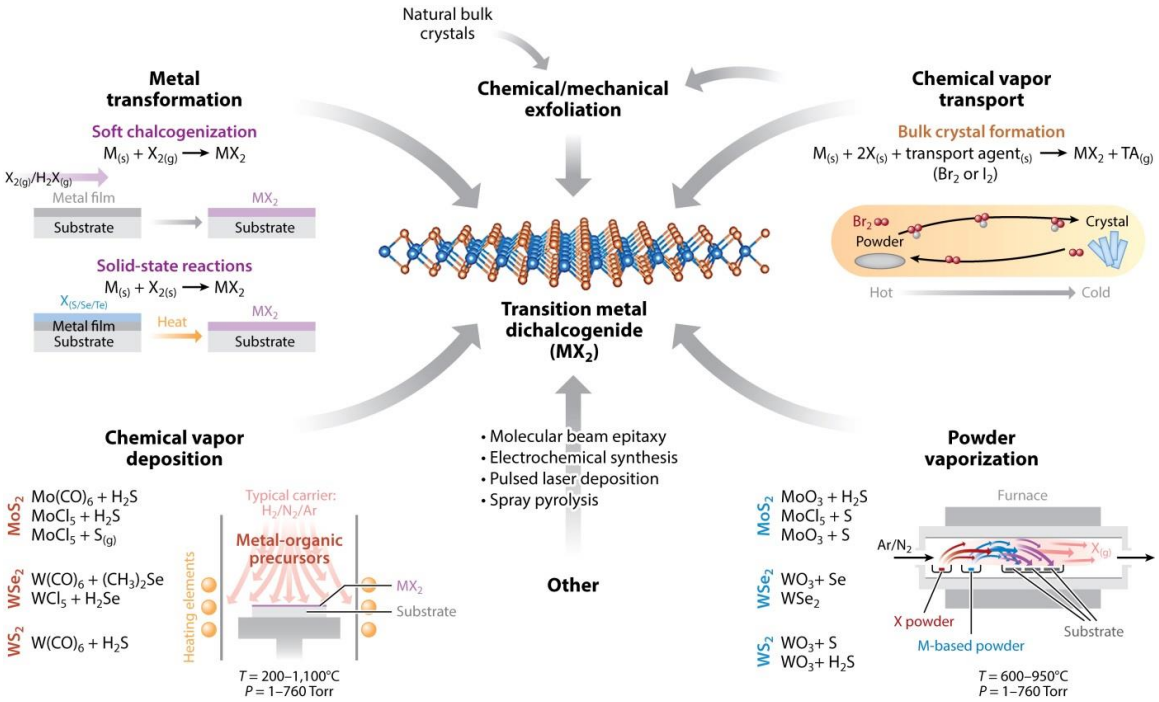

Das S, et al. 2015.
Annu. Rev. Mater. Res. 45:1–27

Figure 1-7 Summary of primary growth techniques for the formation of monolayers of transition metal dichalcogenides.[101] These methods include chemical vapor deposition, powder vaporization, metal transformation, chemical vapor transport, chemical exfoliation, pulsed laser deposition, molecular beam epitaxy, spray pyrolysis, and electrochemical synthesis. Reprinted with permission from Das et al., Beyond Graphene: Progress in Novel Two-Dimensional Materials and van der Waals Solids. *Annual Review of Materials Research* 2015, *45*, 1-27. Copyright 2015 Annual Reviews.

Different metal and chalcogen precursors are used for the vapor phase synthesis of TMDs. Sulfur powders are the most commonly used sulfur sources for the sulfides. Sulfur has the melting point of 115 °C and will evaporate into sulfur gas. The sulfur powder can be placed in a crucible in the furnace and transported to the substrate by carrier gases, usually inert gases, for example, N_2 or Ar. The sulfur vapor pressure depends on the temperature[102], the amount of sulfur powder in the crucible and the

chamber pressure of the furnace. The direct use of sulfur powder in the furnace is simple but may cause some problems for reproducibility. Alternatively, bubbler or heated canister filled with sulfur powder can be installed outside the reacting chamber and provide sulfur vapor through the gas pipe upon heating, the flow of sulfur vapor can be controlled using valves or mass flow controller. Beside elemental sulfur, colorless hydrogen sulfide (H_2S) gas is another commonly used sulfur source. A more cautious design should be adopted for using H_2S because it is poisonous, corrosive and explosive. Similarly, Se powder/pellet and H_2Se are the most common Se sources for the vapor-phase synthesis of selenides.

Depending on the synthesis methods, molybdenum can be supplied through the Mo-containing vapor or Mo or Mo-compound-coated substrates. Mo is a refractory metal with the melting point of 2623 ºC, so it is extremely difficult to vaporize Mo metal in a crucible directly. Instead, to provide a Mo-containing vapor, Mo compounds including MoO_3, $MoCl_5$ and $Mo(CO)_6$ are commonly used. Similarly, WO_3, $WOCl_4$, WCl_6 are commonly used W source.

First, TMDs can be synthesized using both M and X gaseous precursors. Typically, S and Se solids are place in the crucible upstream of the furnace while M-containing precursors are placed near the substrate. The chalcogen vapor was transported downstream and react with M precursors, for example, MoO_3 and WO_3 at higher temperature, typically > 650 °C. During the sulfurization, MoO_3 and WO_3 will firstly be reduced to suboxides, MoO_{3-x} and WO_{3-x}, by S vapors and then transported to the substrates.[103-106] The suboxides will further react with S and from MoS_2 or WS_2.[107-108] The proposed mechanism for MoS_2 synthesis is:

$$2MoO_3 + S \rightarrow 2MoO_{3-x} + SO_2$$

$$2MoO_{3-x} + (7-x)S \rightarrow 2MoS_2 + (3-x)SO_2$$

where x = 1 indicates the formation of intermediate phase MoO_2. According to Mo-O-S ternary phase diagram as shown in Figure 1-8, MoO_{3-x} suboxide is a facile intermediate phase to react with S and form MoS_2.[109] As a result, a reducing environment, for example, H_2, promotes the formation of suboxides and benefit the synthesis of TMDs. The proposed reaction involving H_2 atmosphere is:

$$MoO_3 + H_2 \rightarrow 2MoO_2 + H_2O$$

$$MoO_2 + S_2 \rightarrow MoS_2 + O_2$$

Note that the real reaction of MoO_{3-x} or MoO_2 formation can be a combined effect from both S and H_2.

It is also reported that the presence of suboxides is not only important for sulfurization but also, especially, selenization due to the lower reactivity of Se than S.[110] The proposed mechanism for WSe_2 synthesis is:

$$WO_3 + 2Se + H_2 \rightarrow WSe_2 + H_2O + SeO_2$$

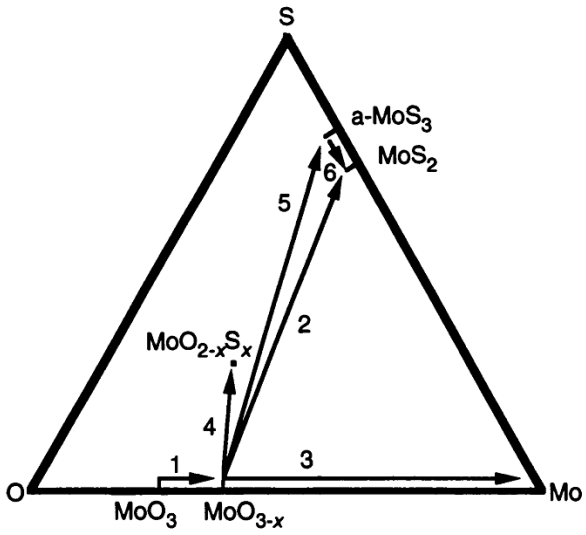

Figure 1-8 Ternary phase diagram of Mo-O-S system.[109] Reprinted with permission from Feldman et al., High-Rate, Gas-Phase Growth of MoS_2 Nested Inorganic Fullerenes and Nanotubes. *Science* 1995, *267*, 222-225. Copyright 1995 The American Association for the Advancement of Science.

Typically, the aforementioned vapor-vapor synthesis results in relatively small MX_2 triangular grains (<100 μm) due to the nucleation-initiated growth.[104-105] Because atoms around the edges of triangular grain have higher reactivity than the ones on the basal plane, the lateral growth of a grain is preferred under controlled condition.[99] The resulting triangular grains will then coalesce into a larger film. Figure 1-9 shows an optical image of MoS_2 sample from vapor-vapor CVD synthesis. It is observed that the film consists of numbers of triangular grains in the size around 10 – 20 μm. Other precursors, such as $MoCl_5$, have been used to improve grain size and thickness uniformity due to a better control over Mo partial pressure.[111] In addition, nucleation promoters (seeds) were proposed to improve the uniformity by providing the controlled nucleation sites.[112-113] Alternatively, large-scale growth of TMD films using metal-

organic CVD (MOCVD) were recently demonstrated using gaseous metal-organic precursors including $Mo(CO)_6$, $W(CO)_6$, $(CH_3)_2S_2$, $(CH_3)_2Se$ and H_2S.[114-116] Atomic layer deposition (ALD) is another promising method to achieve precise thickness control, uniformity and conformity due to the self-limiting supply of the precursors and purging steps using appropriate precursors.[117-119]

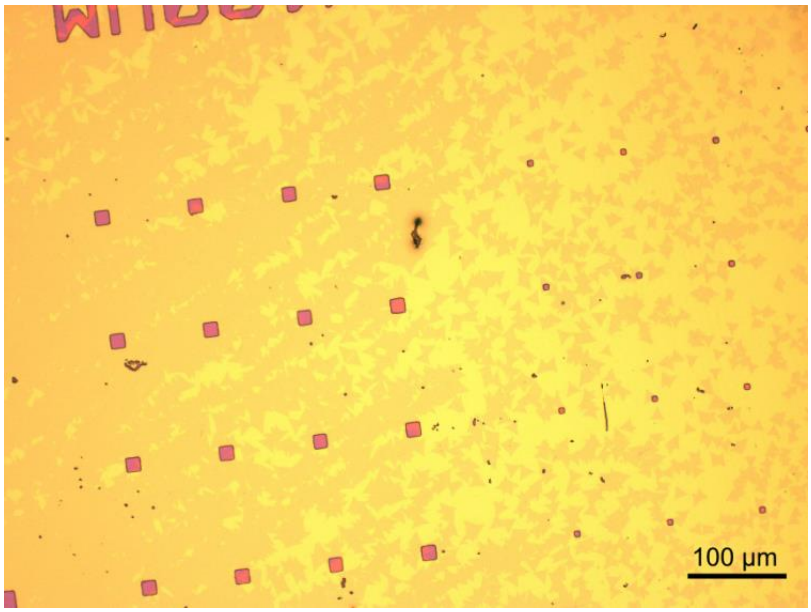

Figure 1-9 Optical image of MoS_2 film showing the coalescence of individual triangular grains into a continuous film using CVD growth.

Finally, one of the most convenient ways to synthesize large-area TMD films is the direct sulfurization of selenization of metal (or metal oxide) films predeposited on the substrates.[120-128] In principle, this method has the advantage of controlling the thickness by adjusting the thickness of metal or metal-containing layers and can provide a wafer-

scale material with high uniformity. Figure 1-10 shows the optical images and STEM images of trilayer MoS_2 by direct sulfurization of 1 nm Mo films. Metal films are usually deposited with e-beam evaporation or sputtering; lower melting point compounds including MoO_3 and WO_3 are also commonly used as a starting layer. Despite the fact that the conversion process is convenient, high temperature (> 750 °C) is usually required for complete sulfurization or selenization of the thin films. Prior work has demonstrated that the quality of the TMD film highly depends on the growth temperature.[124] While the A_{1g} and E^1_{2g} peak separations in Raman spectra of MoS_2 films remains unchanged under different growth temperatures, the full width at half maximum (FWHM) decreases with growth temperature and reaches the bulk crystal value for 1050 °C samples. In addition, grazing incident angle x-ray diffraction (GIAXRD) analysis confirmed the decrease of FWHM with increasing growth temperature toward bulk value, indicating improved crystallinity at higher growth temperature. When a metal is deposited on the substrate, ambient air will typically result in the formation of a thin native oxide on the surface. Similar to the vapor-vapor CVD process, the conversion of either this native oxide or MoO_3 film into more reactive suboxides is critical in the synthesis. As a result, a reducing H_2/Ar or H_2/N_2 environments are usually use to reduce the metal oxides on the surface before introducing chalcogen species. The reaction mechanisms are similar to those for vapor-vapor CVD process discussed previously.

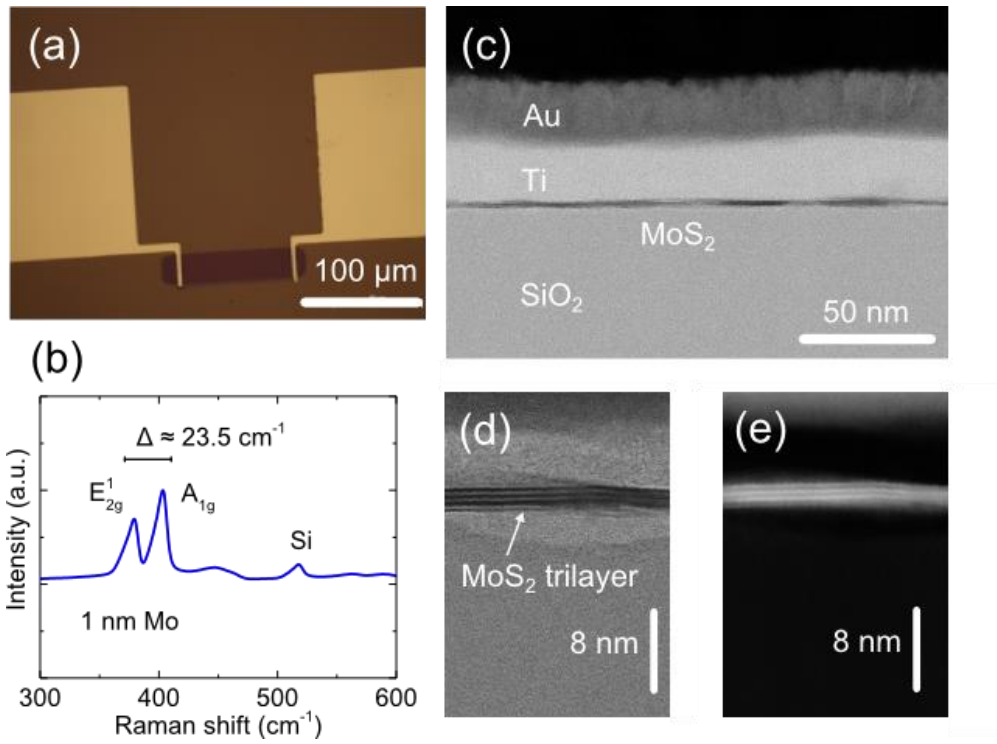

Figure 1-10 (a) An optical image of a fabricated MoS_2 FET. (b) A representative Raman spectrum of trilayer MoS_2 synthesized by direct sulfurization of Mo film. (c) The cross-sectional TEM image of $Au/Ti/MoS_2/SiO_2$ stacking from MoS_2 FET device. The TEM sample was prepared using focused ion-beam (FIB) (d)-(e) Enlarged TEM images under bright and dark field trilayer MoS_2 sample. A trilayer structure is clearly shown.

The thickness of TMD films can be easily controlled by the thickness of deposited layers. However, a transition from horizontally aligned layers to vertically aligned layers may be observed when the starting metal thickness exceeds the threshold value.[122, 129-130] This transition of layer alignment has been experimentally shown in Figure 1-11.[130] The mixture of both horizontally and vertically aligned grains was also observed with intermediate metal thicknesses. In addition, the crystal structure and morphology of TMDs through direct conversion are limited to the starting layers. Therefore, it is critical

to control the thickness, uniformity, coverage and morphology of initial metal (or metal oxide) films to achieve highly uniform TMD films.

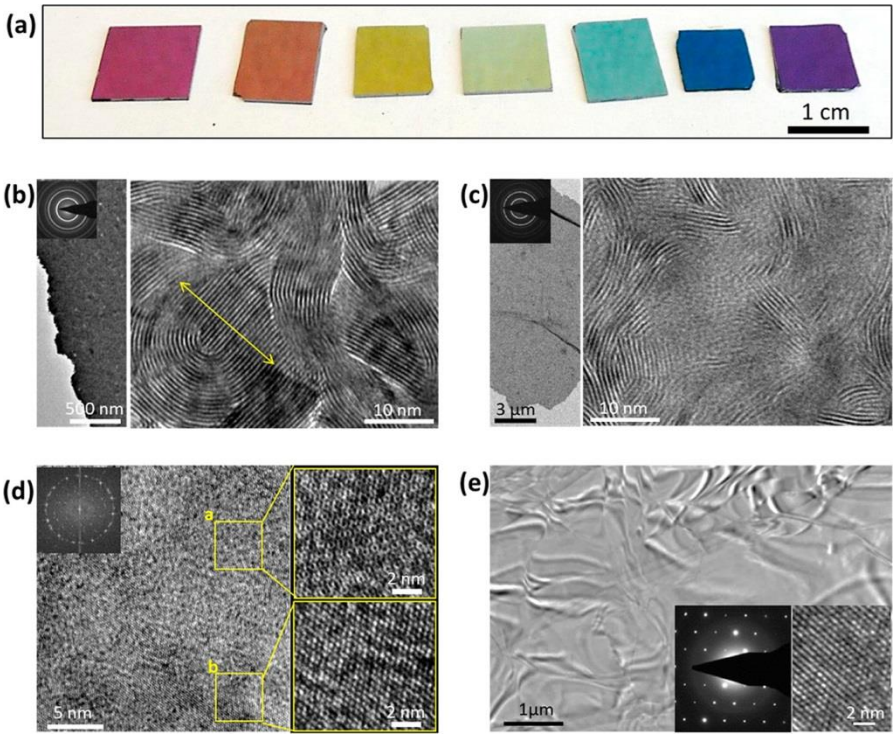

Figure 1-11 (a) A photography of as-grown MoS_2 on SiO_2/Si substrates grown with Mo seed layer of 20, 15, 10, 7, 5, 2, and 0.3 nm, respectively (from left to right). (b–e) TEM characterizations of MoS_2 grown with (b) 10 nm Mo, (c) 4 nm Mo, (d) 1 nm Mo, and (e) 0.3 nm Mo.[130] Reprinted with permission from Jung et al., Metal Seed Layer Thickness-Induced Transition From Vertical to Horizontal Growth of MoS_2 and WS_2. *Nano Lett.* 2014, *14*, 6842-6849. Copyright 2014 American Chemical Society.

In addition to e-beam deposited or sputtered metal films, a solution-processable dip-coating of ammonium thiomolybdates $(NH_4)_2MoS_4$ has been demonstrated as initial layer for MoS_2 conversion. Using a similar conversion process, the Mo-salt is first

converted to MoS_3 at first low temperature step (500 °C) and then again to crystalline MoS_2 at 1000 °C in S vapor environment. The proposed reaction mechanism is:

$$(NH_4)_2MoS_4 \rightarrow 2NH_3 + H_2S + MoS_3$$

$$2MoS_3 \rightarrow 2MoS_2 + S_2$$

H_2 can promote the desulfurization of MoS_3 to MoS_2 by forming H_2S:

$$(NH_4)_2MoS_4 + H2 \rightarrow 2NH_3 + 2H_2S + MoS_3$$

$$MoS_3 + H_2 \rightarrow MoS_2 + H_2S$$

Alloying of TMD films by controlling the metal of chalcogen species is possible during the CVD synthesis. The final composition of the 2D TMD depends on the composition of the precursors. For example, the synthesis of WS_2Se_{2-x} by co-evaporation of WS_2 powder and WSe_2 powder in a CVD furnace.[131] The bandgap of resulting ternary alloy depends on the S to Se ratio and follow the linear relationship $E_g(WS_{2x}Se_{2-2x}) = xE_g(WS_2) + (1-x)E_g(WSe_2)$. Using similar approach, $MoS_{2x}Se_{(2-2x)}$ can also be synthesized by using MoO_3 and S/Se mixture precursors under an 800 ˚C growth process.[132-133] Tunable bandgap of $MoS_{2x}Se_{(2-2x)}$ is linearly dependent on the S/Se composition ranging from 1.85 eV (for pure MoS_2) to 1.55 eV (pure $MoSe_2$). The evolution of PL peaks of $WS_{2x}Se_{(2-2x)}$ and $MoS_{2x}Se_{(2-2x)}$ with S/Se composition is shown in Figure 1-12(a) and (b), respectively.[131] A linear relationship between bandgap of $MoS_{2x}Se_{(2-2x)}$ and S/Se ratio calculated from PL peak positions is shown in Figure 1-12(c).[132] In addition, the transition of electrical transport behaviors from n-type WS_2 to p-type WSe_2 transistors is shown in Figure 1-12(d).[131]

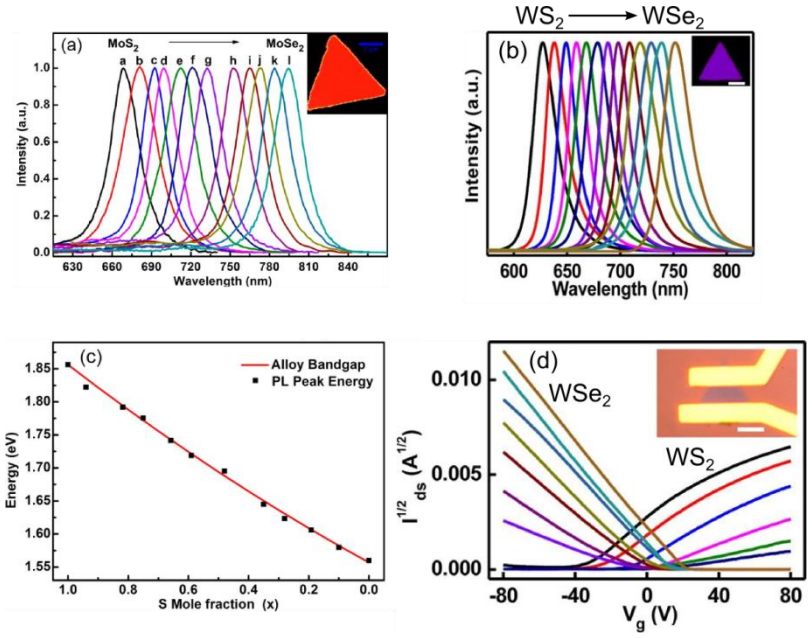

Figure 1-12 PL properties of $WS_{2x}Se_{(2-2x)}$ and $MoS_{2x}Se_{(2-2x)}$.[131-132] (a) The evolution of PL peak of $MoS_{2x}Se_{(2-2x)}$ from pure MoS_2 to pure $MoSe_2$. (b) The evolution of PL peak of $WS_{2x}Se_{(2-2x)}$ from pure WS_2 to pure WSe_2. (c) The optical band gap of $MoS_{2x}Se_{(2-2x)}$ measured from PL peak position. The band gap decreases as S content decreases. (d) The transition of electrical transport behaviors from n-type WS_2 to p-type WSe_2 transistors. (a) and (c): Reprinted with permission from Li et al., Growth of Alloy $MoS_{2x}Se_{2(1–x)}$ Nanosheets with Fully Tunable Chemical Compositions and Optical Properties. *J. Am. Chem. Soc.* **2014,** *136*, 3756-3759. Copyright 2014 American Chemical Society. (b) and (d): Reprinted with permission from Duan et al., Synthesis of $WS_{2x}Se_{2–2x}$ Alloy Nanosheets with Composition-Tunable Electronic Properties. *Nano Lett.* **2016,** *16*, 264-269. Copyright 2016 American Chemical Society.

Similar to the substitution of chalcogen atoms, transition metal atoms substitution in TMDs can also be achieved. Group V elements, for example, Nb, can serve as an acceptor in group VI TMDs system due to one less electron in its *d*-orbital. Nb-doped p-type MoS_2 can be synthesized by sulfurization of Mo-Nb-Mo stacked structure.[134] In contrast, Re from group VII has one more *d*-electron than group VI metals and can create

donor levels and n-doping the group VI TMDs. In addition, Re-doping can induce the phase change from 2H semiconductor phase to 1T metallic phase in MoS_2.[135]

In summary, various techniques have been demonstrated for bottom-up synthesis of transition metal dichalcogenides. Large-area, scalable, high-quality, uniform and homogeneous film is especially important for the practical application of TMDs. Some challenges including defects, grain size, synthesis temperature and cost of TMDs fabrication remain to be overcome.

1.6 Doping of TMD semiconductors

Doping is a powerful tool to control the electrical and optical properties of both bulk[136] and 2D semiconductors.[50, 137-138] Traditionally, doping can be achieved in bulk semiconductors by introducing substitutional impurities into the lattice of host materials. These impurities with different valencies from the host materials will produce extra carriers, and create donor or acceptor levels. Among all, thermal diffusion and ion implantation are two of the most efficient yet controllable way to dope bulk semiconductors.

It have been reported that even low-energy ion-implantation process could cause structural defects and degrade the graphene,[139] and other atomically thin 2D materials. Therefore, several alternate processes for doping of 2D materials have been proposed. Plasma treatment with SF_6, CF_4, CHF_3, O_2 and phosphorus can be used to p-dope MoS_2 by introducing atoms with larger electron affinity into the films.[140-141] The n-doping

effect can also be achieved in WSe_2 by inducing Se vacancies using H_2 or He plasma.[142] However, it is difficult to avoid surface etching and lattice damage under plasma. Extremely careful control of the RF power of the plasma source and the treatment time is required.

Controlled doping of 2D semiconductors using surface charge transfer doping provides a promising method to modify their electrical properties and improve device performance for both bulk and low-dimension materials.[143-144] The charge transfer doping requires electron exchange between dopants and the semiconductors when matching disposition of empty and occupied electronic levels for involved species are present. Depending on the electron affinity of the dopants, i.e., the ability to accept or donate electrons, the carriers can be induced in the semiconductor channel.[145-146] The comparative mechanisms of classical substitutional doping and surface charge transfer doping of semiconductors are illustrated in Figure 1-13.[145] p-Doping is used as an example here. In classical doping, as discussed previously, the dopant (or impurity) atoms typically have lower valency than the host atoms, and tend to "steal" electrons and create acceptor levels as shown in the left panel of Figure 1-13. Similarly, such electron exchange can also be achieved when the lowest unoccupied molecular orbital (LUMO) of the molecular dopants is close to the valence band maximum (VBM) of the semiconductors. As a result, holes will be induced in the semiconductors while electrons will be localized on the surface acceptors. The resulting electrostatic force due to the charge separation will confine the holes in the perpendicular direction to the surface but leave them free to move parallel to the surface. The existence of surface and interfacial states that will accept the electrons/holes will undermine the effects of surface charge

transfer doping especially in conventional bulk semiconductors.[144] In addition, the localized carriers close to the surface can make little contribution to the bulk properties of conventional semiconductors.

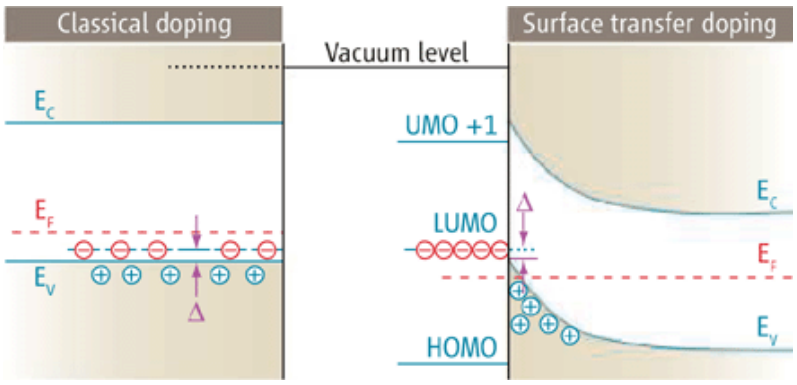

Figure 1-13 The comparative mechanisms of classical substitutional doping and surface charge transfer doping of semiconductors.[145] Reprinted with permission from Ristein, J., Surface Transfer Doping of Semiconductors. *Science* **2006,** *313*, 1057-1058. Copyright 2006 The American Association for the Advancement of Science.

Instead, charge transfer doping is an effective doping tool for low-dimension materials, especially 2D materials, due to large surface-to-volume ratio in these materials. The advancement of controllable charge transfer doping on 2D materials, especially TMDs, will be discussed in the following paragraphs. The strategies of stable charge transfer doping methods for long-term device operation will be also discussed.

1.6.1 Volatile doping

The electrical properties of TMDs are sensitive to the outer environments. As a result, it has been demonstrated that the adsorbed gas molecules will affect the concentration as well as distribution of carriers in the host materials, theoretically[147-148]

and experimentally.[77, 89, 148-150] It was observed that the PL intensity of MoS_2 increases upon the continuous exposure to air, H_2O and O_2 gases, while no change in inert atmospheres.[148] The exposure to air, H_2O and O_2 gases also caused p-doping in the MoS_2 transistors due to the electron transfer from MoS_2 to the gaseous acceptors. However, the doping is reversible and volatile because these physisorbed gas molecules can be removed by inserting the MoS_2 samples back into vacuum.[148] This partial charge transfer relies on the existence of gas dopants on the surface. Once the supply of the gas is terminated in the environment, the surface molecules are desorbed and MX_2 instantly go back to undoped states.[50, 137] For MoS_2 and WSe_2, NO_x, H_2O and O_2 are demonstrated to be volatile p-dopants due to their high redox potential;[65, 148, 150] ethanol and NH_3 are n-dopants.[149-150] Further treatment may convert the physisoprtion to chemisorption. For example, WSe_2 can react with physisorbed NO_2 after annealing at 150 ˚C and form $WSe_{2-x-y}O_xN_y$ species.[151] After chemisorption, a degenerate doping effect was observed and the WSe_2 channel becomes metallic. However, the disruption of lattice structure of WSe_2 is irreversible. In addition, the chemisorption and p-doping can be also achieved by the interaction between PH_3 gas molecules and the chalcogen vacancies in MX_2 induced by laser-assisted doping.[152]

1.6.2 Non-volatile doping

Non-volatile doping using solid-state substances including alkali metals, noble metals and inorganic/organic compounds provides a refined technique for charge transfer doping, and solve the issues of aforementioned volatile doping methods relying on gas adsorption. Recently, potassium ions were used to n-dope the MoS_2 and WSe_2,[153] and an increase in channel current was observed in the expense of reduced on/off ratio.

However, K is not CMOS-compatible due to its high diffusivity and the resulting stability issues for semiconductor devices. Also, the high reactivity of K with ambient environment further hinders this method for practical applications. Alternatively, other alkali metal salt including $CsCO_3$ and LiF are also n-dopants.[154-155] The nanoparticles (NPs) of noble metals, including Au, Ag, Pd and Pt NPs, can be used for charge transfer doping of TMDs.[62, 156] These noble NPs can induce p-doping effect on MoS_2-flake based FETs due to the electron transfer from MoS_2 to metal particles with higher work function. The doping strength increases with the metal work function as well as the amount of noble NPs on the TMD surface.[156] Similarly, p-doping effects were also observed by immersion of TMD films in $AuCl_3$ solution and the resulting Au cluster formation on the TMD surface.[157-158]

Inorganic compounds have been demonstrated for doping of TMDs. The doping mechanism and the charge transfer were explained by the re-alignment of Fermi level of TMDs upon the contact with low/high-work-function materials.[159-160] Oxides with high work function are demonstrated to be p-dopants, for example, WO_x,[159] MoO_x,[161-164] etc. In contrast, oxides with low work function including ZnO_x[31] and TiO_x[162, 164-165] are n-dopants. Apart from charge transfer, the metal oxides can be used as interlayer materials at metal/semiconductor interface. The alignment of fermi levels and the relative position to valence band maximum (VBM) or conduction band minimum (CBM) can facilitate or hinder the carrier transport.[83, 164] The doping effect using metal oxide overlayers depends on the concentration of oxygen vacancies because of its influence on the work function of metal oxides. Similar stoichiometry related work function difference of MoO_x and their doping effect on TMDs was also observed.[161] Using metal oxide dopants, the doping

effect can be controlled by deposition parameters, thickness, stoichiometry and phase of the oxides using PVD, CVD or solution process.

Organic compounds are by far the most commonly used dopants for 2D TMDs due to a versatile choice of dopants, convenient solution process and controllable doping effects. The doping is achieved by charge transfer between semiconductors and organics which are mostly physisorbed on the surface in solution. Generally, dopants with low redox potential or negative-pole (δ^-) functional groups tend to induce n-doping effect and vice versa. Redox potentials of commonly used dopants for TMDs are summarized in Figure 1-14.[50] Organics containing $-NH_2$ with a lone pair of electron and can draw holes from the host materials. Commonly used $-NH_2$ containing n-dopants including polyethylenimine (PEI),[166] (3-aminopropyl)triethoxysilane (APTES),[167] hydrazine,[168] etc. are explored. In contrast, organics containing $-CH_3$ positive poles, for example, octadecyltrichlorosilane (OTS),[167, 169] will draw electrons from the host materials and induced p-doping effects. By adjusting dopants type, solution concentration and immersion time, the doping strength can be controlled. In addition, oxidizing agents including 7,7,8,8-tetracyanoquinodimethane (TCNQ) and 2,3,5,6-tetrafluoro-7,7,8,8-tetracyanoquinodimethane (F_4TCNQ), and reducing agents such as nicotinamide adenine dinucleotide (NADH) were used as p- and n- dopants, respectively.[170] Air-stable benzyl viologen (BV) was demonstrated to induce non-degenerate and degenerate n-doping of MoS_2 by controlling the solution concentration.[171] Recently, electron-rich octahedral superatom $Co_6Se_8(PEt_3)_6$ was used as an effective n-dopant.[172] WSe_2 FETs based on exfoliated flakes can be converted from p-channel to n-channel after the n-doping using this superatom treatment. Although the aforementioned dopants provide a wide range of

choices for charge transfer doping of TMDs, they are physically adsorbed on the surface and can be desorbed by the dissolution back to the solvent. For example, the doping effect using BV is reversible by reinserting the sample into toluene.[171] In addition, electron-rich or electron-deficient organics can induce n-doping or p-doping only via partial charge transfer, i.e. the displacement of electron distribution at the dopant/TMD interface, and can be undoped easily.

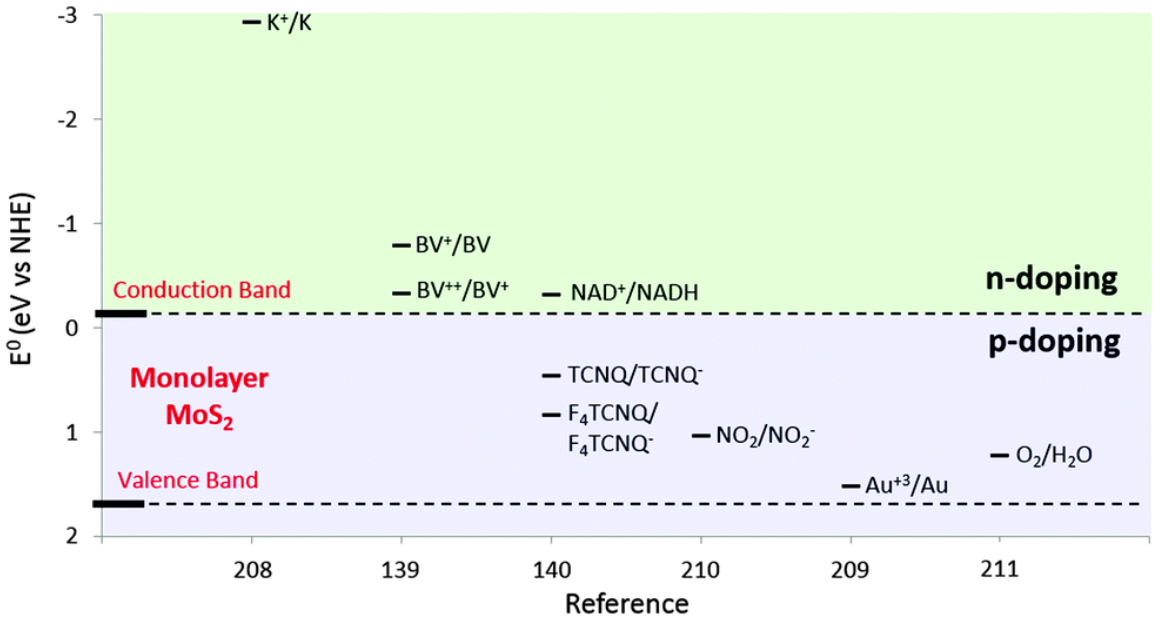

Figure 1-14 Standard reduction potentials of chemicals used for charge-transfer doping of TMDs and the energy level of the valence and conduction band edges of monolayer MoS_2.[50] BV, benzyl viologen; NADH, nicotinamide adenine dinucleotide; TCNQ, 7,7,8,8-tetracyanoquinodimethane; F_4TCNQ, 2,3,5,6-tetrafluoro-7,7,8,8-tetracyanoquinodimethane. Reprinted with permission from Schmidt et al., Electronic transport properties of transition metal dichalcogenide field-effect devices: surface and interface effects. *Chem. Soc. Rev.* **2015,** *44*, 7715-7736. Copyright 2015 The Royal Society of Chemistry.

In order to achieve stable charge transfer doping, a surface charge transfer process coupled with a chemical reaction provides a promising approach due to the formation of ions. As a result, doping with metal-organic redox-active molecules that form large, stable ions after charge transfer can be potentially advantageous.[173-174] After charge transfer, the doping products stay on the surface of host materials due to the stable electrostatic force. The doping mechanisms for n-doping using metal-organic redox-active dimers are described in Figure 1-15.[173] Such electron-donating and electron-accepting molecular species are widely used to modify organic semiconductors,[175-176] carbon nanotubes[177-178] and graphene[174] and offer a simple, yet scalable, doping process by changing the dopant concentration and treatment time. However, there has been limited research to date on the doping of TMDs using molecular reductants and oxidants. As one example, Figure 1-16 shows a schematic of the n- and p- doping of graphene using different metal-organic redox-active molecules.[174]

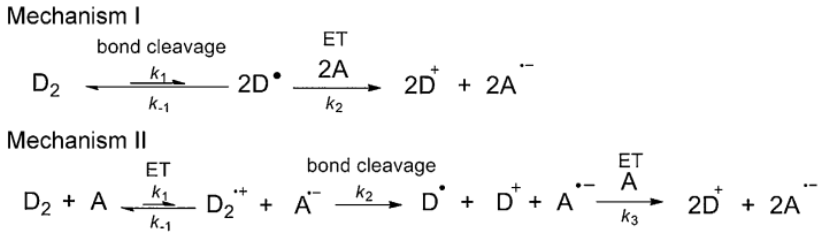

Figure 1-15 Doping mechanisms by which dimeric n-dopants (D_2) can react with acceptors (A).[173] Reprinted with permission from Zhang et al., n-Dopants Based on Dimers of Benzimidazoline Radicals: Structures and Mechanism of Redox Reactions. *Chem. Eur. J.* **2015,** *21*, 10878-10885. Copyright 2015 John Wiley & Sons.

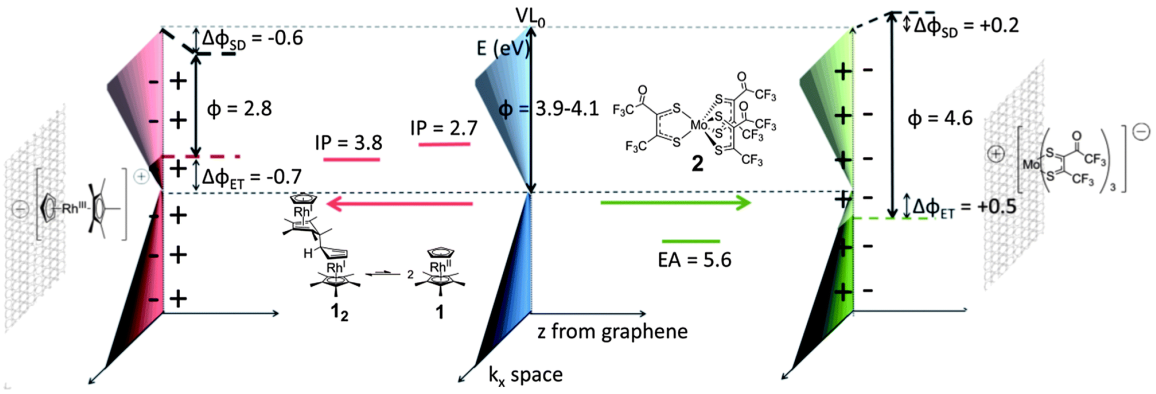

Figure 1-16 Chemical doping of graphene using redox molecules. The carrier concentration in the material is changed due to the electron transfer between dopants and graphene. Extra electron filling above conduction band of graphene after n-doping with electron-donating molecules, untreated graphene (middle) and decreased number of electrons in valence band after p-doping with electron-accepting molecules (right) are shown.[174] Schematic representation of n- and p-doping of graphene by 1_2 (in equilibrium with 1, 10 min dip) and 2 (overnight dip), with associated energy levels. IP, EA and WF (ϕ) values were estimated from electrochemical and UPS data. The pristine graphene ϕ depended on the batch (4.1 eV for the sample before n-doping and 3.9 eV before p-doping). After treatment, the ϕ is affected by electron transfer (ET) between dopant and graphene, shifting the Fermi level (E_F) relative to the Dirac point (E_D), and the induced surface dipoles (SD) from the resulting charges, which change the local vacuum level (VL). Reprinted with permission from Paniagua et al., Production of heavily n- and p-doped CVD graphene with solution-processed redox-active metal-organic species. *Mater. Horiz.* **2014,** *1*, 111-115. Copyright 2014 The Royal Society of Chemistry.

Beyond charge transfer doping, solution-processed chemical treatment can also passivate and repair the defects in TMDs. For example, the surface S vacancies in MoS_2 can be filled and repaired via the attachment of thiol by immersing the sample in solution.[179-180] Recently, solution-processed superacid treatment was used in both S-based and Se-based TMDs.[181-182] It was demonstrated that bis(trifluoromethane)sulfonimide (TFSI) superacid can passivate/repair the S-based TMDs and significant improvement of photoluminescence quantum yield to near unity was observed. However, the Se-based

TMDs are insensitive to superacid treatment. The underlying mechanism of superacid treatment remains unknown and should be investigated.

1.7 Strain-band structure relationship of TMDs

Tunable electronic band structure via strain engineering is another interesting property that 2D TMDs can offer. Similar to graphene, TMD layers exhibit very high tensile strength and maintain linear stress-strain behavior before rupture, enabling the elastic strain engineering of ultra-strength materials.[183-184] As discussed in Chapter 1-1, the atomically thin nature of 2D materials has the potential for a large strain before failure and is promising for flexible electronics applications.[185-186] Comparison of Young's moduli, tensile strength and elongation before fracture for several engineering materials are summarized in Table 1-2.[184, 186-187] Especially the elongation before fracture, 2D materials, including graphene and TMDs, provide a significant elastic strain limit without yielding. The experimental elongation of suspended monolayer MoS_2 can reach up to 10 % before fracture in agreement with its theoretical Mo-S chemical bond strength. [184, 186-187]

Table 1-2 Mechanical properties of strong engineering materials, including 2D materials[184, 186-187]

material	Young's modulus E_{Young} (GPa)	Tensile strength σ_{max}^{eff} (Gpa)	Elongation before fracture (%)
Stainless steel ASTM-A514	205	0.9	0.4
Steel alloy 4340	207	1.76	12
Polyimide	2.5	0.23	9
Tungsten	400	0.76	2
Kevlar 49	112	3	2.6
Carbon fiber	200 - 750	4.65 – 7.1	1.8
Bulk MoS_2	238	-	-
Carbon nanotube	1000	11 - 63	1.1 – 6.3
Graphene	1000	130	13
Monolayer MoS_2	270 - 330	16 - 30	6 - 11

Mechanical strain has a large impact on the band structure of 2D materials. Tensile strains applied to 2D TMDs will induce a spatial extension of mainly an increase of the X-M-X bond angles but only a slight increase in M-X bond lengths.[188-190] As a result, the increased distance between metal atoms leads to the reduction in the *d*-orbital hybridization and *d*-band width that govern the electronic structure of TMDs.[190-193] One of the strongest electro-mechanical effects is the reduction of the band gap upon applied tensile strain shown both theoretically and experimentally. The unit cell of TMD lattice

and the corresponding Brillouin zone are depicted in Figure 1-17. The valence band maximum (VBM) and conduction band minimum (CBM) of TMD are mainly described by the orbital hybridization d_{xy}-$d_{x^2-y^2}$ and d_{z^2}, respectively.[192] In the case of monolayer MX_2 with direct band gap, the Γ to K indirect band gap became smaller than the K to K direct band gap under tensile strain of ~ 1%, leading to a direct to an indirect transition.[191, 194-195] For multilayer MX_2, the Γ to K indirect band gap continues to shrink with increasing tensile strain.[191, 196] With the tensile strain increase to ~ 10%, the energy of the VBM at Γ point and that of CBM at K point overlap with each other, and both monolayer and multilayer MX_2 become metallic.[197] In contrary, the compressive strain will increase the Γ to K indirect band gap.[188, 195, 198] The calculated band structure and band gap values of MoS_2 under both compressive and tensile strain using first-principle density functional theory (DFT) method are shown in Figure 1-18.[195] The equilibrium of lattice constant *a* is 3.16 Å. Compressive and tensile strain will decrease (a < 3.16 Å) and increase (a > 3.16 Å) the lattice constant, respectively.

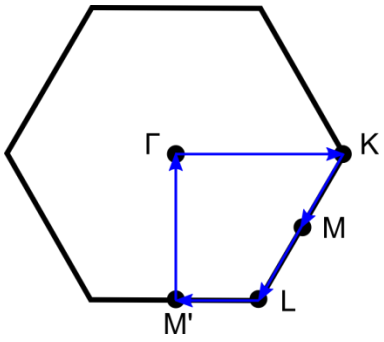

Figure 1-17 Brillouin zone of MX_2. Under symmetrical strain, M' is reduced to M and the irreducible path is ΓKML. ΓKMLM'L enclosure represents the asymmetrical strain conditions.

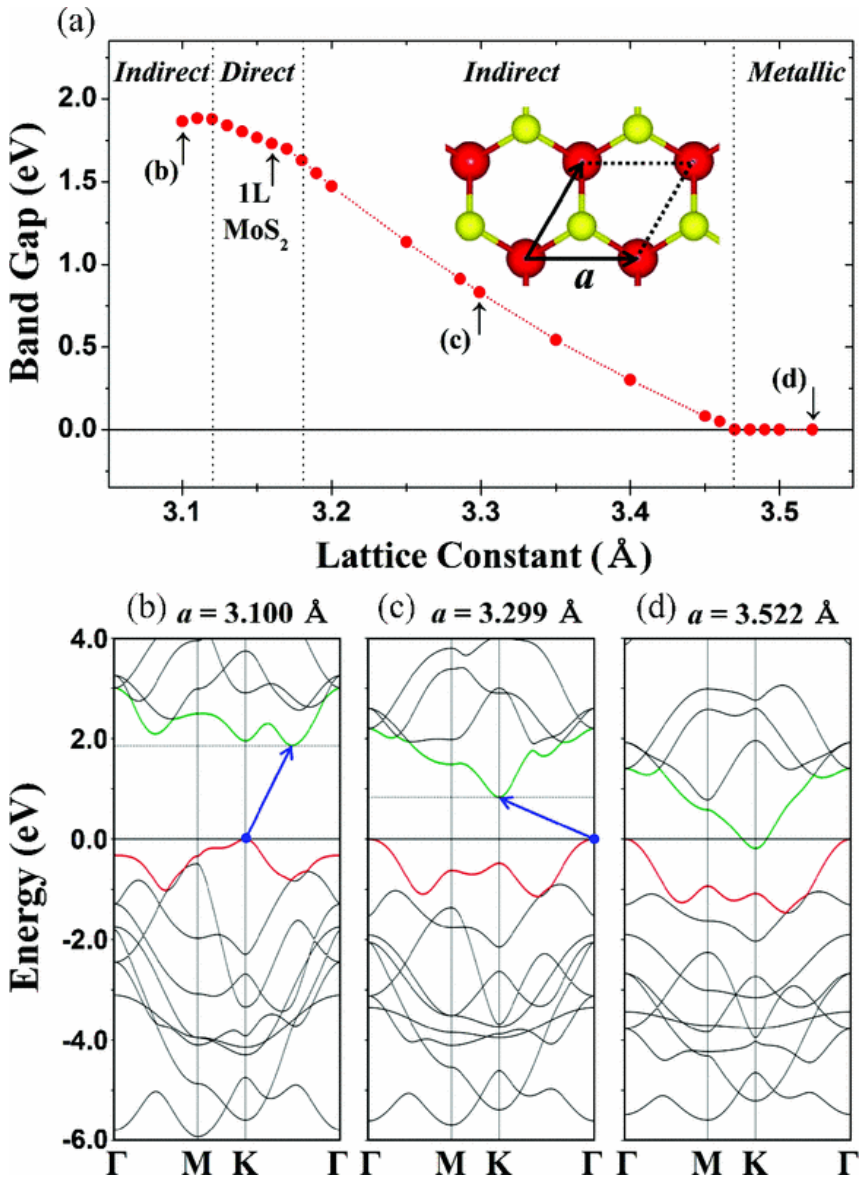

Figure 1-18 (a) Strain dependence of band gap energies of 1L-MoS_2 (a=3.160 Å). The representative band structures for the (b) compressive and (c), (d) tensile stresses are displayed, respectively. Inset indicates the hexagonal structure consisting of Mo (red/gray balls) and S (yellow/light gray balls) from the top views.[195] Reprinted with permission from Yun et al., Thickness and strain effects on electronic structures of transition metal dichalcogenides: 2H-MX_2 semiconductors (M = Mo, W; X = S, Se, Te). *Phys. Rev. B* **2012,** *85*, 033305. Copyright 2012 American Physical Society.

The evolution of band structure in graphene and TMDs depends on the direction of applied strain. For example, due to a symmetrical lattice structure, the band structure of graphene is insensitive to uniaxial and symmetrical biaxial tensile strain, and only responds to shear or a combination of shear and uniaxial strain.[199-201] In the case of TMDs, strain of any direction will cause the distortion of the lattice and orbital hybridization. However, the direction of the strain affects the magnitude of the band gap change.[192, 202] Comparison of band gap change from a theoretical study using DFT of several MX_2 under different directions of strain is shown in Figure 1-19.[192] It was also observed that the strain-induced change of band gap decreases with the increasing size of chalcogen atoms, for example, MoS_2 is more sensitive to strain compared to $MoTe_2$.

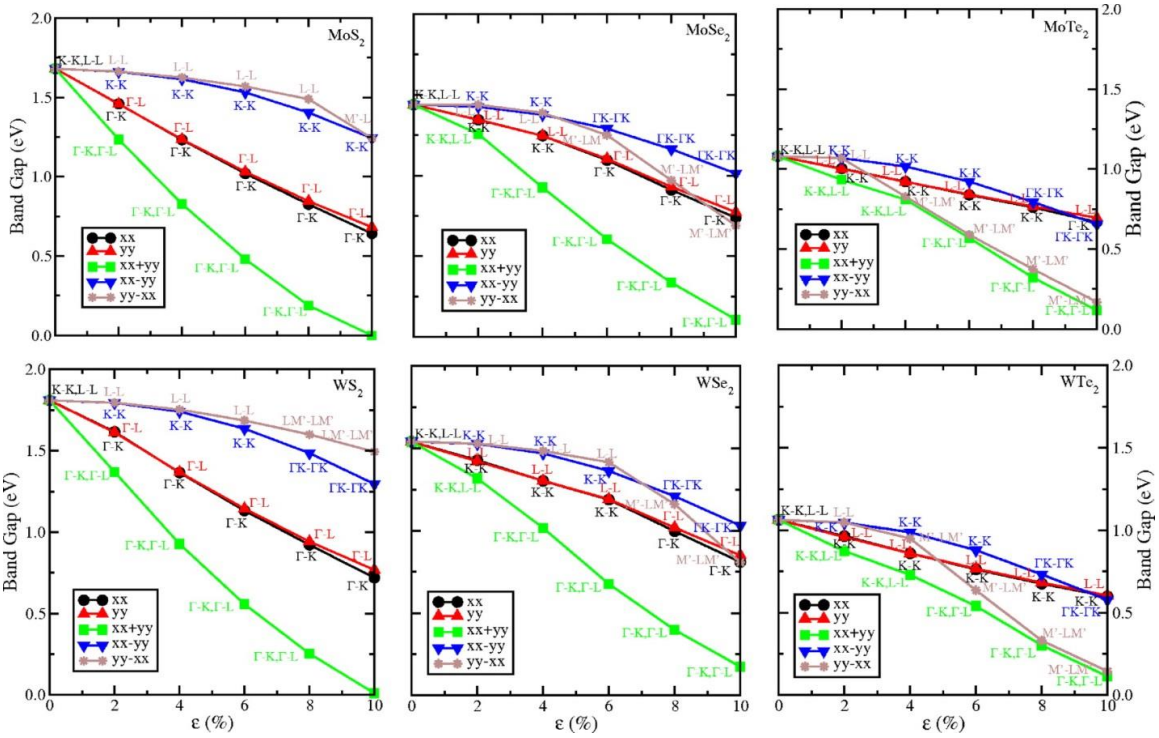

Figure 1-19 Band gap of monolayer TMDs with respect to strain, ε, which varies from 0 to 10%. Strain is applied to the optimized structures (ε = 0) through various approaches, such as uniaxial expansion in x-direction (xx), y-direction (yy), homogeneous expansion in both x- and y-directions (xx+yy), expansion in x-direction and compression in y-direction (xx–yy), and compression in x-direction and expansion in y-direction (yy–xx) with same magnitude of strain. The first three strain profiles correspond to tensile strain, while the latter two represent pure shear strain. The top (left, middle, and right) panels of Figure 2 depict the graphs corresponding to MoX_2 (WX_2), while the bottom panels show the same for MS_2, MSe_2, and MTe_2, respectively, where M denotes Mo or W.[192] Reprinted with permission from Johari et al., Tuning the Electronic Properties of Semiconducting Transition Metal Dichalcogenides by Applying Mechanical Strains. *ACS Nano* **2012,** *6*, 5449-5456. Copyright 2012 American Chemical Society.

The photoluminescence (PL) spectrum and absorbance spectrum are direct ways to monitor the strain-induced band structure change.[187, 189, 194, 196, 198, 203-207] Strain-induced optical absorption spectra simulated by DFT calculation under different bi-axial strains have suggested that tensile strain will cause a red-shift, i.e. lower excitation energy and lower band gap.[204] Experimental PL spectra also suggest a similar phenomenon. Figure

1-20(a)[189] shows the absorbance spectrum (left panel) and photoluminescence (PL) spectrum (right panel) of bilayer MoS_2 under applied tensile strain. A decrease of the optical band gap shift upon increasing tensile strain was observed.[189, 203, 208] Figure 1-20(b) and (c) summarize the peak position of absorbance and PL spectrum, respectively. Both absorbance and PL spectra experimentally suggest the tensile strain-induced band gap shrinkage. On the contrary, a blue-shift, i.e. higher energy, is observed in PL spectrum when a trilayer MoS_2 sample is under compressive strain, indicating an increase of the optical band gap, as shown in Figure 1-21.[198]

In addition, the band gap change also depends on the number of MoS_2 layers, due to thickness-dependent differences in band structure. For monolayer MoS_2, the theoretically calculated band gap change lies between -0.05 and -0.085 eV per percent tensile strain,[197, 208] while experimental results show a similar trend with the value around -0.05 eV per percent strain.[203, 208] The band gap change due to strain becomes more prominent in bilayer samples with theoretical values ranging from -0.1 to -0.2 eV per percent strain[197, 208] and experimental values around -0.12 eV.[189, 203, 208] The predicted theoretical value for bulk MoS_2 reaches -0.3 eV per percent strain.[202]

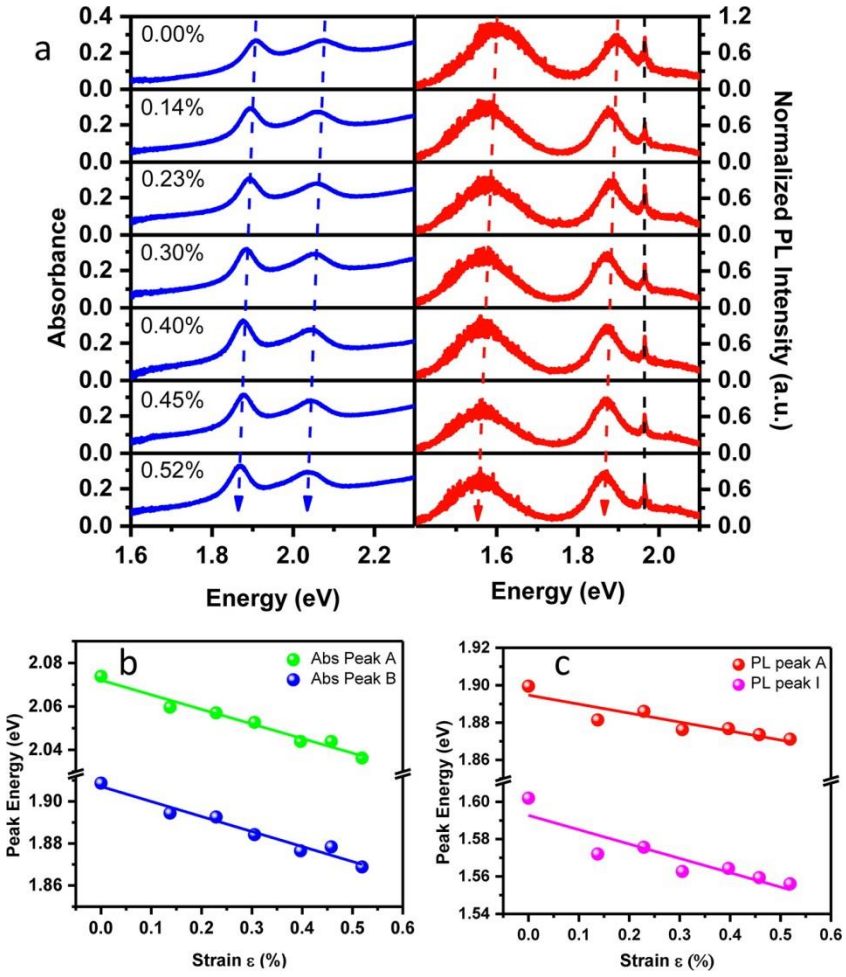

Figure 1-20 Absorbance and PL spectrum for a bilayer MoS_2 sample under tensile strain. (a) Absorption (left panel) and PL (right panel) spectrum of a monolayer MoS_2 sample under tensile strains up to 0.52% along the zigzag direction. The dashed blue and red lines are guide to the eye of the redshift of the peaks. Strain dependence of the A and B peak energies determined from absorption and of the A and I peak energies determined from PL is summarized in (b) and (c), respectively.[189] Reprinted with permission from He et al., Experimental Demonstration of Continuous Electronic Structure Tuning via Strain in Atomically Thin MoS_2. *Nano Lett.* **2013,** *13,* 2931-2936. Copyright 2013 American Chemical Society.

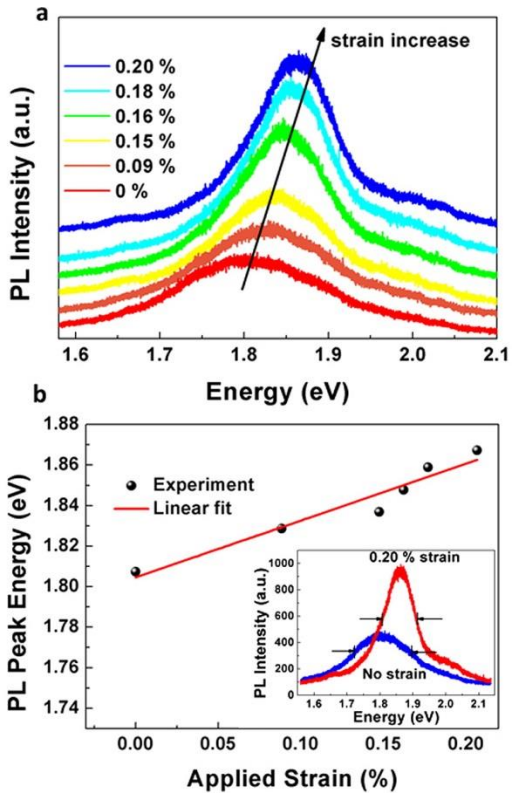

Figure 1-21 Photoluminescence property of trilayer MoS_2 under compressive strain.[198] (a) PL spectra of the MoS_2 under various strains. (b) PL peak energy as a function of compressive strain. The inset shows PL spectra of the sample under 0.0% and 0.2% strain. Reprinted with permission from Hui et al., Exceptional Tunability of Band Energy in a Compressively Strained Trilayer MoS_2 Sheet. *ACS Nano* **2013,** *7*, 7126-7131. Copyright 2013 American Chemical Society.

Beyond electronic structure, strain can also affect the phonon vibration of the TMD lattice and can be monitored by strain-induced shifts in Raman spectra.[209] Under tensile strain, a significant red-shift to lower wavenumbers (phonon softening) of E^1_{2g} in-plane mode of MX_2 was observed but the effect is small for A_{1g} out-of-plane vibration mode.[203, 206-207] A strong response of in-plane E^1_{2g} mode can be attributed to that the tensile strain has more effect on the lattice vibration mode parallel to the surface plane. In contrast, in-plane strain plays a negligible role in out-of-plane vibration, i.e. A_{1g} mode. It

is also observed in high-resolution Raman spectra, the degenerate E^1_{2g} peak will split into two subpeaks due to the break of crystallographic symmetry by the strain.[203] The tensile strain dependence of Raman spectra of MoS_2 is shown in Figure 1-22.[206] For compressive strain, a blue-shift is observed.[198]

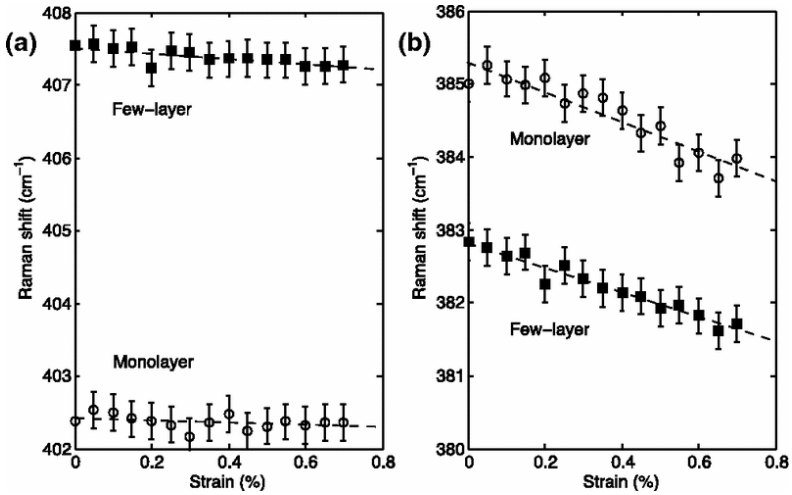

Figure 1-22 Strain-induced Raman shifts in MoS_2.[206] Position of the (a) A_{1g} and (b) E^1_{2g} Raman peaks from monolayer (open circles) and few-layer (filled squares) MoS_2. Dashed lines are linear fits to the data discussed in the text. Error bars indicate the spectrometer resolution. Reprinted with permission from Rice et al., Raman-scattering measurements and first-principles calculations of strain-induced phonon shifts in monolayer MoS_2. *Phys. Rev. B* **2013,** *87*, 081307. Copyright 2013 American Physical Society.

Finally, piezoresistivity is a direct result of the change of band gap in semiconductors due to the relative position of Fermi level to the CBM and the resulting change of the conductance of the materials.[210] There have been a few reports of strain-induced piezoresistive applications for TMD devices.[188, 205] Recently, Manzeli et al. demonstrated piezoresistivity by applying a strain to suspended MoS_2 flake with an AFM

probe.[205] The strain-dependent resistance for mono-, bi- and tri-layer MoS_2 exfoliated flakes are shown in Figure 1-23(a), (b) and (c), respectively. The gauge factors of MoS_2 piezoresistivity is summarized in Figure 1-23(d). As expected, the resistivity of the MoS_2 decreases as the tensile strain increases. However, the microscopic scale of the strain application and the use of exfoliated flake impede its practical application. Beyond piezoresistive behavior, MoS_2 is also a piezoelectric material because of the non-centrosymmetric lattice structure from the absence of inversion center.[211-214]

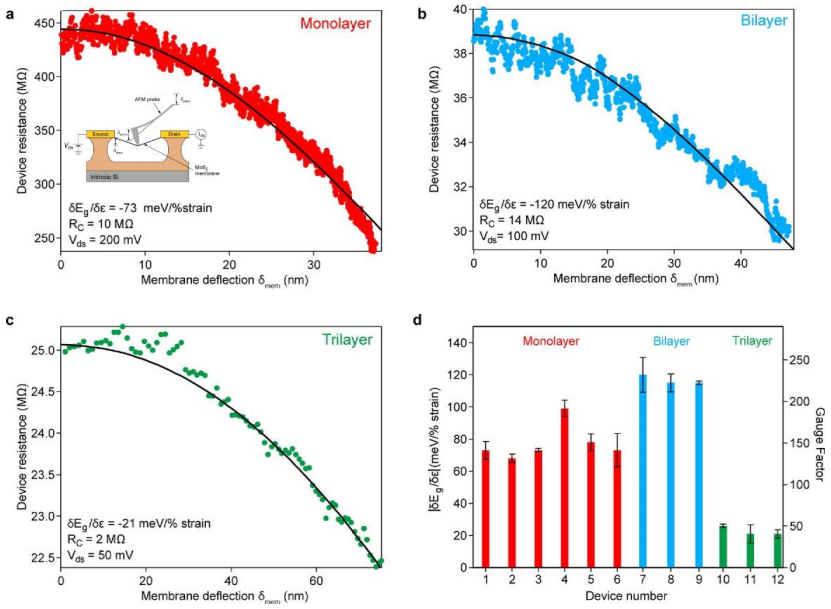

Figure 1-23 Strain-induced band gap tuning in mono and few-layer MoS_2 flakes and modulation of the device resistance due to mechanical deformation of the MoS_2 membrane. (a) Measurements and the corresponding simulation results for a monolayer MoS_2 indicating a reduction of the band gap $\partial E_g/\partial \varepsilon$ with a rate of −73 meV/%. (b) Bilayer MoS_2 with $|\partial E_g/\partial \varepsilon|$ = −120 meV/% and (c) trilayer MoS_2 with $|\partial E_g/\partial \varepsilon|$ = −21 meV/%. (d) Extracted rate of band gap change $|\partial E_g/\partial \varepsilon|$ and piezoresistive gauge factor for six monolayers, three bilayers, and three trilayers.[205] Reprinted with permission from Manzeli et al., Piezoresistivity and Strain-induced Band Gap Tuning in Atomically Thin MoS_2. *Nano Lett.* **2015,** *15*, 5330-5335. Copyright 2015 American Chemical Society.

1.8 Chemical and biological sensing using ISFETs and EGFETs

1.8.1 Working principles of ISFET and EGFET

Detecting chemical and biological species is essential for medical care, disease screening and diagnosis, food safety and environmental monitoring. Among all the available tools, potentiometric sensors measure the change of potential on the sensing surface upon the binding events of analytes to the sensing surfaces. Since Bergveld *et al.* introduced the idea in 1970,[215] ion-sensitive FETs (ISFETs) are proven to be a rapid, label-free yet highly sensitive tool for chemical and biological sensing by detecting the potentiometric difference across the sensing surface upon the absorption of charged species.[216-218] A schematic of an ISFET is shown in Figure 1-24. A single device of ISFET serves both functions: sensors and transducer. The current of the ISFET channel is affected by the potential change on the sensing surface, i.e. the physical gate of the MOSFET. When the first layer of surface charges are built up on the surface immersed in a liquid environment, oppositely charged species will absorbed to it due to Coulomb attraction and an electrical double layer is formed. Therefore, the gate of the FET can be considered as a series of RC circuits consisting of liquid and solid-state gates. The sensing signal can be obtained by analyzing the transfer characteristics of the sensors. When the charged analytes attached to the sensing surface, the charges will change the potential across the surface, and therefore the effective gate bias of FETs. The drain current (I_d) of ISFET with MOSFET transducer can be expressed as:[136, 218]

Under linear regime,

$$I_d = \frac{W}{L}\mu C_{dielectric}\left[(V_g - V_{th,ISFET})V_{ds} - \frac{1}{2}{V_{ds}}^2\right] \quad (1)$$

Under saturation regime,

$$I_d = \frac{W}{L}\mu C_{dielectric}\left[\frac{1}{2}(V_g - V_{th,ISFET})^2\right] \quad (2)$$

where W and L is the channel width and length, respectively; μ is the mobility of the channel material; $C_{\text{dielectric}}$ is the dielectric constant of the gate dielectric; V_{g} is the applied gate bias to the reference electrode in the liquid; V_{th} is the threshold voltage of the ISFET; V_{ds} is the drain to source voltage. When the device is exposed to the solution, a surface potential (ψ_0) develop at the sensing surface, i.e. the interface of sensing surface and electrolyte. This surface potential depends on the surface attachment of analyte species and the choice of the electrolyte. Under FET operation, the only variable that changes with the solution is V_{th}. The V_{th} of an ISFET can be expressed as a function of surface and solution characteristics by substituting the metal gate to liquid gate:[218-219]

$$V_{th(ISFET)} = \phi_{liq.gate} - \phi_{Semiconductor} - \frac{Q_{oxide} + Q_{it} + Q_{depletion}}{C_{oxide}} + 2\phi_f \quad (3)$$

$$\phi_{liq.gate} = E_{ref} - \psi_0 + \chi^{sol,IHP} + \Delta\chi_{loss} \quad (4)$$

where E_{ref} is the applied potential to the reference electrode, $\chi^{sol,HP}$ is the surface dipole due to the solvation of the solvent at Helmholtz plane (HP), $\Delta\chi_{loss}$ is the potential loss to the electrolyte, $\phi_{liq.gate}$ is the work function of the liquid gate, $\phi_{semiconductor}$ is the work function of the semiconductor channel, Q_{oxide} is the charges in the oxide dielectric, Q_{it} is the interface trap charges at semiconductor-dielectric interface, $Q_{depletion}$ is the depletion charges in the semiconductor, C_{oxide} is the capacitance of the oxide dielectric and ϕ_f is the Fermi potential. As a result, in a certain solution system, the only variable term in the equation is ψ_0, which is the origin of the sensing signal detected by potentiometric sensors.

Various nano-materials systems have been used in potentiometric ISFETs including silicon nanowires (Si NWs),[220-223] graphene,[224-225] carbon nanotubes (CNTs),[226] and MoS_2.[227-228] In addition, it has been reported that graphene transducers have the advantage of faster response time and better signal-to-noise ratio because of the low intrinsic noise and high mobility of graphene.[229]

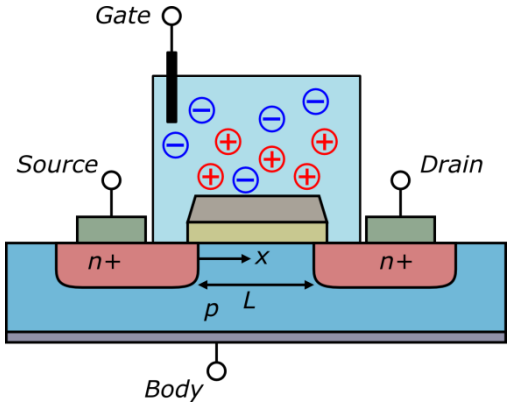

Figure 1-24 A representative scheme of ISFET. The gate of the MOFET serves as the active sensing surface of the ISFET sensors and is immersed in the electrolyte. When the charged species attach to the sensing surface, the change of the surface potential will change the gate voltage to the MOSFET, which generates the sensing signal.

Due to the configuration of the ISFET, all the electrical components including metal gate, gate dielectric, semiconductors and metal contacts can be exposed to the liquid environment, which may undermine the reliability and stability of the materials and devices. Possible reliability issues include the degradation or corrosion of materials in the liquid environment and penetration of ions into the dielectrics.[230] Additionally, the production of ISFETs is costly and time consuming and if either the sensing surface or the readout component fails, the entire ISFET sensor becomes unusable. Therefore, a simpler design for potentiometric liquid phase sensing is desired. Van der Spiegel *et al.* previously proposed an extended gate field effect transistor (EGFET) as a chemical sensor in early 1980s by separating the sensing chip (an extended gate) from the readout transducer (a FET).[231] The schematic structure of an EGFET is shown in Figure 1-25. In EGFET configuration, an extended gate (sensing chip) is electrically connected to the gate terminal of a transistor (transducer). The active sensing surface of the separated

sensing chip can be oxides, metals, or chemically functionalized materials depending on the application. For example, a SnO_2 sensing surface was demonstrated for pH sensing and Nernstian response was achieved.[232-233] EGFET-based sensors for biomolecules detection have also been also reported.[234-235] EGFET sensors provide several advantages over the traditional ISFET ones such as improved reliability by operating the transducer in dry environment, cheap and easy fabrication of the sensing chip, reusability of readout transducer, disposability of the sensing chip, and high compatibility with state-of-art semiconductor technologies.

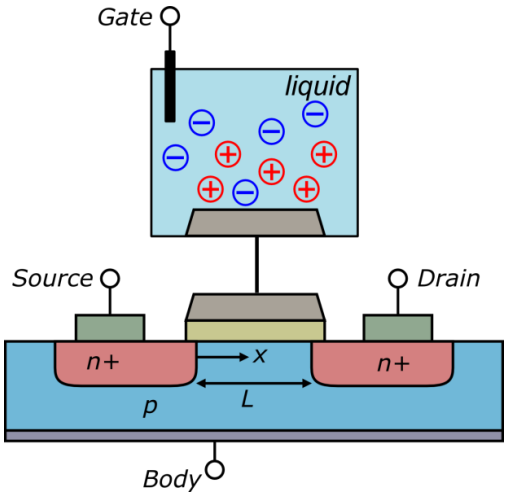

Figure 1-25 A schematic structure of EGFET. The extended gate (i.e. the active sensing surface) is separated from a MOSFET (i.e. a readout transducer) with electrical interconnection and is immersed in the electrolyte, while the MOSFET is operated in a dry environment. The change of surface potential due to the attachment of charged species onto the sensing chip (extended gap) is transmitted to the MOSFET.

However, the size of the extended gate of an EGFET may impact the sensor sensitivity. According to the numerical simulation, Dak *et al.* suggested that the

sensitivity of the EGFET is maintained if the size of the extended gate sensing surface is larger than the physical gate of the MOSFET transducer.[230] Although, nano-scale sensing surfaces provide faster response by reducing the diffusion layer thickness,[236] the issue of miniaturization needs to be considered for using the nano-scale surfaces in EGFET configuration.

1.8.2 Binding events at the sensing surface

Numerous approaches have been made to describe the binding events at the sensing surface. However, the fundamental of the binding event is the adsorption of the adsorbates to the adsorbents on the surface. A classical model of adsorption was first described by Langmuir in 1918 by treating the adsorbates as ideal gases.[237] This model is known as "Langmuir Isotherm Theory" and describes that the adsorbate gas molecules bind to the empty sites on the surface. The Langmuir adsorption model can be expressed as:

$$A_{gas}(adsorbate\ gas) + S(empty\ sites) \xrightarrow{k_{ads}} AS(absorbed\ complex) \quad (5)$$

$$A_{gas} + S \underset{k_{des}}{\longleftarrow} AS \quad (6)$$

where reaction equation (1) describes the adsorption and (2) the desorption process, respectively. The equilibrium constant k_{ads} and k_{des} are used to define the adsorption and desorption, respectively. As a result, the binding fraction θ can be expressed as:

$$\frac{attached\ sites}{unattached\ sites} = \frac{[AS]}{[S]} = \frac{\theta}{1-\theta} \quad (7)$$

Inserting the equation (3) into the definition of equilibrium constant k_{ads}, k_{ads} can be therefore expressed by the concentration of the adsorbate gas [A_{gas}]:

$$k_{ads} = \frac{[AS]}{[A_{gas}][S]} = \frac{\theta}{(1-\theta)[A_{gas}]} \tag{8}$$

For a general form of adsorption, defining the concentration of the adsorbate is [C]. The binding can be expressed as:

$$\theta = \frac{k_{ads}[C]}{1 + k_{ads}[C]} = \frac{[C]}{1/k_{ads} + [C]} = \frac{[C]}{k_{des} + [C]} \tag{9}$$

A similar but more general Hill equation describes the binding between receptors (R) to surface ligands (L) with multiple sites under steady state is:[238-239]

$$R + nL \xrightarrow{k_{forward}} RL_n \tag{10}$$

$$R + nL \xleftarrow[k_{backward}]{} RL_n \tag{11}$$

The dissociation constant K_D can be defined as the ratio of the equilibrium constant of backward reaction over forward reaction, k_b/k_f, indicating the binding affinity of ligands to receptors. The binding fraction θ can be expressed using K_D and the concentration of the receptors [C]:

$$\theta = \frac{[C]^n}{K_D + [C]^n} \tag{12}$$

where n is Hill coefficient that indicates the number of binding sites involved. For example, 1 hemoglobin can take 4 oxygen molecules, and n = 4.

A combination of the Hill equation and Michaelis-Menten kinetics provides a relationship between sensing signal and the concentration of the analyte for a biosensor:[240-241]

$$\frac{S}{S_{max}} = \frac{[C]}{K_D + [C]} \tag{13}$$

where S is the measured sensing signal, S_{max} is the maximum measured sensing signal, [C] is the concentration of the analyte, K_D is dissociation constant and a simple 1:1 binding is assumed. For practical sensing, K_D can be determined experimentally by measure the dynamic range of sensing response to different analyte concentration.

Finally, a site-binding model has previously been used to explain the change of surface potential ψ_0 when charged species attached to the surface sites in potentiometric sensors. Yates *et al.* proposed the site-binding model for the pH sensor.[242] The change of the surface potential of the pH sensor in different pH solutions results from the protonation and deprotonation of hydroxyl groups on the sensing surface. The graphical description of the protonation and deprotonation process of an oxide-based pH sensor is shown in Figure 1-26. The −OH groups will be protonated to become $-OH_2^+$, and the surface becomes positively charged when decreasing the pH of the electrolyte. The −OH groups will be deprotonated to become $-O^-$, and the surface becomes negatively charged when increasing the pH of the electrolyte.

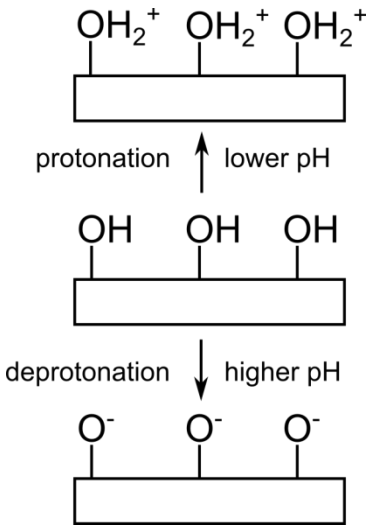

Figure 1-26 Protonation and deprotonation of surface hydroxyl groups of a pH sensor. The −OH groups will be protonated to become $-OH_2^+$, and the surface becomes positively charged when decreasing the pH of the electrolyte. The −OH groups will be deprotonated to become $-O^-$, and the surface becomes negatively charged when increasing the pH of the electrolyte.

Later, Bousse *et al.* derived the change of surface potential ψ0 for a pH sensor based on the site-binding model.[219] The surface reaction of protonation and deprotonation can be described as:

$$\mathrm{A-OH_2^+ \xleftrightarrow{k_+} A-OH + H^+_{surface}} \tag{14}$$

$$\mathrm{A-OH \xleftrightarrow{k_-} A-O^- + H^+_{surface}} \tag{15}$$

where

$$k_+ = \frac{[AOH][\mathrm{H^+_{surface}}]}{[AOH_2^+]} \tag{16}$$

$$k_{-} = \frac{[AO^{-}][\mathrm{H}^{+}_{\mathrm{surface}}]}{[AOH]} \tag{17}$$

The concentration of protons at the surface [$H^+_{surface}$] is related to the bulk [H^+] via Boltzmann distribution. The total available sites on the surface N_s = [AOH] + [AO^-] + [AOH_2^+] and the surface charge per unit area σ_0 is q([AOH_2^+] - [AO^-]), where q is elementary charge. To maintain the electrical neutrality of the surface, i.e. the point of zero charge (PZC), the hydrogen ion concentration at the surface is [H+] = $(k_-/k_+)^{1/2}$. As a result, the notation of relative change υ on the sensing surface is:

$$\upsilon = \ln[H^+] - \ln\left(\frac{k_-}{k_+}\right)^{1/2} = 2.303(pH_{pzc} - pH) \tag{18}$$

$$v = \frac{q\psi_0}{kT} + \sinh^{-1}\frac{\sigma_0}{2qN_s\sqrt{k_+k_-}} - \ln(1 - \frac{\sigma_0}{qN_s}) \tag{19}$$

where k is Boltzmann constant, T is the temperature, $\sigma_0 = \psi_0 \cdot C_{eq}$ and C_{eq} is the capacitance of electrical double layer under equilibrium. Equation (19) can be further simplified into for a small value inside inverse hyper sine function:

$$v = \frac{q\psi_0}{kT} + \frac{q\psi_0}{kT}(\frac{C_{eq}kT}{2qN_s\sqrt{k_+k_-}}) \tag{20}$$

Let $\beta = \frac{2qN_s\sqrt{k_+k_-}}{C_{eq}kT}$ and combining equation (18) and (20):

$$v = \frac{q\psi_0}{kT}\left(\frac{\beta + 1}{\beta}\right) = 2.303\left(pH_{pzc} - pH\right) = 2.303(\Delta pH) \tag{21}$$

Therefore, the change of the surface potential ψ_0 due to the change of the pH can be expressed as:

$$\psi_0 = 2.303\frac{kT}{q}\left(\frac{\beta}{\beta+1}\right)(\Delta pH) \quad (22)$$

where β is a dimensionless sensitivity parameter. For every one pH value change, the highest achievable surface potential change is 59.2 mV at 298K, which is also known as Nernstian limit for a pH sensor. Detailed derivation and assumptions can be found in the original work of Bousse *et al*.[219] Similar to the protonation/deprotonation process, site-binding model can also be used in the modeling the signal of biosensors due to the attachment of charge biomolecules to the sensing surface.[243-245]

1.9 TMD-based Sensors

Two-dimensional materials are advantageous for sensing applications due to their large surface-to-volume ratio, mechano-electric properties and the compatibility for flexible devices.[25] For chemical and biological sensing, the all-surface 2D materials provide a large sensing surface area and enable immobilization of large amount of sensing molecules that can achieve fast response and low detection limit.[246] It has been demonstrated that graphene-based field effect transistors can be used as electric sensing transducers for chemical and biomolecules detection.[224-225] Beyond graphene, TMD-based semiconductor devices are expected to provide a better platform for electrical sensors because the high on/off ratio and tunable electronic properties.[247-248] For

mechanical sensing, the high strain limit and mechanical force-sensitive properties of 2D TMDs, especially, make them promising for strain gauges. TMD-based sensors can be further categorized into: (1) optical sensors using the PL response and fluorescence quenching effect of TMDs; (2) electrical sensors using TMD-based transistors coupled with non-TMD sensing surface; (3) electrical sensors using TMD-based transistors with TMD as the sensing surface; (4) mechanical sensors using mechno-electric properties of TMDs. The current status, applications and challenges of TMD-based sensors will be discussed in this section.

1.9.1 Gas sensors

Among all, gas sensing is the most widely investigated application using TMD-based sensors due to its relative simplicity.[55, 77, 249-251] Similar to the charge transfer doping discussed previously, the principle of the gas sensing involves the physical adsorption of the gas molecules to the TMD sensing surface, for example, MoS_2. The gas molecules act as electron donors or electron acceptors, for example, NH_3 or NO_2, respectively as theoretically and experimentally confirmed by Zhou *et al*. and Late *et al*.[252-253] The partial charge transfer between gas molecules and TMD will affect the channel conductance. Physisorption of NH_3 or NO_2 results in the increase or decrease of the channel current of an n-channel MoS_2 FET, respectively. Due to the superficial interaction between sensing materials and the absorbents, it has been reported that the sensitivity can be enhanced by increasing the surface-to-volume ratio. As a result, 2D materials are especially promising for gas sensors because of the ultra-high surface-to-volume ratio of the atomically thin materials. Li *et al.* reported a proof-of-concept gas sensing for toxic NO using TMD FETs based on exfoliated monolayer and several-layer

MoS_2, with a detection limit of 0.8 ppm.[89] The channel current of MoS_2 FETs decrease when exposed to NO gas, which agrees with the fact that NO acts as an electron acceptor. It was also suggested that multilayer MoS_2 devices provide a higher and more stable sensitivity than monolayer ones. Later, Perkins *et al.* used exfoliated monolayer MoS_2 FETs to detect different chemical vapors, including trimethylamine and acetone.[77] Compared to CNT-network sensor, monolayer MoS_2 sensors provided a comparable but selective sensitivity to certain gases, while CNT-network sensors showed no selectivity and responded to all kinds of gases of choice. The scheme and the results of MoS_2 sensor in response to different chemical vapors are shown in Figure 1-27.[77] In addition, extra surface functionalization using high work function noble metal nanoparticles was used for H_2 detection.[156] Sarkar et al. demonstrated p-doping of MoS_2 using high work function Pd NPs. Upon the absorption of H_2, the work function of Pd NPs decreases as well as the p-doping effect. As a result, H_2 sensing was achieved by monitoring the de-doping effect. A flexible version of MoS_2-based gas sensor for NO_2 was also reported.[76] Despite the reported high sensitivity of gas sensing based on 2D TMDs, the physisorption of the gas molecules on the sensing surface provides little selectivity for different species.[224] As a result, the selectivity remains the biggest challenge for these TMD-based gas sensors in a complicated analyte system.

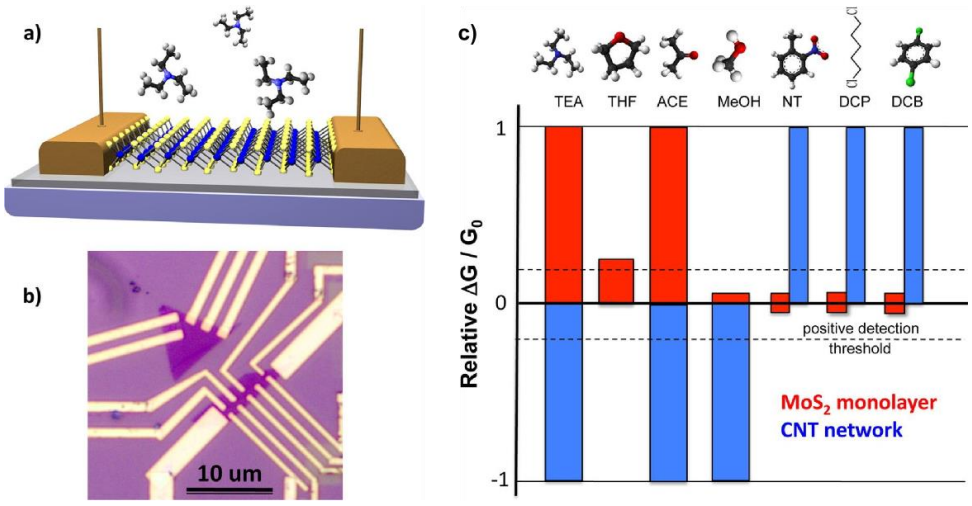

Figure 1-27 The scheme and the results of MoS_2 sensor in response to different chemical vapors. (a) A single monolayer of MoS_2 is supported on a SiO_2/Si substrate and contacted with Au contact pads. Transient physisorption of molecules induces temporary changes in the conductivity of the monolayer channel. (b) An optical image of the processed devices showing the monolayer MoS_2 flakes electrically contacted by multiple Au leads. (c) Histogram of MoS_2 and CNT-network sensor responses to various analytes. A qualitative summary of the response of the sensors to the analytes tested. The responses are broadly categorized as high, low, or null. The MoS_2 sensor exhibits a much higher selectivity and a complementary response to the CNT-network sensor. The analytes from left to right are triethylamine (TEA), tetrahydrofuran (THF), acetone, methanol, nitrotoluene (NT), 1,5-dichloropentane (DCP), and 1,4-dichlorobenzene (DCB). Ball-and-stick models of the analyte molecules are shown, in which nitrogen atoms are blue, oxygen atoms are red, carbon atoms are black, chlorine atoms are green, and hydrogen atoms are light gray.[77] Reprinted with permission from Perkins *et al.*, Chemical Vapor Sensing with Monolayer MoS_2. *Nano Lett*. 2013, 13, 668-673. Copyright 2013 American Chemical Society.

1.9.2 Chemical sensors

Even though the gas sensing using 2D materials is extensively studied, detection of chemical species in liquid environment remains relatively unexplored. Unlike gas sensing, liquid phase detection involves the operation of electric transducers in liquid environment. Similar to the charge transfer reaction for gas sensing, Jiang *et al.* demonstrated the detection of Hg^{2+} using MoS_2 FETs by monitoring the p-doping effects

when the MoS_2 sensing surface exposed to Hg^{2+} containing solution.[254] A possible sensing mechanism is explained by a high binding affinity between superficial S^{2-} on MoS_2 surface and Hg^{2+} and the resulting partial charge transfer from MoS_2 to Hg^{2+}. Although detection of chemical species based on partial electron transfer has been demonstrated, selectivity and specificity toward target species remains a major challenge without designated binding chemistry.

Monitoring of pH values of the solution is another application of TMD-based chemical sensors. As discussed previously, the attachment of charged analytes to the binding sites on the sensing surface will cause the drop of the surface potential across the sensing surface and therefore change the effective gate bias of ISFETs in the liquid environment. The sensing signal can be obtained by analyzing the transfer characteristics of the sensors. The pH sensing relies on the reaction between hydroxyl (-OH) functional group on the sensing surface and the protons (H^+) in the solution. First introduced by Ang *et al.* in 2008, graphene based pH sensing is a result of a pH-dependent surface potential change when H^+ ions attach to the defect sites on graphene surface.[255] If the graphene surface is perfect without defects and dangling bonds, it is insensitive to the H^+ concentration, i.e. pH values.[256] Sarkar et al. demonstrated the MoS_2 FETs based pH sensor with HfO_2 sensing surface.[228] In this case, MoS_2 FET only serves as a transducer. The reported pH sensitivity reached the Nernstian response of 59 mV/pH.

1.9.3 Biological sensors

Similar to pH sensing, detection of other biological species, for example, proteins, relies on the potential change on the sensing surface as well. The only difference is that

the sensing surface needed to be decorated for the specific attachment of target analytes. In 2014, Lee *et al*. showed a preliminary result of MoS_2 biosensor without surface treatment for protein immobilization.[257] The MoS_2 serves as channel material as well as sensing material. The attachment of protein onto the MoS_2 sensing surface relies on the hydrophobicity of the MoS_2. However, the selectivity of physisoprtion is a significant concern. To improve the selectivity and specificity of the biosensing, a more complicated yet well-known strategy is covalent immobilization of biomolecular probes onto the chemically functionalized sensing surface, for example, silane decorated oxide surface or thiol decorated gold surface. Wang *et al.* demonstrated a MoS_2 FET based biosensor for prostate specific antigen (PSA) detection by decorating the HfO_2 with silane on top of MoS_2 channel.[258] 3-aminopropyl(triethoxy)silane (APTES) is one of the most commonly used self-assembly monolayer (SAM) on oxide surfaces. A similar approach was demonstrated by Sarkar *et al*. by immobilizing biotin on silane-modified HfO_2 sensing surface of MoS_2 FET-based biosensor for streptavidin detection.[228] When the HfO_2 sensing surface was exposed to streptavidin containing solution with a pH value larger than the isoelectric point pH (pI) of the streptavidin, an increase of V_{th} was observed, indicating the streptavidin was negatively charged. On the contrary, if pH < pI, a decrease of V_{th} was observed, indicating the streptavidin carried positive charges. Figure 1-28 shows the biosensor (left panel) and pH sensor (right panel) of MoS_2 FET-based biochemical sensors with HfO_2 sensing surface.[228]

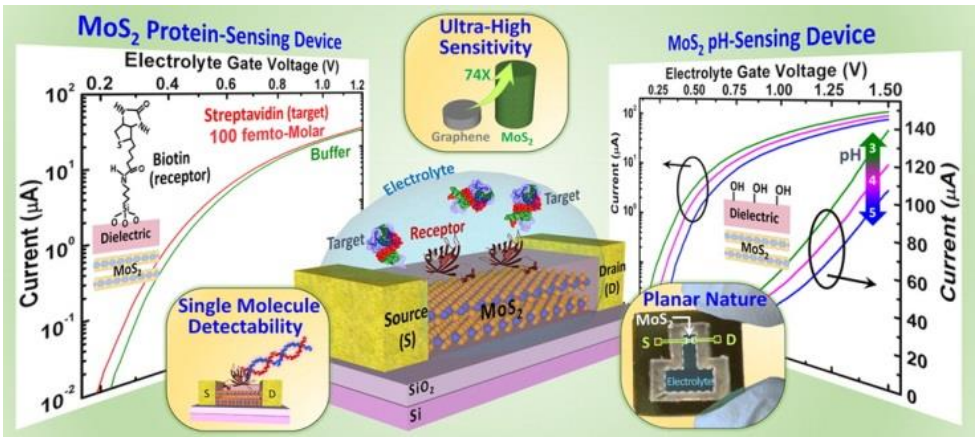

Figure 1-28 MoS_2-based FET biochemical sensor for pH and streptavidin detection. The structure of MoS2 FET sensor is shown in the middle panel. HfO_2 top-dielectric was deposited on MoS_2 channel as sensing surface. For pH sensing, HfO_2 is used as sensing surface (right panel). For biotin-streptavidin sensing, the N-hydroxysulfosuccinimide (sulfo-NHS)-biotin was immobilized onto silane-modified HfO_2 sensing surface. Reprinted with permission from Sarkar *et al.*, MoS_2 Field-Effect Transistor for Next-Generation Label-Free Biosensors. *ACS Nano* 2014, 8, 3992-4003.[228] Copyright 2014 American Chemical Society.

Finally, biosensing using TMD induced fluorescence quenching effects have been demonstrated for detection of proteins and DNAs. For example, dye-labeled single-stranded DNA tend to attach to the basal plane of MoS_2 and WS_2 through van der Waal reaction, and the fluorescence of the dye is then be quenched. However, when the single-stranded DNA is hybridized to double-stranded DNA by its complementary target DNA, the quenching effect is inhibited as shown in Figure 1-29.[259-261] Similarly, MoS_2 can quench the fluorescence of dye-labeled aptamer, but the luminescence will not be affected after the capture of PSA protein.[262]

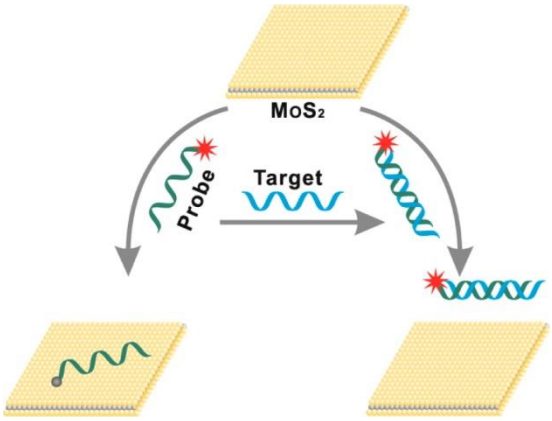

Figure 1-29 Schematic illustration of the Fluorimetric DNA Assay using MoS_2. Reprinted with permission from Zhu *et al.*, Single-Layer MoS_2-Based Nanoprobes for Homogeneous Detection of Biomolecules. *J. Am. Chem. Soc.* 2013, 135, 5998-6001.[259] Copyright 2013 American Chemical Society.

1.9.3.1 Functionalization of 2D TMDs for biochemical sensors

Selective biochemical sensing using thiol or silane chemistry on Au or oxide capping layer on top of TMD, respectively, provides a feasible way to covalently link the probe biochemical species to the sensing surface. However, the deposition of such capping layer complicates the fabrication process and may influence the surface charge coupling upon the attachment of analyte molecules. Alternatively, in order to exploit TMDs for biochemical sensing applications with high selectivity, direct functionalization of the TMD surface with surface linkers is important.[263] By a proper design of the end functional groups of the linkers, the probe species can be further attached to the linkers covalently. For graphene, it has been reported that proteins can bind onto graphene surface via π-π bonding between carbon structures.[264] For TMDs, due to their X-M-X sandwich structure, chalcogen atoms and vacancies are exposed to the environment. As a

result, surface functionalization using chalcogen related chemistry is the most common approach. Among all, functionalization of S-based TMDs has been extensively studied. Take MoS_2 for example, metal-acetate salts ($M(OAc)_2$; where M = Cu, Ni, Zn) can coordinate with the surface S atoms on MoS_2 and form metal-sulfur dative bonds.[265] Alternatively, linkers can also be grafted onto the MoS_2 surface by filling the S-vacancies using S-containing chemicals, including thiophene, thiols, etc.[179, 266-268] Possible coordination mechanisms including filling S-vacancies (left) and metal-S coordination (right) are shown in Figure 1-30.[263] Some available linkers for the functionalization of S-based TMDs are shown in Figure 1-31.[263] Unlike classical thiol chemistry on Au that form Au-S bonds, thiol molecules serve as S-atom donors and will fill the S-atom vacancies in S-based TMDs. In other words, surface S vacancies can be repaired by external S sources. Organic thiols including thiophenol, alkane thiols, etc. were reported for the purposes.[269] The evidence of the S-atom vacancy filling is usually observed through the distinct S 2p peaks in XPS spectrum. Furthermore, it is interesting that Kim *et al.* reported a surface functionalization of MoS_2 using mercaptoundecanoic acid for gas sensing of volatile organic compounds,[270] which is similar to the thiol SAM used in amine coupling of biomolecules on Au. The functionalization of MoS_2 surface with carboxylated thiol SAM suggests a possible covalent immobilization of biomolecules to the TMD surfaces. Although several surface functionalization techniques have been demonstrated for TMD surfaces, challenges including controlling the density and arrangement of S-atom vacancies and the resulting thiol SAM formation still need to be solved.

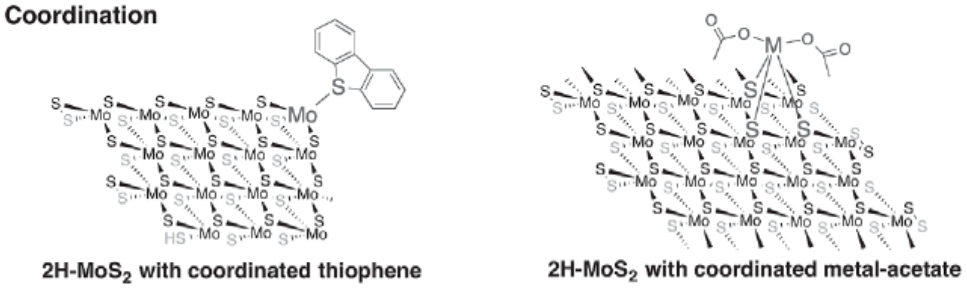

Figure 1-30 Graphical representations of various modes of MoS_2 functionalization with small molecules. The attachment using S-atom vacancies filling (left) and metal-sulfur dative bonds formation (right). Reprinted with permission from Chen *et al.*, Functionalization of Two-Dimensional Transition-Metal Dichalcogenides. *Adv. Mater.* 2016, 28, 5738-5746.[263] Copyright 2016 John Wiley and Sons.

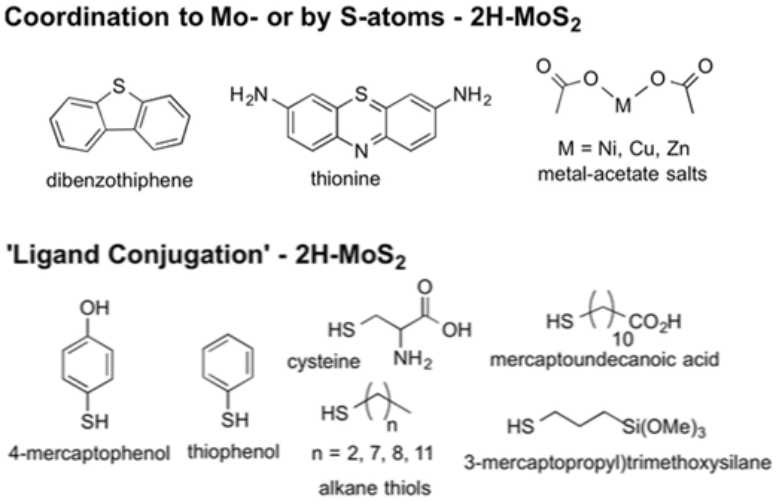

Figure 1-31 Some organic compounds for the functionalization of TMDs. Reprinted with permission from Chen *et al.*, Functionalization of Two-Dimensional Transition-Metal Dichalcogenides. *Adv. Mater.* 2016, 28, 5738-5746.[263] Copyright 2016 John Wiley and Sons.

1.9.4 Mechanical sensors

Strain-induced piezoresistive and piezoelectric effects have been observed in TMDs.[205, 211-213] Using either piezoresistive or piezoelectric properties, TMDs can be use as strain gauges. Wu *et al.* have experimentally demonstrated MoS_2 piezoelectric strain gauges based on MoS_2 Schottky diode devices.[211] It was observed that the output piezoelectric potential due to the strain-induced polarization increases with external strain. Theoretical works by Yu *et al.* later reported mechano-electric piezoelectric strain sensors based on TMD homo- and hetero-junction devices[271], and the maximum voltage output at 8% strain can reach as high as 0.356 V for WS_2 pn junction devices. Alternatively, MoS_2 piezoresistive strain sensors measuring the strain-induced resistivity has also been demonstrated.[205] However, aforementioned proof-of-concept TMD-based strain sensors were fabricated on exfoliated TMD flakes, which limit their practical applications. Therefore, development of TMD-based strain gauges based on large-area TMD films in compatible with state-of-the-art photolithography fabrication process is important for the future applications of TMD mechanical sensors.

1.10 Summary of background

2D TMDs is promising for next generation electronics with controllable electrical and optical properties as well as improved mechanical properties. Different synthesis techniques for the fabrication of two-dimensional TMD thin films have been reviewed. Due to the atomically thin nature of TMDs, their electrical and optical properties are sensitive to the internal, for example, thickness, and external environments. The

properties of TMDs related to the electrons and phonons have been discussed. Using this sensitivity to the external environment, the electrical properties of TMDs can be modified through surface doping. Selected doping techniques available for TMDs have been compared. External mechanical strain can influence the electronic structure of TMDs. The strain-induced properties and strain engineering of TMDs has been reviewed. Furthermore, the sensitivity of TMDs to the environment renders them good candidates for sensing applications, including gas sensor, chemical sensor, biological sensor, mechanical sensor, etc. Although TMD is a promising alternative to bulk semiconductors, the thin film quality needs to be optimized to fully exploit these atomically thin materials.

The fundamental of chemical and biological potentiometric sensors have been discussed. Two FET-based potentiometric sensing configurations, ion-sensitive FETs and extended-gate FETs, have been reviewed. The understanding of the sensing mechanism and sensing techniques can leads to a universal sensing strategy that is suitable for various FET-based transducers, including TMD-based devices.

CHAPTER 2. CHARGE TRANSFER DOPING OF 2D TMD SEMICONDUCTORS

This chapter describes the charge transfer doping of two TMD materials, n-type MoS_2 and p-type WSe_2, using redox-active metal-organic molecules. This work was performed in close collaboration with Dr. Siyuan Zhang and Dr. Alexey Tarasov. The molecular dopants were acquired from Dr. Seth Marder's group. My role in this work involved performing doping treatments to TMD devices, electrical characterization and physical characterization. Section 2.1 gives a brief introduction to the charge transfer doping. Section 2.2 describes the experimental methods for the doping treatment and the physical characterizations. Section 2.3 includes n- and p-doping of trilayer MoS_2 samples. Detailed physical characterization including XPS, UPS and Raman spectroscopy and electrical characterization of FETs after doping treatment were used to verify the doping effect. Section 2.4 includes n- and p-doping of trilayer WSe_2 samples. Systematic physical and electrical characterizations were presented.

2.1 Introduction

Two-dimensional (2D) transition-metal dichalcogenides (TMDs), particularly MoX_2 or WX_2 (X = S, Se), have been widely explored recently as a class of semiconducting materials in transistors,[123-124, 272] tunneling devices,[35, 273] sensors,[272, 274] flexible electronics,[25] and optoelectronics[275-276] due to the ability to tune their band structure through thickness control and strain engineering. MoS_2, which, as synthesized,

is an n-type semiconductor, has received particular attention. However, for integrated circuits applications consisting of CMOS, p-n diodes, and other logic components, both n-type and p-type semiconductors are required. WSe_2 is a promising p-type candidate for numerous electrical and optical applications due to its controllable band structure; its bandgap can range from ~1.2 eV (indirect) for the bulk form to ~1.64 eV (direct) for monolayers.[59] To date, most reports on 2D TMD-based devices involve the use of exfoliated flakes or CVD-grown discontinuous grains, which are usually several micrometers in size. This hinders their practical application using state-of-art semiconductor fabrication techniques. As a result, the ability to synthesize high-quality 2D materials over large areas and that are compatible with conventional CMOS technologies is essential. Our recent work demonstrated a wafer-scale synthesis of TMDs with thickness and electrical uniformity through the direct sulfurization or selenization of metal thin films,[123-124] providing an important step toward practical device applications.

Doping is an effective tool to further control the electrical and optical properties of semiconductors as required for device applications, both through modulation of the carrier concentration and of the work function. Several approaches to dope TMDs using various modifiers have been reported. Firstly, diffusion or implantation of metals, such as potassium for n-doping,[277] and gold for p-doping[62] has been used; however, diffusion of metal atoms and/or ions is not easily controllable, and can cause unexpected leakage pathways and even failure during operation, while metal inclusion in 2D layers and the implantation process can cause damage to TMD crystal structures. Secondly, physi- and/or chemisorption of gases, such as NO_2,[65] has been used; gas molecules physisorbed through weak van der Waals interactions can easily desorb, with attendant de-doping of

the TMDs, while chemisorption can potentially perturb the original band structure. Thirdly, organic modifiers, such as ethoxylated poly(ethyleneimine) (PEIE) or octyldecyltrichlorosilane (OTS)[166, 169] have been used; the mechanism of doping using these modifiers varies depending on the modifier in question, but can involve partial charge transfer, or build-up of a surface dipole. These previous studies have mostly been conducted using the exfoliated TMD flakes.

2.2 Experimental methods

2.2.1 Device fabrication

Both MoS_2 and WSe_2 was synthesized on 300 nm of thermally grown SiO_2 on low-resistivity (0.1 – 0.5 Ω cm, boron-doped) silicon wafers. Prior to deposition of 1 nm of molybdenum or tungsten via e-beam evaporation (0.3 Å/s) onto the substrate, the substrate was cleaned using acetone, methanol and isopropanol. In the case of MoS_2, vaporized S from a heated canister was used as S source for the sulfurization of Mo thin film. For WSe_2, the W thin film was selenized in a furnace using Se pellets in a crucible as Se source. The furnace chamber was pumped down to approximately 10^{-6} Torr to eliminate atmospheric contaminants. A 1 h H_2/Ar annealing was used to remove the native oxide on Mo thin film prior to S vapor incubation at 1050 °C to convert Mo to MoS_2. Similarly, a 1 h H_2/Ar annealing along with Se vapor at 800 °C was used to remove the native oxide on W thin film and supply the Se source for WSe_2 synthesis. Finally, a 30 min purge under Ar flow (200 sccm) at 800 °C was used to remove excess selenium from the WSe_2 surface. The furnace was then allowed to cool down to room

temperature before unloading the sample. The synthesized MoS_2 is expected to be three layers based on the initial thickness of 1 nm Mo as confirmed by the Raman spectrum. The synthesized WSe_2 is expected to be three layers based on the initial thickness of 1 nm W and a final thickness of 2.5 nm WSe_2. The detailed procedure for MoS_2 and WSe_2 synthesis can be found in our previous published protocols.[123-124]

The FETs were fabricated on the as-synthesized MoS_2 or WSe_2 sample using standard photolithography. The Au (100 nm) or Ti/Au (30 nm/ 70 nm) source and drain contacts were deposited using e-beam evaporation followed by lift-off process. The active channel was patterned by plasma etching using mixture gas of SF_6 (45 sccm) and O_2 (5 sccm) at 30 W RF power for 5 min. The electrical characterization of fabricated WSe_2 was taken using a Keithley 4200-SCS semiconductor parameter analyzer and a Lakeshore probe station at room temperature under vacuum (~10^{-6} Torr) to minimize the effect of surface absorption from the ambient. A bottom gate configuration was used with a 300 nm SiO_2 dielectric. Even though the doping treatments were conducted in a N_2-filled glove box, the samples experience a short exposure (< 5min) to air before being transferred into the vacuum measurement chamber.

2.2.2 Doping treatment

For MoS_2 doping, n-Dopants, $(2\text{-Fc-DMBI})_2$ (**N1**) and 2-Fc-DMBI-H (**N2**) were dissolved in anhydrous deoxygenated toluene to make a 2.5 mM (**N1**) and a 5 mM (**N2**) solution, respectively (the differences being chosen to reflect that the two dopants can contribute two and one electrons, respectively). The p-dopant tris(4-bromophenyl)ammoniumyl hexachloroantimonate ("Magic Blue", **P1**) was dissolved in

CH_2Cl_2 to make a 5 mM solution. Samples were then exposed to dopant solutions for various times, followed by rinsing in fresh solvent 3 times with shaking to remove physisorbed materials, and dried out with N_2 from a rubber bulb.

For WSe_2 doping, dichloromethane (DCM) and toluene were purchased from Sigma-Aldrich (anhydrous grade solvent packed under argon) and used as received. Tris(4-bromophenyl)ammoniumyl hexachloroantimonate ("Magic Blue", **P1**) was purchased from Sigma-Aldrich and used as received. $(Bu_4N)^+[Ni(mnt)_2]^-$ (**P2**) and $(RhCp^*Cp)_2$ (**N1**) were synthesized according to literature reported methods.[175, 278-279] All operations were carried out under an atmosphere of nitrogen or argon, unless stated otherwise. The doping treatments were conducted inside a Unilab MBraun glovebox with both water and oxygen level <0.5 ppm. **P1** and **P2** were dissolved in anhydrous DCM to make a 5 mM solution, while **N1** was dissolved in anhydrous toluene to make a 2.5 mM solution. WSe_2 samples were immersed into the dopant solutions for various treatment time, and were then rinsed with fresh solvent several times to remove physisorbed dopants.

2.2.3 Electrical characterization

All measurements were performed using a LakeShore Cryotronics probe station and a Keithley 4200-SCS parameter analyzer at room temperature. First, as-fabricated transistors were tested in high vacuum (~ 10^{-6} Torr) to minimize the effect of surface absorption from the ambient. The devices were then dip-coated in dopant solutions inside a glove box and measured again in vacuum. Even though the doping treatments were

conducted in a N_2-filled glove box, the samples experience a short exposure (< 5min) to air before being transferred into the vacuum measurement chamber.

2.2.4 Physical characterization

X-ray and ultraviolet photoelectron spectroscopy (XPS and UPS) were acquired with Kratos Axis UltraDLD XPS/UPS system, using the monochromatic Al Kα line and He-I lamp radiation (21.2 eV), respectively. The base pressure of the analysis chamber is 10^{-8} Torr. MoS_2 and WSe_2 films were transferred onto gold substrates for the XPS/UPS measurements before doping treatments because their intrinsic conductivity is too low for the UPS measurement. The Fermi level was calibrated using atomically clean silver. Peak fits of high resolution scans were done with Vision Processing Software 2.2.8 using mixed Gaussian/Lorentzian distributions to minimize chi squared. The work function was calculated based on the binding energy corresponding to the secondary electron edge (SEE) (φ = 21.22 eV – SEE) for each film, and the position of the valence band maximum was determined from the onset of photoemission relative to zero binding energy (Fermi level).

Raman spectroscopy was acquired in a Renishaw InVia microscope spectrometer with laser excitation at 488 nm. For all of the Raman measurements, the samples were transferred from the glovebox using a sealed microscope stage (Linkam TS 1500) to avoid air exposure during transfer and measurements steps. A quartz window was used to allow optical access to the sample during the measurements. All Raman peaks were fitted with Gauss-Lorentzian line shapes to determine the peak position, the linewidth and the intensity.

2.3 Doping of MoS_2[a]

Previous studies have demonstrated the feasibility of molecular doping using exfoliated TMDC flakes, there have been few multi-technique studies comparing different dopants on large-area TMDCs. Since powerful molecular n-dopants that operate by simple electron transfer are inevitably sensitive to air and moisture, several approaches to more easily handle molecular n-dopants have been developed recently in which the reduction chemistry is coupled to chemical reactions. These include species formally related to stable cations by a hydride reduction, such as dihydrobenzimidaolze derivatives[280] (2-R-DMBI-H, shown in Figure 1 for R = Fc), and dimers of highly reducing odd-electron species, including those of various 19-electron sandwich compounds[280] and benzimidazoline radicals (see $(Fc\text{-}DMBI)_2$, Figure 2-1).[281] Although developed as dopants for organic semiconductors, both classes of air-stable dopants have also been applied to the surface n-doping of the 2D material graphene.[282-283]

Here, we use examples of these two classes of stable n-dopants, $(2\text{-}Fc\text{-}DMBI)_2$ (**N1**) and 2-Fc-DMBI-H (**N2**) (Figure 2-1), to dope large-area (>10 cm^2) highly uniform trilayer MoS_2 films. We use electrical measurements, ultraviolet and x-ray photoelectron spectroscopy (UPS and XPS respectively), and Raman spectroscopy, to compare the n-doped films to pristine MoS_2 and to MoS_2 treated with a p-dopant tris(4-bromophenyl)ammoniumyl hexachloroantimonate[284] ("Magic Blue", P1, which is stable in dry air and dry CH_2Cl_2).

[a] Adapted with permission from Tarasov, A.; Zhang, S.; Tsai, M.-Y.; Campbell, P. M.; Graham, S.; Barlow, S.; Marder, S. R.; Vogel, E. M., Controlled Doping of Large-Area Trilayer MoS_2 with Molecular Reductants and Oxidants. *Adv. Mater.* **2015,** *27*, 1175-1181. Copyright 2015 WILEY-VCH.

Electrical measurements were performed on back-gated field-effect transistors made from wafer-scale trilayer MoS_2 grown on a highly doped Si wafer with 260 nm thermal SiO_2. A detailed description of this growth process and of the physical and electrical characterization of MoS_2 grown this way has been reported elsewhere. For this study, a sample containing several hundred transistors was diced into three dies to compare different dopants. As we have previously shown,[124] the devices have an intrinsic field-effect mobility of ~7 $cm^2V^{-1}s^{-1}$ and exhibit highly reproducible characteristics across the whole sample area (> 10 cm^2), which enables an accurate comparison of different dopants. The device schematic and transistor characteristics prior to doping are presented in Figure 2-1, as well as the chemical structures of the compounds.

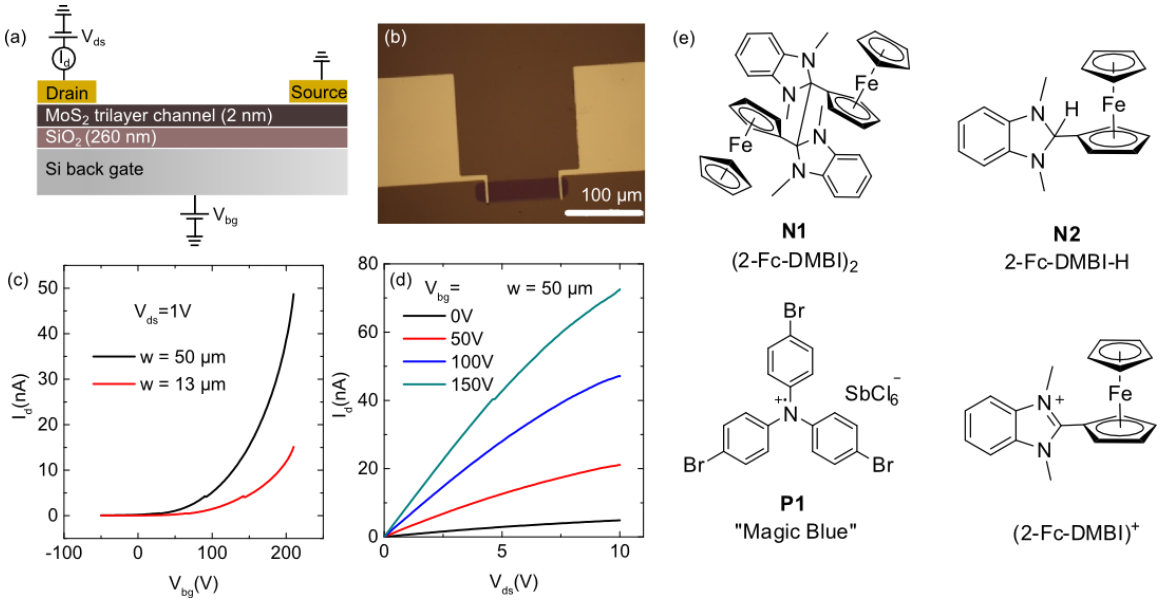

Figure 2-1 (a) Schematics of a back-gated trilayer MoS_2 transistor. The drain-source voltage V_{ds} is applied to the Ti/Au contacts on top of MoS_2. The back-gate voltage V_{bg} is applied to the highly doped Si wafer (resistivity: 0.001-0.01 Ωcm). (b) Optical image of the MoS_2 transistor. (c) Drain current I_d through the MoS_2 channel as a function of the applied back-gate voltage V_{bg} (transfer curve) at constant drain-source voltage V_{ds} = 1V

for two different channel widths (50 µm and 13 µm). The channel length is 100 µm. The maximum currents are limited by extrinsic resistance associated with the contacts; the intrinsic mobility after subtracting these contributions is around ~7 $cm^2V^{-1}s^{-1}$. (d) Output curves I_d vs. V_{ds} at different back-gate voltages V_{bg}. (e) Molecules used in this study. N1, N2 are n-dopants, P1 is a p-dopant. The cation 2-Fc-DMBI$^+$ is also shown and is the expected product of doping with both N1 and N2; in the case of N2/MoS_2 doping, the fate of the H atom is unknown. Treatment with P1 is expected to form neutral tri(4-bromophenyl)amine and leave $SbCl_6^-$ anions on the surface.

To investigate the doping effects, we first perform electrical characterization on three different samples that were dip-coated in 2.5-5 mM solutions of the dopants presented above for up to 10 min. Each sample contained several tens of transistors. Doping treatments were performed inside a glove box, and all electrical measurements were performed in high vacuum (ca. 10^{-6} mbar) after a short exposure to air during the transfer step (ca. 1 min). The electrical measurements are summarized in Figure 2-2 a-c. Figure 2-2a shows a representative transfer characteristic of a MoS_2 FET before and after doping with N1 (on a semi-logarithmic scale). Even a short immersion (dip) in a N1 solution significantly shifts the threshold voltage of the transistor V_{th} (defined as the voltage necessary to achieve a current of 10^{-10}A) to more negative values, indicated by the arrow. After this measurement, the sample was treated in the same solution for 10 min and measured again. An even more pronounced V_{th} shift and a further current increase are observed. These results are consistent with n-doping of the channel.

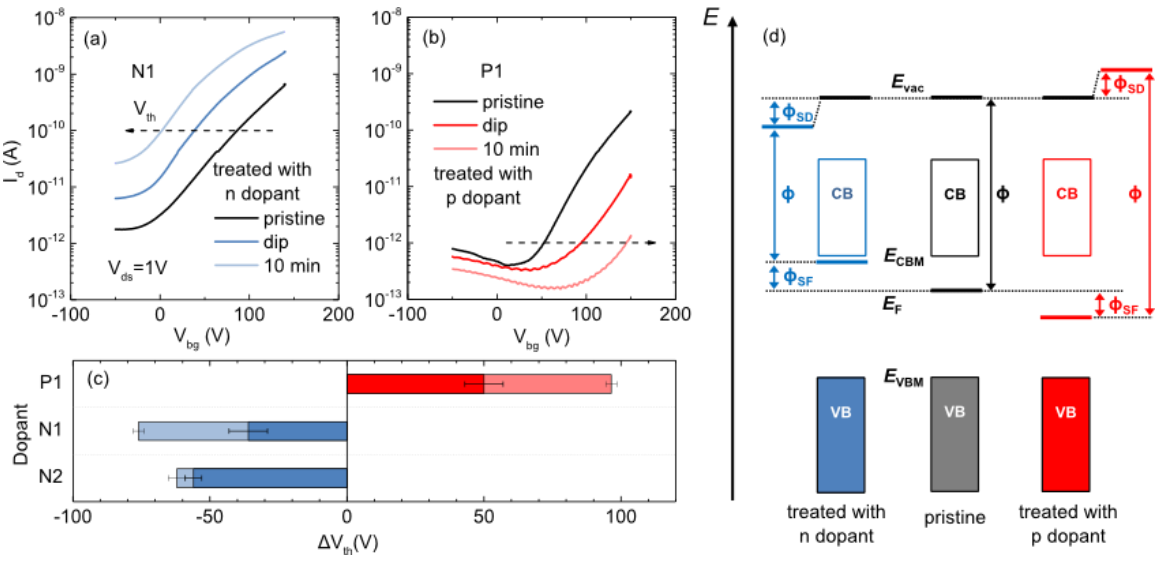

Figure 2-2 (a) Representative transfer characteristics of a MoS_2 FET before and after doping with N1. Treating the transistor with N1 shifts the threshold voltage V_{th} to more negative values, indicating n-doping (arrow). The drain current I_d at a given back-gate voltage V_{bg} is increased by one order of magnitude. (b) In contrast, the P1 treatment shifts the transfer curves to more positive gate values and decreases the overall current. (c) Effects of different n-dopants (N1, N2) and p-dopants (P1) on the threshold voltage V_{th}. Several transistors were measured in each case. Threshold voltage shifts ΔV_{th} are shown relative to the pristine sample (i.e. $V_{th,\ pristine} = 0$ V). Dark bars show the mean ΔV_{th} values after a short dip, whereas light bars represent a 10 min treatment. Error bars indicate the standard deviation from averaging the results obtained with different devices. (d) Effect of molecular surface doping on the band structure of an n-type semiconductor. In the pristine case (center), E_F is closer to the conduction band (CB) than to the valence band (VB). The work function of the pristine material ϕ (center), which is the difference between the vacuum level E_{vac} and the Fermi level E_F, decreases upon treatment with an n-dopant (left) and increases for the p-dopant (right). The total ϕ change consists of two different contributions. Firstly, filling (emptying) of semiconductor states ($\Delta\ \phi_{SF}$) due to electron transfer between the n-(p-)dopants and the channel shifts the Fermi level E_F relative to the valence band maximum E_{VBM}. Secondly, the negatively (positively) charged semiconductor and the positively (negatively) charged dopant ions result in a surface dipole that leads to a shift in the local vacuum level E_{vac} across the surface ($\Delta\ \phi_{SD}$).

In contrast, the P1 treatment shifts the transfer curves to more positive gate values and decreases the overall electron current (Figure 2-2b). However, we do not observe a significant p-type or hole transport at negative gate voltages, consistent with UPS data

(see below), which indicate that the Fermi level is still located far from the valence band. Therefore, the p-dopant is better regarded as neutralizing electrons present in adventitiously n-doped pristine films than as introducing holes into the valence band. We will discuss the band structure changes induced by different treatments further below. Extracted threshold voltage shifts, ΔV_{th}, are plotted relative to the pristine sample (i.e. $V_{th,\,pristine}$ = 0V) in Figure 2-2c for all dopants (N1, N2, P1). Dark bars show the mean ΔV_{th} values after a short dip, whereas light bars represent a 10 min treatment. Error bars indicate the standard deviation from averaging the results obtained with different devices. We observe that both n dopants induce a significant negative ΔV_{th} shift, with a larger effect for N1 than N2. This is consistent with our previous observation that $(DMBI)_2$ dimers are stronger dopants for a naphthalene diimide-based polymer than DMBI-H derivatives.[281] These differences in dopant strength may be due to both thermodynamics and kinetics and can be attributed to the different chemical reactions that are coupled to the electron-transfer reactions required to form stable $DMBI^+$ cations and n-doped semiconductor. In the case of the dimers a C—C bond is broken, whereas in DMBI-H derivatives a C—H bond is broken, leading to the formation of additional side products, the identity of which is unclear in the case of MoS_2 doping. On the other hand, the p-dopant P1 gave a significant positive value of ΔV_{th}. Based on these shifts, we can estimate the charge density n in MoS_2 after doping using the following expression:

$$n = \frac{C_{bg}\Delta V_{th}}{e} \tag{23}$$

where e = 1.6×10^{-19} C is the electron charge, and $C_{bg} \approx 1.33\times10^{-8}$ Fcm^{-2} is the estimated back-gate capacitance $C_{bg} = \varepsilon_0\varepsilon_r/d$, with ε_0 = 8.85×10^{-12} Fm^{-2} being the vacuum permittivity, ε_r =3.9 the relative permittivity of SiO_2, and d = 260 nm the oxide thickness. With ΔV_{th} values from Figure 2-2d (after 10 min), we estimate the following densities of electrons introduced by the n dopants: $n_{N1} \approx 6.3\times10^{12}$ cm^{-2}, $n_{N2} \approx 5.2\times10^{12}$ cm^{-2}; and the density of carriers removed by the p dopant: $n_{P1} \approx 8.0\times10^{12}$ cm^{-2}. Other charge densities can be achieved by changing the treatment time or the solution concentration, providing effective control over the doping level. Our values are slightly lower than the n-doping densities recently reported for doping few-layer exfoliated flakes of MoS_2 with potassium (~1×10^{13} cm^{-2})[153] and benzyl viologen (~1.2×10^{13} cm^{-2}).[285] This discrepancy could be due to different charged state densities at the SiO_2/MoS_2 interface, different material quality of the grown and exfoliated MoS_2, or due to a brief exposure to air after the doping treatment in the present study. It should be noted that the extremely high electron densities induced by doping in these previous reports resulted in a dramatic loss of the current on/off ratio in a back-gated device geometry,[153, 285] yet our back-gated devices retain their on/off ratio after doping while still providing a large change of the work function (see below) and the threshold voltage. The effect of molecular surface doping can be understood in terms of changes to the band structure of a semiconductor, in this case n-type MoS_2 with a band gap of ~1.8 eV (derived from absorption measurements). This value is higher than previously reported for exfoliated trilayer MoS_2 (~1.5 eV[286]), and slightly higher than predicted (~1.7 eV[287]), which may be due to increased interlayer distance as a result of twist between the individual MoS_2 layers.[288-289] In Figure 2-2d, the band structure of an n-type semiconductor is sketched for 3 different cases: untreated or

pristine (center), treated with an n-dopant (left), and treated with a p-dopant (right). The key physical quantities here are the work function, ϕ, and the position of the Fermi level, E_F, relative to the valence band maximum (VBM) or the conduction band minimum (CBM). The work function, ϕ, is the difference between the vacuum level outside the surface of interest, E_{vac}, and E_F. As shown in the left part of Figure 2-2d (n dopant), E_F shifts closer to the CBM because of *filling of states* close to the CB edge by electron transfer (denoted by ϕ_{SF}), while the E_{vac} is lowered across the interface due to the formation of a *surface dipole* between the resultant negatively charged semiconductor and positively charged dopant ions (denoted by ϕ_{SD}). Both of these effects are expected to contribute to lowering of ϕ upon treatment with an n-type dopant, i.e. $\Delta\phi = \Delta\phi_{SF} + \Delta\phi_{SD}$. Conversely, E_F and E_{vac} are shifted to the opposite direction when the material is treated with a p-type dopant, thereby increasing the work function ϕ (right part).

To experimentally determine the work function ϕ and the position of E_{VBM} relative to E_F (i.e. ϕ_{SF}, see Figure 2-2d), we used ultraviolet photoelectron spectroscopy (UPS). Figure 2-3a shows the high binding energy cutoff regions (i.e., secondary edge) of the UPS spectra for a representative sample doped with N1. The secondary electron edge (SEE) shifts to increasingly higher binding energy with increasing dopant treatment time. The work function is given by the difference between the energy of the UV photons (21.21 eV for the He I radiation used here) and the binding energy of the SEE. The work function of pristine MoS_2 is ϕ = 4.63 eV, similar to previous reports,[290] and decreases significantly by around ~1 eV after 10 min N1 treatment. Figure 2-3b shows the corresponding low binding energy part of the UPS spectra close to the Fermi energy (E_F = 0 eV). Prior to doping, the Fermi level of pristine MoS_2 is located ~1.32 eV above the

VBM in the upper half of the band gap (the band gap is ~ 1.8 eV), consistent with the n-type nature of MoS_2, which could be intrinsic due to sulfur vacancies[291-294] or extrinsic due to defects at the substrate/MoS_2 interface.[295] With increasing doping time, we observe an increasing shift of E_{VBM} to higher binding energy. As a result, the Fermi level is now very close to the conduction band minimum (~1.76 eV). On the other hand, after successive treatments of MoS_2 with the p-dopant P1 (Figure 2-3e), an increase in the work function is observed, i.e., the SEE shifts to lower binding energies with increasing treatment times, and the VBM shifts to lower binding energy relative to E_F (Figure 2-3f). However, the Fermi level is still far away (~1.06 eV) from the valence band maximum, because the band gap is relatively large, and the Fermi level of pristine (n-type) MoS_2 lies in the upper half of the band gap (cf. Figure 2-2d). Hence, even though the treatment with the p-dopant removes electrons from MoS_2 and shifts the Fermi level downward, the changes are not sufficient to convert n-type MoS_2 into a truly p-type material. To the best of our knowledge, this is the first observation of work function and Fermi level shifts in MoS_2 upon treatment with a p-type dopant.

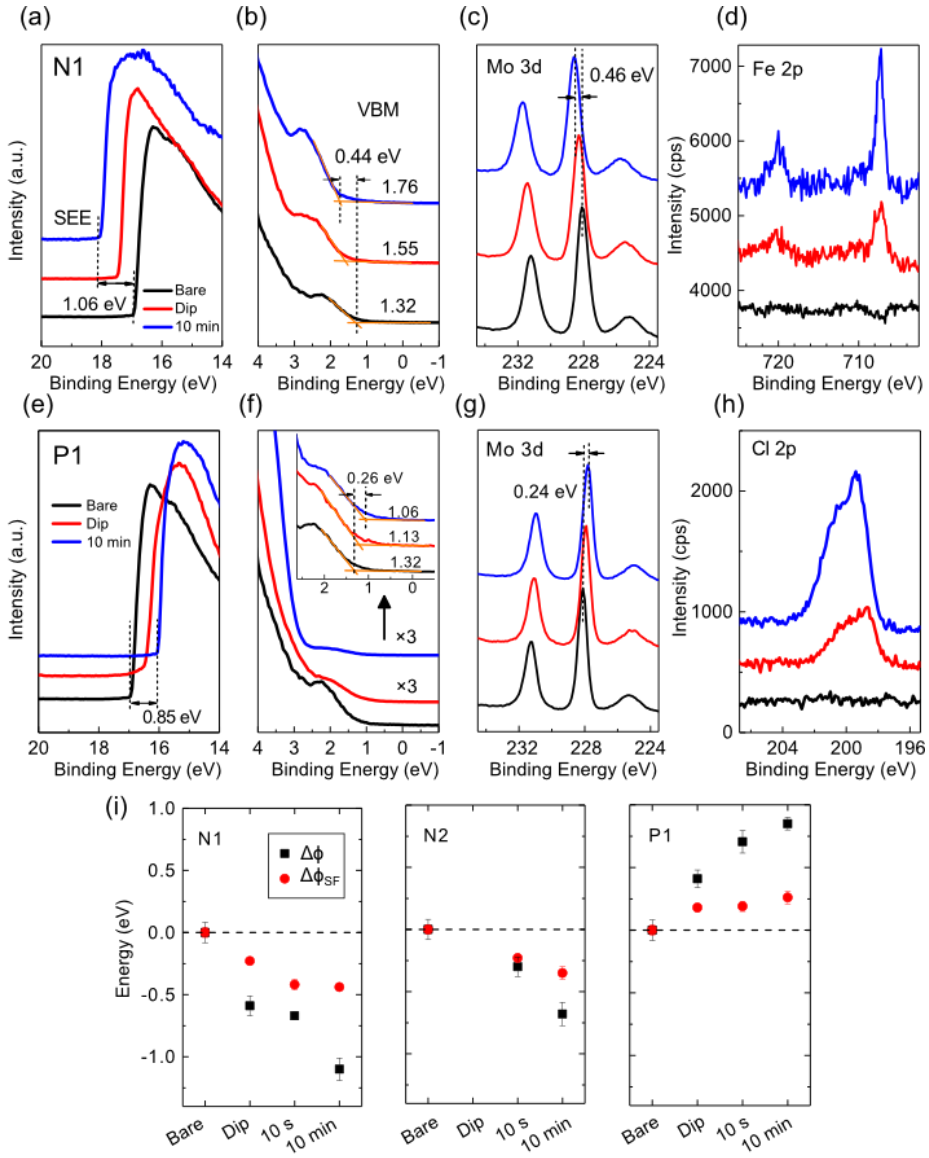

Figure 2-3 UPS and XPS spectra of MoS_2 before and after treatment with N1 (a-d) and P1 (e-h). In a-h, the bottom curves ("bare") are the pristine MoS_2 spectra, middle curves ("dip") are for samples following a short dip in 2.5 mM (N1) or 5 mM (N2 and P1) dopant solution, and the top curves ("10 min") are obtained following a 10 min treatment in the same solution. (a, e) Secondary electron edge shifts (SEE) of MoS_2 after various treatment times. (b, f) Low binding energy region (near the Fermi energy $E_F = 0$ eV). The onset of ionization of filled states relative to zero binding energy is used to track the shifts of E_F relative to VBM. (c, g) XPS core level spectra of Mo 3d. (d, h) XPS core level ionizations characteristic of N1 (Fe 2p) and P1 treatment (Cl 2p), respectively. (i) Summary of total work function shifts $\Delta\phi$ (black squares) and the contribution to the WF change from state filling/emptying $\Delta\phi_{SF}$ (red circles) for different dopants and treatment times, shown relative to the pristine value (energy = 0 eV, dashed line). The contribution from the surface dipole is the difference $\Delta\phi_{SD} = \Delta\phi - \Delta\phi_{SF}$.

As mentioned above (cf. Figure 2-2d), the total ϕ change consists of two different contributions: one from the shift of the Fermi level E_F relative to the VBM and attributable to (de)population of semiconductor states on doping (ϕ_{SF}), and another from the change of the vacuum level, E_{vac}, arising from surface dipole formation (ϕ_{SD}). Figure 2-3i shows the total change in work function $\Delta\phi$ and the portion of the change that is attributed to state (de)population $\Delta\phi_{SF}$, with the difference being induced by the surface dipole ($\Delta\phi_{SD} = \Delta\phi - \Delta\phi_{SF}$). In all cases, both effects make significant contribution, with the relative importance of the dipole contribution generally increasing with the treatment time. For a given treatment time, both contributions from N1 doping are larger than those using N2, consistent with the electrical measurements discussed above.

X-ray photoelectron spectroscopy (XPS) was also used to investigate the doping effects. As seen in Figure 2-3c, the binding energy (BE) of the main Mo 3d peak of n-doped MoS_2 shifts to a higher value (cf. Figure 2-3b). This upshift of peaks is attributed to the population of semiconductor states upon n-doping, and the Fermi level shift toward the conduction band edge. This upshift is also consistent with previous studies on doped MoS_2 flakes.[154] On the other hand, depopulation of filled states through P1 treatment shifts the MoS_2 Mo 3d peak to lower binding energies since the Fermi level is being lowered relative to the VBM (Figure 2-3 g).

Moreover, XPS also reveals increasing surface concentrations of N1 (based on the Fe 2p spectrum), and P1 (based on Cl 2p) as the treatment time increases (Figure 2-3d, h). Assuming that all the dopants fully reacted (only cations and anions present on the surface for n- and p-dopants respectively), we can estimate the surface concentrations of N1 and N2 dopants from the Fe/Mo ratios. The coverage is calculated based on the

dopant to MoS_2 ratio relative to the theoretical value, which is estimated from how many dopant monomers can fit in a close packed arrangement on the surface of trilayer MoS_2. Similarly, the P1 concentration can also be estimated based on the Cl/Mo ratio. For N1, we obtain coverage of 23% and 82% of a molecular monolayer for a quick dip and a 10 min immersion in a dilute toluene solution, respectively. N2 gives lower coverage than N1 (up to 56%), consistent with other evidence – see above – that it dopes MoS_2 to a lesser extent than N1. Calculation details and the close-packed monolayer model are described in our published report.[296] Assuming a 100% doping efficiency, i.e. one electron is transferred for each monomer cation, the change of electron sheet density induced by n-doping with N1 can be estimated as 7.9×10^{13} cm^{-2}, which is about 10 times higher than electron sheet densities calculated based on ΔV_{th} ($n_{N1} \approx 6.3 \times 10^{12}$ cm^{-2}). There are several possible reasons for this discrepancy. Firstly, both dopant ions and unreacted dopants may be present on the surface (although in the case of the p-dopant, XPS is consistent with only $SbCl_6^-$ anions resulting from complete reaction being present). Previous results on graphene doping showed that the doping efficiency for a similar dimeric dopant can be as low as 50%.[282] Secondly, some of the electrons transferred from the dopant may be trapped, for example by strong electrostatic interactions with dopant ions, and, therefore, may not contribute to the drain current. Thirdly, the short exposure to air before the electrical measurements may quench some of the electrons in the n-doped devices.

We have also performed Raman spectroscopy to further understand the doping effects. Figure 2-4a displays the characteristic MoS_2 double peak before and after the doping treatments with N1. The E_{2g}^1 phonon mode represents the in-plane vibrations of

Mo and S atoms, whereas the A_{1g} peak is the out-of-plane vibration of S atoms.[55] The peak positions of both vibrational modes are plotted in Figure 2-4b for the N1 case. We observe a significant downshift of the A_{1g} peak position by ~ 1 cm^{-1} ("softening" or red shift), while the $E_{2g}{}^1$ peak position shows almost no change (< 0.2 cm^{-1}). For doping with N2, the A_{1g} downshift is smaller than for N1 (< 0.3 cm^{-1}, Figure 2-4c), in agreement with the electrical and UPS measurements. All peak shifts are also accompanied by peak broadening (see Figure 2-5) and intensity decrease after the treatment. An opposite trend is observed upon treatment with P1 (Figure 2-4d), with both peak positions shifting slightly (by ~ 0.5 cm^{-1}) to higher values ("stiffening" or blue shift) and narrowing of the peaks (see Figure 2-5).

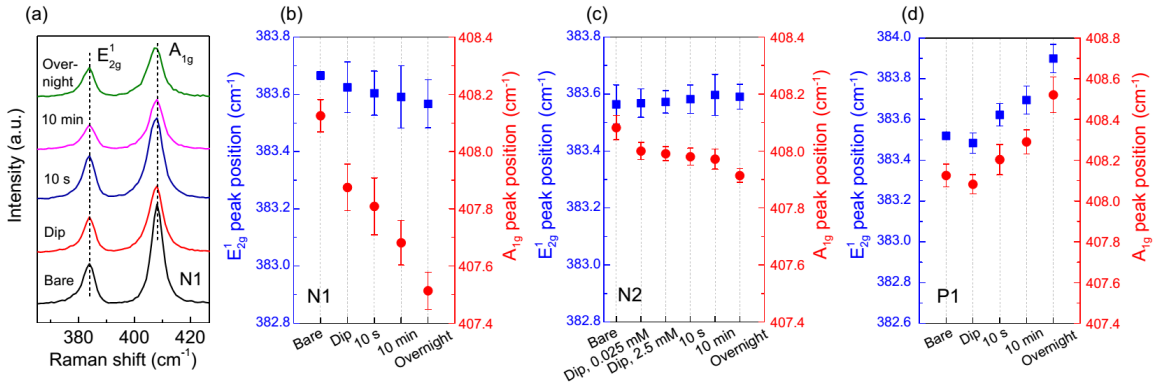

Figure 2-4 (a) Raman spectra of trilayer MoS_2 before and after different treatments with N1. The peak separation is A_{1g}-$E_{2g}{}^1 \approx 23.5$ cm^{-1}, confirming that the MoS_2 film consists of three layers.[56, 297] (b-d) $E_{2g}{}^1$ and A_{1g} peak position shifts upon doping with different compounds.

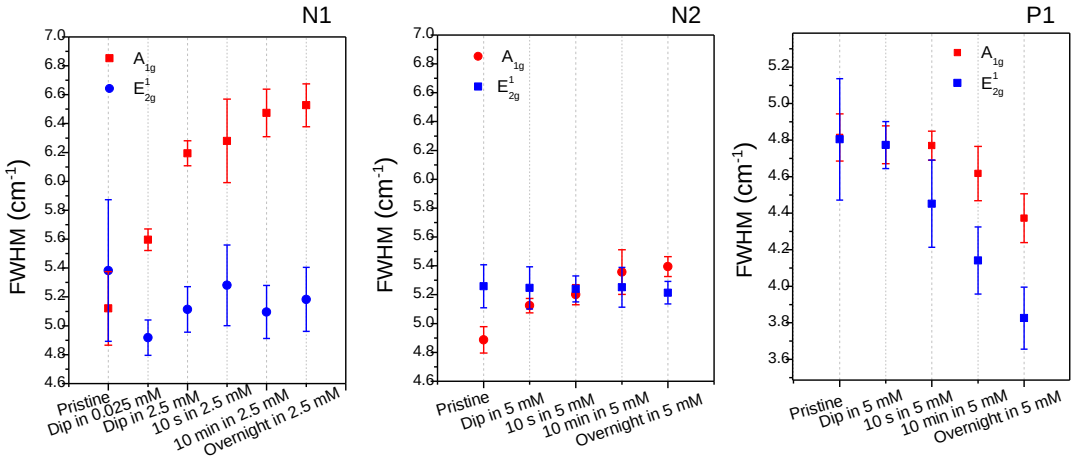

Figure 2-5 Full width at half maximum (FWHM) of A_{1g} and E_{2g}^1 peaks before and after successive dopants treatment. A_{1g} peak broadening is observed after n-doping of MoS_2, with N1 causing a stronger effect than N2. The E_{2g}^1 peak width is barely affected. After P1 treatment, both peaks become slightly narrower.

The n-doping results are consistent with previous work on electrostatic[298] and chemical doping[60] of monolayer MoS_2 flakes. The higher electron concentration in the n-doped MoS_2 increases the electron-phonon scattering, which affects the frequency and the full width at half maximum (FWHM) of phonons via renormalization of their self-energy.[299] In our experiment, this leads to Raman mode softening (i.e., shift to lower frequency) and peak broadening after n-doping with N1 and N2. The difference between the A_{1g} and E_{2g}^1 shifts was previously explained by stronger electron-phonon coupling of the A_{1g} mode based on symmetry arguments.[298] As a result, the A_{1g} peak is affected more strongly by n-doping than the E_{2g}^1 mode. On the other hand, the treatment with P1 depopulates filled states in MoS_2. Therefore, the electron-phonon scattering is reduced and we observe stiffening (i.e., shift to higher frequency) of both Raman-active modes. Unlike in the case of n-doping, the shifts are similar for both A_{1g} and E_{2g}^1 phonons,

suggesting a similar electron-phonon coupling. However, future experimental and theoretical studies are needed to fully understand this effect.

In conclusion, we have studied surface doping of wafer-scale trilayer MoS_2 using solutions of redox-active molecular dopants. Carrier densities of up to 8×10^{12} cm^{-2} and work function changes of up to ± 1 eV can be achieved; however, both these parameters can be controlled through the choice of dopant, treatment time, and the solution concentration. The change in work function arises from a combination of electron transfer from the adsorbed dopants to the MoS_2 channel, as well as the resultant surface dipoles. Both the recently reported neutral dimer of a benzimidazoline radical $(2\text{-Fc-DMBI})_2$ and the related compound 2-Fc-DMBI-H have been shown to be effective solution-processable n-type dopants for MoS_2. Electrical measurements, UPS, XPS and Raman results indicate that the dimer (N1) exhibits a stronger n-doping effect than the monomer (N2), consistent with previous studies of their strength as dopants for organic semiconductors.[281] On the other hand, the treatment with a p-type dopant (P1) neutralized electrons in adventitiously n-doped pristine films, and resulted in less strongly n-type MoS_2 than pristine, rather than truly p-type MoS_2.

The solution-based surface doping described here provides a simple and readily scalable process for tailoring electrical and optical properties of two-dimensional semiconductors. Future work will investigate the influence of the SiO_2/MoS_2 interface charges, device encapsulation with a top-gate dielectric, contact engineering and p-channel transport behavior of doped MoS_2.

2.4 Doping of WSe_2[b]

In this section, we expand the application of solution-processed molecular electron-transfer doping to another 2D layered semiconductor, WSe_2, which is a p-type semiconductor due to intrinsic defects.[300] As in our previous work with few-layer MoS_2,[301] we used tris(4-bromophenyl)ammoniumyl hexachloroantimonate, "Magic Blue" (**P1**), as a strong p-dopant (the $[N(C_6H_4\text{-}p\text{-}Br)_3]^+$ cation is reduced at +0.70 V vs. $(FeCp_2)^{+/0}$).[284] The tetra-*n*-butylammonium salt of the nickel bis(1,2-dicyanoethane-1,2-dithiolene) anion, $(Bu_4N)^+[Ni(mnt)_2]^-$ (**P2)**, was also used as a considerably milder p-dopant (the $[Ni(mnt)_2]^-$ anion is reduced at –0.26 V vs. $(FeCp_2)^{0/+}$).[302] Pentamethylrhodocene dimer $(RhCp^*Cp)_2$ (**N1**), which is used here as an n-dopant for WSe_2, is moderately air-stable in the solid state, has been applied to the surface n-doping of the 2D material graphene,[282] carbon nanotubes,[178] and various metal and metal-oxide electrode materials,[303] as well as to the bulk doping of organic semiconductors;[176] moreover, $(RhCp^*Cp)_2$ reacts an analogous fashion to the dimeric benzimidazoline-based dimer[173] that we have previously used as an n-dopant for few-layer MoS_2,[301] with bond cleavage accompanying electron transfer leading to the formation of two monomeric cations (here $(RhCp^*Cp)^+$) and has a similar effective redox potential ($E((RhCp^*Cp)^+/0.5(RhCp^*Cp)_2)$ estimated to be ca. –2.0 V vs. $(FeCp_2)^{+/0}$).[304-305] The redox potentials of dopants used in this study is shown in Figure 2-6. Physical characterization using ultraviolet and X-ray photoelectron spectroscopy (UPS and XPS) as well as Raman spectroscopy are used to confirm the doping effects and to understand

[b] Adapted with permission from Tsai, M.-Y.; Zhang, S.; Campbell, P. M.; Dasari, R. R.; Ba, X.; Tarasov, A.; Graham, S.; Barlow, S.; Marder, S. R.; Vogel, E. M., Solution-Processed Doping of Trilayer WSe_2 with Redox-Active Molecules. *Chemistry of Materials* **2017**. Copyright 2017 ACS. DOI: 10.1021/acs.chemmater.7b01998

the underlying doping mechanisms. In addition, the *I-V* characteristics of WSe_2 field-effect transistors (FET) modified with both p- and n-dopants are characterized, and highly reproducible electrical performance is achieved.[306]

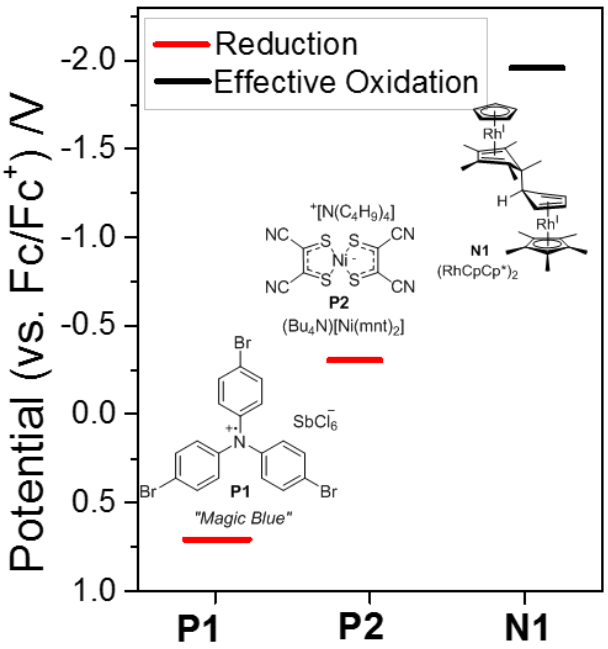

Figure 2-6 The redox potentials of dopants used in this study. On reaction with WSe_2, **P1** is expected to form neutral tris(4-bromophenyl)amine and leave $(SbCl_6)^-$ anions on the surface, **P2** is expected to form the corresponding $[Ni(mnt)_2]^{2-}$ dianion, which may or not be accompanied by $(NBu_4)^+$ cations on the surface (see discussion in the SI), and **N1** is expected to form monomeric $(RhCp^*Cp)^+$.

Similar to the discussion in section 2-3,[301] large-area trilayer WSe_2 was exposed to molecular oxidants and reductants by dipping in solutions (in dichloromethane for **P1** and **P2** and in toluene for **N1**) for various times in an inert atmosphere glove-box. The

effects of n- and p-doping on the band structure of the semiconductor were directly characterized using the ultraviolet photoelectron spectroscopy (UPS) in high vacuum (ca. 10^{-8} Torr) without exposure to air; UPS was used to determine the work function, WF, ϕ (ϕ = 21.22 eV – E_{SEE}, where SEE denotes the secondary electron edge, Figure 2-7a) and the position of the valence band maximum (E_{VBM}) relative to the Fermi level E_F. As WSe_2 is p-doped, the Fermi level (E_F) is expected to shift closer to the valance band maximum (VBM) as filled states are emptied by electron transfer to the p-dopants, while the concomitant formation of a surface dipole resulting from the positive charge carriers formed in the doped film and the negatively charged doping products on the surface is expected to increase the vacuum level E_{vac}, both effects contributing to an increased WF. Conversely, in the n-doping case, E_F will shift closer to the conduction band minimum (CBM) and E_{vac} will be reduced by a surface dipole of opposite sign from that obtained on p-doping. The UPS results are summarized in Figure 2-7b. The pristine sample of WSe_2 used for doping exhibited a WF of 4.10 ± 0.08 eV, and the low-binding-energy valence-band section of the spectrum showed that the VBM lies 0.78 eV below the Fermi level. In the case of **P1** doping, the SEE successively shifted to lower binding energy with increased exposure time, corresponding to an increase of the WF up to 5.00 eV after 1 hour treatment, which, to the best of our knowledge, is the largest increase in WF reported for WSe_2. Over the same exposure time, the Fermi level shifted to within 0.44 eV of the VBM, indicating that 0.34 eV of the total WF increase of 0.9 eV is attributable to the downward shift of the Fermi level, with the remaining 0.56 eV being, therefore, attributable to the raising of E_{vac} by the surface dipole built up on the WSe_2 film. Consistent with the p-dopant redox potentials shown in Figure 2-6, **P1** acts as a stronger

p-dopant than **P2** under a given set of conditions, inducing larger shifts in WF and in E_{vac} vs. E_{VBM}. As expected, increasing exposure of WSe_2 to the n-dopant **N1** (Figure 2-7b) results in successive decreases in the WF and shifts of the Fermi level away from the VBM.

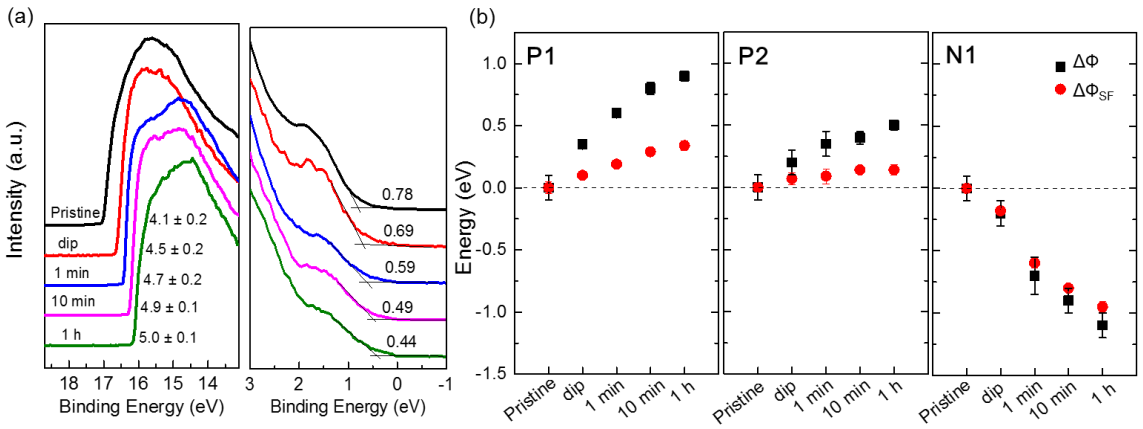

Figure 2-7 UPS spectra of WSe_2 before and after treatment with **P1**, **P2** and **N1** (5×10^{-3} and 2.5×10^{-3} M p- and n-dopant solutions, respectively). In (a) the subsequent treatments from top to bottom are pristine WSe_2 spectra, dip, 1 min dip, 10 min and 1 h dipping using **P1**. The values given in the left and right panels correspond to the WFs and to the position of the Fermi level relative to the VBM. (b) Summary of total WF shifts, $\Delta\phi$ (squares), and the contribution to the WF change from state emptying/ filling $\Delta\phi_{SF}$ (circles) for different dopants and treatment times, shown relative to the pristine value (energy = 0 eV, dashed line). The contribution to the WF shift from the surface dipole is given by $\Delta\phi_{SD} = \Delta\phi - \Delta\phi_{SF}$.

The doped surface was then characterized by XPS to investigate the density and nature of dopant species present. Figure 2-8a shows the binding energy (BE) of the main W 4f peak from the **P1**-doped films. Removal of electrons from the valance band through p-doping is expected to shift the main W 4f peak (W $4f_{7/2}$) to lower binding energies

since the Fermi level is being lowered relative to the VBM. Indeed, a 0.32 eV shift of the main W 4f peak was observed, which is consistent with the E_F shifts relative to the E_{VBM} characterized by the UPS shown previously in Figure 2-7; a similar trend was observed for **P2**-doped surface. On the contrary, n-doping leads to the upshift (i.e. toward higher binding energy) of the W 4f peak since the Fermi level is being shifted away from the VBM (shown in Figure S2). Figure 2-8b to d shows the increased concentration of the dopants on the surface based on the Cl 2p (**P1** dopants), Ni 2p (**P2**) and Rh 3d (**N1**) peaks, respectively, as the treatment time increases. This is consistent with expectations that the neutral tris(4-bromophenyl)amine, formed after the tris(4-bromophenyl)ammoniumyl radical cation accepts an electron from the WSe_2, will largely remain in solution and/or to be washed away in the following rinsing step, leaving on the surface mostly hexachloroantimonate counter ions, which serve to balance the charges introduced to the film. A coverage of 38% of a molecular monolayer was obtained for a 10 min immersion in the dilute solution of Magic Blue; thus the change of hole sheet density induced by p-doping with **P1** can be estimated as 6.3×10^{13} cm^{-2}.

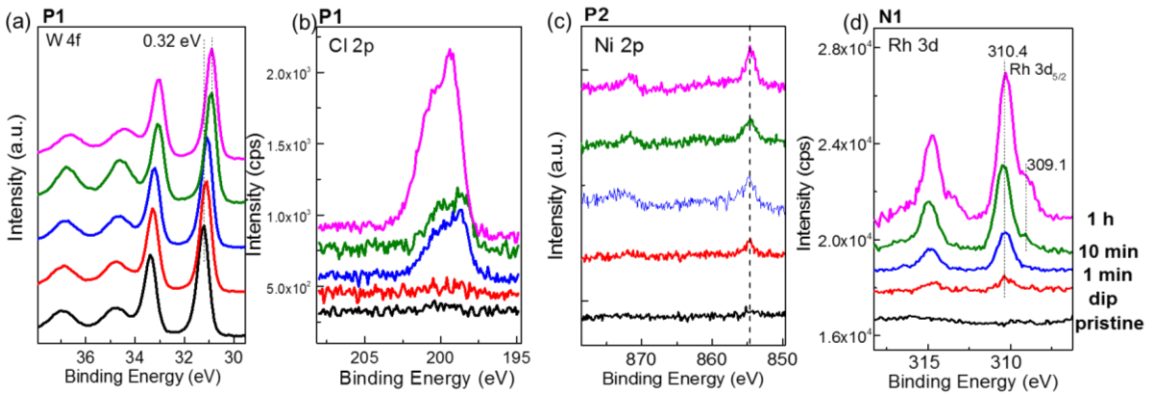

Figure 2-8 (a) XPS core-level W 4f spectra before and after doping with **P1** (the pair of peaks at higher binding energy are attributed to the presence of WO_x). XPS core-level peaks indicating the presence of doping products on WSe_2: (b) Cl 2p from the anion of **P1** "Magic Blue", (c) Ni 2p attributed to $[Ni(mnt)_2]^{n-}$ (n = 1 and/or 2) anions from **P2** and (d) Rh 3d from **N1**, attributed primarily to the $(RhCp^*Cp)^+$ cation, with the low-BE shoulders likely attributable to unreacted $(RhCp^*Cp)_2$.[174, 303]

Next, we examine the changes in Raman spectra induced by doping. Figure 2-9 shows the Raman spectra of the trilayer WSe_2 used in this study. As shown in Figure 4a, the E_{2g}^1 phonon mode, which corresponds to the in-plane vibrations of W and Se atoms, and the A_{1g} peak, the out-of-plane vibration of Se atoms, are overlapped, consistent with the reported literature for trilayer WSe_2 films.[307] The Raman spectra were fitted using Gaussian functions to extract the peak positions for both vibrational modes. For Magic Blue (**P1**) doping, significant red shifts of both A_{1g} and E_{2g}^1 peaks are observed (Figure 2-9b); this is caused by the change of the hole-phonon scattering in the doped film. A similar but weaker trend is observed after **P2** treatment as shown in Figure 2-9c. This observation is also consistent with previous work on p-doping of WSe_2 films.[62] On the n-doping side, blue shifts are observed for A_{1g} and E_{2g}^1 peaks, and are presumably caused by the lower charge-carrier concentration in the film, in Figure 2-9d. This is the first

demonstration of an n-doping effect using electron transfer from redox-active molecules on WSe_2; future experimental and theoretical studies are needed to fully understand this.

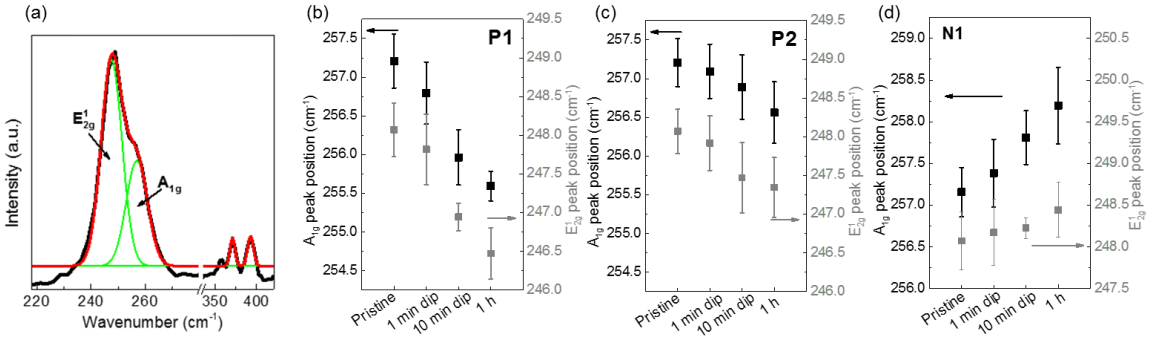

Figure 2-9 Raman spectra of trilayer WSe_2 used in this research. (a) Deconvolution of the overlapping $E_{2g}{}^1$ and A_{1g} peaks in WSe_2. (b)-(d) Summary of $E_{2g}{}^1$ and A_{1g} peak position shifts upon doping with **P1**, **P2** and **N1** dopants, respectively.

To investigate the electrical effects of doping on the WSe_2, FETs were fabricated using trilayer film by CMOS-compatible photolithography processes with a bottom-gate configuration and treated with three different dopants (**P1**, **P2** and **N1**) using the dip-coating method in 5 mM (for **P1** and **P2**) or 2.5 mM (for **N1**) solutions. The trilayer WSe_2 film used in this study through direct selenization can reach the maximum field-effect mobility of 10 $cm^2\ V^{-1}\ s^{-1}$ after the subtraction of contact resistance.[123] This mobility value is comparable to previous work on CVD-grown few-layer WSe_2.[308] Figure 2-10a and Figure 2-10b show representative transfer characteristics (drain current (I_d) - gate voltage (V_{bg}) curves) of the WSe_2 FETs after doping with **P1** and **P2**, respectively. Using Au as contact material, WSe_2 FETs show p-type behavior because the work

function of Au aligns well with the valence band of WSe_2, resulting in efficient hole injection. After an initial short dip into the **P1** solution, a significant shift of the I_d-V_{bg} curve to the positive bias side was observed as shown in Figure 2-10a, which indicates the WSe_2 was p-doped, consistent with the UPS data. As the duration of doping treatment increases, the I_d-V_{bg} curves shifts further toward a higher positive voltage, i.e. a stronger p-doping effect. The **P2**-treated devices show a similar trend but the changes are less dramatic than those obtained with **P1** treatment (Figure 2-10b). The shift of the I_d-V_{bg} curve can be summarized using the threshold voltage shift (ΔV_{th}), which is defined here as the difference between the applied V_{bg} value corresponding to a I_d value for the doped device equal to 5×10^{-8} A and that for the untreated sample (denoted as pristine; i.e. $\Delta V_{th,\ pristine} = 0$) as shown in Figure 2-10c. A trend of positive ΔV_{th} (a shift of I_d-V_{bg} curve toward positive voltage) is clearly observed for both **P1** and **P2** treated devices and a significant ΔV_{th} up to 80 V is achieved after 10 minutes of **P1** treatment. Using simple $\Delta p = C_{bg}\Delta V/q$ expression, where back-gate capacitance C_{bg} is estimated using parallel-plate capacitor model, $C_{bg} = \varepsilon_0\varepsilon_r/d$ with $\varepsilon_r = 3.9$ for SiO_2 and the thickness of the gate dielectric $d = 300$ nm, the change of hole sheet density can be estimated as 5.8×10^{12} cm^{-2}, which is much smaller compared with the XPS results (6.3×10^{13} cm^{-2}). As explained earlier, and consistent with the comparison of UPS measured and FET-estimated Fermi-level shifts, many of the charge carriers introduced from the dopant may be trapped and, therefore, may not contribute to the current. From short dip to 1 minute **P1** treatment, the ΔV_{th} is doubled from 33 to 60 V, consistent with a fast and efficient electron-transfer reaction between the **P1** dopants and the WSe_2. After a short dip in **P2** solution, the 31 V

shift of V_{th} is comparable to the 33 V shift obtained using **P1**, but the **P2** doping effect saturates faster with time due to its less oxidizing redox potential.

The doping of the WSe_2 also impacts the off state current (I_{min}). Figure 2-10d shows the relative change of I_{min} ($\Delta I_{min}/I_{min,0}$) with respect to the pristine (untreated) sample at V_{bg} = 70 V for the **P1** and **P2** treatments. The conductance of the WSe_2 can be tuned by more than 3 orders of magnitude using **P1** doping for less than 10 minutes, which offers a facile mechanism to tailor the conducting properties of the WSe_2. A less pronounced impact on the off-state current is seen for **P2** than for the stronger oxidant **P1**. We emphasize that under such gate bias conditions, the WSe_2 FET devices are in their 'off' state and the number of carriers induced by the gate bias is negligible. Therefore, the change of the I_{min} is mainly attributed to the change of carrier concentration due to the electron transfer between the WSe_2 and the dopants.

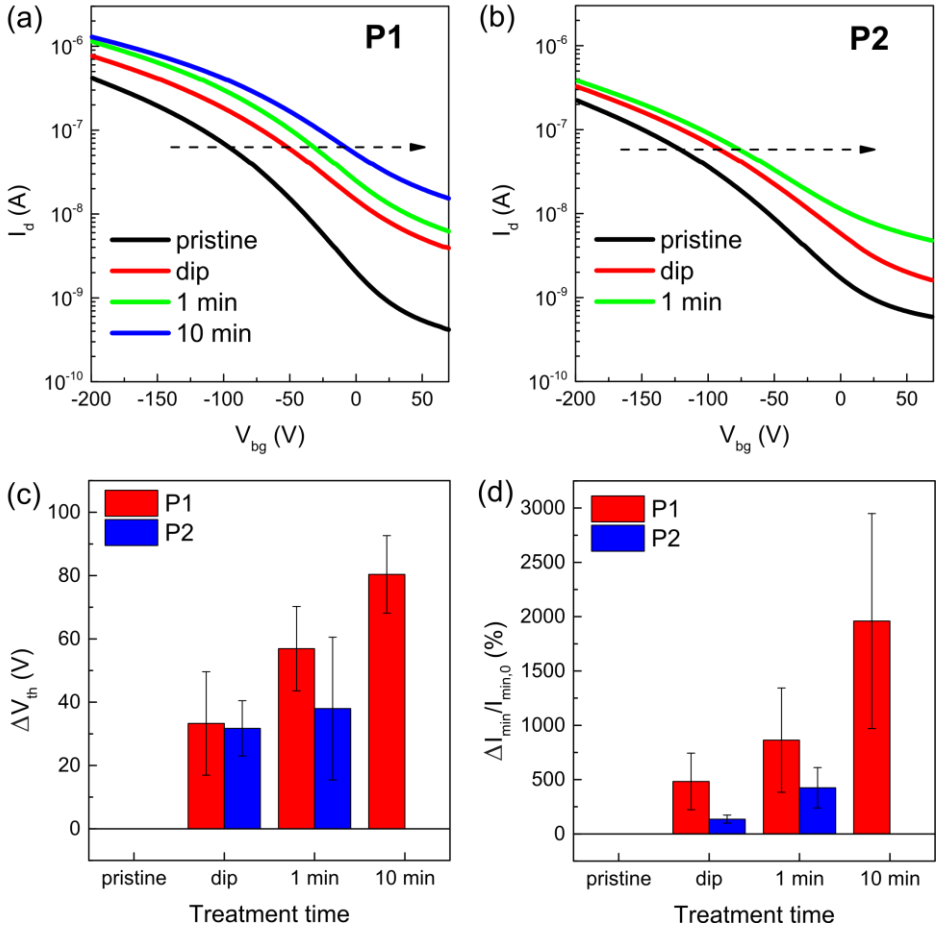

Figure 2-10 Representative I_d-V_{bg} characteristics of WSe_2 transistors treated with (a) **P1** and (b) **P2** dopants. After treatment with p-dopants, the transfer curves shift to the more positive bias side, indicating p-doping. The doping strength can be controlled by the treatment time. (c) The evolution of the change of V_{th} (ΔV_{th}) after p-doping. **P1** dopant is more effective than **P2** and can shift V_{th} up to 80 V after 10 min treatment. (d) The evolution of I_{min} (i.e. off state current) of treated WSe_2 devices.

As discussed above, the change of the Fermi level in WSe_2 semiconductors after doping can be measured using UPS. Alternatively, the *I*-*V* characteristic of FET devices can also be used to estimate the Fermi level shift. The dopants are expected to impact both the channel current in the on-state, as well as the off-state current of the device due to changes in the Schottky barrier height at the metal-semiconductor interface. Therefore,

two techniques were used to estimate the Fermi level shift relative to VBM (1) the I_d-V_{ds} equation in the on-state and (2) a thermionic emission model (TE) in the off-state.[309] The I_d-V_{ds} relationship of a transistor is expressed in Equation (25).

$$\Delta I = \mu q \Delta p \left(\frac{W}{L}\right) V_{ds} \tag{24}$$

$$\Delta p = \left(\frac{g_v m_v^*}{\pi \hbar^2}\right) ln\left[exp\left(\frac{-q\Delta\varphi_p}{k_B T}\right) + 1\right] \tag{25}$$

where ΔI is the change of the I_d, μ is the minimum mobility (1 $cm^2 V^{-1} s^{-1}$ is a measured value under the small gate bias being considered here)[123], q is the electron charge, W is the width of the channel, L is the length of the channel, drain to source voltage V_{ds} is 10 V and Δp is the change of carrier concentration. The change of carrier concentration in the semiconductor channel can be estimated using the change in I_{ds} through Equation 1. The change of carrier concentration ($\Delta\varphi_p$) will determine the relative position of Fermi level to the VBM in the semiconductor channel, which can be estimated using Equation 2, where the effective mass of holes m_v* is 4.19 × 10^{-31} kg,[310] g_v = 2 is the degeneracy of valence band, $\hbar$ is the reduced Plank's constant and k_B is Boltzmann's constant. The resulting Fermi level shift after doping can be estimated by monitoring the change of channel current I_d. For the off-state current, a thermionic emission model is used to estimate the relationship between I_d and the Schottky barrier height (Φ_B) at the metal-semiconductor interface:[309, 311]

$$I_{ds} = A_{2D}^* S T^{3/2} \, exp\left[-\frac{q}{k_B T}\left(\phi_B - \frac{V_{ds}}{n}\right)\right] \tag{26}$$

$$A_{2D}^{*} = \frac{q\left(8\pi {k_B}^3 {m_v}^*\right)^{1/2}}{h^2} \quad (27)$$

where A^*_{2D} is the Richardson constant for 2D materials as expressed in Equation 28,[311] n = 1 is the ideality factor, T is the temperature and $s = -\frac{1}{1000k_B}(\phi_B - \frac{V_{ds}}{n})$. The calculated and measured values of Fermi level shift are summarized in Table 2-1. The calculated values of Fermi-level shift in the WSe_2 channel (denoted as I_d-V_{ds}) are slightly larger than that under the metal contacts (denoted as TE) but very similar to each other, verifying the existence of extra carriers in the WSe_2 channels as well as under the contacts. However, values Fermi level shift calculated in either way are smaller than the measured values from UPS. For example, after 1 min **P1** treatment, the calculated values are 70.0 meV (from I_d-V_{ds}) and 69.4 meV (from TE), while the UPS measured value is 190 meV; after 10 min treatment, the calculated values are 93.5 meV (from I_d-V_{ds}) and 92.6 meV (from TE) compared to 290 meV from UPS. A similar phenomenon is observed after **P2** treatment. The discrepancy between the values from physical characterization and *I-V* characteristics may be attributed to the high defect density in WSe_2. It is possible that some extra carriers are trapped in the defect states and become immobile, contributing little to the current of FETs. However, the relationship between the defect levels and the doping effect in WSe_2 should be further investigated. It will also be crucial to optimize the fabrication process of WSe_2 films in order to improve the materials quality as well as reduce the defect density.

Table 2-1 Summary of the Fermi level shift after p-doping using P1 and P2 relative to the pristine sample. The values of the Fermi level shift were obtained from three different approaches: (1) estimated value using I_d-V_{ds} relationship from the change of I_d upon doping, denoted as I_d-V_{ds}; (2) estimated value using room-temperature thermionic emission model by monitoring the change of Schottky barrier height induced by the Fermi level shift, denoted as TE; and (3) measured values from UPS analysis, denoted as UPS. The calculated values are smaller than the UPS-measured values.

Treatment	**Fermi level shift (meV)**					
Dopant	**P1**			**P2**		
Method	I_d-V_{ds}	TE	UPS	I_d-V_{ds}	TE	UPS
Short dip	58.1	57.6	90.0	28.4	28.2	65.0
1 min	70.0	69.4	190	56.3	55.9	90
10 min	93.5	92.6	290	--	--	140

Finally, Figure 2-11a and Figure 2-11b show representative transfer characteristics of the WSe_2 FETs with Au or Ti/Au stacking source and drain (S/D) contacts after doping with **N1**, respectively. Figure 2-11c and Figure 2-11d show the evolution of ΔV_{th} and I_{min} of WSe_2 FETs with Au or Ti/Au stacking source and drain (S/D) contacts after **N1** n-doping treatments, respectively. After n-doping, the I_d-V_{bg} curve shift to a more negative bias side and a negative ΔV_{th} is observed. In Au-contact devices, the n-doping effect is limited even after a long (14 hours) immersion in the **N1** solution. According to the UPS analysis, the Fermi level of WSe_2 is expected to shift

upward and approach the CBM after n-doping, and the source and drain contacts using lower work function metals are desired. Indeed, in contrast to Au-contact devices, WSe_2 FET devices using Ti/Au contacts show a much more significant shift of V_{th} to negative bias value, which is highly controllable through variation of treatment time and affords the largest achievable ΔV_{th} of -200 V after 14 hours treatment, much larger than the ΔV_{th} values obtained in Au-contact devices. Thus, the limited n-doping effects in Au-contact devices can be attributed to the mismatch of the work function of contacts to the semiconductors after doping. Similarly, the decrease of I_{min} is also scalable with treatment time in Ti/Au devices. While a significant decrease of V_{th} was achieved after prolonged n-doping, no strong evidence of inversion from p-channel to n-channel behavior was observed in WSe_2 devices. This can be attributed to the high defect density in WSe_2. Amani *et al.* also reported that donor impurities on the surface of 2D metal selenides make them less responsive to n-doping than their sulfur analogues.[181]

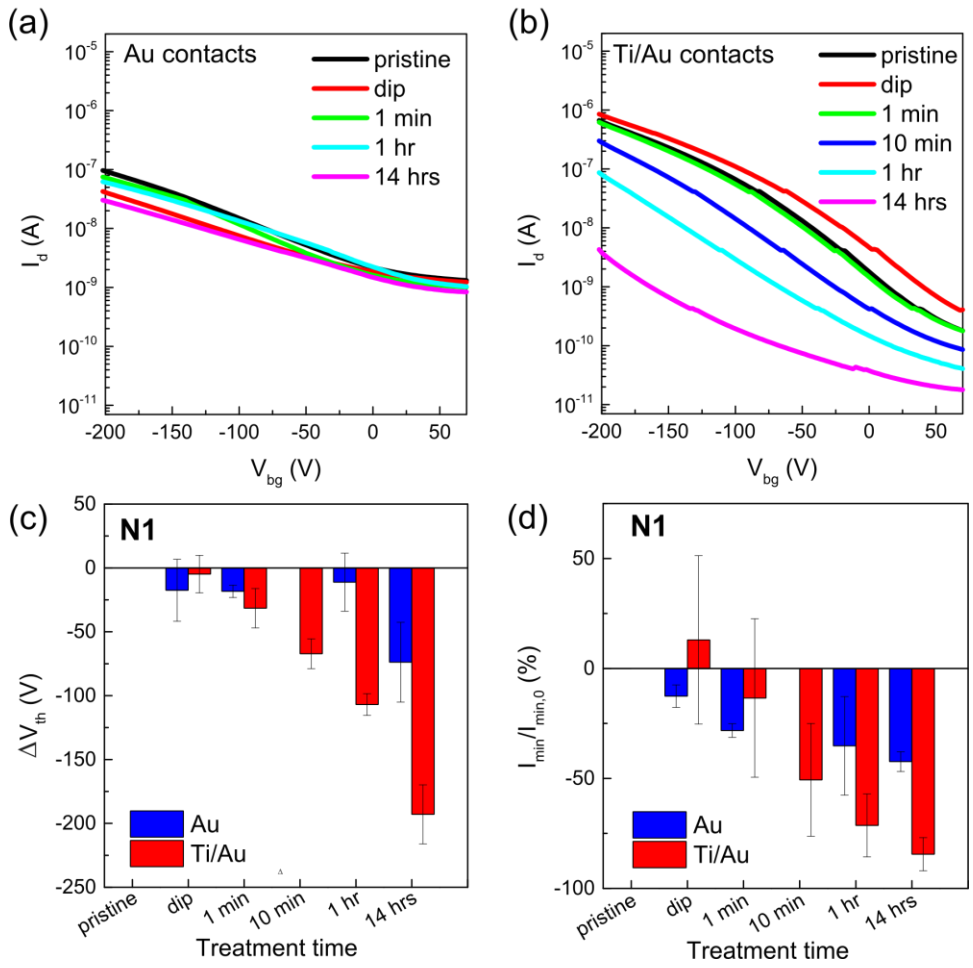

Figure 2-11 Summary of WSe_2 devices treated with **N1** n-dopants. Two types of source and drain contacts were deposited to investigate the impact of contact metals on the n-doping efficiency: Au (100 nm thick) or Ti/Au stacking (30 nm/70 nm thick). Representative I_d-V_{bg} characteristics of WSe_2 transistors treated with **N1** with (a) Au contacts and (b) Ti/Au contacts. (c) The evolution of the change of V_{th} (ΔV_{th}) after n-doping using **N1** dopants solution. The Ti/Au devices show a larger response ton-doping and the shift of the V_{th} is up to -200 V after 14 h treatment. (d) The evolution of I_{min} of treated WSe_2 devices, relative to pristine case $I_{min,0}$, using two types of metal contacts.

In conclusion, the electron-transfer p- and n-doping of wafer-scale trilayer WSe_2 using solutions of redox-active metal-organic oxidants and reductants has been demonstrated. Bidirectional doping and work function changes of up to ±1 eV can be

achieved. The doping strength as well as the direction of doping is highly controllable through the choice of dopants, treatment time and the concentration of doping solution. The p-doping process introduces extra carriers into the WSe_2 by electron transfer to the dopant species from the semiconductor, and leaves charged dopant ions on the surface. As a result, the change of work function after doping is a combined effect of Fermi level shift relative to VBM and of surface dipole formation. After **P1** and **P2** treatment, strong p-doping effects including the changes of band structure, were indicated by UPS, XPS and Raman spectroscopy. In addition, electrical characterization of WSe_2 FETs after doping showed the increase of V_{th} and the increase of the channel current which again supported the observation of strong p-doping effects. However, many of the extra carriers generated from the doping process might be trapped in the defect states and become immobile; this is suggested by the discrepancy between the Fermi level shift estimated by *I-V* characteristics and that measured by UPS. On the contrary, even though the **N1** dopant is able to decrease the work function of p-type WSe_2 significantly, a truly n-type WSe_2 could not be achieved.

2.5 Conclusion

The solution-based electron-transfer doping approach provides a simple yet effective route to tailor the band structure of the 2D materials, and control the resulting electrical and optical properties. Using the metal-organic redox-active molecules, the doping strength can be controlled by the choice of dopants, the concentration of dopant solution and treatment time. Unlike commonly reported organic dopants used in surface

doping of TMDs, the redox-active molecules used here provide a stable charge transfer between the dopants and semiconductors with coupled chemical reaction, i.e. salt formation on the surface. Both n- and p-doping of large-area MoS_2 and WSe_2 has been demonstrated. The doping effects have been verified by the change of work function, the position of Fermi level, the phonon-electron interaction and electrical characterization. Overall, this solution-based charge transfer doping technique provides a non-destructive yet scalable method to control the electrical properties of atomically thin 2D TMDs. Future studies on the optimization of the quality of TMD films, defects and contact engineering will be important in further assessing the potential of the utility of this approach.

CHAPTER 3. FLEXIBLE MOS_2 FET-BASED PIEZORESISTIVE MECHANICAL STRAIN SENSOR[c]

This chapter describes MoS_2-based flexible FET devices and their application for mechanical sensing applications. Section 3.1 highlights the strain-induced properties in TMD semiconductors. Section 3.2 presents a device transfer technique for the fabrication of flexible TMD-based devices and other experimental details. Section 3.3 discusses (1) the influence of transfer process and the substrate; (2) bending stability of flexible devices and (3) the performance of flexible MoS_2 piezoresistive strain sensors.

3.1 Introduction

Molybdenum disulfide (MoS_2) provides superior mechanical and electrical properties, and better long-term stability compared to organic semiconductors. As a result, MoS_2 is an ideal candidate for high-performance flexible and transparent electronics.[312-316] Such flexible MoS_2-based devices can offer new functionality, such as the recently observed piezoelectricity for energy conversion.[211] In addition, a wide range of devices can be realized using the piezoresistive effect typically occurring in semiconductors, including strain gauges and pressure or acceleration sensors. Even though recent spectroscopic studies and theoretical works showed that the band gap of

[c] Adapted with permission from Tsai, M.-Y.; Tarasov, A.; Hesabi, Z. R.; Taghinejad, H.; Campbell, P. M.; Joiner, C. A.; Adibi, A.; Vogel, E. M., Flexible MoS_2 Field-Effect Transistors for Gate-Tunable Piezoresistive Strain Sensors. *ACS Appl. Mater. Interfaces* **2015,** *7*, 12850-12855. Copyright 2015 American Chemical Society.

MoS_2 can be changed under strain,[189, 197, 202-203, 207-208] the implications of these strain-induced band gap changes on electrical devices have not been carefully explored. The work by Lee *et al.* has studied MoS_2 FETs under strain but, surprisingly, the authors did not observe any strain-induced changes in the electrical signal.[316] These results are in contradiction to previous optical studies and theoretical predictions.

In this chapter, the properties of flexible MoS_2 FETs under applied strain are investigated. It is shown that the devices are highly sensitive to strain, which is in agreement with theoretical studies and optical measurements. The origin of this effect is shown to be the strain-induced band gap change, which is confirmed by optical reflection spectroscopy. In addition, the strain sensitivity can be significantly tuned by adjusting the MoS_2 Fermi level by applying a gate bias.

3.2 Experimental methods

3.2.1 Fabrication of flexible MoS_2 FETs

First, a 300 nm thick SiO_2 layer was grown via thermal oxidation on heavily phosphorus-doped Si wafer (<100>, 0.01-0.05 Ohm-cm). MoS_2 was synthesized by sulfurizing an electron-beam evaporated 1 nm thick Mo film on a SiO_2/Si wafer at 1050°C. A more detailed description of the MoS_2 synthesis and characterization is presented elsewhere.[317] The MoS_2 FETs were fabricated using a two-step standard photolithography process. As a first step, 60 nm thick gold source and drain contacts were deposited by e-beam evaporation in a lift-off process using a positive photoresist

(Shipley Microposit S1813). Second, the transistor channels were defined by the photoresist, and the pattern was transferred to MoS_2 by reactive ion etching in a gas mixture of SF_6 and O_2.

The fabrication of flexible devices using a device transfer technique is schematically shown in Figure 3-1. The as-fabricated MoS_2 FETs were first coated with a thin layer of poly(methyl methacrylate) (PMMA) followed by drying at room temperature (Figure 1a). The PMMA-coated sample was then immersed in buffer oxide etch (BOE, 40% NH_4F : 49% HF = 6 : 1 v/v in water) for one day to remove the underlying SiO_2. The released FETs from the substrate were held together by the PMMA supporting layer and floated on the acid bath (Figure 3-1b). The floating devices were then transferred to a deionized water bath and transferred (fished) (Figure 3-1c) onto a flexible Al_2O_3 (80nm)/ITO/PET substrate (Figure 3-1d) (17 Ω/square ITO on 100 μm thick PET substrate, Solaronix). The 80 nm thick Al_2O_3 gate dielectric was deposited with atomic layer deposition (ALD) at 100°C. Subsequently, the sample was heated on a hot plate at 150°C for 5 minutes and the PMMA layer was removed by soaking the sample in an acetone bath for 3 hours (Figure 3-1e).

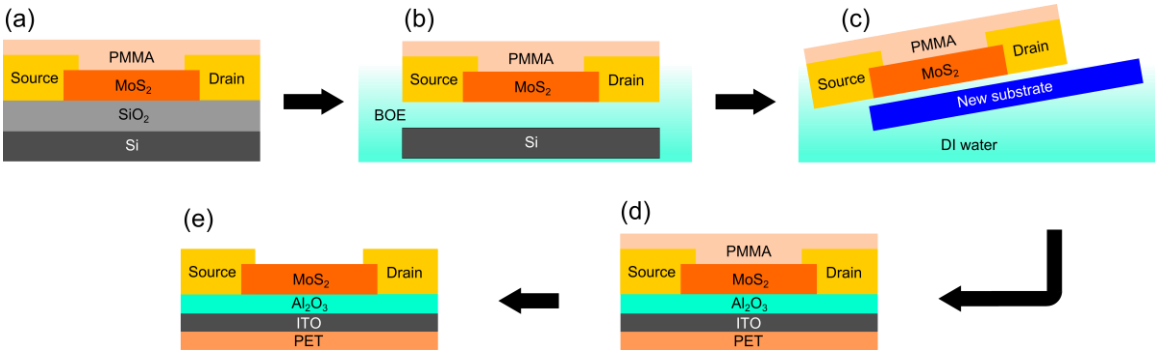

Figure 3-1 Fabrication of flexible MoS_2 field-effect transistors using a device transfer technique. (a) MoS_2 field-effect transistors are fabricated on a SiO_2/Si wafer and coated with a layer of PMMA. (b) The SiO_2 layer is chemically etched in a BOE bath to release the devices from the substrate. (c) Floating devices are held together by the PMMA layer and are transferred from a DI water bath onto a new substrate, which, in principle, can be any water-stable material. A flexible PET substrate with a conductive ITO back-gate electrode and ALD-grown Al_2O_3 dielectric is chosen here (d). (e) The PMMA layer is then removed in an acetone bath.

3.2.2 Electrical characterization of MoS_2 under bending condition

The electrical measurements were performed using a Keithley 4200-SCS parameter analyzer at room temperature. The drain current at a constant drain-source voltage of V_{ds} = 10 V was measured versus the applied back-gate voltage sweeping bi-directionally from 0 to 200 V for devices on SiO_2/Si, and from 0 to 35 V for devices on the Al_2O_3/ITO/PET substrate. The threshold voltage is defined as the applied back-gate voltage V_{bg} where the drain current I_d equals 10^{-10} A, *i.e.* the intersection between the transfer curve and the horizontal dashed line in Figure 3-7. The current on/off ratio is defined as the ratio of the maximum and the minimum current in the measured gate voltage range. The bending tests were performed sequentially by bending the samples along the longitudinal direction of the MoS_2 channels using substrates with defined radii (R= 7, 2.5 and 0.9 cm). The schematic description of the bending of MoS_2 devices is shown in Figure 3-2. After bending, the devices were measured in the flat state in a high

vacuum (~10^{-5} Torr) chamber to avoid environmental contamination. To test the device performance under strain, the sample was taped on curved (cylindrical) surfaces with different well-defined radii. Each curvature corresponds to a different strain value. The transfer curves of both unstrained and strained devices were recorded.

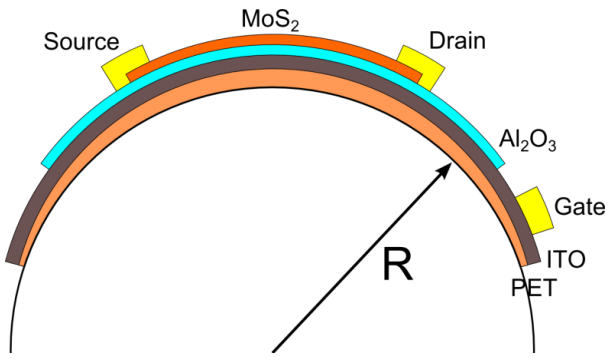

Figure 3-2 The schematic description of the bending of MoS_2 devices.

3.2.3 Optical band gap measurement

A halogen lamp was used as the broad band light source. The light was focused on the MoS_2 sample using a 50X objective lens, resulting in a spot size of 5-6 μm. Reflected light from the sample was collected using another 50X lens in a backscattering configuration and was sent to a single-pass spectrometer. Two polarizers were inserted before and after the sample to maximize the intensity at the spectrometer. In order to cancel out the effects of the optical elements and the substrate on the reflection spectra, a reference spectrum (on the substrate away from the MoS_2 film) was measured and then subtracted from the MoS_2 spectra. The signal was detected with a typical integration time of 3 seconds.

3.3 Gate-tunable flexible MoS_2 piezoresistive strain sensors

Figure 3-3 shows the optical images of the as-fabricated MoS_2 devices before transfer (a, b), the floating device released from the growth substrate (c), and transferred MoS_2 devices on a flexible substrate (d, e).

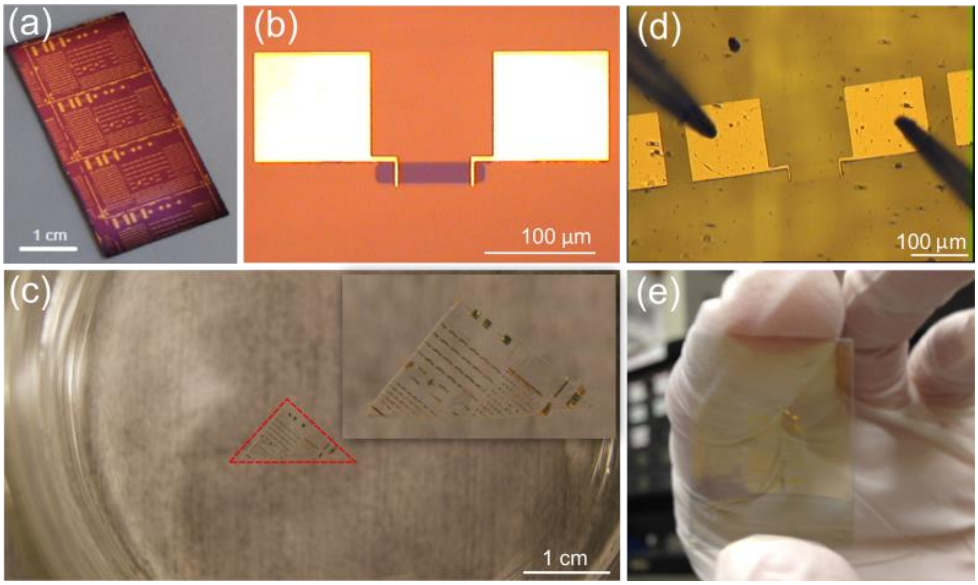

Figure 3-3 Optical images of as-fabricated and flexible MoS_2 devices. (a) A top view optical image of MoS_2 FETs after fabrication on a SiO_2/Si wafer. (b) A typical transistor with 100 µm MoS_2 channel length from the die in (a). (c) The released MoS_2 FETs held with the PMMA layer floating on water (the inset shows higher magnification of the same floating sample). (d) A flexible transistor on the Al_2O_3/ITO/PET substrate with probes touching the source and drain contacts during electrical measurements. (e) Flexible MoS_2 FETs on a transparent and flexible PET substrate covered with an ITO back-gate electrode and an 80 nm Al_2O_3 dielectric layer.

To investigate the feasibility and reliability of the direct device transfer process, we transferred the as-fabricated devices onto a new Si/SiO_2 substrate. The electrical

properties of 7 randomly chosen MoS_2 devices before and after transfer are compared in Figure 3-4. In Figure 3-4a and b, the measured drain current I_d from a representative device before and after transfer is plotted versus the applied back-gate voltage V_{bg} at a fixed source-drain voltage V_{ds} = 10V (transfer curve) on a linear and semi-logarithmic scale, respectively. After transfer, the drain current is increased by nearly two orders of magnitude at a fixed V_{bg} and the threshold voltage (V_{th}) is lowered by as much as 100 V (Figure 3-4b). It is surprising that such significant improvement is observed after transferring the MoS_2 transistors to a new and clean SiO_2/Si substrate. This improvement can be attributed to the removal of combination of intrinsic tensile strain during the MoS_2 growth process and interfacial contamination in as-grown substrate as suggested by Amani et al.[313] The threshold voltage V_{th} is extracted as the V_{bg} value at $I_d = 10^{-10}$ A, i.e. the intersection between the transfer curve and the dashed line in Figure 3-4b. Figure 3-4c summarizes the threshold voltages V_{th} (left axis) and the on/off ratios I_{max}/I_{min} (right axis), extracted from 7 different devices. The current on/off ratio larger than 10^4 is observed for all measured transistors with small device-to-device variation of the V_{th}, indicating a good reproducibility of the device transfer technique.

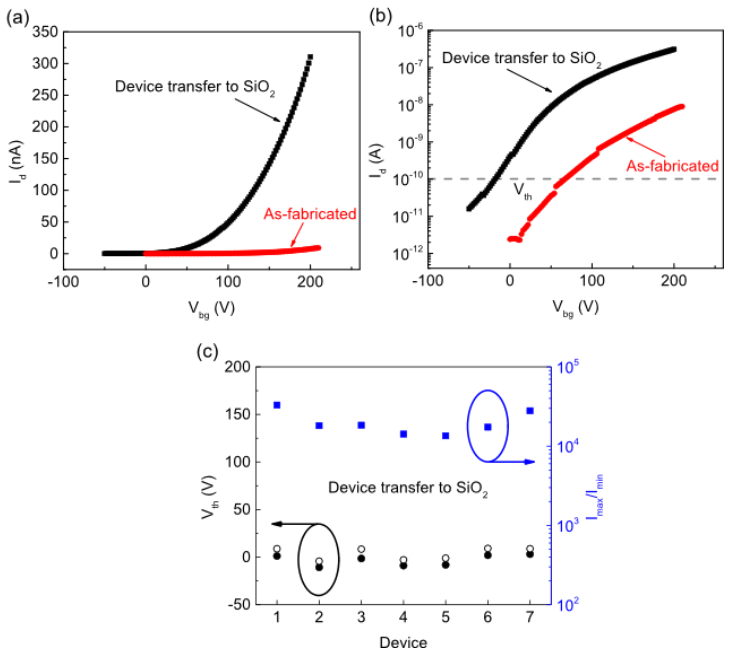

Figure 3-4 Drain current (I_d) as a function of applied back-gate voltage (V_{bg}) of a MoS_2 FET before and after transfer to a new SiO_2/Si substrate on (a) linear and (b) semi-logarithmic scale at a constant drain-source voltage of V_{ds} = 10 V. (c) Threshold voltage ($V_{th,}$ left axis) extracted from forward (closed circles) and backward sweeping (open circles), and I_{max}/I_{min} ratio of 7 measured FET devices (right axis, squares).

Next, we transfer a different die of as-fabricated devices onto a flexible poly(ethylene terephthalate) (PET) substrate. To measure the transferred devices in a back-gated geometry, we used a PET substrate coated with a conductive indium tin oxide (ITO) layer that is used as a back-gate contact. Prior to device transfer, an 80 nm Al_2O_3 back gate dielectric is deposited using atomic layer deposition (ALD). Like the device transfer performed on SiO_2/Si substrate, the sample was released from the original SiO_2/Si substrate and the floating sample was fished out onto the flexible Al_2O_3/ITO/PET substrate. Again, total 7 randomly chosen transistors were measured before and after

transfer onto the flexible substrate. Figure 3-5a shows the drain current I_d as a function of the applied back-gate voltage V_{bg} (transfer curve) of a representative transferred device on a flexible PET substrate at fixed V_{ds} = 10V on a linear (right axis) and a semi-logarithmic scale (left axis). Figure 3-5b summarizes the threshold voltages V_{th} (left axis) and the on/off ratios I_{max}/I_{min} (right axis), extracted from 7 different devices. Again, all devices exhibit very similar threshold voltages, low hysteresis, and an average on/off ratio of ~104. However, a larger fluctuation of on/off ratio in flexible devices than that of devices on rigid substrate was observed. Figure 3-5c shows the values of Imax and Imin for all seven devices. The Imax is governed by the channel current and the Imin is dominated by the leakage current through gate dielectrics. For flexible MoS2 devices, the Imax is stable across all devices while fluctuation is observed in Imin, which means the fluctuation of on/off ratio mainly results from the instability of gate dielectrics. This observation implies the quality of Al2O3 on ITO/PET substrate is not good enough possibly due to the roughness of PET substrate or the quality of ALD Al2O3 and, therefore, additionally efforts should be taken to further optimize the quality of gate dielectrics for flexible electronics.

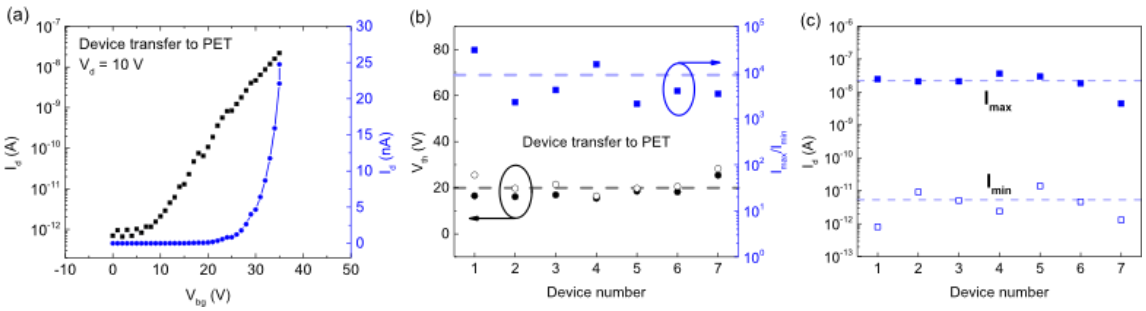

Figure 3-5 Transistor behavior of MoS_2 FETs transferred to flexible PET/ITO/Al_2O_3 (80 nm) substrate. (a) Drain current (I_d) flowing through the MoS_2 channel as a function of the applied back-gate voltage (V_{bg}) on a linear (right vertical axis) and semi-logarithmic scale (left vertical axis) at a constant drain-source voltage of V_{ds} = 10 V. (b) Drain current (I_d) as a function of drain voltage (V_d) at different applied back-gate voltage ranging between 0 V and 26.25 V. (c) Threshold voltage (V_{th}) extracted from forward (solid circles) and backward sweeping (open circles), and I_{max}/I_{min} ratio of 7 measured FET devices (squares). Dashed lines represent the average V_{th} and I_{max}/I_{min} values of 7 devices.

Output curves I_d vs V_{ds} of a representative transferred device onto a new SiO_2/Si substrate and a flexible PET substrate are plotted in Figure 5a and 5b, respectively. Both families of I_d vs V_{ds} curves in Figure 5a and Figure 5b show corresponding output behaviors that I_d increases, i.e. channel conductance increases, when V_{bg} increases. However, only linear region presents in transferred devices on SiO_2/Si while both linear and saturation regions are observed in devices on PET. It is because that the saturation region of I_d can be only achieved under two conditions: V_{bg} is larger than V_{th} and applied V_{ds} is larger than V_{ds}(saturation). The relationship between V_{ds}(saturation) and V_{bg} is described as: V_{ds}(saturation) = V_{bg} - V_{th}.

In the case of transferred device on SiO_2/Si, the I_d cannot reach the saturation region until V_{ds} reaches around 200V at V_{bg} =210V, which is beyond the V_{ds} =10V applied here. On the other hand, the I_d can reach the saturation region when V_{ds} reaches as

low as ~6V at V_{bg} =26.25V. The insufficient V_{ds} applied here explains why the saturation of I_d is not observed in transferred devices on SiO_2/Si but in transferred devices on PET.

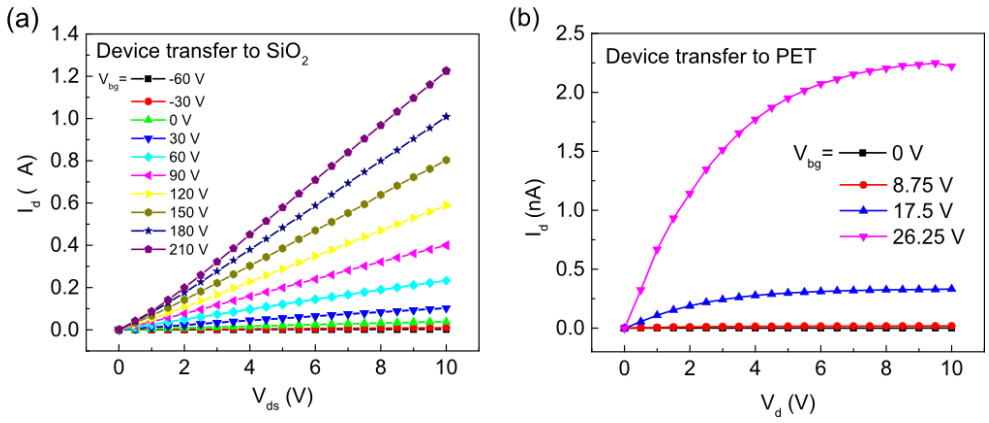

Figure 3-6 The I_d-V_{ds} characteristics of MoS_2 FETs transferred to a (a) new SiO_2/Si substrate and (b) flexible Al_2O_3/ITO/PET substrate. The response of channel conductance increase is observed for both types of devices.

Figure 3-7a shows the transfer curve of a representative MoS_2 FET in which drain current (I_d) versus back-gate voltage (V_{bg}) is measured and shown on both linear (dashed line) and a semi-logarithmic scale (solid line). The as-fabricated MoS_2 transistors on the SiO_2/Si substrate reveal a large on-off current ratio (I_{max}/I_{min}) of ~10^4.

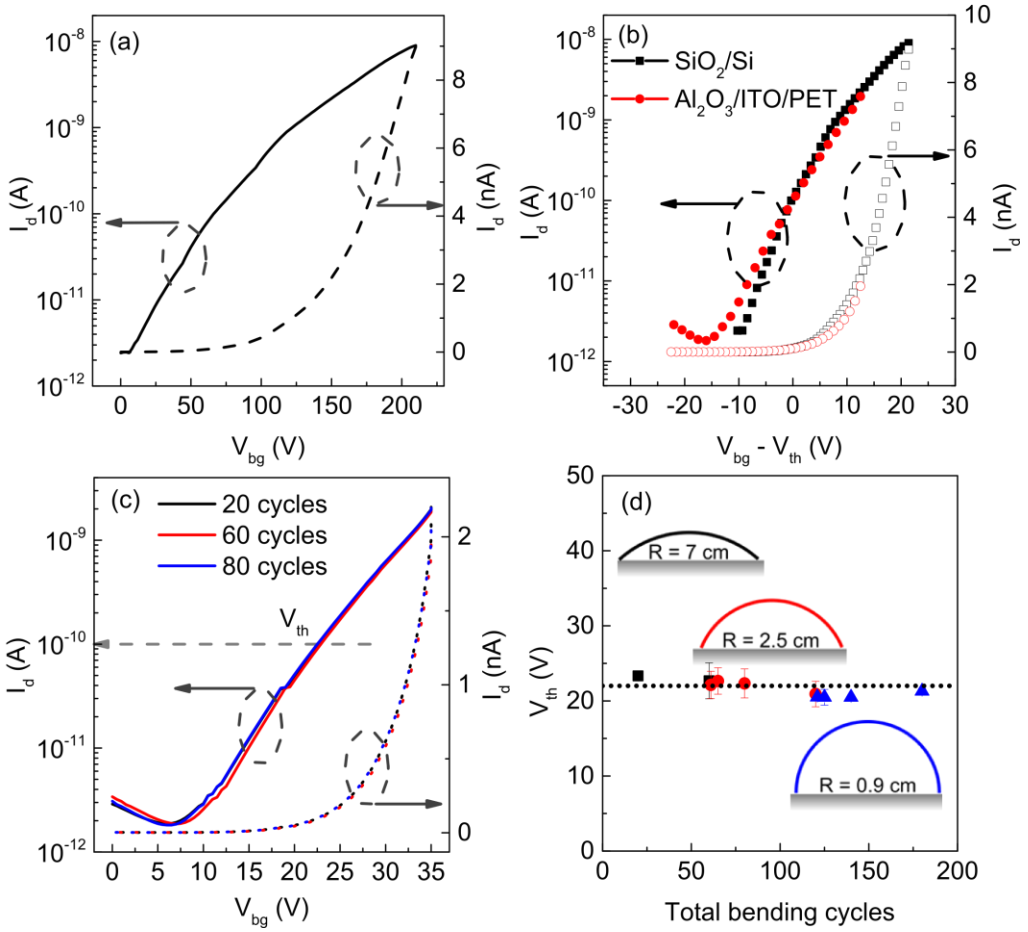

Figure 3-7 (a) Drain current (I_d) as a function of applied back-gate voltage (V_{bg}) of an as-fabricated MoS_2 FET (W/L = 13μm/100μm) on a Si substrate with 265 nm thick SiO_2 gate dielectric, plotted on semi-logarithmic scale (solid) and linear scale (dashed) at a constant drain-source voltage of V_{ds} = 10 V. All results shown are from the backward voltage sweeps (from high to low V_{bg}). (b) The I_d-V_{bg} curves of an as-fabricated device on a SiO_2/Si wafer (squares), and a transferred device on an Al_2O_3/ITO/PET substrate (circles) on semi-logarithmic scale (solid symbols) and linear scale (open symbols). Since the capacitances of both dielectrics are not the same (265 nm SiO_2 vs. 80 nm Al_2O_3), the samples require different gate voltage to achieve the same drain current. Therefore, the horizontal axis is normalized by their capacitance ratio: $C_{Al2O3,\ 80\ nm}/C_{SiO2,\ 265\ nm}$ ~6.6 for a better comparison. (c) A representative flexible MoS_2 FET on the Al_2O_3/ITO/PET substrate measured after 20, 60 and 80 bending cycles in vacuum (~10^{-5} Torr). All curves align well on top of each other. (d) The threshold voltage (V_{th}) evolution of flexible MoS_2 FETs as a function of total bending cycles. The error bars represent the results obtained with different devices. The observed device-to-device variations are small. No significant change of V_{th} is seen even after 180 bending cycles. The samples were bent around surfaces with different curvature (bending radii r = 7 (square), 2.5 (circle) and 0.9 cm (triangle), which correspond to strain ε = ~0.07, ~0.2 and ~0.54%, respectively). All

devices were measured sequentially in the flat state after a given number of bending cycles.

Figure 3-7b compares the electrical performance of the as-fabricated and flexible devices after transfer. Note that the applied back gate voltages for the flexible devices are lower than those for the as-fabricated devices because the capacitance of the new gate dielectric is approximately 6.6 times larger (here we use 80 nm thick Al_2O_3 with a relative permittivity $\varepsilon_r \approx 7.8$ instead of 265 nm thick SiO_2, $\varepsilon_r = 3.9$) using the relationship as follows:

$$C_{Al2O3} \Big/ C_{SiO2} = \frac{\varepsilon_{Al2O3}}{d_{Al2O3}} \Big/ \frac{\varepsilon_{SiO2}}{d_{SiO2}} \tag{28}$$

In order to make a fair comparison between FETs on the SiO_2/Si substrate and the Al_2O_3/ITO/PET substrate (without any strain applied), the horizontal axis in Figure 3b was normalized by V_{th}, thickness and the relative permittivity of the dielectric layer. Both curves show similar behavior and overlap after this normalization with minor deviations that can be attributed to differences in interface quality and surface roughness of the SiO_2/Si and the Al_2O_3/ITO/PET substrates. The results suggest that the transfer process does not significantly alter the device performance, and therefore, provides a reliable method to fabricate flexible devices.

A series of bending tests was then performed on the flexible MoS_2 transistors to investigate the influence of the number of bending cycles and the bending radius on the stability of device performance. Uniaxial strain (ε) along the longitudinal direction of the MoS_2 channel was applied by placing the sample on a rigid cylindrical surface with a well-defined curvature and the strain was estimated using the following equation[203]: ε =

(t/r)/2, where t is the substrate thickness (100 μm for the PET substrates used here) and r is the bending radius, which is the radius of the curved surface (a cylinder). After a specific number of bending cycles, the devices were then measured again in the flat state without strain. The I_d-V_{bg} characteristic of a representative device is plotted in Figure 3c on a linear (dashed lines) and semi-logarithmic scale (solid lines) as a function of the number of bending cycles (20, 60 and 80 cycles). The effect of bending on the device performance is observed to be negligible. To evaluate the influence of bending in more detail, we define the threshold voltage, V_{th}, as the applied V_{bg} value needed to achieve a drain current of $I_d = 10^{-10}$ A, *i.e.* the intersection between the transfer curve and the horizontal dashed line in Figure 3c. The evolution of V_{th} versus the total number of bending cycles is shown in Figure 3d, for at least 5 devices (error bars) and various bending radii (r = 7, 2.5 and 0.9 cm, which correspond to applied strain ε = ~0.07, ~0.2 and ~0.54%, respectively). Again, the observed variation in V_{th} is small, suggesting good mechanical stability and good device-to-device reproducibility even after more than 180 bending cycles, measured over several days.

Next, the device performance under different strain conditions is compared in Figure 3-8. Figure 3-8a shows a representative transfer curve of a flexible MoS_2 transistor measured first without strain in the flat state (solid line), and afterwards in a stretched state (dashed line), with an applied uniaxial strain of $\varepsilon \approx 0.07\%$ along the transistor channel direction. Under strain, a shift of the entire transistor curve towards lower back-gate voltages and an electron current increase is observed, as indicated by the arrow. In addition, the output curves of the same device at different back gate voltages V_{bg} are plotted on a semi-log scale (Figure 3-8b). It is clear from Figure 3-8 a-b that the MoS_2

transistor is highly strain sensitive. The resistivity change as well as the current change of a semiconducting material in response to applied strain is known as the piezoresistive effect. To our knowledge, this is the first observation of the piezoresistive effect in field-effect transistors based on large-area MoS_2.

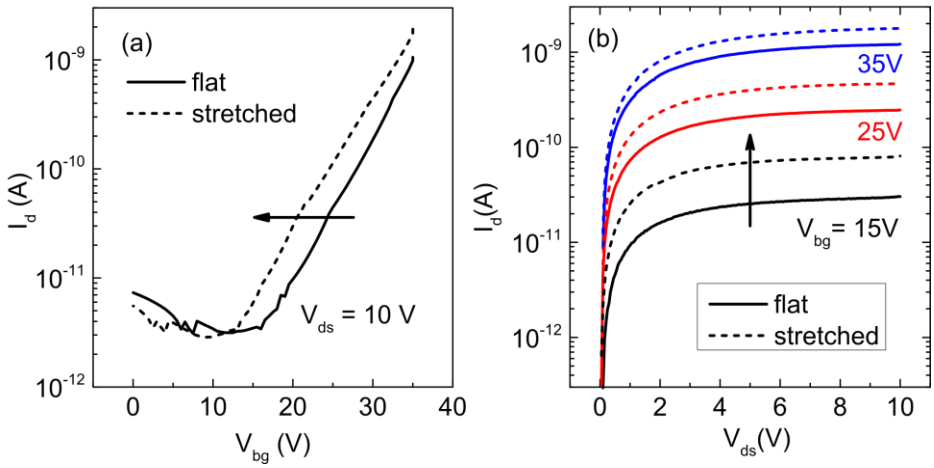

Figure 3-8 (a) A representative transfer curve (I_d-V_{bg}) of a flexible MoS_2 transistor measured in the flat state (solid line) and the stretched state (dashed line; applied strain ε = 0.07%). A shift of the transfer curve is observed under strain. Several devices were measured with all showing similar behavior. (b) Output characteristic (I_d-V_{ds}) of the same device at different back gate voltages V_{bg} on a semi-log scale. (W/L = 13µm/100µm)

Although other effects such as strain-induced capacitance change of the gate dielectric may also cause a shift of the I_d-V_{bg} curve, this capacitance-related shift is approximately 3 orders of magnitude smaller than the changes observed here,[318] and is therefore neglected in the following. To confirm that the observed effect results from a band gap change, reflection spectroscopy was performed as discussed below.

Strain-induced band gap changes have been previously investigated in monolayer and bilayer MoS_2 using optical spectroscopy and simulations.[189, 197, 202-203, 207-208] However, the effect of strain on trilayer material remains unexplored. Figure 3-9a shows optical reflection spectra of trilayer MoS_2 for different applied strain values. The band gap (E_g) is estimated from the wavelength (λ) of the valley position in the reflection spectrum through $E_g = 1240/\lambda$, where E_g has the units of eV and λ is the wavelength in nm. A clear red-shift of the reflection minimum upon increasing strain is observed, indicating the decrease of E_g. Figure 3-9b shows that the extracted band gap decreases linearly with increasing strain with a slope of ~ -0.3 eV per percent strain applied, which is similar to that reported in literature.[189, 197, 202-203, 207-208] However, the band gap change also depends on the number of MoS_2 layers, due to thickness-dependent differences in band structure. For monolayer MoS_2, the theoretically calculated band gap change lies between -0.05 and -0.085 eV per percent strain,[197, 208] while experimental results show a similar trend with the value around -0.05 eV per percent strain.[203, 208] The band gap change due to strain becomes more prominent in bilayer samples with theoretical values ranging from -0.1 to -0.2 eV per percent strain[197, 208] and experimental values around -0.12 eV.[189, 203, 208] The predicted theoretical value for bulk MoS_2 reaches -0.3 eV per percent strain,[202] which is very similar to the band gap change observed in the present study using trilayer MoS_2.

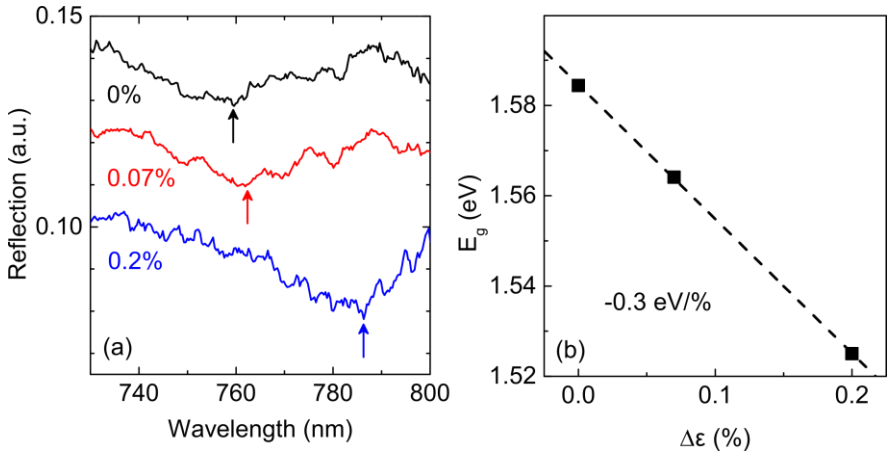

Figure 3-9 (a) Optical reflection spectra of trilayer MoS_2 under different applied strain. The position of the reflection minimum shifts to higher wavelength with increasing strain, as indicated by the arrows. The spectra are shown vertically offset for clarity. (b) Band gap E_g vs. applied strain $\Delta\varepsilon$, estimated from the minimum position in (a). The band gap linearly decreases with increasing strain. The slope is -0.3eV/% strain, in agreement with previous reports on exfoliated MoS_2.

In addition to the strain-induced band gap change, the applied strain can affect the position of the Fermi level (φ_n) relative to the conduction band edge.[203] In a field-effect transistor, the Fermi level can also be moved with respect to the band edges of the semiconductor by chemical doping[296] or electrostatically by applying a gate bias. In order to estimate the Fermi level change, the strain-induced current change ΔI is converted to electron concentration change, *i.e.* Δn, using:

$$\Delta I = \mu q \Delta n \left(\frac{W}{L}\right) V_{ds} \tag{29}$$

where μ is the field-effect mobility, q is the elementary charge, W is the channel width, L is the channel length and V_{ds} is the drain-source voltage. According to previous studies, the field-effect mobility of MoS_2 has a negligible dependence on the applied strain over a

wide range (down to a bending radius = 2.2 mm).[315, 319] Here, moderate strain values (≥ 9 mm) are applied and, therefore, a constant mobility at a given V_{bg} can be assumed independent of the applied strain. The change in the electron concentration (Δn) is then estimated from ΔI and related to the Fermi level changes ($\Delta\varphi_n$) using the following expression:[320]

$$\Delta n = \left(\frac{g_c m_c^*}{\pi \hbar^2} \right) \ln\left[\exp\left(\frac{-q\Delta\varphi_n}{kT} \right) + 1 \right] \tag{30}$$

where g_c = 2 is the degeneracy factor,[321] m_c^* = 3.44x10^{-31} kg is the effective electron mass,[202] $\hbar$ is the reduced Planck's constant, k is the Boltzmann constant and T is the temperature (300 K). The estimated Fermi level change ($\Delta\varphi_n$) vs. strain ($\Delta\varepsilon$) at different applied V_{bg} is plotted in Figure 3-10a. Similar to the optical reflection measurements, a linear relationship is observed between the Fermi level change relative to the conduction band edge and the applied strain. However, the slope of the linear fit depends on the gate voltage. At V_{bg} = 35 V, $\Delta\varphi_n$ decreases by ~ -0.19 eV per percent strain applied, while at V_{bg} = 15.5 V, the slope becomes ~ -0.24 eV/% strain. A negative slope means that the Fermi level moves closer to the conduction band edge. To study this effect in more detail, Figure 3-10b shows the back gate voltage dependence of the Fermi level change ($\Delta\varphi_n$) estimated from the electrical measurements of a device under $\varepsilon \approx 0.07\%$. The right vertical axis shows $\Delta\varphi_n$ per percent strain applied. A non-monotonic dependence of $\Delta\varphi_n$ on V_{bg} is observed with a maximum in the subthreshold region. Because of the exponential change of I_d with V_{bg} in the subthreshold region, the relative current change (ΔI) between the stretched and the flat transistors is large and so is the change in carrier concentration. As a result, with increasing V_{bg}, the movement of the Fermi level toward

the conduction band edge in this region is abrupt and a local maximum of $\Delta\varphi_n$ is formed near V_{th}. However, above V_{th}, the Fermi level change with gate bias is weaker causing less sensitivity to applied strain.

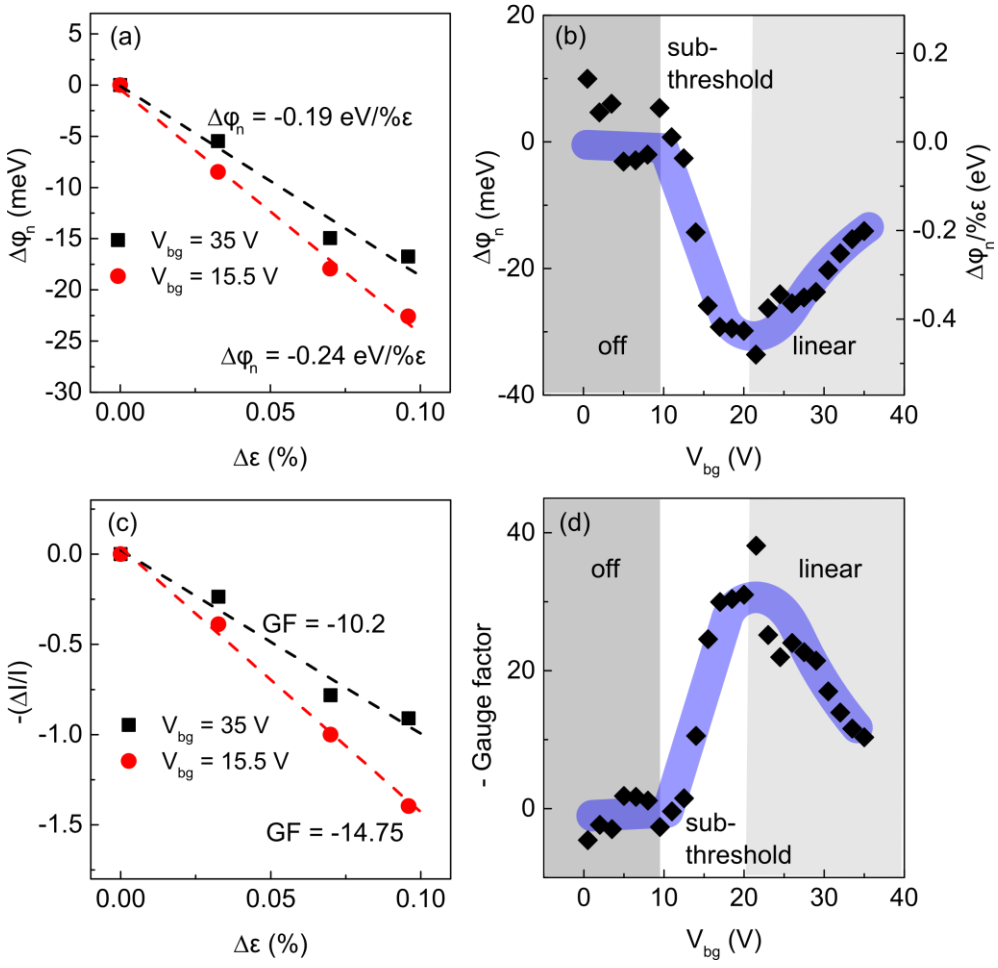

Figure 3-10 The change of the Fermi level relative to the conduction band edge ($\Delta\varphi_n$) and the gauge factor (GF) were estimated from electrical measurements. (a) The plots of strain dependence of $\Delta\varphi_n$ at different back gate voltages. The right vertical axis is scaled to $\Delta\varphi_n$ per percent strain applied. (b) The relationship between $\Delta\varphi_n$ and V_{bg} of a representative device. (c) The plots of the strain dependence of $-(\Delta I)/I$ at different back gate voltages. The slope of the linear fit in (c) is the gauge factor (GF) by definition. (d) The relationship between GF and V_{bg} of the same device as shown in (b). Similar back gate dependence is observed for both (b) and (d), while both (a) and (c) show a linear relationship with increasing strain. Solid bands in (b) and (d) are guides to the eye.

To compare the sensitivity of the presented MoS_2 strain sensors with conventional silicon-based devices, a commonly used figure of merit of a piezoresistive strain sensor, the so-called gauge factor (GF), can be estimated.[322] The GF is defined as the normalized resistance change per unit strain: $GF=(\Delta R)/R\varepsilon$, where ΔR is the change in resistance compared to the unstrained device, R is the resistance of the unstrained device, and ε is the applied strain. Because the FET is operated in the ON state, the GF can also be defined as: $GF=-(\Delta I)/I\varepsilon$, where ΔI is the current change due to strain and I is the current of the unstrained device. The GF is negative for n-type materials (like the MoS_2 used here), because the resistance decreases with increasing strain, leading to $\Delta R<0$ ($\Delta I>0$).[323] Figure 3-10c shows the $-(\Delta I)/I$ vs. $\Delta\varepsilon$ relationship (GF) at selected V_{bg} values. The GF vs. V_{bg} relationship is plotted in Figure 6d. Consistent with the back gate dependence of $\Delta\varphi_n$, this definition leads to a gate-dependent gauge factor in transistor-based devices, with the highest values in the subthreshold regime,[324-325] where an exponential dependence of I_d on V_{bg} occurs, and the changes ΔI and Δn are large. A similar non-monotonic behavior has also been reported in carbon nanotube-based devices.[326] Since the GF is derived from I_d, the aforementioned mechanism that relates to the gate voltage dependence of $\Delta\varphi_n$ is also applicable to GF. Indeed, if we estimate the magnitude of the gauge factor (Figure 3-10d), it has the same pronounced gate dependence. The GF is close to zero if the transistor is switched off ($V_{bg}<10$ V) and reaches a maximum of approximately -40 in the subthreshold regime (around $V_{bg}=20$ V), before decreasing again in the transition region to the linear regime ($V_{bg}>20$V). This observed non-monotonic shape can be explained by the combined effect of the band gap change under strain and the Fermi level evolution with changing V_{bg}. This magnitude of GF compares well with

polycrystalline n-type silicon (-30),[323] while it is lower than that of single crystal silicon (-125).[323] Note that the MoS_2 material used here is polycrystalline; larger GF may occur in single-crystal MoS_2. Further work is needed to investigate the influence of MoS_2 crystallinity and crystallographic orientation on the gauge factor as well as the electrical response of the device.

Wu *et al.* previously observed piezoelectricity in two-terminal un-gated MoS_2 devices with an odd number of MoS_2 layers.[211] However, piezoelectricity can only occur when large Schottky barriers are formed between the source-drain metal contacts and the MoS_2 due to an asymmetric modulation of the two Schottky barriers by strain-induced charges. In our experiments, three-terminal field-effect transistors are used, and the Schottky barriers are lowered significantly by the applied gate bias, because the MoS_2 under the contacts is also modulated by the gate biasing.[79, 317, 327] Therefore, the piezoresistive band gap change dominates the piezoelectric effects.

3.4 Conclusion

In conclusion, we have demonstrated piezoresistive strain sensors based on flexible MoS_2 field-effect transistors made from a highly uniform large-area trilayer film. The flexible MoS_2 transistors were fabricated using a direct device transfer technique. These flexible transistors show stable performances after bending and remain operational after more than 200 bending cycles. The origin of the piezoresistive effect in MoS_2 is explained to be a strain-induced band gap change, as confirmed by optical spectroscopy. The results are in good agreement with recently reported simulations and spectroscopic

studies on strained exfoliated MoS_2. In addition, the strain sensitivity can be tuned by over one order of magnitude by modulating the MoS_2 Fermi level with an applied gate bias. The gate-tunable gauge factors can be as high as -40, comparable to polycrystalline silicon, but for a much thinner active layer (~2 nm).[323] For practical sensing applications, the gate-tunable piezoresistivity is a useful property of transistor-based devices, because the relative sensitivity to strain can be adjusted by changing the gate bias.[325]

CHAPTER 4. FET-BASED POTENTIOMETRIC SENSORS FOR THE DETECTION OF BIOCHEMICAL SPECIES

This chapter describes the chemical and biological sensing using FET-based potentiometric sensors. Section 4.1 provides a brief background about the biochemical sensor technologies and current challenges. Section 4.2 focuses on the fabrication of graphene ISFET, Au extended-gate sensing chip and the functionalization of the sensing surface. Section 4.3 starts with the demonstration of biochemical sensing using traditional ISFET and move on to a simplified design using EGFET. Highly comparable sensing performance suggests that the EGFET is advantageous for practical potentiometric biochemical sensing applications. This work was performed in close collaboration with Dr. Alexey Tarasov. Section 4.4 presents the application of EGFET-based biosensors for animal disease diagnosis and compares different sensing techniques, including potentiometric sensors, surface plasmon resonance (SPR) biosensors and commercial enzyme-linked immunosorbent assay (ELISA). The work described in Section 4.4 was performed in close collaboration with Dr. Alexey Tarasov, Dr. Darren Gray, Niall Shields, Dr. Mark Mooney (Queen's University Belfast (QUB), Northern Ireland, UK), Dr. Armelle Montrose, Niamh Creedon, Dr. Pierre Lovera and Dr. Alan O'Riordan (Tyndall National Insitute, Ireland) with the support from NSF US-Ireland "AgriSense project". My involvement mainly focused on the biosensing using EGFET-based potentiometric biosensors.

4.1 Introduction

4.1.1 Nanoelectronic ISFET and Simplified EGFET

The detection of chemical and biological species is critical for applications in healthcare, environmental monitoring, food safety and drug screening. Among the currently available devices, ion-sensitive field-effect transistors (ISFETs)[328] are promising as rapid, highly sensitive, and label-free diagnostic tools[329-330] that can be fabricated using mainstream CMOS technology.[331] Although different nanoscale materials have been used in ISFETs, all these FET-based devices rely on the same sensing principle: the adsorption of charged species on the sensor surface changes the surface potential of the material and, hence, the channel current inside the FET. They also share the same device geometry, i.e. the active sensing surface is also the gate of the FET, which converts the surface potential changes into channel current changes. However, this geometry can cause reliability issues since the readout transducer is exposed to the electrolyte solution during the experiment.[332] Additional encapsulation steps are required to ensure stable FET performance in the liquid environment, increasing the device complexity.[333] A possible solution to this stability problem is to separate the sensing surface from the readout transducer, forming a so called extended gate sensor.[334] This approach can result in a simple disposable sensing chip, consisting, for example, of a thin gold film evaporated on an insulating substrate, and a reusable readout transducer, for instance a commercial MOSFET. During the sensing experiment, only the gold surface of the sensor chip is exposed to the electrolyte, while the readout transistor is not in contact with the solution. At the same time, the gate terminal of the transistor is electrically connected to the gold-coated sensor surface to read out the potential changes on this

"extended" gate. Even though there has been a lot of research on extended gate biochemical sensors,[335-342] a direct experimental comparison of sensing capabilities of these structures with nanoelectronic ISFETs has not been performed yet. However, numerical simulations suggest that extended gate sensors should have the same charge sensitivity as ISFETs.[343]

4.1.2 On-site detection of animal diseases

The global population is predicted to increase to 9.3 billion by 2050 and food production will need to double to meet demand. With most suitable land already in use, this increase will need to come from greater efficiency facilitated by improved technology. At least 20% of animal-based food production is lost by infectious diseases and there is an overriding need to prevent and control animal disease. Due to advantages of high throughput and relatively low cost relative to other techniques such as PCR or IHC, serological testing by ELISA is routinely employed for disease surveillance purposes, but is performed in dedicated laboratories leading to long sample turnaround times and delays in result reporting. The development of low-cost point-of-care (POC) diagnostic devices would provide significant benefits in reducing the impacts of animal disease by enabling rapid identification, isolation and treatment of infected animals. Bovine Respiratory Disease (BRD) is currently the leading cause of economic loss ($2 billion annually in the US [344]) to the cattle and dairy industry through concomitant clinical disease, therapeutic treatment, reduced animal performance and mortality [345-346]. The BRD complex is therefore an exciting and realistic prospect for the application of POC sensor devices capable of multiplexing detection and facilitating on-site assessment of animal disease prevalence.

To date no commercial POC devices currently exist for the serological assessment of pathogen related responses that can yield rapid quantifiable results with performance comparable to ELISA. Amongst available sensor technologies, potentiometric biosensors based on EGFET are most promising due to their high sensitivity, rapid electronic readout, and compatibility with mainstream CMOS technology. Potentiometric sensors have not been thoroughly explored as possible diagnostic tools for monitoring immunological responses to infections. Moreover, none of these studies attempted systematic comparison to established assay technologies such as SPR or ELISA to evaluate FET performance against current 'gold-standards' and assess true potential for real-world application.

Bovine Herpes Virus 1 (BHV-1) is a BRD viral pathogen [347] that induces respiratory tract damage and suppression of innate and adaptive immune responses leading to opportunistic bacterial [348] and mycoplasma [349] infections. BHV-1 virus is prevalent worldwide, however a number of countries have gained BHV-1 free status through the application of "test and cull" disease eradication programs [350] in combination with the use of efficacious marker vaccines based on a glycoprotein E (gE) negative BHV-1 strain.[351] Differentiation of infected from vaccinated animals (DIVA) is achieved through the detection (using commercial companion anti-gE blocking ELISAs) of BHV-1 gE antibodies which are only present in animals exposed to wild-type virus.[352] Currently, disease surveillance schemes rely on centralized testing laboratories for the serological screening of bovine samples, with a minimum sample turnaround time of 72 h (including 19 h for gE blocking ELISA performance). BHV-1 exposed animals can also become latent carriers, with virus reactivation and shedding occurring during periods of stress e.g.

animal mixing and transportation.[353] Therefore, rapid on-site identification of animals undergoing BHV-1 reactivation using quantitative POC devices (with DIVA capacity) would significantly reduce the risks of disease spread to BHV-1-free herds. The use of unpurified recombinant gE as a capture antigen in indirect ELISAs for serological diagnosis of BHV-1 has been shown to increase assay sensitivity enabling use of higher test sample dilutions.[354] Furthermore, purified recombinant viral capture antigen can improve test sensitivity by increasing the proportion of relevant antigenic material immobilized on test surfaces.[355] The development of a POC FET-based test for BHV-1 diagnosis using purified recombinant gE antigen would therefore allow for increased sample dilution overcoming Debye length limitations whilst maintaining assay sensitivity and facilitating rapid test result reporting.

4.2 Fabrication of potentiometric biochemical sensors

4.2.1 Fabrication of graphene ISFET and electrical measurement

A highly doped silicon wafer with 260 nm oxide was used as a substrate for device fabrication, and as a back gate. First, source and drain contacts were deposited using UV lithography in a lift-off process (10 nm Cr, 40 nm Au). Graphene was grown by CVD on copper foil and then transferred onto the wafer with prefabricated source and drain contacts using the PMMA method described elsewhere.[356] After that, the graphene sheet was patterned using UV lithography and O_2 plasma etching to define the transistor channels. These back-gated transistors were routinely characterized in air to test their performance. Then, the source and drain contacts were sealed with a photoresist for the

operation in liquid environment. The bare graphene surface was exposed to electrolyte solutions with different pH to measure its pH response. Subsequently, a thin Ti film (~1 nm) was evaporated on the sample. After oxidizing in air, the resulting TiO_x film was used as a seeding layer for alumina growth by atomic layer deposition (30 nm, 100°C). The devices were measured again in pH buffer solutions after this step. As a last fabrication step, a thin (30 nm) gold film was evaporated on the alumina-coated graphene FETs. These devices were used for pH and biosensing experiments. A home-made polydimethylsiloxane (PDMS) liquid cell with Teflon inlet and outlet tubing was pressed on the samples to deliver the different solutions. An Ag/AgCl flow-through micro-reference electrode (Microelectrodes, Inc.) was placed in the tubing next to the cell and used to control the liquid potential. All electrical measurements were performed with a Keithley 4200-SCS parameter analyzer and a Cascade Microtech Summit 12000 probe station.

4.2.2 Fabrication of EGFET and electrical measurement

A silicon wafer with 260 nm oxide was used as a substrate for the sensing chip. Note that any other insulating substrate can be used, in principle, including plastic or paper. A thin gold film (100 nm) was deposited by e-beam evaporation through a shadow mask to form 4 individual gold strips. A home-made PDMS microfluidics cell was pressed on the chip for the functionalization and for the measurements. The area of the strips in contact with the liquid was 2 mm×3 mm, defined by the liquid cell dimensions. Two of 4 strips were coated with gE, and the remaining 2 were coated with Hp, closely following the immobilization protocol developed on Biacore. Each individual gold strip was electrically connected to the gate terminal of a commercial MOSFET. Any type of

transistor can be used for the readout, including nanomaterial-based FETs. An Ag/AgCl flow-through reference electrode (Microelectrodes Inc.) was placed in the tubing close to the sensor to gate the transistor through the liquid during the measurements. The electrical measurements were performed using a semiconductor parameter analyzer (Keithley 4200-SCS and HP 4145A).

4.2.3 Functionalization of sensing surface

All chemicals were purchased from Sigma-Aldrich: 16-mercaptohexadecanoic acid (MHA) (Product Number: 448303); Ethanol (459844); *N*-Hydroxysuccinimide (NHS; 130672); *N*-(3-Dimethylaminopropyl)-*N′*-ethylcarbodiimide hydrochloride (EDC; E7750); Bovine serum albumin (BSA; A7906); Anti-bovine albumin, antibody produced in rabbit (anti-BSA; B7276); Ethanolamine hydrochloride (E6133); Phosphate buffer saline (PBS; 10 mM in deionized water, pH 7.4; P4417); Human haptoglobin (Hp; H3536) and anti-Haptoglobin IgG produced in rabbit (anti-Hp; H8636). gE protein was synthesized in Mooney group at Queen's University Belfast.

The gold surface of the sensors was cleaned by a cleaned by gentle oxygen plasma treatment (time = 1 min, power = 15 W, flow = 100 sccm). The samples were then immersed in a solution of 16-mercaptohexadecanoic acid (MHA, Sigma Aldrich, 5 mM in ethanol) and left overnight (approx. 18 hours) to create a self-assembled monolayer (SAM) with functional carboxyl (COOH) groups. The samples were rinsed with ethanol and DI water. Then, the microfluidic chip was placed on the sample equipped with 4 different channels to selectively functionalize the active and the control samples. The sample was flushed with HBS-EP buffer before each functionalization step.

A fresh NHS/EDC mixture (115 mg NHS in 10 ml DI water and 750 mg EDC in 10 ml DI water) was prepared, and injected into the microfluidic cell and left inside to activate the surface for approx. 30 min. For BSA sensing, the BSA solution (1 wt. % BSA in PBS buffer pH 7.4) was injected and left for 30 minutes to immobilize the protein on the activated surface. For gE active channels, BHV-1 gE protein solution (50 µg/ml, prepared in 10 mM sodium acetate buffer, pH 4.0) was delivered to the activated chip and left for 30 minutes for the protein immobilization. Haptoglobin (Hp) was used as control protein for gE sensing. In Hp control channels, a solution of the control protein Hp (50 µg/ml, 10 mM sodium acetate, pH 4.0) was injected and left for 30 minutes for the protein immobilization. The chip surface was deactivated by injection of ethanolamine-HCl pH 8.5 for 30 min. Measurements were performed in different dilutions of anti-BSA, anti-BHV-1 antiserum or anti-Hp (as a control), sequentially from highest (1:10000) to lowest dilution (1:10). The reaction time with anti-BSA, antiserum or anti-Hp was 20 min, the volume was approx. 300 µl for each dilution. All dilutions were prepared in 10 mM PBS buffer pH 7.4 (anti-BSA) or 10 mM HBS-EP buffer pH 7.4 (antiserum and anti-Hp). The samples were regenerated with 300µl of 10mM glycine pH 2 with 1 min contact time.

4.3 Comparison between graphene ISFET and EGFET potentiometric sensors for chemical and biological sensing[d]

NanoISFETs were fabricated using large-area high-quality graphene grown by chemical vapor deposition (CVD) as described in Section 4.2.1. The nanoISFETs with 3 different active surfaces were tested as pH sensors to validate their performance: (i) bare graphene, (ii) Al_2O_3-coated graphene and (iii) gold-coated graphene (Figure 4-1). The schematic of the final device with a thin gold film and the measurement setup is shown in Figure 4-1a. A microfluidic cell is pressed on the chip to deliver the buffer solution. A Ag/AgCl reference electrode is used to control the potential in the liquid and to gate the graphene FET. The measured transfer curves in different pH buffer solutions are plotted in Figure 4-1b. A shift of the transfer curves to more positive voltages is observed with increasing pH. The pH response strongly depends on the active surface, as seen in Figure 4-1c. If bare graphene is directly exposed to the electrolyte solution, its pH response is very small, because only few active binding sites are available at defects. The intrinsic pH response of ideal graphene is zero, as has been discussed previously.[256, 357] After these initial measurements, the devices were coated with a thin alumina layer using atomic layer deposition (ALD). To improve the growth of the high-k dielectric on graphene, a very thin (~1 nm) TiO_x seeding layer was evaporated prior to the ALD process. The devices were measured again after this step, and showed a nearly ideal Nernstian response to pH (~58 mV/pH). To our knowledge, this is the first demonstration of a

[d] Adapted with permission from Tarasov, A.; Tsai, M.-Y.; Flynn, E. M.; Joiner, C. A.; Taylor, R. C.; Vogel, E. M., Gold-coated graphene field-effect transistors for quantitative analysis of protein–antibody interactions. *2D Mater.* **2015,** *2*, 044008. Copyright 2015 IOP Publishing.

close-to-ideal pH response with alumina-coated graphene. These results are attributed to the improved dielectric growth on the seeding layer and an oxygen plasma cleaning step prior to the measurements in liquid, which activates the surface hydroxyl groups.[333] Subsequently, a thin gold film was evaporated on top of the alumina dielectric and another pH sensing experiment was carried out. The pH response is significantly reduced, because of a much lower density of pH-sensitive hydroxyl groups on the gold surface.[358] The observed pH response (~34 mV/pH) is very similar to the recent results obtained with gold-coated Si NWs.[358] This is the first time that an electrolyte-gated gold-coated graphene FET is demonstrated. Because of the well-established protocols for the self-assembly of monolayers of functional molecules, the gold surface is an ideal candidate for the specific detection of species other than protons, as will be discussed further below. Also, the moderate pH response of the gold surface can now directly be compared with other potentiometric sensors.

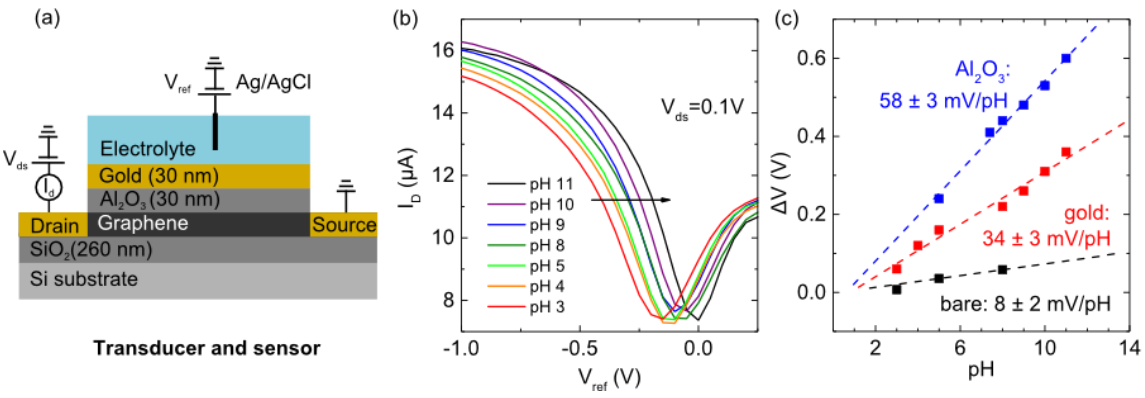

Figure 4-1 (a) A schematic of a gold-coated graphene FET, which acts as both the sensing surface and the readout transducer. (b) Transfer curves of a graphene sensor, coated with Al_2O_3 and gold, measured vs. voltage applied to the reference electrode V_{ref}

in different pH solutions. (c) Sensor response to pH for bare graphene (black squares), coated with Al_2O_3 only (blue triangles); and with Al_2O_3 plus gold (red circles). The response of the gold-coated sample is smaller than that of alumina because much less surface hydroxyl (-OH) groups are available that can interact with protons. In the case of the bare graphene, a very small amount of hydroxyl groups exists at defect sites, leading to a small pH response. The intrinsic response of ideal graphene is zero since no binding sites are available for protons.

A simple potentiometric extended gate sensor with 2 different readout schemes is used for comparison (Figure 4-2). As mentioned in the introduction, the sensing surface is physically separated from the readout part in this configuration, dramatically simplifying the device fabrication. As shown in Figure 4-2a, the sensing part consists of a thin gold film evaporated on an insulating substrate through a shadow mask to define several distinct gold strips. This process requires a single fabrication step. Using microfluidic channels, the individual gold strips can be independently functionalized to enable selective differential measurements, as will be discussed later. For now only one gold strip is used and electrically connected to the gate terminal of a commercial MOSFET. The MOSFET is simply a readout transducer, converting the potential changes at the gold surface to drain current changes. The same microfluidic cell with a reference electrode is pressed on the sensing chip. If the voltage V_{ref} is swept at the reference electrode, the MOSFET is gated and a transfer curve can be recorded (Figure 4-2b). Similar to the nanoISFET, the curves shift to the right with increasing pH (Figure 4-2c). The pH response is consistent with gold-coated graphene results (Figure 4-1c) and with gold-coated SiNWs,[358] suggesting that both the standard (nano)ISFET geometry as well as the extended gate configuration yield equivalent results, as long as the active sensing surface is the same, i.e. gold in this case. To further emphasize the potentiometric nature

of these sensors, a simple experiment was performed as illustrated in Figure 4-2d. Here, instead of a commercial transducer or a nanoISFET, a voltmeter is used to measure the potential difference between the active gold surface and ground. In Figure 4-2e, the relative potential difference ΔV is plotted vs. time in different pH buffer solutions, at a constant V_{ref}. The ΔV as a function of pH (Figure 4-2f) shows very similar response to both nanoISFETs and the extended gate FETs. Again, this further supports our conclusion that the pH response is only determined by the surface potential which depends on the properties of the surface itself and of the surrounding electrolyte but not on the type of readout used.

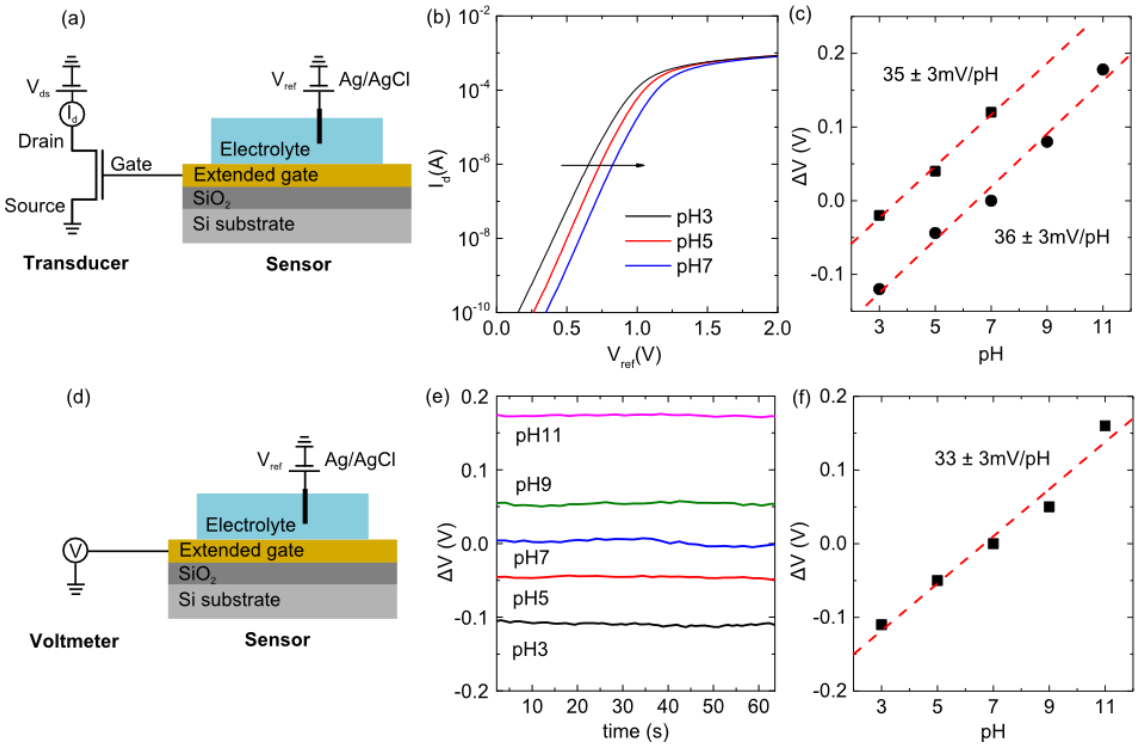

Figure 4-2 pH sensing with two different extended gate readout configurations. The sensing surface is the same in both cases, i.e. 100 nm thick gold strips evaporated on a

Si/SiO_2 substrate. (a) Here, a commercial MOSFET is used to convert potential changes to current changes. The extended gate gold surface is connected to the gate terminal of the transistor. (b) The transistor drain current I_d is measured vs. V_{ref} in different pH buffer solutions. A shift of the transfer curve to the right is observed with increasing pH. This shift is the pH response of the sensor and is plotted in (c) for two different measurements. (d) The potential changes at the gold surface can also be directly monitored by a voltmeter. (e) The measured voltage is shown vs. time for different pH values. (f) The resulting pH response is very similar to the data presented in (c).

Next, the biosensing capabilites of a gold-coated graphene nanoISFET are compared with an extended-gate MOSFET. As mentioned above, the gold surface is an ideal choice for the biosensing experiments because of the well-established surface functionalization techniques based on the thiol-gold chemistry, and because of its moderate pH response which reduces the effect of interfering reactions.[358-359] In addition, the results can directly be compared with surface plasmon resonance (SPR) studies that also use a gold-coated chip as a sensing surface. Here, the specific protein-antibody interaction of bovine serum albumin (BSA) and its antibody (anti-BSA) is studied. The sensing results are summarized in Figure 4-3(a,b) for gold-coated graphene and in Figure 4-3(c,d) for a MOSFET with an extended gold gate. The gold surfaces of both sensors were functionalized with BSA, following a protocol described in the Experimental Section. The sensors were then tested in different solutions of anti-BSA in PBS buffer (10 mM, pH 7.4). The interaction is schematically shown in the inset of Figure 4-3a. As seen in part (a) and (c), both sensors respond to increasing anti-BSA concentration by a shift of the transfer curve to the right (toward more positive values). This suggests that anti-BSA is negatively charged at this pH value (7.4), which is consistent with the reported isoelectric points for anti-BSA (4.8-5.2[360]). In Figure 4-3b and d, the sensor

response is plotted vs. anti-BSA concentration in nM on a linear scale (main graph) and semi-log scale (inset). Both active sensors exhibit similar behavior and a significant response which can be quantitatively described by Langmuir adsorption, as discussed in the next section. To assess the effect of non-specific binding, control measurements were performed on gold surfaces without the BSA immobilization step. These control samples were measured in the same anti-BSA concentrations as the active BSA-coated samples. The results are plotted in the inset Figure 4-3b and d for graphene and the extended-gate sensor, respectively. The response of the control samples is small and does not show a clear trend, indicating that the effect of non-specific binding is small, and the interaction between BSA and anti-BSA is highly specific.

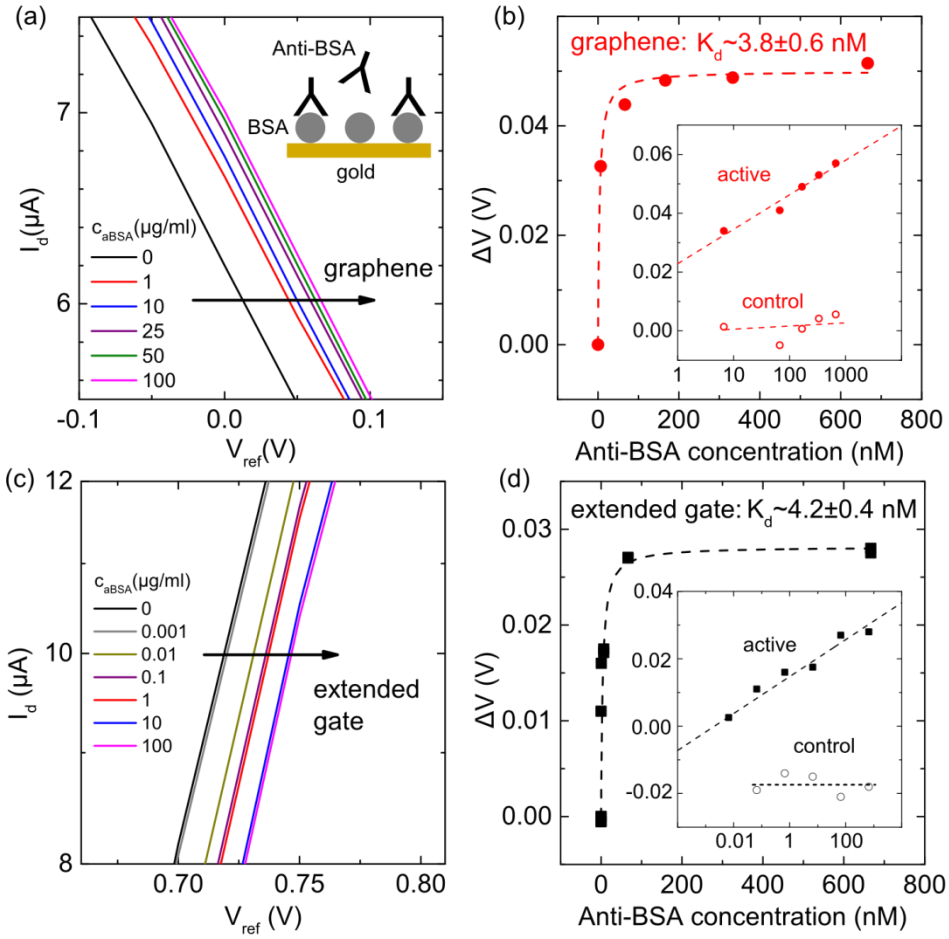

Figure 4-3 Study of the BSA/anti-BSA interaction using a gold-coated graphene sensor (a-b) and an extended gate MOSFET sensor (c-d). The interaction is sketched in the inset of part (a). The protein BSA is immobilized on the gold surface of both sensors. The BSA-coated surface is then exposed to different concentrations of BSA antibody in 10 mM PBS buffer (pH=7.4). (a, c) For both sensors, a shift of the transfer curve to the right is observed, because anti-BSA is negatively charged at pH=7.4 (the isoelectric point is ≈4.8-5.2[360]). (b, d) Potential changes (ΔV) are shown vs. anti-BSA concentration in PBS buffer relative to the value measured in buffer without antibodies (i.e. ΔV=0 *at* $c_{anti\text{-}BSA}$=0). Both sensor systems exhibit a similar response, which can be fitted using Langmuir adsorption model (dashed lines). The dissociation constant K_D can be estimated from these fits. The values are in good agreement with the SPR data (~4.4 ±0.2 nM, Figure S1). Insets in (b) and (d) show the data on a semi-log scale (solid symbols), as well as the results obtained with control samples (open circles). The control samples did not have BSA immobilized on the gold surface. The control measurements do not show a clear trend, suggesting that the non-specific binding to the gold surface is small.

The strength of a specific biological interaction is typically characterized by its dissociation constant (K_D). As a final step in our analysis, K_D is estimated using our sensing results and compared with independent SPR measurements. The data in the main graphs of Figure 4-3b and d is fitted with a Langmuir adsorption isotherm[361-362]

$$\Delta V = \frac{\Delta V_{\max}[C]}{K_D + [C]} \tag{31}$$

where ΔV is the sensor response, ΔV_{max} is the maximum (or saturation) response, $[C]$ is the antibody concentration in solution, and K_D is the dissociation constant, treated as a fitting parameter. From these fits, represented by the dashed lines in the main graph of Figure 4-3b and d, the corresponding fitting parameters can be derived with $K_D \sim 3.8 \pm 0.6$ nM for graphene and $K_D \sim 4.2 \pm 0.4$ nM for the extended gate sensor. The dissociation constant obtained from this additional data set is $K_D \sim 4.0 \pm 0.6$ nM, in good agreement with the first device. Furthermore, these estimates agree well with previous SPR studies,[363] and our own SPR measurements ($K_D \sim 4.4 \pm 0.2$ nM, see Figure 4-4) using the same surface modification protocol as for the potentiometric sensors. To our knowledge, this is the first quantitative study of a protein-antibody interaction with gold-coated graphene field-effect transistors.

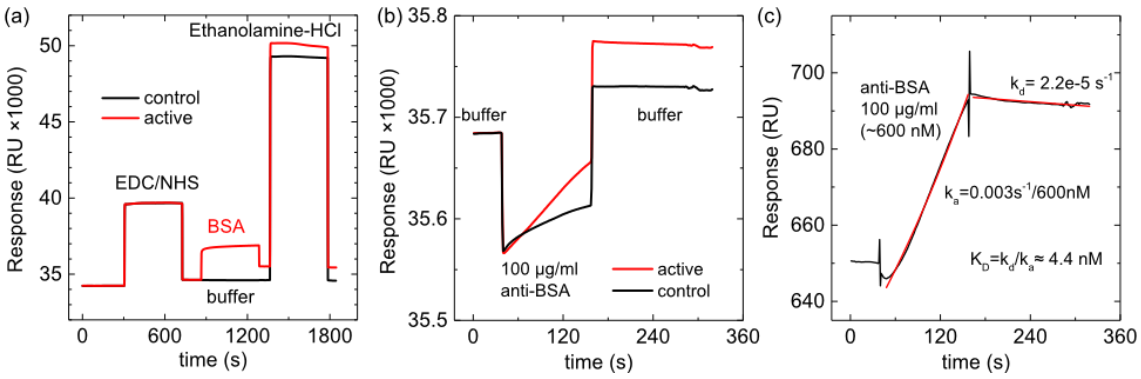

Figure 4-4 Surface plasmon resonance (SPR) results, showing refractive index units change (RU) vs. time. (a) Immobilization of BSA via amine coupling. A 1:1 EDC:NHS mixture was used to activate the carboxyl groups of the mercaptohexadecanoic acid (MHA) on gold surface. A 1% BSA solution in 10 mM PBS buffer (pH=7.4) was injected to immobilize the protein on the active sample. Plain buffer without the protein was injected on the control sample. Both chip surfaces were deactivated with injection of ethanolamine-HCl (pH 8.5). (b) To demonstrate the binding of anti-BSA, a 100 µg/ml anti-BSA solution was injected on both samples. A clear difference between active and control is observed, which is plotted in (c).

The exact amount of the available BSA binding sites is determined by the sensor surface and the details of the immobilization protocol. The observed surface potential changes are mainly caused by specific adsorption of charged anti-BSA molecules and depend on the anti-BSA concentration in solution. In general, the relationship between the surface potential and the concentration of an analyte in solution can be quantitatively described by the site-binding model.[364-367] The strength and the exact shape of this function are determined by the parameters associated with: (i) the interface, i.e., the type and the number of available binding sites;[365] (ii) the specific interaction described by the dissociation constant K_D mentioned above; (iii) and the properties of the surrounding electrolyte, i.e., the Debye screening length and the pH value.[368] Importantly, none of these parameters is related to the type of transducer used. This is the reason why both

potentiometric sensors studied here show similar response. The transducer merely converts or amplifies the surface potential change $\Delta\psi$ into a current, potential, or another signal change ΔS as follows

$$\Delta S = A\Delta\psi$$

where *A* is the transfer function determined by the transducer properties. In principle, any type of (nanoscale) transducer can be used for this purpose. Again, the surface potential changes remain the same as long as the above mentioned critical parameters are the same, independent of the transfer function *A*. Criteria for choosing a transducer can be important, such as its long-term stability, the ability to reuse the readout chip, and a simple fabrication process.

To conclude, the pH and biosensing capabilities of a gold-coated graphene nano-ISFET with an extended gate FET in two different readout configurations are compared. Because all these sensors are based on the same potentiometric principle, their response is solely determined by the changes in surface potential, which depends on the active interface in contact with the electrolyte. Regardless of the type of readout used, all potentiometric sensing devices exhibit consistent response to pH, as long as their active surfaces are the same. Moreover, potentiometric devices can be used as effective detectors to quantitatively study protein-antibody interactions. The extended gate sensors have the same sensing capabilities as any ISFET while being dramatically easier to fabricate. By separating the device in a disposable sensor chip and a reusable readout part, these sensors can be manufactured in an extremely cost-effective way. In contrast to nanoISFETs, the readout part is not exposed to the electrolyte solution, eliminating possible stability and reliability issues. These results are important for practical

application of potentiometric devices as rapid and label-free biodetectors for diagnostics of diseases, food safety or environmental monitoring.

4.4 Animal disease diagnosis using potentiometric EGFET biosensors[e]

The purpose of this study was to develop a tool for diagnostic disease surveillance using serological tests for low-cost and rapid POC disease detection using recombinant BHV-1 gE on extended-gate FET sensor platforms. A surface immobilization and regeneration protocol was developed for gE based on an SPR system by our collaborators at QUB, and selective binding of anti-gE to immobilized viral protein demonstrated. Haptoglobin (Hp) protein was used to assess potential non-specific binding issues due to a similar glycosylation pattern and molecular weight to that of recombinant gE.

Figure 4-5 shows a schematic of the device consisting of two parts: a sensor for signal generation (right) and a transducer for signal amplification and readout (left). The active sensing surface is a thin gold film (100 nm) evaporated on a Si/SiO_2 substrate. The gold film is in contact with the electrolyte and its surface potential depends on the amount of charged molecules attached to the surface. The gold surface can be chemically modified to achieve specific adsorption of certain biomolecules. There are several reasons for choosing a gold film: first, access to well-established thiol-based surface chemistry for self-assembly of linker molecules; second, the possibility of a direct

[e] Adapted with permission from Tarasov, A.; Gray, D. W.; Tsai, M.-Y.; Shields, N.; Montrose, A.; Creedon, N.; Lovera, P.; O'Riordan, A.; Mooney, M. H.; Vogel, E. M., A potentiometric biosensor for rapid on-site disease diagnostics. *Biosens. Bioelectron.* **2016,** *79*, 669-678. Copyright 2016 Elsevier.

comparison to commercial tools based on SPR, which also typically use a gold surface; and, third, excellent chemical stability even in harsh environments. To read out the potential changes on the gold surface, a commercial MOSFET was used as the readout transducer. The gold film acts as the so-called "extended gate" of the MOSFET, and is electrically connected to the gate terminal. An Ag/AgCl reference electrode was immersed in the solution to gate the transistor through the liquid. Different solutions were delivered to the surface using microfluidics. In Figure 4-5b**,** a typical transfer curve of the liquid-gated extended-gate FET (EGFET) in buffer is shown. The drain current I_d can be modulated by sweeping the voltage at the reference electrode V_{ref}. To enable different functionalization on one chip, a disposable sensing chip with 4 gold strips was used (Figure 4-5c) - each gold strip can be independently functionalized using a liquid cell (shown in Figure 4-5d).

Glycoprotein gE was covalently immobilized on the gold surface of the EGFET via amine coupling to the carboxyl groups of a self-assembled monolayer (SAM) of thiol linker molecules. To ensure the best possible comparison between the FET sensors and SPR, the SPR chip surface was functionalized with carboxylated thiol SAMs using the same protocol for EGFET sensors.

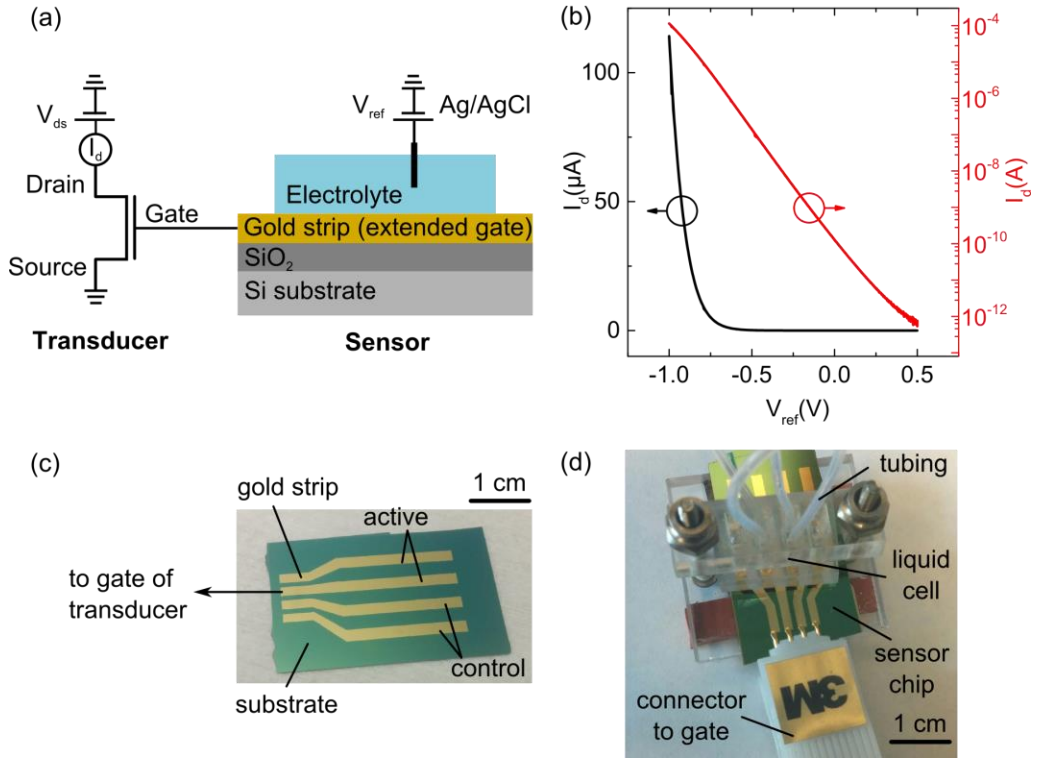

Figure 4-5 Fabrication of EGFET sensor. (a) Schematic of the potentiometric sensing device, consisting of two parts: a sensor part for signal generation and a transducer part for signal amplification and readout. The active sensing surface is a thin gold film (Au) evaporated on a Si/SiO_2 substrate. The gold film is contact with the electrolyte and its surface potential depends on the amount of charged molecules attached to the surface. The gold surface can be chemically modified to achieve specific adsorption of certain biomolecules. To read out the potential changes on the gold surface, a commercial MOSFET is used as the readout transducer. The gold film acts as the so-called "extended gate" of the MOSFET, and is electrically connected to the gate terminal. An Ag/AgCl reference electrode is immersed in the solution to gate the transistor through the liquid. Different solutions are delivered to the surface using microfluidics. (b) A typical transistor transfer curve showing that the drain current I_d can be modulated by sweeping the voltage at the reference electrode V_{ref}. This measurement was recorded in 10 mM PBS buffer. The same curve is shown on linear scale (left axis) and semi-log scale (right axis). (c) Image of a disposable sensing chip used in this study. Four 100 nm thick gold strips were e-beam evaporated through a shadow mask. Using a liquid cell shown in (d), two gold strips were functionalized with the protein gE (active), and the other two were functionalized with protein Hp (control). To read out the potential changes generated on the sensor surface, the individual gold strips were connected using a test clip shown in (d) to the gate of the transducer.

To evaluate EGFET sensor performance for the detection of BHV-1, the gE-coated gold strip was measured in different dilutions of anti-BHV-1 antiserum and Figure 4-6a illustrates the transfer curves shifting to the left with increasing antibody concentration. As a control for non-specific binding, a second gold strip was coated with human Hp, and measured in the same antiserum dilutions. The response of the active EGFET, defined as the gate voltage required to achieve a drain current of 10 nA, is plotted versus antiserum dilution in Figure 4-6b (squares), together with SPR responses (circles). Both sensors exhibit significant and very similar response even at antiserum dilutions as low as 1:1000. In contrast to the active sensor, the Hp-coated control does not show a clear trend with changing antiserum concentration (Figure 4-6c). On FET and SPR sensors the observed response due to non-specific binding is small (Figure 4-6d) compared to the specific response shown in Figure 4-6b. To test the selectivity of the sensor, the active gE-coated gold strip was measured in different dilutions of Hp antibody (anti-Hp) (illustrated in Figure 4-7). The EGFET only weakly responds to changes in anti-Hp concentration with minimal shift to the right (squares in Figure 4-7b) - a similar weak response was observed with SPR (circles). These calibration results suggest that the expressed gE protein is functional on the sensor surface, and the EGFET sensor is highly sensitive and selective to anti-gE within the antiserum with very similar performance to SPR. As an additional control, the Hp-coated chip was also measured in different anti-Hp dilutions (Figure 4-8). As expected, a strong response was observed, providing more evidence for the high specificity of the interactions studied here.

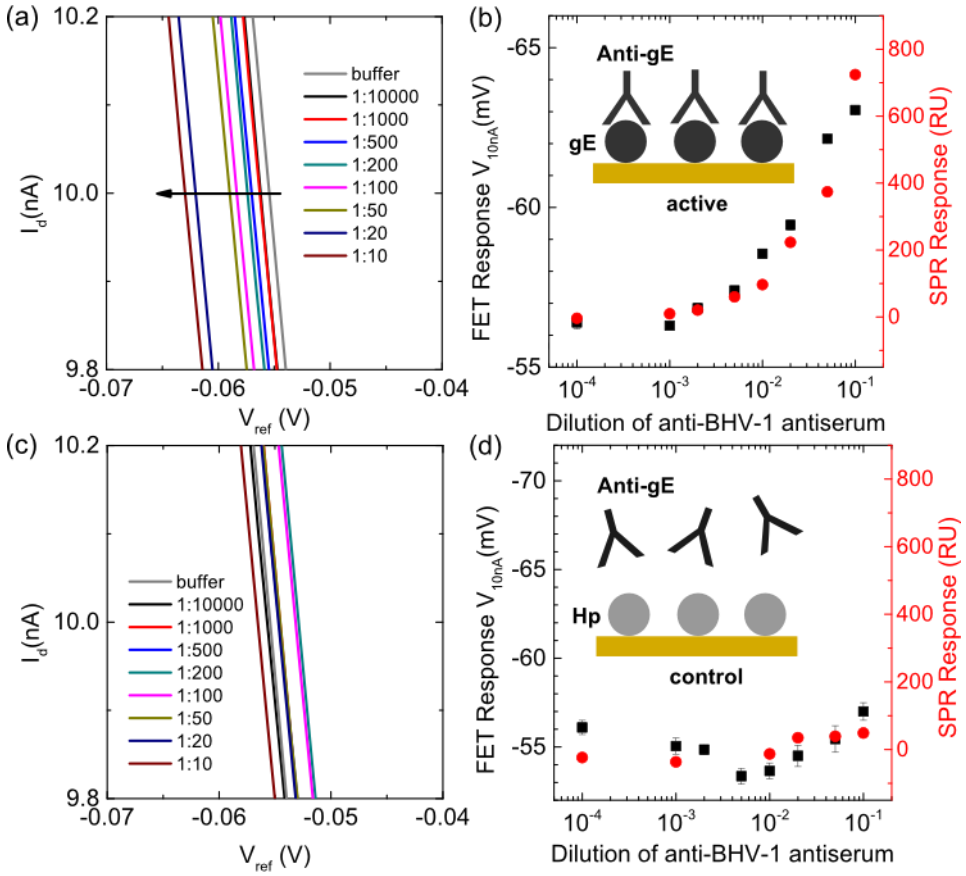

Figure 4-6 Evaluation of EGFET and SPR performance for anti-BHV-1 antibody detection in serum. Two gold strips were functionalized differently and used as the active sensor (a-b) and the control (c-d). Both surfaces were measured in the same dilutions of antiserum. (a-b) The BHV-1 glycoprotein E (gE) was immobilized on the active gold strip using amine coupling, and acts as a capture antigen for anti-gE antibody present in antiserum (inset in b). (a) The transistor curves measured with the active gE-coated device shift to the left with increasing serum dilution in 10 mM HPS-EP buffer. (b) The calibration curve in different antiserum dilutions. The FET response is defined as the voltage shift at I_d=10 nA (along the arrow in (a)). The results are in excellent agreement with surface plasmon resonance (SPR) measurements (SAM chip, right axis). (c,d) The control sample was coated with the protein Haptoglobin (Hp) as a control for possible non-specific binding. (c) The Hp-coated control does not show a clear trend with changing antiserum dilution. (d) The observed response due to non-specific binding is small compared to the specific response shown in (b).

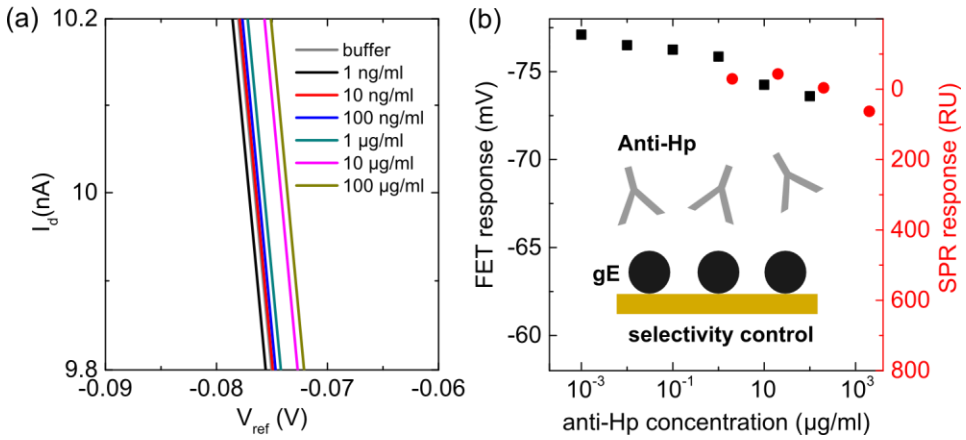

Figure 4-7 Selectivity control of EGFET and SPR sensors immobilized with gE. (a) The active gE-coated sensor was measured in different concentrations of the haptoglobin antibody (anti-Hp) in 10 mM HBS-EP buffer. At higher concentrations, a small shift to more positive values is observed, opposite to the response direction to anti-gE. The FET and SPR responses (CM5 chip) are compared in (b). The results suggest high selectivity of the gE-coated sensor toward anti-gE in solution.

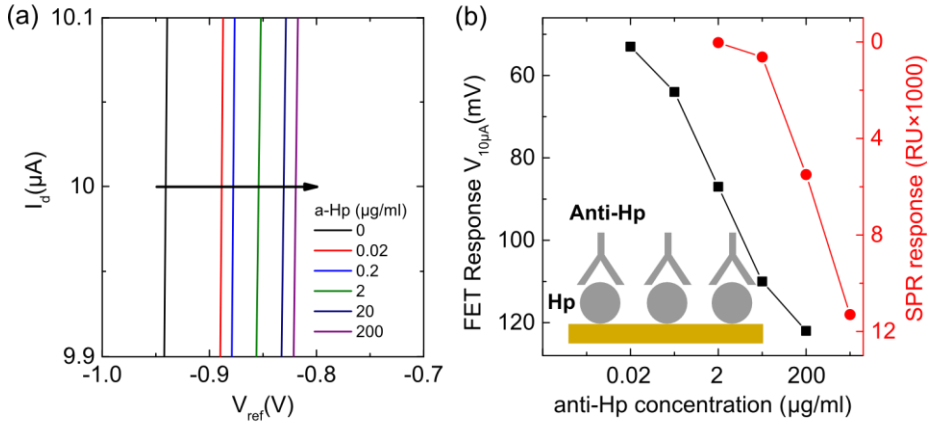

Figure 4-8 Measurements of Hp-coated control sample in different anti-Hp dilutions. (a) Transfer curves shift significantly to the right. (b) FET (squares) and SPR (CM5 chip, circles) response vs. anti-Hp dilution and concentration. Both sensors show similar behavior, suggesting that anti-Hp binds strongly to the Hp-coated surface (inset).

The EGFET results were further verified using commercial gE ELISA kits (IDEXX). In Figure 4-9, data from the gE-coated FET sensor (from Figure 4-6b) is compared with ELISA absorption measurements, performed in the same dilutions of anti-BHV-1 antiserum. All test platforms (FET, SPR, ELISA) have a similar dynamic range and approach the limit of detection for sera dilutions < 10^{-3}. These results indicate that EGFET sensors can have a performance comparable to well established and optimized ELISA assays. In addition, the EGFET sensors provide results much faster than ELISA (<10 min vs 19 hr), making them very promising for rapid diagnostic applications.

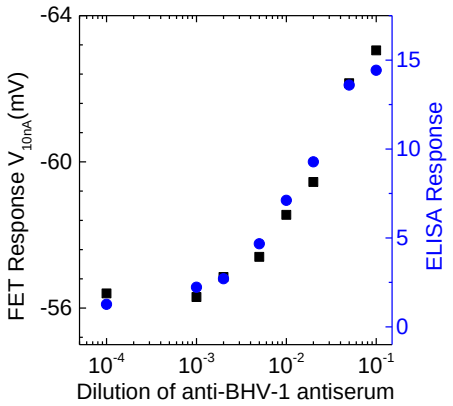

Figure 4-9 Comparison of EGFET and ELISA for anti-BHV-1 antibody detection in serum. The response of a gE-coated FET sensor from Figure 4-6b is plotted together with IDEXX gE blocking ELISA (1/absorbance) vs. the dilution of anti-BHV-1 antiserum. Comparable results (sensitivity and assay linearity) were obtained for both diagnostic platforms.

The respective sensors were also tested in several dilutions of bovine serum samples. The results are presented in Figure 4-10a for the EGFET sensor, and Figure

4-10b for the SPR, with both sensors showing similar response. Serum sample 1 is from a BHV-1 negative animal whilst sera samples 2 and 3 originate from BHV-1 positive animals. As expected, FET and SPR responses were higher for BHV-1 positive animals compared to negative animals, with increasing response (maintaining the same trend) with sera concentration (1:50, 1:20, 1:10). Furthermore, the sensor can be regenerated by removing bound antibodies with glycine pH 2.0 solution without damaging the immobilized gE proteins (Figure 4-11). Whilst the sensor part can also be designed as a single-use disposable, this feature can be a significant cost advantage enabling a single sensor to test multiple samples. Whilst these initial results are extremely promising, further work will be required to fully establish the FET sensors for disease monitoring purposes within populations.

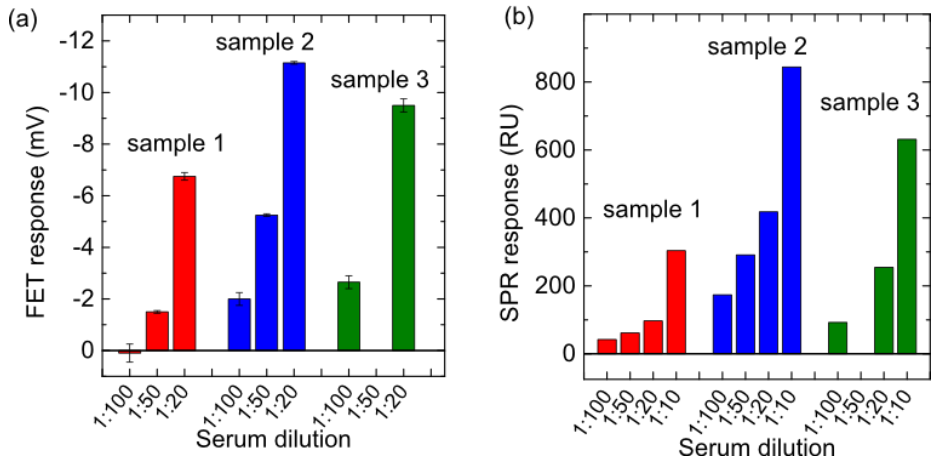

Figure 4-10 Assessment of EGFET and SAM SPR performance for anti-BHV-1 detection in serum from BHV-1 infected animals. Sample 1 was from a BHV-1 negative animal, whereas samples 2 and 3 originated from BHV-1 positive animals. The measurements were performed in different dilutions of the same 3 blood samples. (a) The FET response is shown vs. the dilution of the 3 samples. The sensor response increases in higher dilutions, because more antibodies can bind to the surface. (b) SPR results, obtained with the same blood samples, show very similar behavior validating the FET response. In

general, the response to sample 2 > sample 3 > sample 1, indicating different levels of antibodies in the serum.

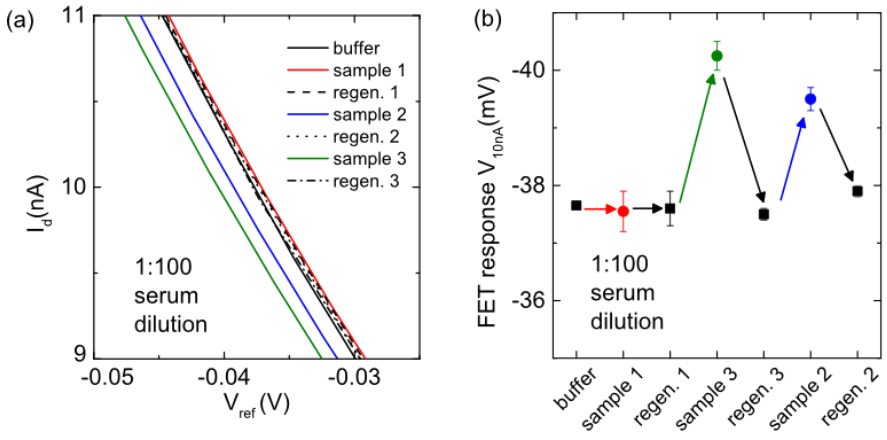

Figure 4-11 Regeneration of an FET sensor. (a) The blood serum was diluted 1:100 in 10 mM HPS-EP buffer and injected on the sensor surface. No shift was observed upon addition of sample 1. Significant response was observed with samples 2 and 3. After each measurement with a blood sample, the surface was regenerated using a short injection of glycine (pH 2.0), and flushed with HPS-EP buffer. The measurements performed in buffer after the regeneration steps align very well on top of each other (black lines), indicating that the sensor is reusable. This regeneration step had been previously tested on SPR. The sensor response in the 1:100 serum dilution is plotted in (b). The red, blue and green arrows indicate injections of different blood samples, while the black arrows represent a regeneration step with glycine and buffer.

Currently there is no commercial low-cost point-of-care device for the serological diagnosis of pathogen related responses in blood that can yield rapid quantifiable results approaching the sensitivity of ELISA. FET based biosensors are particularly promising for user-friendly, rapid diagnosis required for effective on-site disease control. This is the first demonstration of a potentiometric sensor for diagnosis of animal diseases using blood. The endemic BRD virus BHV-1 was selected as a model pathogen for

investigating FET sensor performance due to the high level of screening required for current and planned disease eradication programs. BHV-1 gE glycoprotein was engineered to allow for high level secretion and simple purification with minimal sample preprocessing via the removal of the intracellular and transmembrane regions as achieved with similar viral membrane proteins [369-370]. Produced gE was found to be suitable for diagnostic test development with antigenicity confirmed through positive reaction with anti-BHV-1 antiserum. By using identical sensing surface (gold) and protein immobilization protocols, SPR and FET sensor systems were evaluated and found to yield equivalent results for antibody binding to gE (in serum) and Hp. Reduced Debye length and non-specific binding have traditionally been limiting factors for direct FET sensing in serum, requiring complicated sample pre-treatment and reducing their potential for rapid POC testing. Compared to complicated desalting approaches[371], this study applied simple dilution in a fixed ionic strength buffer to increase Debye length and whilst signal response was low, a sigmoidal response was achieved for anti-BHV-1 binding to immobilized gE with comparable sensitivity and dynamic range to SPR and commercial ELISA. The application of a reference electrode with immobilized Hp glycoprotein allowed for the elimination of non-specific binding effects observed in SPR and FET sensors at higher serum dilutions (1:10 – 1:20). Particularly interesting is the observation that in actual serum samples from BHV-1 positive or negative animals, the FET sensors gave results comparative to that achieved by SPR. These results are extremely promising and highlight that the application of FET sensors to serological disease diagnosis is transferable to a multitude of pathogenic microorganisms.

Unlike SPR, FET sensors do not require any optical components, are low-cost and portable. The use of extended-gate geometry rather than a conventional ISFET further simplifies device fabrication and reduces the cost of the sensor. Separating the readout transducer from the gold sensing surface has the following main advantages: 1. reliability issues can be avoided because the transducer is not in contact with the biological solution; 2. the transducer is reusable and can be developed independent of the sensor surface to optimize the signal-to-noise ratio [357, 372-373]; 3. the sensing chip can be designed as an inexpensive disposable in a very simple fashion (chemically modified thin gold strips on an arbitrary low-cost substrate). Having several gold strips can potentially enable multiplexed detection of several analytes. The presented sensors can be easily manufactured at a large scale, resulting in very low cost per test. Compared to ELISA, the FET sensor is several orders of magnitude faster (<10 min POC vs. >72 hours for laboratory based testing), which is critical for the diagnosis of highly contagious diseases. Future work will focus on increasing the density of attachment sites and optimizing incubation times and other relevant assay parameters to further improve FET performance.

4.5 Conclusion

It has been demonstrated that extended-gate FETs is a promising platform for potentiometric chemical and biological sensors. By comparing extended-gate and graphene-based ion-sensitive FETs, EGFET can perform a comparable sensing performance but in a simpler configuration. In addition, possible stability issues of the

sensors in liquid environment can be avoided using EGFET due to the separation of sensing chip from the transducer. We conclude that the sensitivity of the chemical and biological sensors only depends on the sensing surface instead of the transducer. Furthermore, EGFET configuration is readily compatible with state-of-the-art FET-based transducers as well as next-generation nanoelectronics including TMD-based transistors.

The field application of EGFET biosensors have been demonstrated for the animal disease diagnosis. The EGFET electrical sensors are advantageous for point-of-care portable devices due to the easy miniaturization. In addition, EGFET potentiometric biosensors provide an easier operation and faster response over commercialized ELISA and SPR sensors. EGFET biosensors are expected to help early on-site screening and diagnosis of diseases.

Overall, extended-gate FETs is promising for environmental monitoring, chemical detection and disease diagnosis. Due to the separation of extended-gate sensing chip and the transducer, the stability can be improved by avoiding the exposure of the electrical component to the liquid environment. In addition, versatile choices of transducers are available, for example, silicon-based devices and nanoelectronics, including TMD-based transistors. Future works that focuse on the design of the sensing surface, reliability of sensors, optimization of surface chemistry, are crucial to further improve the EGFET potentiometric sensors and commercialize in the future.

CHAPTER 5. INTEGRATED POTENTIOMETRIC AND IMPEDIMETRIC BIOSENSING SYSTEM[f]

Among the currently available sensor technologies, electrical biosensors using potentiometric biosensors based on field-effect transistors (FETs) and impedimetric biosenosrs based on EIS are very promising due to their high sensitivity, rapid electronic readout, and simple integration into portable and easy-to-use devices. Despite significant research, the integration of potentiometric and impedimetric biosensors remains unexplored, and there is little study on the correlation between these two electrical biosensing techniques.

In this chapter, we demonstrated the integrated FET/EIS biosensor system for the first time.[374] This novel configuration enables the sequential measurement of the same immunological binding event on the same sensing surface, and helps understand the origin of the sensing signals produced by FET and EIS biosensors. Here, we use both bovine serum albumin (BSA) versus antibody BSA prototype system and hemagglutinin-neuraminidase (HN) versus bovine parainfluenza virus type 3 (BPIV3) animal blood system as test vehicles for integrated sensors. We further demonstrated that potentiometric and impedimetric sensors are linked through the surface potential, and the correlation can be explained using electrochemical kinetics and the Butler-Volmer equation. In addition, we proposed that potentiometric sensor is inherently sufficient for

[f] Adapted with permission from Tsai, M.-Y.; Creedon, N.; Brightbill, E.; Pavlidis, S.; Brown, B.; Gray, D. W.; Shields, N.; Sayers, R.; Mooney, M. H.; O'Riordan, A.; Vogel, E. M., Direct correlation between potentiometric and impedance biosensing of antibody-antigen interactions using an integrated system. *Appl. Phys. Lett.* **2017**, *111*, 073701. Copyright 2017 AIP Publishing LLC.

practical biosensing applications, while providing added benefits of rapid response and low-cost scalability.

Section 5.1 gives a brief introduction to the electrical biosensors and the working principle of FET/EIS integrated system. Section 5.2 describes the fabrication of the integrated system and the experimental setup. Section 5.3 presents a direct comparison between potentiometric and impedimetric biosensors via the sequential measurement of the same immunological binding event on the same sensing surface. This direct comparison sheds light on the fundamental origins of sensing signals produced by FET and EIS biosensors, as well as the correlation between the two. The sensor chips used in this work were fabricated and provided by Niamh Creedon and Dr. Alan O'Riordan at Tyndall National Institute, Ireland.

5.1 Introduction

The ability to detect biochemical species rapidly without complicated sample preparations in a centralized laboratory is essential for medical care, disease diagnosis, food safety and environmental monitoring. Optical biosensors require markers to label target biomolecules (e.g., fluorescence spectroscopy), or rely on expensive equipment that cannot be readily miniaturized, as in the case of surface plasmon resonance (SPR).[375-376] In contrast, label-free electrical biosensors are particularly promising as point-of-care sensor devices since they can be miniaturized through cost-effective microfabrication. Relying directly on the immunological affinity between immobilized surface probes (e.g., antigens) and targets in an analyte solution (e.g., antibodies), the

resulting change of the surface properties is amplified and converted to an electrical output signal by a transducer. Potentiometric and impedance biosensors are two of the most common transducers for label-free biosensing. Potentiometric biosensors detect the change of surface potential under DC operation due to the attachment of charged target biomolecules to the probes on the sensing surface, and are most commonly implemented in the form of ion-sensitive FETs (ISFETs) or extended gate FETs (EGFETs).[215, 274, 377-378] Alternatively, impedance biosensors use electrochemical impedance spectroscopy (EIS) to measure the change of electrical current and, in turn, the electrical impedance of a biological interface under DC bias and AC oscillation.[379-382] Cost-effective potentiometric and impedance sensors are capable of label-free operation that both simplifies the sample preparation steps and enable on-site detection with shorter turnaround time.

Although various nanomaterial-based ISFETs have been used for potentiometric biosensors including silicon nanowires,[222] graphene,[224] carbon nanotubes,[226] we have reported that the sensitivity of a potentiometric biosensor is independent of the choice of the transducer, and instead relies only on the sensing surface.[274] Moreover, ISFETs require a sophisticated encapsulation scheme to protect the semiconductor device from exposure to the liquid environment that can hamper reliability and stability.[230] Consequently, if either the sensing surface or the readout component fails, the entire ISFET sensor becomes unusable. EGFET biosensors, by contrast, provide a simpler and a more robust design for liquid phase sensing by separating the sensing chip (an extended gate) from the readout transducer (FET), and the sensitivity is comparable to the conventional ISFET.[274] Moreover, the EGFET is a promising tool for disease diagnosis

with a comparable performance to ELISA and SPR.[378] Finally, since the transducer is separated from the sensing surface, the EGFET configuration readily enables the integration of potentiometric sensors with other sensor platforms.

EIS-based impedimetric biosensors measure change of impedance when species attach to the sensing surface. Under faradaic operation involving redox couples, the measured impedance spectrum can be further analyzed using an equivalent circuit model. Two of the most important parameters, charge transfer resistance (R_{ct}) and surface capacitance ($C_{surface}$) can be resolved in this way. The change of surface potential and the formation of the biomolecular layer will prevent the redox species from approaching the working electrode due to electrostatic repulsion and steric hindrance, respectively.[380] The phenomenon is often reflected in an increase of the R_{ct} which dominates the overall measured impedance.

In this chapter, we demonstrate a fully integrated system that combines both two-terminal EGFET-based potentiometric and three-terminal EIS-based impedance biosensing on a shared active sensing surface. This system enables the sequential measurement of the same binding event on the same sensing surface using two different sensing techniques. Consequently, we are able to perform a fundamental investigation into the origins of the sensing signal produced by FET and EIS biosensors. A bovine serum albumin (BSA) versus antibody-BSA (anti-BSA) prototype system was used as the test vehicle for the integrated biosensors. In addition, detection of bovine parainfluenza antibodies in a complex blood system with hemagglutinin-neuraminidase (HN) has also been demonstrated. Comparison of the EGFET and EIS sensor responses reveals similar dynamic ranges, and motivates our study of the relationship between surface potential

and impedance, which is explained by electrochemical kinetics and the Butler-Volmer equation.

5.2 Fabrication of integrated biosensors and electrical characterization

All the chemicals and proteins were purchased from Sigma-Aldrich and used as received. The sensor chip was fabricated on a borofloat wafer. The metallic structures including Au micro-strip working electrode (WE), Au (Ti/Au 10/90 nm) counter electrode (CE) and Pt (Ti/Pt 10/90 nm) on-chip pseudo-reference electrode (RE) were deposited and patterned using e-beam evaporation and photolithography, respectively. A commercial n-MOSFET (VN0104, Supertex) was used as the transducer for EGFET biosensors and the I-V characterization was measured using a Keithley 4200-SCS semiconductor analyzer. The V_d was 0.2 V and a positive V_{ref} sweep was applied to the liquid through a commercial dip-in Ag/AgCl reference electrode (Princeton Applied Research / Ametek #K0260). EIS biosensors were characterized using a Gamry Interface 1000 potentiostat. The DC bias was -0.4 V and the RMS AC oscillation was 5 mV. The WE was coated with o-aminobenzoic acid (o-ABA, 50 mM in H_2SO_4) carboxylated film through 10 cyclic voltammetry scans (0 to 0.8 V, 50 mV/s). The BSA proteins (1% in PBS) were immobilized onto the sensing surface through amine coupling using NHS/EDC. 1M ethanolamine-HCL solution was used to deactivate and block the sensing surface. This sensing surface was exposed to anti-BSA dilutions in PBS with 20 min contact time. Similar to the above-mentioned BSA immobilization, HN proteins (50 ug/ml in acetate buffer pH 4.0) were immobilized to the sensing surface through amine

coupling. Blood samples taken from calves in Northern Ireland were processed to plasma and screened for the presence of anti-BPI3V antibodies using the Svanovir PI3V-Ab ELISA. The sensing surface was blocked using 1M ethanolamine followed by diluted bovine plasma (50X dilution in HBS-EP buffer, pH 7.4) after the immobilization of HN proteins. The HN-immobilized sensing surface was then exposed to dilutions of positive blood plasma in HBS-EP buffer for 30 min contact time. The surface was rinsed with HBS-EP buffer to remove the weakly bound antibodies and possible non-specific binding. The electrical measurement was performed in buffer with 10 mM hexaammineruthenium (III) chloride in PBS (for BSA/aBSA) or HBS-EP (for HN/BPIV3) as the redox couple. In the EGFET sensor, the Au active sensing surface serves as the WE, i.e. extended gate of a MOSFET. A DC voltage sweep is applied to the liquid through a commercial Ag/AgCl RE. For EIS sensor, the aforementioned Au WE is the active sensing surface. On-chip Pt pseudo-RE and Au CE are used. The signal, i.e. surface potential, of potentiometric sensors was extracted from the I_d-V_{ref} curve as the V_{ref} value when I_d = 1 μA. The EIS spectra were modeled using ZView (Scribner Associates Inc.) by minimizing the chi square value.

5.3 Direct correlation between potentiometric and impedance biosensors of antibody-antigen interactions using an integrated system

Comparing EGFET and EIS sensors, the Au working electrode plays a common role: an active sensing surface and WE. As a result, a fully integrated sensing system combining EGFET potentiometric and EIS impedance biosensors can be achieved by

sharing a common Au WE as schematically shown in Figure 5-1a. Using this integrated system, the steps of chemical functionalization and biomolecular attachment can be achieved for both sensors concurrently. Furthermore, this design offers a direct comparison between potentiometric and impedance sensors because the same binding events will be measured on a shared sensing surface.

The optical image of the sensor chip is shown in Figure 5-1c and the enlarged view of Au micro-strip WE in Figure 5-1d. The dimension of the Au micro-strip is 50 μm long and 0.8 μm wide ($4x10^{-7}$ cm^2). The use of a microscale electrode provides the benefit of minimizing the mass transfer limited behaviors in EIS at low frequency, due to the decreased diffusion length around the miniaturized working electrode.[382-384] The conventional Randle circuit model comprises of series resistance (R_s), surface capacitance ($C_{surface}$ usually modeled using constant phase elements, CPE), Warburg resistance (W) and charge transfer resistance (R_{ct}). When the nominal size of the working electrode decreases, the diffusion layer thickness decreases, and the current is no longer dominated by the diffusion of reacting species toward the WE.[385] As a result, the mass transfer dominated W becomes negligible and the Randle circuit can be simplified to a simple RC circuit as shown in Figure 5-1b.[386-387] The measured impedance spectra will be modeled using the simplified circuit model to extract the circuit elements, including R_{ct}. Using an n-channel MOSFET as the transducer, a positive voltage is applied to the solution for FET biosensor measurement and, therefore, a redox probe that has negative redox potential is desired. As a result, hexaammineruthenium (III) chloride, which has both negative reduction and oxidation potentials, qualifies for the application in this study.

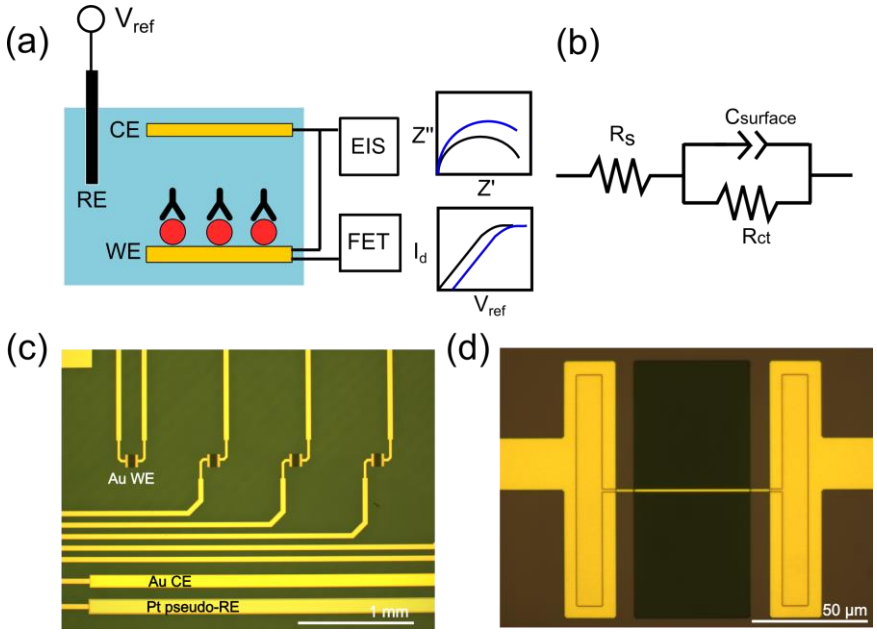

Figure 5-1 The scheme and the optical image of the integrated FET/EIS biosensor system. (a) The experimental setup of the integrated system. (b) The equivalent circuit model for the impedance spectroscopy. (c) - (d) The optical images of the biosensor chip and the enlarged view of the Au micro-strip working electrode.

The FET/EIS integrated sensor's responses to the BSA versus anti-BSA system are shown in Figure 5-2. The I_d-V_{ref} curve of the transistor will shift horizontally depending on the magnitude and the polarity of the change of surface potential on the Au sensing surface. Figure 5-2a depicts the shift of I_d-V_{ref} curves of the potentiometric sensor in the positive direction in response to the increasing concentration of anti-BSA in the PBS, indicating that the anti-BSA (isoelectric point 4.8 – 5.2) is negatively charged in the PBS buffer (pH 7.4).[363] Figure 5-2b shows the change of surface potential measured by FET potentiometric sensor versus anti-BSA concentration in linear scale and logarithmic scale (inset of Figure 5-2b). The change of surface potential due to the attachment of charged antibodies to the WE, i.e. extended gate, was obtained using the change of the

FET's threshold voltage (V_{th}). A typical Langmuir adsorption response with a gradual saturation toward high antibody concentration was observed.[274] Measuring the same binding event at the working electrode, the change of EIS spectra with respect to anti-BSA concentration is presented in a Nyquist plot (Figure 5-2c). Taking advantage of the miniaturized working electrode, no obvious mass transfer limited characteristics were observed in the recorded impedance spectra. As a result, the change of surface properties on the sensing surface is mainly reflected through the change of R_{ct}. As the anti-BSA concentration increases, the overall size of the semicircle increases, indicating an increase of R_{ct} and total impedance. By fitting the impedance spectra with the equivalent circuit model (Figure 5-1b), biomolecular binding-related circuit elements, R_{ct} and $C_{surface}$, could be extracted. Figure 5-2d shows the relationship between R_{ct} and anti-BSA concentration. A similar Langmuir adsorption behavior with saturation at high anti-BSA concentration was again observed. The result proves the successful operation of the integrated FET/EIS biosensor system. However, the surface capacitance shows a much smaller response to various anti-BSA concentrations after a large drop of capacitance value upon the introduction of 10 ng/ml anti-BSA solution (Figure 5-3b). The insensitivity of $C_{surface}$ to the attachment of antibodies can be attributed to the poorly dielectric poperties of the semipermeable biolayer. Furthermore, the similar response obtained from both sensing platforms suggests a possible correlation between surface potential and the impedance, which is explored in the following.

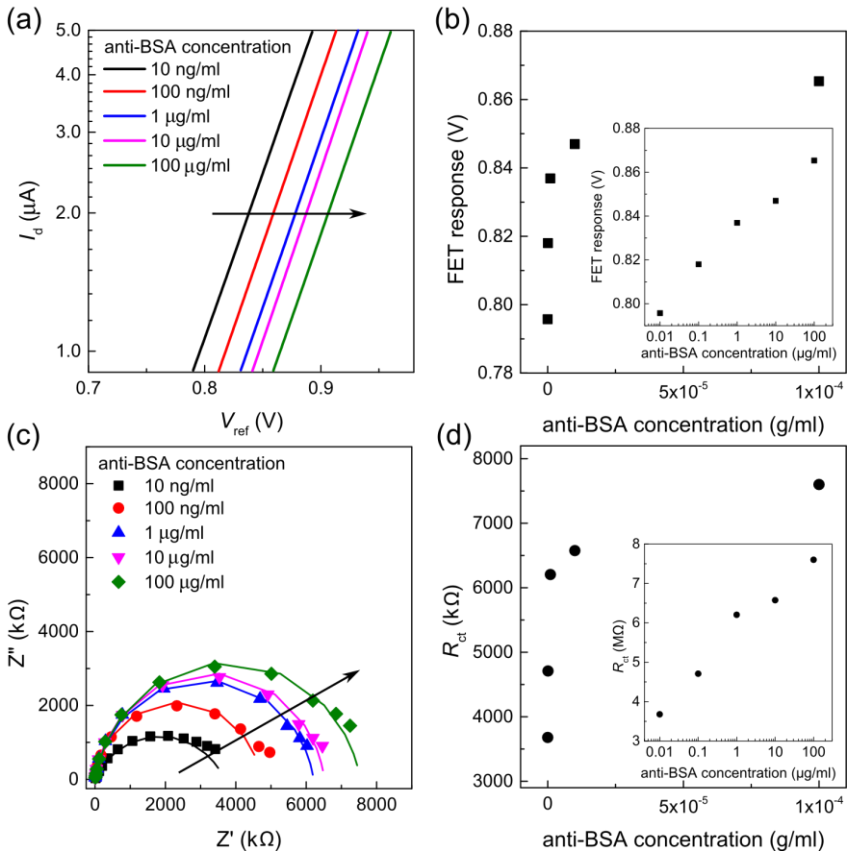

Figure 5-2 The responses of FET potentiometric and EIS impedance biosensors to anti-BSA concentrations. (a) The shift of I_d-V_{ref} curve measured with FET and (b) the FET signal (surface potential) in response to anti-BSA concentrations in linear scale and logarithmic scale (inset). (c) Nyquist plots of impedance spectra measured with EIS and (d) the R_{ct} change in response to anti-BSA concentrations in linear scale and logarithmic scale (inset).

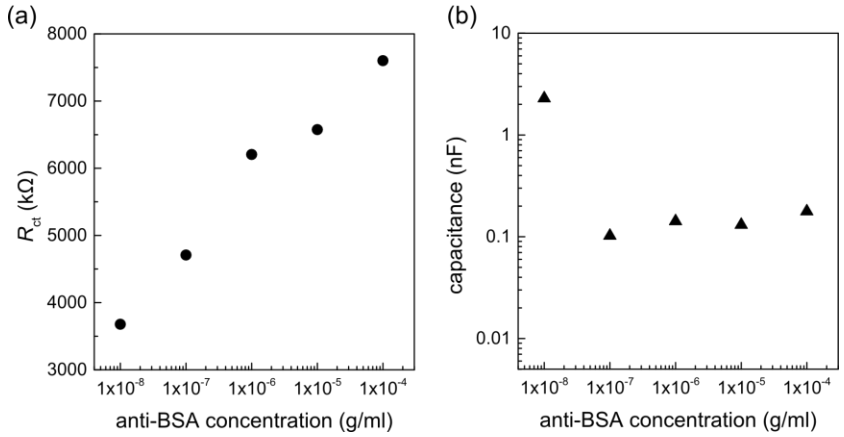

Figure 5-3 The values of circuit elements from the fitting of measured impedance spectra versus different anti-BSA concentrations. (a) The plot of R_{ct} versus different anti-BSA concentrations. (b) The plot of $C_{surface}$ versus different anti-BSA concentrations.

According to classical electrochemical kinetics, the electrical current that flows through the electrode is governed by the effective potential on the electrode surface.[388] This relationship is expressed by the Butler-Volmer equation. Under bias conditions that deviate from equilibrium, i.e. Tafel behavior, the Butler-Volmer equation that links the charge transfer resistance and the surface potential can be simplified to:[388-389]

$$R_{ct} = R_0 \exp\left(\frac{\alpha q \Delta V}{k_B T}\right) \tag{32}$$

where $R_0 = E_{app}/FAK^0C$, F is Faraday constant, A is the area of the working electrode, k^0 is the standard rate constant, C is the concentration of the redox couple species at the electrolyte-electrode interface, transfer coefficient α is commonly assumed to be 0.5 for a symmetrical energy barrier, E_{app} is the bias applied to the system, ΔV is the change of surface potential on the working electrode, q is the elementary charge of an electron, k_B is

Boltzmann's constant and T is the temperature. It is reported that k^0 exhibits a wide range from 10^{-9} to several hundred cm/s depending on the choice of the redox couple, the surface morphology of the WE, the formation of the biolayer, different charge transfer mechanisms, buffer concentration, etc.[388, 390-391] In effect, the Butler-Volmer equation predicts that R_{ct} is exponentially related to the change of surface potential (ΔV). Figure 3 shows the relationship between R_{ct}, measured with EIS, and the exponentiation of ΔV, i.e. $\exp(\alpha q \Delta V / k_B T)$, obtained from the FET. A high linearity is observed which agrees well with the prediction of Butler-Volmer theory. The fitted R_0 is 1.43 x 10^6 Ω and is comparable to the calculated value of 1.04 x 10^6 Ω, where A = 4 x10^{-7} cm^2, k^0 is 1 cm/s for a simple electron transfer,[391] and C is 10^{-5} mol/cm^3. In the case of affinity sensors, the ΔV results from the binding of charged biomolecules to the surface, i.e. WE. EGFET sensors directly measure this surface potential change, which concurrently influences the electrical current and the resulting impedance measured by EIS sensors by increasing the hindrance for redox species from reaching the WE. This finding confirms that the origin of the sensing signals for both potentiometric biosensors and impedance biosensors is the change of surface potential. Also, the signal output from potentiometric biosensors can be linked to that of impedance biosensors using the Butler-Volmer equation.

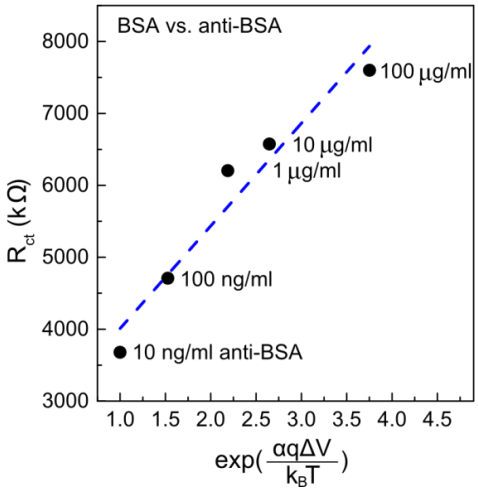

Figure 5-4 The relationship between the exponentiation of change of surface potential ($\exp(\alpha q \Delta V/k_B T)$) and the charge transfer resistance (R_{ct}), measured with potentiometric and impedemetric biosensors, respectively. The linear relationship fits well into Butler-Volmer equation and confirms that both potentiometric and impedance biosensors are charge sensitive.

Beyond the BSA/anti-BSA system, a complex serological system of bovine hemagglutinin-neuraminidase (HN) versus bovine parainfluenza virus protein type-3 (BPIV3) in blood samples was also tested.[392] The change of EIS spectra with respect to BPIV3 blood dilution is presented in a Nyquist plot (Figure 5-5a). Again, the relationship between signals from potentiometric and impedance sensors, ΔV and R_{ct}, respectively, agrees well with Butler-Volmer theory as shown in Figure 5-5b. The results further confirm the correlation between potentiometric and impedance sensors and suggest that the electrical sensor is a promising tool for the disease diagnostic applications.

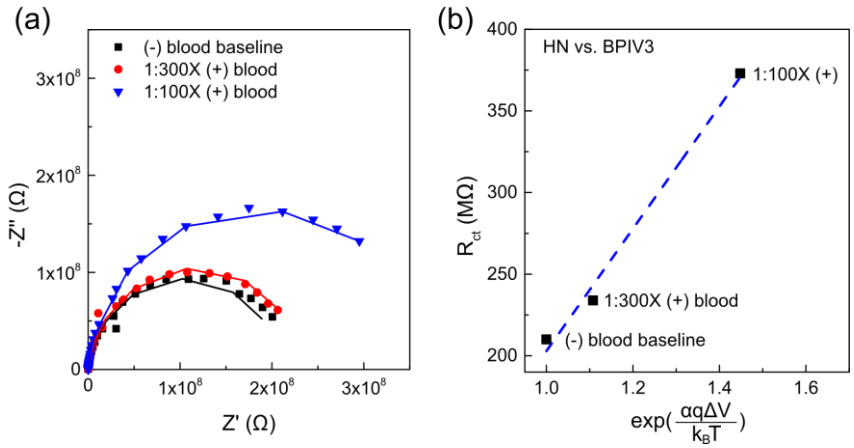

Figure 5-5 The sensing response of HN vs. BPIV3 using integrated biosensor system (a) The Nyquist plot of impedance spectra after the sensing surface exposed to different BPIV3 antibody dilutions. (b) The relationship between exponentiation of ΔV and the R_{ct}. A linear relationship is observed and agrees with the prediction of Butler-Volmer theory.

Impedance spectroscopy is a powerful tool to analyze the interfacial properties for corrosion, coatings, batteries, solar cells, etc. through complex analysis of the frequency responses.[393-397] However, for biosensor applications, the frequency response of surface capacitance is insensitive to the formation of the biomolecular layer on the sensing surface because: (1) the biolayer is semipermeable and is not a good capacitor; and, (2) the double layer capacitance dominates.[379-380, 387] As a result, it is difficult to resolve the mass-related properties of biomolecules alongside their charge information using impedance biosensors. The surface potential related R_{ct} remains the dominating contribution for the sensing signal. In this way, simple FET-based potentiometric biosensors provide sufficient information for practical biosensing applications.

To further illustrate their suitability for cost-effective and rapid point-of-care detection, large area Au extended gate sensor chips (0.1 cm^2) were also prepared without

the use of photolithography steps, instead using e-beam metal evaporation and patterning with shadow masks. The DC operation of the EGFET at steady state is not limited by the diffusion and, therefore, alleviates the constraints of using microscale electrodes. The BSA proteins were immobilized onto widely used thiol SAM through amine coupling. The sensor response of the large area Au chips is compared to the micro-strip sensors in Figure 5-6. In both cases, the BSA/anti-BSA sensitivities are around 17 - 18 mV/decade change of anti-BSA concentration. The results indicate no sensitivity advantage to the micro-strip design in EGFET biosensor at steady state.

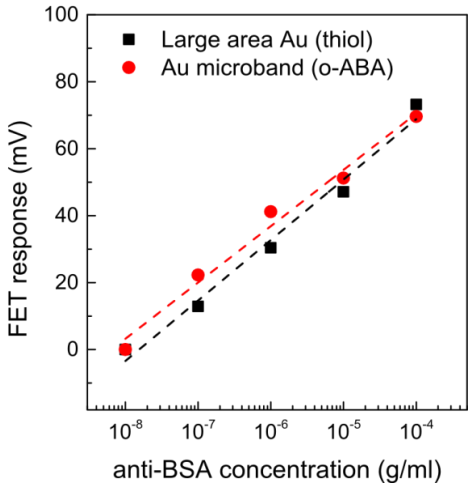

Figure 5-6 The comparison between EGFET biosensors using large area Au sensing surface (black square) and Au micro-strip (red circle). The BSA/anti-BSA sensitivities using either approach are comparable.

5.4 Conclusion

In conclusion, biosensing using an integrated two-sensor system that combines EGFET-based potentiometric biosensors and EIS-based impedimetric biosensors has been successfully demonstrated. The correlation between sensor signals – that is, surface potential and R_{ct} from FET and EIS, respectively – was linked using the Butler-Volmer equation. The results suggest that both FET and EIS biosensors are sensitive to the change of surface potential due to the attachment of charged biomolecules to the sensing surface, whereas the mass-dependent value of $C_{surface}$ does not vary significantly. Therefore, EGFET biosensors are inherently sufficient as electrical transducers for label-free biomolecule detection, while providing the added benefits of rapid response and low-cost scalability. For scenarios where detailed information about both charge and mass properties of biomolecular targets is required, the FET/EIS integrated sensing system that we have proposed may be deployed to great effect. Future studies involving complex biofluids and advanced modeling will help to identify how the mass-related properties extracted from EIS can be leveraged.

CHAPTER 6. SUMMARY AND FUTURE WORK

Two-dimensional transition metal dichalcogenides are promising candidates for next generation flexible electronics toward wearable sensing applications. The ability to control the electronic structure of TMD semiconductors is the cornerstone for the practical applications of these flexible semiconductor and electronics. Using solution-based charge transfer doping, the carrier concentration and the electronic band structure of the TMD semiconductors can be controlled through the electron transfer between semiconductors and the redox-active molecular dopants, and the device performance can be tailored and improved. In addition, this doping technique is versatile and controllable by the choice of molecular dopants, concentration of the dopant solution, and the doping treatment time. The redox-active molecular dopants used in this work provide stable doping effects due to the coupled chemical reactions and ion formations after the charge transfer. The doping effects were confirmed using both physical and electrical characterization. XPS results verified the shift of peaks to a higher binding energy side due to the decrease of Fermi level after n-doping. An opposite trend to lower binding energy was observed after p-doping, indicating the increase of Fermi level. UPS directly confirmed the increase of work function and decrease of the distance between Fermi level and the valence band maximum after p-doping. On the contrary, the observations of the decrease of work function and Fermi level moving away from valence band maximum provided a strong evidence of n-doping. The change of carrier concentration in the semiconductor channel can be monitored using the phonon-carrier interaction through the Raman spectroscopy as well. The doping effect can also be evaluated by the evolution of

threshold voltage from the transfer characteristics of the FET devices. An increase of threshold toward a more positive gate bias indicates p-doping, while decrease of threshold voltage toward negative gate bias side indicates n-doping. This doping method provides a simple, scalable yet effective tool to modify the electronic and optical properties of both n- and p-type TMDs. Furthermore, the work function of the TMD semiconductors can be tuned up/down to 1 eV after p- and n-doping, respectively, which is useful for the contact engineering for the TMD systems.

It is crucial to understanding the impact of external strain to 2D TMD-based flexible electronics. Using MoS_2 as a model system, flexible FETs based on large-area trilayer MoS_2 were fabricated using the direct device transfer technique by transferring the devices fabricated on the rigid substrate (e.g. SiO_2/Si wafer) to desired flexible substrate (e.g. PET). First, it was confirmed that the device transfer method did not degrade the device performance by comparing devices fabricated on growth SiO_2/Si wafer against the same set of devices transferred to a new SiO_2/Si wafer. Next, flexible MoS_2 FETs were characterized after bending and remained operational and stable after > 200 bending cycles. Furthermore, the band structure of the TMDs is sensitive to the external mechanical strain due to the lattice distortion. Using the strain-induced properties change in TMDs, the flexible MoS_2 FETs can be used as mechanical strain sensors. It was demonstrated that the transfer characteristics of the MoS_2 FETs is sensitive to the applied mechanical strain, where the threshold voltage decreases with increase of tensile strain. The origin of the strain sensitivity was explained by the decrease of the band gap with increase of strain, and was confirmed by the optical absorption spectroscopy. In addition, the strain sensitivity, and gauge factor, can be

controlled by the gate-biasing by adjusting the relative Fermi level position through gate modulation. This work provides initial steps for TMDs in flexible, transparent mechanical strain sensing applications.

Detection of chemical and biological species in the liquid using potentiometric sensors is important for numerous applications, for example, disease diagnosis, health screening, environmental monitoring, etc. However, it is still challenging to use large-area TMD-based FETs for the liquid phase sensing because of the weak top-gate coupling and large back-gate voltage needed to operate the devices. Alternatively, graphene ISFET was demonstrated as an example for 2D materials-based biochemical sensors. Using pH sensing as a test vehicle, we concluded that the pH sensitivity of graphene ISFET is dependent on the sensing surface. A bare graphene sensing surface provided limited pH sensitivity due to the lack of active hydroxyl groups, but an Al_2O_3 coated surface yielded a close-to-ideal Nernstian response (~59 mV/pH). Furthermore, the ISFET was compared to a simplified Au-coated EGFET. EGFET is highly similar to the ISFET and is able to detect the change of the surface potential on the sensing surface. However, the design of EGFET is simplified by separating the sensing surface from the transducer, which helps alleviate the reliability issues due to the exposure of electronic componenets to the liquid environment. In addition, EGFET provides an accessible integration to commercial FETs and any next generation electronics, including 2D TMD-based FETs. By comparing the ISFET and EGFET for both pH sensing and affinity biosensing, highly similar sensing results were observed using both sensing platforms. This finding suggested that the sensor sensitivity depends only on the sensing surfaces instead of transducers. It was also demonstrated that EGFET-based potentiometric

sensors is a promising tool for animal disease diagnosis. Using the immunological interaction between viral proteins on the sensing surface and their antibodies in the blood sample, the detection of bovine respiratory disease (BRD) was demonstrated using label-free EGFET biosensors. The dynamic range of the BRD sensing using EGFET is similar to that of SPR and commercial ELISA. However, the EGFET potentiometric biosensors are advantageous because of the much shorter response time, which is suitable for on-site point-of-care applications. This work concludes that the sensor sensitivity is dominated by the construction of sensing surfaces, and provides a simple yet efficient sensor technique using EGFET for chemical and biological sensing.

The advantage of EGFET is further supported by the direct comparison between EGFET-based potentiometric biosensors to electrochemical impedance spectroscopy (EIS)-based impedimetric biosensors. In order to directly compare two electrical sensing techniques, an integrated sensor system that combines EGFET and EIS was demonstrated. This integrated system enables the sequential sensing of the same biological layer on the shared sensing electrode and allows the direct comparison of sensing responses from both sensing techniques. Using both BSA/anti-BSA and HN/BPIV3 antibody-antigen systems as examples, similar responses and dynamic ranges of sensing were observed, suggesting a correlation between two electrical sensing techniques. EIS-based impedimetric sensor detects the change of impedance at the sensing surface while EGFET-based potentiometric sensor detects the change of surface potential at the same sensing surface. The surface impedance measured by EIS is dominated by the charge-transfer resistance, a result of the motion of ions reaching the sensing electrode, which is sensitive to the surface potential. Therefore, the two sensing

signals can be linked using electrochemical kinetics and Butler-Volmer equation. In other words, both EIS-based and EGFET-based sensors detect the same charge properties of biomolecules. This work suggests that EGFET-based potentiometric can resolve the charge information of biomolecules and is sufficient for practical biosensing applications.

6.1 Future work

This thesis provides the ground work for (1) using large-area 2D TMDs in electronics as well as flexible sensor applications; (2) design of chemical and biological potentiometric sensors for practical applications. However, more works are crucial in order to improve the materials quality of the 2D TMDs and the resulting device performance. In addition, the challenges of specificity, selectivity and reliability for biochemical sensors need to be improved to meet the requirements for commercialization.

6.1.1 Optimization of the growth of TMDs

The ability to synthesize large-area TMDs with good materials quality is one of the most important tasks for their practical applications. The challenges include increasing the grain size, decreasing the defect density, lowering the growth temperature, etc. The existence of the defects in the TMDs undermines the doping effects due to a possible entrapment of extra carriers in the defect states. For CMOS and rectification applications, it is desired to be able to convert n-type TMD to p-type, and vice versa, through chemical doping, which is difficult to achieve using highly defective materials

currently used in this work. In addition, high temperature used in sulfurization or selenization synthesis of TMDs hinders the flexible applications that usually involve heat sensitive plastic substrates. Direct fabrication of large-area high-quality TMDs on flexible substrates at low temperature is a crucial step to achieve the practical flexible TMD applications. Possible approaches to achieve large-area and low-temperature growth of TMDs include plasma-assisted synthesis, for example, plasma-enhanced chemical vapor deposition (PECVD), atomic layer deposition (ALD), etc. These methods can provide better control of the deposition rate, and improve the thin film formation.

6.1.2 Strain-engineering of large-area TMDs

Piezoresistive mechanical strain sensors have been demonstrated with large-area MoS_2-based transistors. However, the relationship between the strain response and the crystallinity and defects of the large-area TMD film should be further studied. While most of current studies focused on the application of tensile strain, the response of the TMDs to the compressive strain is equally important. In addition, the ability to control the two-dimensional crystal orientation of the TMD grains can improve the strain sensitivity. Furthermore, understanding the piezoelectric properties of large-area TMDs are also important for the self-powered electronics and power generation. Beyond piezoresistivity and piezoelectricity, external strain can be actively used to control the electrical and optical properties of the TMDs. Strain-engineering of TMDs can serve as a complementary method to the doping and improve the device performance.

6.1.3 Interface engineering of TMD-based devices

It has been demonstrated that MoS_2 can be doped from the top surface using redox-active molecular dopants. The advantage of replacing the growth substrate that might be damaged after a high temperature growth process was also demonstrated. Therefore, interface engineering between TMD active layer and the back-gate/top-gate dielectric layer is important to optimize the TMD-based devices. For bottom-gate configuration, self-assembly monolayers, for example, phosphonic acid, can be used to decorate the surface of gate dielectric layer. By providing polarized end functional groups pointing out of the surface, doping of TMD semiconductors due to the charge transfer between these functional groups and TMD films atop is expected. By a proper design of these end functional groups, they can also be used to fill the atom vacancies on TMD surfaces. By combining above-mentioned surface doping techniques, a "sandwich-like" doping can be achieved and the synergistic improvement is expected. For top-gate configuration, the interface between TMD semiconductors and the top dielectric plays an important role in FET modulation. Especially for potentiometric biosensing applications that require liquid gate operation, the efficiency of top-gate coupling is a determinant factor for the TMD-based biosensor. Further optimization of the top-gate operation through the reduction of interfacial defects, the deposition methods for dielectrics on top of TMDs and post-deposition treatments, can lower the operation gate bias and make it compatible with liquid gate operation.

6.1.4 Reliability and stability of potentiometric biosensors

Reliable and stable biosensing is the most important criteria toward the practical applications. Although reliability and stability of the biosensing is a result of multiple factors, the signal instability can be related to (1) the surface functionalization on the sensing surface and (2) the reference electrode. While covalent binding of biomolecules to the self-assembly monolayer (SAM) provides a strong immobilization, the stability of SAM is important and should be carefully investigated. The controllable formation, high packing density, orderliness, stability in the electrolyte, and formulated composition of the SAM on the sensing surface should be developed. SPR and detailed physical characterization including XPS, FTIR and STM may provide useful information on the SAM. Alternatively, different surface chemistry, for example, replacing thiol by carbene on Au sensing surface, can be used to improve the SAM stability. In addition, a stable SAM formation on the sensing surfaces that yield predictable initial surface potential across samples should be developed for the potentiometric sensors. It is also important to have a stable reference electrode with negligible drift, which can supply a stable voltage to the liquid gate. Strategies to reduce the drift, including surface coating and optimization of electrolyte junctions, should be developed.

6.1.5 Surface blocking in practical biosensors

Non-specific binding (NSB) remains one of the biggest challenges in practical biosensing, especially when complex blood samples are involved. NSB increases the background signals and undermine the sensor accuracy. NSB is a result mainly from (1) poor design of immunological pairs and (2) sensing surface imperfection. For example,

proteins tend to attach to the hydrophobic surfaces due to the maximization of the contact area to the hydrophobic polypeptide chains and the minimization of the free energy. From the aspect of sensor system design, a general strategy to reduce non-specific binding is to minimize the interaction between the sensing surface and the unwanted biomolecular species in the analyte solution. Surface blocking is a promising method to deactivate some of the surface sites and to reduce NSB. Surface blocking techniques include (1) chemical deactivation of the covalent binding sites; (2) saturation of NSB sites with inert proteins, for example, gelatin, collagen and serum proteins; (3) reduction of the number of reactive sites by mixed SAM, for example, mixture of hydroxylated SAM and polyethylene glycol terminated SAM. Further exploration of surface blocking is necessary in order to minimize the NSB yet maintain the sensor response.

Alternatively, differential sensing can provide a passive method to eliminate the NSB-related background signal by creating a reference channel with comparable biomolecular properties to the active channel. The design of the control channel should be optimized to accurately represent the NSB in the biosensing system.

REFERENCES

(1) Bardeen, J.; Brattain, W. H., Physical Principles Involved in Transistor Action*. *Bell Syst. Tech. J.* **1949,** *28*, 239-277.

(2) Bardeen, J.; Brattain, W. H., The Transistor, A Semi-Conductor Triode. *Phys. Rev.* **1948,** *74*, 230-231.

(3) Brock, D. C.; Moore, G. E., *Understanding Moore's Law: Four Decades of Innovation*. Chemical Heritage Foundation: Philadelphia, PA, 2006.

(4) Gray, P. V., The silicon-silicon dioxide system. *Proc. IEEE* **1969,** *57*, 1543-1551.

(5) Plummer, J. D.; Deal, M.; Griffin, P. D., *Silicon VLSI Technology: Fundamentals, Practice, and Modeling*. Prentice Hall: Upper Saddle River, NJ, 2000.

(6) Moore, G. E., Cramming More Components onto Integrated Circuits. *Electronics* **1965,** *38*, 114-117.

(7) Mollick, E., Establishing Moore's Law. *IEEE Annals of the History of Computing* **2006,** *28*, 62-75.

(8) Thompson, S. E.; Parthasarathy, S., Moore's law: the future of Si microelectronics. *Mater. Today* **2006,** *9*, 20-25.

(9) Mack, C. A., Fifty Years of Moore's Law. *IEEE Transactions on Semiconductor Manufacturing* **2011,** *24*, 202-207.

(10) Cavin, R. K.; Lugli, P.; Zhirnov, V. V., Science and Engineering Beyond Moore's Law. *Proc. IEEE* **2012,** *100*, 1720-1749.

(11) Salleo, A.; Wong, W. S., *Flexible Electronics: Materials and Applications*. Springer US: 2009; Vol. 11.

(12) Stoppa, M.; Chiolerio, A., Wearable Electronics and Smart Textiles: A Critical Review. *Sensors* **2014,** *14*, 11957.

(13) Das, R.; Ghaffarzadeh, K.; Chansin, G.; He, X. *Printed, Organic & Flexible Electronics Forecasts, Players & Opportunities 2017-2027*; IDTechEX: 2017.

(14) Nathan, A.; Ahnood, A.; Cole, M. T.; Lee, S.; Suzuki, Y.; Hiralal, P.; Bonaccorso, F.; Hasan, T.; Garcia-Gancedo, L.; Dyadyusha, A.; Haque, S.; Andrew, P.; Hofmann, S.; Moultrie, J.; Chu, D.; Flewitt, A. J.; Ferrari, A. C.; Kelly, M. J.; Robertson, J.;

Amaratunga, G. A. J.; Milne, W. I., Flexible Electronics: The Next Ubiquitous Platform. *Proc. IEEE* **2012,** *100*, 1486-1517.

(15) Rogers, J. A.; Someya, T.; Huang, Y., Materials and Mechanics for Stretchable Electronics. *Science* **2010,** *327*, 1603-1607.

(16) Kim, D.-H.; Ghaffari, R.; Lu, N.; Rogers, J. A., Flexible and Stretchable Electronics for Biointegrated Devices. *Annual Review of Biomedical Engineering* **2012,** *14*, 113-128.

(17) Sun, Y.; Rogers, J. A., Inorganic Semiconductors for Flexible Electronics. *Adv. Mater.* **2007,** *19*, 1897-1916.

(18) Lewis, J., Material challenge for flexible organic devices. *Mater. Today* **2006,** *9*, 38-45.

(19) Sekitani, T.; Someya, T., Stretchable, Large-area Organic Electronics. *Adv. Mater.* **2010,** *22*, 2228-2246.

(20) Forrest, S. R.; Thompson, M. E., Introduction: Organic Electronics and Optoelectronics. *Chem. Rev.* **2007,** *107*, 923-925.

(21) Kelley, T. W.; Baude, P. F.; Gerlach, C.; Ender, D. E.; Muyres, D.; Haase, M. A.; Vogel, D. E.; Theiss, S. D., Recent Progress in Organic Electronics: Materials, Devices, and Processes. *Chemistry of Materials* **2004,** *16*, 4413-4422.

(22) Whitmarsh, J., Flexible electronics: silicon meets paper and beyond. *Microelectronics International* **2005,** *22*, 16-19.

(23) Park, S.; Vosguerichian, M.; Bao, Z., A review of fabrication and applications of carbon nanotube film-based flexible electronics. *Nanoscale* **2013,** *5*, 1727-1752.

(24) Gao, L., Flexible Device Applications of 2D Semiconductors. *Small* **2017**, 1603994-n/a.

(25) Akinwande, D.; Petrone, N.; Hone, J., Two-dimensional flexible nanoelectronics. *Nat. Commun.* **2014,** *5*, 5678.

(26) Fiori, G.; Bonaccorso, F.; Iannaccone, G.; Palacios, T.; Neumaier, D.; Seabaugh, A.; Banerjee, S. K.; Colombo, L., Electronics based on two-dimensional materials. *Nat Nano* **2014,** *9*, 768-779.

(27) Wang, Q. H.; Kalantar-Zadeh, K.; Kis, A.; Coleman, J. N.; Strano, M. S., Electronics and Optoelectronics of Two-Dimensional Transition Metal Dichalcogenides. *Nat. Nanotechnol.* **2012,** *7*, 699-712.

(28) Jariwala, D.; Sangwan, V. K.; Lauhon, L. J.; Marks, T. J.; Hersam, M. C., Emerging Device Applications for Semiconducting Two-Dimensional Transition Metal Dichalcogenides. *ACS Nano* **2014,** *8*, 1102-1120.

(29) Chhowalla, M.; Shin, H. S.; Eda, G.; Li, L.-J.; Loh, K. P.; Zhang, H., The chemistry of two-dimensional layered transition metal dichalcogenide nanosheets. *Nat Chem* **2013,** *5*, 263-275.

(30) Duan, X.; Wang, C.; Pan, A.; Yu, R.; Duan, X., Two-dimensional transition metal dichalcogenides as atomically thin semiconductors: opportunities and challenges. *Chem. Soc. Rev.* **2015,** *44*, 8859-8876.

(31) Bhimanapati, G. R.; Lin, Z.; Meunier, V.; Jung, Y.; Cha, J.; Das, S.; Xiao, D.; Son, Y.; Strano, M. S.; Cooper, V. R.; Liang, L.; Louie, S. G.; Ringe, E.; Zhou, W.; Kim, S. S.; Naik, R. R.; Sumpter, B. G.; Terrones, H.; Xia, F.; Wang, Y.; Zhu, J.; Akinwande, D.; Alem, N.; Schuller, J. A.; Schaak, R. E.; Terrones, M.; Robinson, J. A., Recent Advances in Two-Dimensional Materials beyond Graphene. *ACS Nano* **2015,** *9*, 11509-11539.

(32) Novoselov, K. S.; Jiang, D.; Schedin, F.; Booth, T. J.; Khotkevich, V. V.; Morozov, S. V.; Geim, A. K., Two-dimensional atomic crystals. *Proceedings of the National Academy of Sciences of the United States of America* **2005,** *102*, 10451-10453.

(33) Geim, A. K.; Novoselov, K. S., The rise of graphene. *Nat Mater* **2007,** *6*, 183-191.

(34) Geim, A. K.; Grigorieva, I. V., Van der Waals heterostructures. *Nature* **2013,** *499*, 419-425.

(35) Pant, A.; Mutlu, Z.; Wickramaratne, D.; Cai, H.; Lake, R. K.; Ozkan, C.; Tongay, S., Fundamentals of lateral and vertical heterojunctions of atomically thin materials. *Nanoscale* **2016,** *8*, 3870-3887.

(36) Roy, T.; Tosun, M.; Kang, J. S.; Sachid, A. B.; Desai, S. B.; Hettick, M.; Hu, C. C.; Javey, A., Field-Effect Transistors Built from All Two-Dimensional Material Components. *ACS Nano* **2014,** *8*, 6259-6264.

(37) Li, D.; Kaner, R. B., Graphene-Based Materials. *Science* **2008,** *320*, 1170-1171.

(38) Neto, A. C.; Guinea, F.; Peres, N.; Novoselov, K. S.; Geim, A. K., The Electronic Properties of Graphene. *Rev. Mod. Phys.* **2009,** *81*, 109.

(39) Geim, A. K., Graphene: Status and Prospects. *Science* **2009,** *324*, 1530-1534.

(40) Novoselov, K. S.; Geim, A. K.; Morozov, S. V.; Jiang, D.; Katsnelson, M. I.; Grigorieva, I. V.; Dubonos, S. V.; Firsov, A. A., Two-dimensional gas of massless Dirac fermions in graphene. *Nature* **2005,** *438*, 197-200.

(41) Mayorov, A. S.; Gorbachev, R. V.; Morozov, S. V.; Britnell, L.; Jalil, R.; Ponomarenko, L. A.; Blake, P.; Novoselov, K. S.; Watanabe, K.; Taniguchi, T.; Geim, A. K., Micrometer-Scale Ballistic Transport in Encapsulated Graphene at Room Temperature. *Nano Lett.* **2011,** *11*, 2396-2399.

(42) Du, X.; Skachko, I.; Barker, A.; Andrei, E. Y., Approaching ballistic transport in suspended graphene. *Nat Nano* **2008,** *3*, 491-495.

(43) Lemme, M. C.; Echtermeyer, T. J.; Baus, M.; Kurz, H., A Graphene Field-Effect Device. *IEEE Electron Device Lett.* **2007,** *28*, 282-284.

(44) Bromley, R. A.; Murray, R. B.; Yoffe, A. D., The band structures of some transition metal dichalcogenides. III. Group VIA: trigonal prism materials. *Journal of Physics C: Solid State Physics* **1972,** *5*, 759.

(45) Yoffe, A., Layer compounds. *Annu. Rev. Mater. Sci.* **1973,** *3*, 147-170.

(46) Wilson, J. A.; Yoffe, A. D., The transition metal dichalcogenides discussion and interpretation of the observed optical, electrical and structural properties. *Adv. Phys.* **1969,** *18*, 193-335.

(47) Kang, J.; Tongay, S.; Zhou, J.; Li, J.; Wu, J., Band offsets and heterostructures of two-dimensional semiconductors. *Appl. Phys. Lett.* **2013,** *102*, 012111.

(48) Chhowalla, M.; Liu, Z.; Zhang, H., Two-dimensional transition metal dichalcogenide (TMD) nanosheets. *Chem. Soc. Rev.* **2015,** *44*, 2584-2586.

(49) Radisavljevic, B.; Radenovic, A.; Brivio, J.; Giacometti, V.; Kis, A., Single-Layer MoS_2 Transistors. *Nat. Nanotechnol.* **2011,** *6*, 147-150.

(50) Schmidt, H.; Giustiniano, F.; Eda, G., Electronic transport properties of transition metal dichalcogenide field-effect devices: surface and interface effects. *Chem. Soc. Rev.* **2015,** *44*, 7715-7736.

(51) Mak, K. F.; Lee, C.; Hone, J.; Shan, J.; Heinz, T. F., Atomically thin MoS_2: a new direct-gap semiconductor. *Phys. Rev. Lett.* **2010,** *105*, 136805.

(52) Splendiani, A.; Sun, L.; Zhang, Y.; Li, T.; Kim, J.; Chim, C.-Y.; Galli, G.; Wang, F., Emerging Photoluminescence in Monolayer MoS_2. *Nano Lett.* **2010,** *10*, 1271-1275.

(53) Zhang, X.; Qiao, X.-F.; Shi, W.; Wu, J.-B.; Jiang, D.-S.; Tan, P.-H., Phonon and Raman scattering of two-dimensional transition metal dichalcogenides from monolayer, multilayer to bulk material. *Chem. Soc. Rev.* **2015,** *44*, 2757-2785.

(54) Saito, R.; Tatsumi, Y.; Huang, S.; Ling, X.; Dresselhaus, M. S., Raman spectroscopy of transition metal dichalcogenides. *Journal of Physics: Condensed Matter* **2016,** *28*, 353002.

(55) Li, H.; Zhang, Q.; Yap, C. C. R.; Tay, B. K.; Edwin, T. H. T.; Olivier, A.; Baillargeat, D., From Bulk to Monolayer MoS_2: Evolution of Raman Scattering. *Adv. Funct. Mater.* **2012,** *22*, 1385-1390.

(56) Lee, C.; Yan, H.; Brus, L. E.; Heinz, T. F.; Hone, J.; Ryu, S., Anomalous Lattice Vibrations of Single- and Few-Layer MoS_2. *ACS Nano* **2010,** *4*, 2695-2700.

(57) Molina-Sánchez, A.; Wirtz, L., Phonons in single-layer and few-layer MoS_2 and WS_2. *Phys. Rev. B* **2011,** *84*, 155413.

(58) Zhao, W.; Ghorannevis, Z.; Amara, K. K.; Pang, J. R.; Toh, M.; Zhang, X.; Kloc, C.; Tan, P. H.; Eda, G., Lattice dynamics in mono- and few-layer sheets of WS_2 and WSe_2. *Nanoscale* **2013,** *5*, 9677-9683.

(59) Sahin, H.; Tongay, S.; Horzum, S.; Fan, W.; Zhou, J.; Li, J.; Wu, J.; Peeters, F. M., Anomalous Raman spectra and thickness-dependent electronic properties of WSe_2. *Phys. Rev. B* **2013,** *87*, 165409.

(60) Lin, J. D.; Han, C.; Wang, F.; Wang, R.; Xiang, D.; Qin, S.; Zhang, X.-A.; Wang, L.; Zhang, H.; Wee, A. T. S., Electron-Doping-Enhanced Trion Formation in Monolayer Molybdenum Disulfide Functionalized with Cesium Carbonate. *ACS Nano* **2014,** *8*, 5323-5329.

(61) Chakraborty, B.; Bera, A.; Muthu, D. V. S.; Bhowmick, S.; Waghmare, U. V.; Sood, A. K., Symmetry-dependent phonon renormalization in monolayer MoS_2 transistor. *Phys. Rev. B* **2012,** *85*, 161403.

(62) Chen, C.-H.; Wu, C.-L.; Pu, J.; Chiu, M.-H.; Kumar, P.; Takenobu, T.; Li, L.-J., Hole mobility enhancement and p -doping in monolayer WSe_2 by gold decoration. *2D Mater.* **2014,** *1*, 034001.

(63) Kaasbjerg, K.; Thygesen, K. S.; Jacobsen, K. W., Phonon-limited mobility in n-type single-layer MoS_2 from first principles. *Phys. Rev. B* **2012,** *85*, 115317.

(64) Li, X.; Mullen, J. T.; Jin, Z.; Borysenko, K. M.; Buongiorno Nardelli, M.; Kim, K. W., Intrinsic electrical transport properties of monolayer silicene and MoS_2 from first principles. *Phys. Rev. B* **2013,** *87*, 115418.

(65) Fang, H.; Chuang, S.; Chang, T. C.; Takei, K.; Takahashi, T.; Javey, A., High-Performance Single Layered WSe_2 p-FETs with Chemically Doped Contacts. *Nano Lett.* **2012,** *12*, 3788-3792.

(66) Allain, A.; Kis, A., Electron and Hole Mobilities in Single-Layer WSe2. *ACS Nano* **2014,** *8*, 7180-7185.

(67) Liu, L.; Kumar, S. B.; Ouyang, Y.; Guo, J., Performance Limits of Monolayer Transition Metal Dichalcogenide Transistors. *IEEE Trans. Electron Devices* **2011,** *58*, 3042-3047.

(68) Yoon, Y.; Ganapathi, K.; Salahuddin, S., How Good Can Monolayer MoS_2 Transistors Be? *Nano Lett.* **2011,** *11*, 3768-3773.

(69) Liu, H.; Neal, A. T.; Ye, P. D., Channel Length Scaling of MoS_2 MOSFETs. *ACS Nano* **2012,** *6*, 8563-8569.

(70) Ando, T.; Fowler, A. B.; Stern, F., Electronic properties of two-dimensional systems. *Rev. Mod. Phys.* **1982,** *54*, 437.

(71) Rücker, H.; Molinari, E.; Lugli, P., Electron-phonon interaction in quasi-two-dimensional systems. *Phys. Rev. B* **1991,** *44*, 3463-3466.

(72) Ridley, B. K., The electron-phonon interaction in quasi-two-dimensional semiconductor quantum-well structures. *Journal of Physics C: Solid State Physics* **1982,** *15*, 5899.

(73) Ming-Wei, L.; Ivan, I. K.; Jason, F.; Xufan, L.; Alexander, A. P.; Christopher, M. R.; David, B. G.; Kai, X., Thickness-dependent charge transport in few-layer MoS 2 field-effect transistors. *Nanotechnology* **2016,** *27*, 165203.

(74) Jariwala, D.; Sangwan, V. K.; Late, D. J.; Johns, J. E.; Dravid, V. P.; Marks, T. J.; Lauhon, L. J.; Hersam, M. C., Band-like transport in high mobility unencapsulated single-layer MoS2 transistors. *Appl. Phys. Lett.* **2013,** *102*, 173107.

(75) Sangwan, V. K.; Arnold, H. N.; Jariwala, D.; Marks, T. J.; Lauhon, L. J.; Hersam, M. C., Low-Frequency Electronic Noise in Single-Layer MoS2 Transistors. *Nano Lett.* **2013,** *13*, 4351-4355.

(76) He, Q.; Zeng, Z.; Yin, Z.; Li, H.; Wu, S.; Huang, X.; Zhang, H., Fabrication of Flexible MoS_2 Thin-Film Transistor Arrays for Practical Gas-Sensing Applications. *Small* **2012,** *8*, 2994-2999.

(77) Perkins, F. K.; Friedman, A. L.; Cobas, E.; Campbell, P. M.; Jernigan, G. G.; Jonker, B. T., Chemical Vapor Sensing with Monolayer MoS_2. *Nano Lett.* **2013,** *13*, 668-673.

(78) Ghatak, S.; Pal, A. N.; Ghosh, A., Nature of electronic states in atomically thin MoS_2 field-effect transistors. *ACS Nano* **2011,** *5*, 7707-7712.

(79) Das, S.; Chen, H.-Y.; Penumatcha, A. V.; Appenzeller, J., High Performance Multilayer MoS_2 Transistors with Scandium Contacts. *Nano Lett.* **2013,** *13*, 100-105.

(80) Zhang, W.; Chiu, M.-H.; Chen, C.-H.; Chen, W.; Li, L.-J.; Wee, A. T. S., Role of Metal Contacts in High-Performance Phototransistors Based on WSe_2 Monolayers. *ACS Nano* **2014,** *8*, 8653-8661.

(81) Liu, W.; Kang, J.; Sarkar, D.; Khatami, Y.; Jena, D.; Banerjee, K., Role of Metal Contacts in Designing High-Performance Monolayer n-Type WSe2 Field Effect Transistors. *Nano Lett.* **2013,** *13*, 1983-1990.

(82) Dankert, A.; Langouche, L.; Mutta, V. K.; Dash, S. P., High Performance Molybdenum Disulfide Field Effect Transistors with Spin Tunnel Contacts. *ACS Nano* **2014,** *8*, 476.

(83) Chuang, S.; Battaglia, C.; Azcatl, A.; McDonnell, S.; Kang, J. S.; Yin, X.; Tosun, M.; Kapadia, R.; Fang, H.; Wallace, R. M.; Javey, A., MoS_2 P-type Transistors and Diodes Enabled by High Work Function MoO_x Contacts. *Nano Lett.* **2014,** *14*, 1337-1342.

(84) Feynman, R. P., There's plenty of room at the bottom. *Engineering and science* **1960,** *23*, 22-36.

(85) Joensen, P.; Frindt, R. F.; Morrison, S. R., Single-layer MoS2. *Mater. Res. Bull.* **1986,** *21*, 457-461.

(86) Frindt, R. F., Single Crystals of MoS_2 Several Molecular Layers Thick. *J. Appl. Phys.* **1966,** *37*, 1928-1929.

(87) Novoselov, K. S.; Geim, A. K.; Morozov, S. V.; Jiang, D.; Zhang, Y.; Dubonos, S. V.; Grigorieva, I. V.; Firsov, A. A., Electric Field Effect in Atomically Thin Carbon Films. *Science* **2004,** *306*, 666-669.

(88) Benameur, M. M.; Radisavljevic, B.; Héron, J. S.; Sahoo, S.; Berger, H.; Kis, A., Visibility of dichalcogenide nanolayers. *Nanotechnology* **2011,** *22*, 125706.

(89) Li, H.; Yin, Z.; He, Q.; Li, H.; Huang, X.; Lu, G.; Fam, D. W. H.; Tok, A. I. Y.; Zhang, Q.; Zhang, H., Fabrication of Single- and Multilayer MoS_2 Film-Based Field-Effect Transistors for Sensing NO at Room Temperature. *Small* **2012,** *8*, 63-67.

(90) Coleman, J. N.; Lotya, M.; O'Neill, A.; Bergin, S. D.; King, P. J.; Khan, U.; Young, K.; Gaucher, A.; De, S.; Smith, R. J.; Shvets, I. V.; Arora, S. K.; Stanton, G.; Kim, H.-Y.; Lee, K.; Kim, G. T.; Duesberg, G. S.; Hallam, T.; Boland, J. J.; Wang, J. J.; Donegan, J. F.; Grunlan, J. C.; Moriarty, G.; Shmeliov, A.; Nicholls, R. J.; Perkins, J. M.; Grieveson, E. M.; Theuwissen, K.; McComb, D. W.; Nellist, P. D.; Nicolosi, V., Two-Dimensional Nanosheets Produced by Liquid Exfoliation of Layered Materials. *Science* **2011,** *331*, 568-571.

(91) Nicolosi, V.; Chhowalla, M.; Kanatzidis, M. G.; Strano, M. S.; Coleman, J. N., Liquid Exfoliation of Layered Materials. *Science* **2013,** *340*.

(92) Smith, R. J.; King, P. J.; Lotya, M.; Wirtz, C.; Khan, U.; De, S.; O'Neill, A.; Duesberg, G. S.; Grunlan, J. C.; Moriarty, G.; Chen, J.; Wang, J.; Minett, A. I.; Nicolosi, V.; Coleman, J. N., Large-Scale Exfoliation of Inorganic Layered Compounds in Aqueous Surfactant Solutions. *Adv. Mater.* **2011,** *23*, 3944-3948.

(93) Hernandez, Y.; Nicolosi, V.; Lotya, M.; Blighe, F. M.; Sun, Z.; De, S.; McGovern, I. T.; Holland, B.; Byrne, M.; Gun'Ko, Y. K.; Boland, J. J.; Niraj, P.; Duesberg, G.; Krishnamurthy, S.; Goodhue, R.; Hutchison, J.; Scardaci, V.; Ferrari, A. C.; Coleman, J. N., High-yield production of graphene by liquid-phase exfoliation of graphite. *Nat Nano* **2008,** *3*, 563-568.

(94) Lv, R.; Robinson, J. A.; Schaak, R. E.; Sun, D.; Sun, Y.; Mallouk, T. E.; Terrones, M., Transition Metal Dichalcogenides and Beyond: Synthesis, Properties, and Applications of Single- and Few-Layer Nanosheets. *Acc. Chem. Res.* **2015,** *48*, 56-64.

(95) Dines, M. B., Lithium intercalation via n-Butyllithium of the layered transition metal dichalcogenides. *Mater. Res. Bull.* **1975,** *10*, 287-291.

(96) Whittingham, M. S.; Gamble, F. R., The lithium intercalates of the transition metal dichalcogenides. *Mater. Res. Bull.* **1975,** *10*, 363-371.

(97) Zeng, Z.; Sun, T.; Zhu, J.; Huang, X.; Yin, Z.; Lu, G.; Fan, Z.; Yan, Q.; Hng, H. H.; Zhang, H., An Effective Method for the Fabrication of Few-Layer-Thick Inorganic Nanosheets. *Angew. Chem. Int. Ed.* **2012,** *51*, 9052-9056.

(98) Eda, G.; Yamaguchi, H.; Voiry, D.; Fujita, T.; Chen, M.; Chhowalla, M., Photoluminescence from Chemically Exfoliated MoS2. *Nano Lett.* **2011,** *11*, 5111-5116.

(99) Bosi, M., Growth and synthesis of mono and few-layers transition metal dichalcogenides by vapour techniques: a review. *RSC Advances* **2015,** *5*, 75500-75518.

(100) Li, X.; Cai, W.; An, J.; Kim, S.; Nah, J.; Yang, D.; Piner, R.; Velamakanni, A.; Jung, I.; Tutuc, E.; Banerjee, S. K.; Colombo, L.; Ruoff, R. S., Large-Area Synthesis of High-Quality and Uniform Graphene Films on Copper Foils. *Science* **2009,** *324*, 1312-1314.

(101) Das, S.; Robinson, J. A.; Dubey, M.; Terrones, H.; Terrones, M., Beyond Graphene: Progress in Novel Two-Dimensional Materials and van der Waals Solids. *Annual Review of Materials Research* **2015,** *45*, 1-27.

(102) Meyer, B., Elemental sulfur. *Chem. Rev.* **1976,** *76*, 367-388.

(103) Lee, Y.-H.; Zhang, X.-Q.; Zhang, W.; Chang, M.-T.; Lin, C.-T.; Chang, K.-D.; Yu, Y.-C.; Wang, J. T.-W.; Chang, C.-S.; Li, L.-J.; Lin, T.-W., Synthesis of Large-Area MoS_2 Atomic Layers with Chemical Vapor Deposition. *Adv. Mater.* **2012,** *24*, 2320-2325.

(104) Najmaei, S.; Liu, Z.; Zhou, W.; Zou, X.; Shi, G.; Lei, S.; Yakobson, B. I.; Idrobo, J.-C.; Ajayan, P. M.; Lou, J., Vapour Phase Growth and Grain Boundary Structure of Molybdenum Disulphide Atomic Layers. *Nat. Mater.* **2013,** *12*, 754-759.

(105) van der Zande, A. M.; Huang, P. Y.; Chenet, D. A.; Berkelbach, T. C.; You, Y.; Lee, G.-H.; Heinz, T. F.; Reichman, D. R.; Muller, D. A.; Hone, J. C., Grains and Grain

Boundaries in Highly Crystalline Monolayer Molybdenum Disulphide. *Nat. Mater.* **2013,** *12*, 554-561.

(106) Zhu, W.; Low, T.; Lee, Y.-H.; Wang, H.; Farmer, D. B.; Kong, J.; Xia, F.; Avouris, P., Electronic Transport and Device Prospects of Monolayer Molybdenum Disulphide Grown by Chemical Vapour Deposition. *Nat. Commun.* **2014,** *5*, 3087.

(107) Lee, Y.-H.; Zhang, X.-Q.; Zhang, W.; Chang, M.-T.; Lin, C.-T.; Chang, K.-D.; Yu, Y.-C.; Wang, J. T.-W.; Chang, C.-S.; Li, L.-J.; Lin, T.-W., Synthesis of Large-Area MoS_2 Atomic Layers with Chemical Vapor Deposition. *Adv. Mater.* **2012,** *24*, 2320-2325.

(108) Zhang, Y.; Zhang, Y.; Ji, Q.; Ju, J.; Yuan, H.; Shi, J.; Gao, T.; Ma, D.; Liu, M.; Chen, Y.; Song, X.; Hwang, H. Y.; Cui, Y.; Liu, Z., Controlled Growth of High-Quality Monolayer WS_2 Layers on Sapphire and Imaging Its Grain Boundary. *ACS Nano* **2013,** *7*, 8963-8971.

(109) Feldman, Y.; Wasserman, E.; Srolovitz, D. J.; Tenne, R., High-Rate, Gas-Phase Growth of MoS_2 Nested Inorganic Fullerenes and Nanotubes. *Science* **1995,** *267*, 222-225.

(110) Huang, J.-K.; Pu, J.; Hsu, C.-L.; Chiu, M.-H.; Juang, Z.-Y.; Chang, Y.-H.; Chang, W.-H.; Iwasa, Y.; Takenobu, T.; Li, L.-J., Large-Area Synthesis of Highly Crystalline WSe_2 Monolayers and Device Applications. *ACS Nano* **2014,** *8*, 923-930.

(111) Yu, Y.; Li, C.; Liu, Y.; Su, L.; Zhang, Y.; Cao, L., Controlled Scalable Synthesis of Uniform, High-Quality Monolayer and Few-layer MoS2 Films. *Sci. Rep.* **2013,** *3*.

(112) Lee, Y.-H.; Yu, L.; Wang, H.; Fang, W.; Ling, X.; Shi, Y.; Lin, C.-T.; Huang, J.-K.; Chang, M.-T.; Chang, C.-S.; Dresselhaus, M.; Palacios, T.; Li, L.-J.; Kong, J., Synthesis and Transfer of Single-Layer Transition Metal Disulfides on Diverse Surfaces. *Nano Lett.* **2013,** *13*, 1852-1857.

(113) Ling, X.; Lee, Y.-H.; Lin, Y.; Fang, W.; Yu, L.; Dresselhaus, M. S.; Kong, J., Role of the Seeding Promoter in MoS_2 Growth by Chemical Vapor Deposition. *Nano Lett.* **2014,** *14*, 464-472.

(114) Kranthi Kumar, V.; Dhar, S.; Choudhury, T. H.; Shivashankar, S. A.; Raghavan, S., A predictive approach to CVD of crystalline layers of TMDs: the case of MoS_2. *Nanoscale* **2015,** *7*, 7802-7810.

(115) Eichfeld, S. M.; Hossain, L.; Lin, Y.-C.; Piasecki, A. F.; Kupp, B.; Birdwell, A. G.; Burke, R. A.; Lu, N.; Peng, X.; Li, J.; Azcatl, A.; McDonnell, S.; Wallace, R. M.; Kim, M. J.; Mayer, T. S.; Redwing, J. M.; Robinson, J. A., Highly Scalable, Atomically Thin WSe_2 Grown via Metal–Organic Chemical Vapor Deposition. *ACS Nano* **2015,** *9*, 2080-2087.

(116) Kang, K.; Xie, S.; Huang, L.; Han, Y.; Huang, P. Y.; Mak, K. F.; Kim, C.-J.; Muller, D.; Park, J., High-mobility three-atom-thick semiconducting films with wafer-scale homogeneity. *Nature* **2015,** *520*, 656-660.

(117) Robert, B.; Prasanna, P.; Raj, S.; Douglas, J. T.; Paul, S.; David, E., Atomic layer deposition of MoS_2 thin films. *Materials Research Express* **2015,** *2*, 035006.

(118) Tan, L. K.; Liu, B.; Teng, J. H.; Guo, S.; Low, H. Y.; Loh, K. P., Atomic layer deposition of a MoS_2 film. *Nanoscale* **2014,** *6*, 10584-10588.

(119) Song, J.-G.; Park, J.; Lee, W.; Choi, T.; Jung, H.; Lee, C. W.; Hwang, S.-H.; Myoung, J. M.; Jung, J.-H.; Kim, S.-H.; Lansalot-Matras, C.; Kim, H., Layer-Controlled, Wafer-Scale, and Conformal Synthesis of Tungsten Disulfide Nanosheets Using Atomic Layer Deposition. *ACS Nano* **2013,** *7*, 11333-11340.

(120) Gatensby, R.; McEvoy, N.; Lee, K.; Hallam, T.; Berner, N. C.; Rezvani, E.; Winters, S.; O'Brien, M.; Duesberg, G. S., Controlled synthesis of transition metal dichalcogenide thin films for electronic applications. *Appl. Surf. Sci.* **2014,** *297*, 139-146.

(121) Lee, Y.; Lee, J.; Bark, H.; Oh, I.-K.; Ryu, G. H.; Lee, Z.; Kim, H.; Cho, J. H.; Ahn, J.-H.; Lee, C., Synthesis of wafer-scale uniform molybdenum disulfide films with control over the layer number using a gas phase sulfur precursor. *Nanoscale* **2014,** *6*, 2821-2826.

(122) Jung, Y.; Shen, J.; Sun, Y.; Cha, J. J., Chemically Synthesized Heterostructures of Two-Dimensional Molybdenum/Tungsten-Based Dichalcogenides with Vertically Aligned Layers. *ACS Nano* **2014,** *8*, 9550-9557.

(123) Campbell, P. M.; Tarasov, A.; Joiner, C. A.; Tsai, M.-Y.; Pavlidis, G.; Graham, S.; Ready, W. J.; Vogel, E. M., Field-effect transistors based on wafer-scale, highly uniform few-layer p-type WSe_2. *Nanoscale* **2016,** *8*, 2268-2276.

(124) Tarasov, A.; Campbell, P. M.; Tsai, M.-Y.; Hesabi, Z. R.; Feirer, J.; Graham, S.; Ready, W. J.; Vogel, E. M., Highly Uniform Trilayer Molybdenum Disulfide for Wafer-Scale Device Fabrication. *Adv. Funct. Mater.* **2014,** *24*, 6389-6400.

(125) Ma, L.; Nath, D. N.; II, E. W. L.; Lee, C. H.; Yu, M.; Arehart, A.; Rajan, S.; Wu, Y., Epitaxial growth of large area single-crystalline few-layer MoS_2 with high space charge mobility of 192 cm2 V^{-1} s^{-1}. *Appl. Phys. Lett.* **2014,** *105*, 072105.

(126) Zhan, Y.; Liu, Z.; Najmaei, S.; Ajayan, P. M.; Lou, J., Large-Area Vapor-Phase Growth and Characterization of MoS_2 Atomic Layers on a SiO_2 Substrate. *Small* **2012,** *8*, 966-971.

(127) Laskar, M. R.; Ma, L.; Kannappan, S.; Park, P. S.; Krishnamoorthy, S.; Nath, D. N.; Lu, W.; Wu, Y.; Rajan, S., Large Area Single Crystal (0001) Oriented MoS$_2$. *Appl. Phys. Lett.* **2013,** *102*, 252108.

(128) Lin, Y.-C.; Zhang, W.; Huang, J.-K.; Liu, K.-K.; Lee, Y.-H.; Liang, C.-T.; Chu, C.-W.; Li, L.-J., Wafer-Scale MoS$_2$ Thin Layers Prepared by MoO$_3$ Sulfurization. *Nanoscale* **2012,** *4*, 6637-6641.

(129) Kong, D.; Wang, H.; Cha, J. J.; Pasta, M.; Koski, K. J.; Yao, J.; Cui, Y., Synthesis of MoS_2 and $MoSe_2$ Films with Vertically Aligned Layers. *Nano Lett.* **2013,** *13*, 1341-1347.

(130) Jung, Y.; Shen, J.; Liu, Y.; Woods, J. M.; Sun, Y.; Cha, J. J., Metal Seed Layer Thickness-Induced Transition From Vertical to Horizontal Growth of MoS_2 and WS_2. *Nano Lett.* **2014,** *14*, 6842-6849.

(131) Duan, X.; Wang, C.; Fan, Z.; Hao, G.; Kou, L.; Halim, U.; Li, H.; Wu, X.; Wang, Y.; Jiang, J.; Pan, A.; Huang, Y.; Yu, R.; Duan, X., Synthesis of $WS_{2x}Se_{2-2x}$ Alloy Nanosheets with Composition-Tunable Electronic Properties. *Nano Lett.* **2016,** *16*, 264-269.

(132) Li, H.; Duan, X.; Wu, X.; Zhuang, X.; Zhou, H.; Zhang, Q.; Zhu, X.; Hu, W.; Ren, P.; Guo, P.; Ma, L.; Fan, X.; Wang, X.; Xu, J.; Pan, A.; Duan, X., Growth of Alloy $MoS_{2x}Se_{2(1-x)}$ Nanosheets with Fully Tunable Chemical Compositions and Optical Properties. *J. Am. Chem. Soc.* **2014,** *136*, 3756-3759.

(133) Gong, Y.; Liu, Z.; Lupini, A. R.; Shi, G.; Lin, J.; Najmaei, S.; Lin, Z.; Elías, A. L.; Berkdemir, A.; You, G.; Terrones, H.; Terrones, M.; Vajtai, R.; Pantelides, S. T.; Pennycook, S. J.; Lou, J.; Zhou, W.; Ajayan, P. M., Band Gap Engineering and Layer-by-Layer Mapping of Selenium-Doped Molybdenum Disulfide. *Nano Lett.* **2014,** *14*, 442-449.

(134) Laskar, M. R.; Nath, D. N.; Ma, L.; II, E. W. L.; Lee, C. H.; Kent, T.; Yang, Z.; Mishra, R.; Roldan, M. A.; Idrobo, J.-C.; Pantelides, S. T.; Pennycook, S. J.; Myers, R. C.; Wu, Y.; Rajan, S., p-type doping of MoS_2 thin films using Nb. *Appl. Phys. Lett.* **2014,** *104*, 092104.

(135) Lin, Y.-C.; Dumcenco, D. O.; Huang, Y.-S.; Suenaga, K., Atomic mechanism of the semiconducting-to-metallic phase transition in single-layered MoS_2. *Nat Nano* **2014,** *9*, 391-396.

(136) Sze, S. M.; Ng, K. K., *Physics of semiconductor devices*. John wiley & sons: 2006.

(137) Zhao, Y.; Xu, K.; Pan, F.; Zhou, C.; Zhou, F.; Chai, Y., Doping, Contact and Interface Engineering of Two-Dimensional Layered Transition Metal Dichalcogenides Transistors. *Adv. Funct. Mater.* **2017,** *27*, 1603484-n/a.

(138) Xing, L.; Jiao, L.-Y., Recent Advances in the Chemical Doping of Two-Dimensional Molybdenum Disulfide. *Acta Phys. -Chim. Sin.* **2016,** *32*, 2133-2145.

(139) Willke, P.; Amani, J. A.; Sinterhauf, A.; Thakur, S.; Kotzott, T.; Druga, T.; Weikert, S.; Maiti, K.; Hofsäss, H.; Wenderoth, M., Doping of Graphene by Low-Energy Ion Beam Implantation: Structural, Electronic, and Transport Properties. *Nano Lett.* **2015,** *15*, 5110-5115.

(140) Chen, M.; Nam, H.; Wi, S.; Ji, L.; Ren, X.; Bian, L.; Lu, S.; Liang, X., Stable few-layer MoS2 rectifying diodes formed by plasma-assisted doping. *Appl. Phys. Lett.* **2013,** *103*, 142110.

(141) Nipane, A.; Karmakar, D.; Kaushik, N.; Karande, S.; Lodha, S., Few-Layer MoS_2 p-Type Devices Enabled by Selective Doping Using Low Energy Phosphorus Implantation. *ACS Nano* **2016,** *10*, 2128-2137.

(142) Tosun, M.; Chan, L.; Amani, M.; Roy, T.; Ahn, G. H.; Taheri, P.; Carraro, C.; Ager, J. W.; Maboudian, R.; Javey, A., Air-Stable n-Doping of WSe_2 by Anion Vacancy Formation with Mild Plasma Treatment. *ACS Nano* **2016,** *10*, 6853-6860.

(143) Choudhury, D.; Das, B.; Sarma, D. D.; Rao, C. N. R., XPS evidence for molecular charge-transfer doping of graphene. *Chem. Phys. Lett.* **2010,** *497*, 66-69.

(144) Rietwyk, K. J.; Smets, Y.; Bashouti, M.; Christiansen, S. H.; Schenk, A.; Tadich, A.; Edmonds, M. T.; Ristein, J.; Ley, L.; Pakes, C. I., Charge Transfer Doping of Silicon. *Phys. Rev. Lett.* **2014,** *112*, 155502.

(145) Ristein, J., Surface Transfer Doping of Semiconductors. *Science* **2006,** *313*, 1057-1058.

(146) Strobel, P.; Riedel, M.; Ristein, J.; Ley, L., Surface transfer doping of diamond. *Nature* **2004,** *430*, 439-441.

(147) Ovcharenko, R.; Yu, D.; Voloshina, E., Adsorption of NO 2 on WSe 2 : DFT and photoelectron spectroscopy studies. *Journal of Physics: Condensed Matter* **2016,** *28*, 364003.

(148) Tongay, S.; Zhou, J.; Ataca, C.; Liu, J.; Kang, J. S.; Matthews, T. S.; You, L.; Li, J.; Grossman, J. C.; Wu, J., Broad-Range Modulation of Light Emission in Two-Dimensional Semiconductors by Molecular Physisorption Gating. *Nano Lett.* **2013,** *13*, 2831-2836.

(149) Huo, N.; Yang, S.; Wei, Z.; Li, S.-S.; Xia, J.-B.; Li, J., Photoresponsive and Gas Sensing Field-Effect Transistors based on Multilayer WS2 Nanoflakes. *Sci. Rep.* **2014,** *4*, 5209.

(150) Cho, B.; Hahm, M. G.; Choi, M.; Yoon, J.; Kim, A. R.; Lee, Y.-J.; Park, S.-G.; Kwon, J.-D.; Kim, C. S.; Song, M.; Jeong, Y.; Nam, K.-S.; Lee, S.; Yoo, T. J.; Kang, C. G.; Lee, B. H.; Ko, H. C.; Ajayan, P. M.; Kim, D.-H., Charge-transfer-based Gas Sensing Using Atomic-layer MoS2. *Sci. Rep.* **2015,** *5*, 8052.

(151) Zhao, P.; Kiriya, D.; Azcatl, A.; Zhang, C.; Tosun, M.; Liu, Y.-S.; Hettick, M.; Kang, J. S.; McDonnell, S.; Kc, S.; Guo, J.; Cho, K.; Wallace, R. M.; Javey, A., Air Stable p-Doping of WSe2 by Covalent Functionalization. *ACS Nano* **2014,** *8*, 10808-10814.

(152) Kim, E.; Ko, C.; Kim, K.; Chen, Y.; Suh, J.; Ryu, S.-G.; Wu, K.; Meng, X.; Suslu, A.; Tongay, S.; Wu, J.; Grigoropoulos, C. P., Site Selective Doping of Ultrathin Metal Dichalcogenides by Laser-Assisted Reaction. *Adv. Mater.* **2016,** *28*, 341-346.

(153) Fang, H.; Tosun, M.; Seol, G.; Chang, T. C.; Takei, K.; Guo, J.; Javey, A., Degenerate n-doping of few-layer transition metal dichalcogenides by potassium. *Nano Lett.* **2013,** *13*, 1991-1995.

(154) Lin, J. D.; Han, C.; Wang, F.; Wang, R.; Xiang, D.; Qin, S.; Zhang, X.-A.; Wang, L.; Zhang, H.; Wee, A. T. S.; Chen, W., Electron-Doping-Enhanced Trion Formation in Monolayer Molybdenum Disulfide Functionalized with Cesium Carbonate. *ACS Nano* **2014,** *8*, 5323-5329.

(155) Khalil, H. M. W.; Khan, M. F.; Eom, J.; Noh, H., Highly Stable and Tunable Chemical Doping of Multilayer WS_2 Field Effect Transistor: Reduction in Contact Resistance. *ACS Appl. Mater. Interfaces* **2015,** *7*, 23589-23596.

(156) Sarkar, D.; Xie, X.; Kang, J.; Zhang, H.; Liu, W.; Navarrete, J.; Moskovits, M.; Banerjee, K., Functionalization of Transition Metal Dichalcogenides with Metallic Nanoparticles: Implications for Doping and Gas-Sensing. *Nano Lett.* **2015,** *15*, 2852-2862.

(157) Choi, M. S.; Qu, D.; Lee, D.; Liu, X.; Watanabe, K.; Taniguchi, T.; Yoo, W. J., Lateral MoS_2 p–n Junction Formed by Chemical Doping for Use in High-Performance Optoelectronics. *ACS Nano* **2014,** *8*, 9332-9340.

(158) Shi, Y.; Huang, J.-K.; Jin, L.; Hsu, Y.-T.; Yu, S. F.; Li, L.-J.; Yang, H. Y., Selective Decoration of Au Nanoparticles on Monolayer MoS_2 Single Crystals. *Sci. Rep.* **2013,** *3*, 1839.

(159) Yamamoto, M.; Nakaharai, S.; Ueno, K.; Tsukagoshi, K., Self-Limiting Oxides on WSe_2 as Controlled Surface Acceptors and Low-Resistance Hole Contacts. *Nano Lett.* **2016,** *16*, 2720-2727.

(160) Kaushik, N.; Karmakar, D.; Nipane, A.; Karande, S.; Lodha, S., Interfacial n-Doping Using an Ultrathin TiO_2 Layer for Contact Resistance Reduction in MoS_2. *ACS Appl. Mater. Interfaces* **2016,** *8*, 256-263.

(161) McDonnell, S.; Azcatl, A.; Addou, R.; Gong, C.; Battaglia, C.; Chuang, S.; Cho, K.; Javey, A.; Wallace, R. M., Hole Contacts on Transition Metal Dichalcogenides: Interface Chemistry and Band Alignments. *ACS Nano* **2014,** *8*, 6265-6272.

(162) Lin, J.; Zhong, J.; Zhong, S.; Li, H.; Zhang, H.; Chen, W., Modulating electronic transport properties of MoS_2 field effect transistor by surface overlayers. *Appl. Phys. Lett.* **2013,** *103*, 063109.

(163) Zhou, C.; Zhao, Y.; Raju, S.; Wang, Y.; Lin, Z.; Chan, M.; Chai, Y., Carrier Type Control of WSe_2 Field-Effect Transistors by Thickness Modulation and MoO_3 Layer Doping. *Adv. Funct. Mater.* **2016,** *26*, 4223-4230.

(164) Xu, K.; Wang, Y.; Zhao, Y.; Chai, Y., Modulation doping of transition metal dichalcogenide/oxide heterostructures. *Journal of Materials Chemistry C* **2017,** *5*, 376-381.

(165) Rai, A.; Valsaraj, A.; Movva, H. C. P.; Roy, A.; Ghosh, R.; Sonde, S.; Kang, S.; Chang, J.; Trivedi, T.; Dey, R.; Guchhait, S.; Larentis, S.; Register, L. F.; Tutuc, E.; Banerjee, S. K., Air Stable Doping and Intrinsic Mobility Enhancement in Monolayer Molybdenum Disulfide by Amorphous Titanium Suboxide Encapsulation. *Nano Lett.* **2015,** *15*, 4329-4336.

(166) Du, Y.; Liu, H.; Neal, A. T.; Si, M.; Ye, P. D., Molecular Doping of Multilayer MoS_2 Field-Effect Transistors: Reduction in Sheet and Contact Resistances. *IEEE Electron Device Lett.* **2013,** *34*, 1328-1330.

(167) Kang, D.-H.; Kim, M.-S.; Shim, J.; Jeon, J.; Park, H.-Y.; Jung, W.-S.; Yu, H.-Y.; Pang, C.-H.; Lee, S.; Park, J.-H., High-Performance Transition Metal Dichalcogenide Photodetectors Enhanced by Self-Assembled Monolayer Doping. *Adv. Funct. Mater.* **2015,** *25*, 4219-4227.

(168) Inyeal, L.; Servin, R.; Lijun, L.; Dongsuk, L.; Muhammad Atif, K.; Kannan, E. S.; Gil-Ho, K., Non-degenerate n-type doping by hydrazine treatment in metal work function engineered WSe_2 field-effect transistor. *Nanotechnology* **2015,** *26*, 455203.

(169) Kang, D.-H.; Shim, J.; Jang, S. K.; Jeon, J.; Jeon, M. H.; Yeom, G. Y.; Jung, W.-S.; Jang, Y. H.; Lee, S.; Park, J.-H., Controllable Nondegenerate p-Type Doping of Tungsten Diselenide by Octadecyltrichlorosilane. *ACS Nano* **2015,** *9*, 1099-1107.

(170) Mouri, S.; Miyauchi, Y.; Matsuda, K., Tunable Photoluminescence of Monolayer MoS_2 via Chemical Doping. *Nano Lett.* **2013,** *13*, 5944-5948.

(171) Kiriya, D.; Tosun, M.; Zhao, P.; Kang, J. S.; Javey, A., Air-Stable Surface Charge Transfer Doping of MoS_2 by Benzyl Viologen. *J. Am. Chem. Soc.* **2014,** *136*, 7853-7856.

(172) Yu, J.; Lee, C.-H.; Bouilly, D.; Han, M.; Kim, P.; Steigerwald, M. L.; Roy, X.; Nuckolls, C., Patterning Superatom Dopants on Transition Metal Dichalcogenides. *Nano Lett.* **2016,** *16*, 3385-3389.

(173) Zhang, S.; Naab, B. D.; Jucov, E. V.; Parkin, S.; Evans, E. G. B.; Millhauser, G. L.; Timofeeva, T. V.; Risko, C.; Brédas, J.-L.; Bao, Z.; Barlow, S.; Marder, S. R., n-

Dopants Based on Dimers of Benzimidazoline Radicals: Structures and Mechanism of Redox Reactions. *Chem. Eur. J.* **2015,** *21*, 10878-10885.

(174) Paniagua, S. A.; Baltazar, J.; Sojoudi, H.; Mohapatra, S. K.; Zhang, S.; Henderson, C. L.; Graham, S.; Barlow, S.; Marder, S. R., Production of heavily n- and p-doped CVD graphene with solution-processed redox-active metal-organic species. *Mater. Horiz.* **2014,** *1*, 111-115.

(175) Guo, S.; Mohapatra, S. K.; Romanov, A.; Timofeeva, T. V.; Hardcastle, K. I.; Yesudas, K.; Risko, C.; Brédas, J. L.; Marder, S. R.; Barlow, S., n-Doping of Organic Electronic Materials Using Air-Stable Organometallics: A Mechanistic Study of Reduction by Dimeric Sandwich Compounds. *Chem. Eur. J.* **2012,** *18*, 14760-14772.

(176) Guo, S.; Kim, S. B.; Mohapatra, S. K.; Qi, Y.; Sajoto, T.; Kahn, A.; Marder, S. R.; Barlow, S., n-Doping of Organic Electronic Materials using Air-Stable Organometallics. *Adv. Mater.* **2012,** *24*, 699-703.

(177) Maiti, U. N.; Lee, W. J.; Lee, J. M.; Oh, Y.; Kim, J. Y.; Kim, J. E.; Shim, J.; Han, T. H.; Kim, S. O., 25th anniversary article: chemically modified/doped carbon nanotubes & graphene for optimized nanostructures & nanodevices. *Adv. Mater.* **2014,** *26*, 40-67.

(178) Geier, M. L.; Moudgil, K.; Barlow, S.; Marder, S. R.; Hersam, M. C., Controlled n-Type Doping of Carbon Nanotube Transistors by an Organorhodium Dimer. *Nano Lett.* **2016,** *16*, 4329-4334.

(179) Makarova, M.; Okawa, Y.; Aono, M., Selective Adsorption of Thiol Molecules at Sulfur Vacancies on MoS_2(0001), Followed by Vacancy Repair via S–C Dissociation. *J. Phys. Chem. C* **2012,** *116*, 22411-22416.

(180) Sim, D. M.; Kim, M.; Yim, S.; Choi, M.-J.; Choi, J.; Yoo, S.; Jung, Y. S., Controlled Doping of Vacancy-Containing Few-Layer MoS_2 via Highly Stable Thiol-Based Molecular Chemisorption. *ACS Nano* **2015,** *9*, 12115-12123.

(181) Amani, M.; Taheri, P.; Addou, R.; Ahn, G. H.; Kiriya, D.; Lien, D.-H.; Ager, J. W.; Wallace, R. M.; Javey, A., Recombination Kinetics and Effects of Superacid Treatment in Sulfur- and Selenium-Based Transition Metal Dichalcogenides. *Nano Lett.* **2016,** *16*, 2786-2791.

(182) Amani, M.; Lien, D.-H.; Kiriya, D.; Xiao, J.; Azcatl, A.; Noh, J.; Madhvapathy, S. R.; Addou, R.; KC, S.; Dubey, M.; Cho, K.; Wallace, R. M.; Lee, S.-C.; He, J.-H.; Ager, J. W.; Zhang, X.; Yablonovitch, E.; Javey, A., Near-unity photoluminescence quantum yield in MoS_2. *Science* **2015,** *350*, 1065-1068.

(183) Li, J.; Shan, Z.; Ma, E., Elastic strain engineering for unprecedented materials properties. *MRS Bull.* **2014,** *39*, 108-114.

(184) Kaplan-Ashiri, I.; Cohen, S. R.; Gartsman, K.; Ivanovskaya, V.; Heine, T.; Seifert, G.; Wiesel, I.; Wagner, H. D.; Tenne, R., On the mechanical behavior of WS_2

nanotubes under axial tension and compression. *Proceedings of the National Academy of Sciences of the United States of America* **2006,** *103*, 523-528.

(185) Akinwande, D.; Petrone, N.; Hone, J., Two-dimensional flexible nanoelectronics. *Nat Commun* **2014,** *5*.

(186) Bertolazzi, S.; Brivio, J.; Kis, A., Stretching and Breaking of Ultrathin MoS2. *ACS Nano* **2011,** *5*, 9703-9709.

(187) Castellanos-Gomez, A.; Poot, M.; Steele, G. A.; van der Zant, H. S. J.; Agraït, N.; Rubio-Bollinger, G., Elastic Properties of Freely Suspended MoS_2 Nanosheets. *Adv. Mater.* **2012,** *24*, 772-775.

(188) Ghorbani-Asl, M.; Borini, S.; Kuc, A.; Heine, T., Strain-dependent modulation of conductivity in single-layer transition-metal dichalcogenides. *Phys. Rev. B* **2013,** *87*, 235434.

(189) He, K.; Poole, C.; Mak, K. F.; Shan, J., Experimental Demonstration of Continuous Electronic Structure Tuning via Strain in Atomically Thin MoS_2. *Nano Lett.* **2013,** *13*, 2931-2936.

(190) Heine, T., Transition Metal Chalcogenides: Ultrathin Inorganic Materials with Tunable Electronic Properties. *Acc. Chem. Res.* **2015,** *48*, 65-72.

(191) Qin, C.; Gao, Y.; Qiao, Z.; Xiao, L.; Jia, S., Atomic-Layered MoS_2 as a Tunable Optical Platform. *Advanced Optical Materials* **2016,** *4*, 1429-1456.

(192) Johari, P.; Shenoy, V. B., Tuning the Electronic Properties of Semiconducting Transition Metal Dichalcogenides by Applying Mechanical Strains. *ACS Nano* **2012,** *6*, 5449-5456.

(193) Rostami, H.; Roldán, R.; Cappelluti, E.; Asgari, R.; Guinea, F., Theory of strain in single-layer transition metal dichalcogenides. *Phys. Rev. B* **2015,** *92*, 195402.

(194) Wang, Y.; Cong, C.; Yang, W.; Shang, J.; Peimyoo, N.; Chen, Y.; Kang, J.; Wang, J.; Huang, W.; Yu, T., Strain-induced direct–indirect bandgap transition and phonon modulation in monolayer WS_2. *Nano Res.* **2015,** *8*, 2562-2572.

(195) Yun, W. S.; Han, S. W.; Hong, S. C.; Kim, I. G.; Lee, J. D., Thickness and strain effects on electronic structures of transition metal dichalcogenides: 2H-MX_2 semiconductors (M = Mo, W; X = S, Se, Te). *Phys. Rev. B* **2012,** *85*, 033305.

(196) Desai, S. B.; Seol, G.; Kang, J. S.; Fang, H.; Battaglia, C.; Kapadia, R.; Ager, J. W.; Guo, J.; Javey, A., Strain-Induced Indirect to Direct Bandgap Transition in Multilayer WSe_2. *Nano Lett.* **2014,** *14*, 4592-4597.

(197) Scalise, E.; Houssa, M.; Pourtois, G.; Afanas'ev, V.; Stesmans, A., Strain-induced semiconductor to metal transition in the two-dimensional honeycomb structure of MoS_2. *Nano Res.* **2012,** *5*, 43-48.

(198) Hui, Y. Y.; Liu, X.; Jie, W.; Chan, N. Y.; Hao, J.; Hsu, Y.-T.; Li, L.-J.; Guo, W.; Lau, S. P., Exceptional Tunability of Band Energy in a Compressively Strained Trilayer MoS_2 Sheet. *ACS Nano* **2013,** *7*, 7126-7131.

(199) Choi, S.-M.; Jhi, S.-H.; Son, Y.-W., Controlling Energy Gap of Bilayer Graphene by Strain. *Nano Lett.* **2010,** *10*, 3486-3489.

(200) Pereira, V. M.; Castro Neto, A. H.; Peres, N. M. R., Tight-binding approach to uniaxial strain in graphene. *Phys. Rev. B* **2009,** *80*, 045401.

(201) Farjam, M.; Rafii-Tabar, H., Comment on ``Band structure engineering of graphene by strain: First-principles calculations". *Phys. Rev. B* **2009,** *80*, 167401.

(202) Peelaers, H.; Van de Walle, C. G., Effects of strain on band structure and effective masses in MoS_2. *Phys. Rev. B* **2012,** *86*, 241401.

(203) Conley, H. J.; Wang, B.; Ziegler, J. I.; Haglund, R. F.; Pantelides, S. T.; Bolotin, K. I., Bandgap Engineering of Strained Monolayer and Bilayer MoS_2. *Nano Lett.* **2013,** *13*, 3626-3630.

(204) Feng, J.; Qian, X.; Huang, C.-W.; Li, J., Strain-engineered artificial atom as a broad-spectrum solar energy funnel. *Nat Photon* **2012,** *6*, 866-872.

(205) Manzeli, S.; Allain, A.; Ghadimi, A.; Kis, A., Piezoresistivity and Strain-induced Band Gap Tuning in Atomically Thin MoS_2. *Nano Lett.* **2015,** *15*, 5330-5335.

(206) Rice, C.; Young, R. J.; Zan, R.; Bangert, U.; Wolverson, D.; Georgiou, T.; Jalil, R.; Novoselov, K. S., Raman-scattering measurements and first-principles calculations of strain-induced phonon shifts in monolayer MoS_2. *Phys. Rev. B* **2013,** *87*, 081307.

(207) Castellanos-Gomez, A.; Roldán, R.; Cappelluti, E.; Buscema, M.; Guinea, F.; van der Zant, H. S. J.; Steele, G. A., Local Strain Engineering in Atomically Thin MoS_2. *Nano Lett.* **2013,** *13*, 5361-5366.

(208) Zhu, C. R.; Wang, G.; Liu, B. L.; Marie, X.; Qiao, X. F.; Zhang, X.; Wu, X. X.; Fan, H.; Tan, P. H.; Amand, T.; Urbaszek, B., Strain tuning of optical emission energy and polarization in monolayer and bilayer MoS_2. *Phys. Rev. B* **2013,** *88*, 121301.

(209) Chang, C.-H.; Fan, X.; Lin, S.-H.; Kuo, J.-L., Orbital analysis of electronic structure and phonon dispersion in MoS_2, $MoSe_2$, WS_2, and WSe_2 monolayers under strain. *Phys. Rev. B* **2013,** *88*, 195420.

(210) Senturia, S. D., Microsystem design. *Kluwer Academic Publishers: Boston.* **2001**.

(211) Wu, W.; Wang, L.; Li, Y.; Zhang, F.; Lin, L.; Niu, S.; Chenet, D.; Zhang, X.; Hao, Y.; Heinz, T. F.; Hone, J.; Wang, Z. L., Piezoelectricity of single-atomic-layer MoS_2 for energy conversion and piezotronics. *Nature* **2014,** *514*, 470-474.

(212) Qi, J.; Lan, Y.-W.; Stieg, A. Z.; Chen, J.-H.; Zhong, Y.-L.; Li, L.-J.; Chen, C.-D.; Zhang, Y.; Wang, K. L., Piezoelectric effect in chemical vapour deposition-grown atomic-monolayer triangular molybdenum disulfide piezotronics. *Nat. Commun.* **2015,** *6*, 7430.

(213) Zhu, H.; Wang, Y.; Xiao, J.; Liu, M.; Xiong, S.; Wong, Z. J.; Ye, Z.; Ye, Y.; Yin, X.; Zhang, X., Observation of piezoelectricity in free-standing monolayer MoS_2. *Nature Nanotechnology* **2015,** *10*, 151-155.

(214) Kolobov, A. V.; Tominaga, J., Electronic Band Structure of 2D TMDCs. In *Two-Dimensional Transition-Metal Dichalcogenides*, Springer International Publishing: Cham, 2016; pp 165-226.

(215) Bergveld, P., Development of an Ion-Sensitive Solid-State Device for Neurophysiological Measurements. *IEEE Trans. Biomed. Eng* **1970,** *17*, 70-71.

(216) Bergveld, P., Development of an Ion-Sensitive Solid-State Device for Neurophysiological Measurements. *Biomedical Engineering, IEEE Transactions on* **1970,** *BME-17*, 70-71.

(217) Bergveld, P., Thirty years of ISFETOLOGY: What happened in the past 30 years and what may happen in the next 30 years. *Sens Actuators B Chem* **2003,** *88*, 1-20.

(218) Mu, L.; Chang, Y.; Sawtelle, S. D.; Wipf, M.; Duan, X.; Reed, M. A., Silicon Nanowire Field-Effect Transistors - A Versatile Class of Potentiometric Nanobiosensors. *IEEE Access* **2015,** *3*, 287-302.

(219) Bousse, L.; Rooij, N. F. D.; Bergveld, P., Operation of chemically sensitive field-effect sensors as a function of the insulator-electrolyte interface. *IEEE Trans. Electron Devices* **1983,** *30*, 1263-1270.

(220) Chen, K.-I.; Li, B.-R.; Chen, Y.-T., Silicon nanowire field-effect transistor-based biosensors for biomedical diagnosis and cellular recording investigation. *Nano Today* **2011,** *6*, 131-154.

(221) Cui, Y.; Wei, Q.; Park, H.; Lieber, C. M., Nanowire Nanosensors for Highly Sensitive and Selective Detection of Biological and Chemical Species. *Science* **2001,** *293*, 1289-1292.

(222) Noor, M. O.; Krull, U. J., Silicon nanowires as field-effect transducers for biosensor development: A review. *Anal. Chim. Acta* **2014,** *825*, 1-25.

(223) Rajan, N. K.; Duan, X.; Reed, M. A., Performance limitations for nanowire/nanoribbon biosensors. *Wiley Interdisciplinary Reviews: Nanomedicine and Nanobiotechnology* **2013,** *5*, 629-645.

(224) Zhan, B.; Li, C.; Yang, J.; Jenkins, G.; Huang, W.; Dong, X., Graphene Field-Effect Transistor and Its Application for Electronic Sensing. *Small* **2014,** *10*, 4042-4065.

(225) He, Q.; Wu, S.; Yin, Z.; Zhang, H., Graphene-based electronic sensors. *Chemical Science* **2012,** *3*, 1764-1772.

(226) Tang, X.; Bansaruntip, S.; Nakayama, N.; Yenilmez, E.; Chang, Y.-l.; Wang, Q., Carbon Nanotube DNA Sensor and Sensing Mechanism. *Nano Lett.* **2006,** *6*, 1632-1636.

(227) Lee, J.; Dak, P.; Lee, Y.; Park, H.; Choi, W.; Alam, M. A.; Kim, S., Two-dimensional Layered MoS(2) Biosensors Enable Highly Sensitive Detection of Biomolecules. *Sci. Rep.* **2014,** *4*, 7352.

(228) Sarkar, D.; Liu, W.; Xie, X.; Anselmo, A. C.; Mitragotri, S.; Banerjee, K., MoS_2 Field-Effect Transistor for Next-Generation Label-Free Biosensors. *ACS Nano* **2014,** *8*, 3992-4003.

(229) Fu, W.; El Abbassi, M.; Hasler, T.; Jung, M.; Steinacher, M.; Calame, M.; Schönenberger, C.; Puebla-Hellmann, G.; Hellmüller, S.; Ihn, T.; Wallraff, A., Electrolyte gate dependent high-frequency measurement of graphene field-effect transistor for sensing applications. *Appl. Phys. Lett.* **2014,** *104*, 013102.

(230) Dak, P.; Nair, P.; Jonghyun, G.; Alam, M. A. In *Extended-gate biosensors achieve fluid stability with no loss in charge sensitivity*, Device Research Conference (DRC), 2013 71st Annual, 23-26 June 2013; 2013; pp 105-106.

(231) Van der Spiegel, J.; Lauks, I.; Chan, P.; Babic, D., The extended gate chemically sensitive field effect transistor as multi-species microprobe. *Sensors and Actuators* **1983,** *4*, 291-298.

(232) Chi, L.-L.; Chou, J.-C.; Chung, W.-Y.; Sun, T.-P.; Hsiung, S.-K., Study on extended gate field effect transistor with tin oxide sensing membrane. *Materials Chemistry and Physics* **2000,** *63*, 19-23.

(233) Yin, L.-T.; Chou, J.-C.; Chung, W.-Y.; Sun, T.-P.; Hsiung, S.-K., Separate structure extended gate H+-ion sensitive field effect transistor on a glass substrate. *Sens Actuators B Chem* **2000,** *71*, 106-111.

(234) Toshiya, S.; Shinya, M.; Yoshio, N.; Yuji, M., Potential Behavior of Biochemically Modified Gold Electrode for Extended-Gate Field-Effect Transistor. *Japanese Journal of Applied Physics* **2005,** *44*, 2860.

(235) Guan, W.; Duan, X.; Reed, M. A., Highly specific and sensitive non-enzymatic determination of uric acid in serum and urine by extended gate field effect transistor sensors. *Biosens. Bioelectron.* **2014,** *51*, 225-231.

(236) Nair, P. R.; Alam, M. A., Performance limits of nanobiosensors. *Appl. Phys. Lett.* **2006,** *88*, 233120.

(237) Langmuir, I., The Adsorption of Gases on Plane Surfaces of Glass, Mica and Platinum. *J. Am. Chem. Soc.* **1918,** *40*, 1361-1403.

(238) Weiss, J. N., The Hill equation revisited: uses and misuses. *The FASEB Journal* **1997,** *11*, 835-41.

(239) Goutelle, S.; Maurin, M.; Rougier, F.; Barbaut, X.; Bourguignon, L.; Ducher, M.; Maire, P., The Hill equation: a review of its capabilities in pharmacological modelling. *Fundamental & Clinical Pharmacology* **2008,** *22*, 633-648.

(240) Chang, R., *Physical chemistry for the biosciences*. University Science Books: 2005.

(241) Berg, J. M.; Tymoczko, J. L.; Stryer, L., *Biochemistry*. 5 ed.; W H Freeman: New York, 2002.

(242) Yates, D. E.; Levine, S.; Healy, T. W., Site-binding model of the electrical double layer at the oxide/water interface. *J. Chem. Soc., Faraday Trans. 1* **1974,** *70*, 1807-1818.

(243) Fernandes, P. G.; Stiegler, H. J.; Zhao, M.; Cantley, K. D.; Obradovic, B.; Chapman, R. A.; Wen, H.-C.; Mahmud, G.; Vogel, E. M., SPICE macromodel of silicon-on-insulator-field-effect-transistor-based biological sensors. *Sens Actuators B Chem* **2012,** *161*, 163-170.

(244) Nguyen, T. C.; Vu, X. T.; Freyler, M.; Ingebrandt, S., PSPICE model for silicon nanowire field-effect transistor biosensors in impedimetric measurement mode. *physica status solidi (a)* **2013,** *210*, 870-876.

(245) Meixner, L. K.; Koch, S., Simulation of ISFET operation based on the site-binding model. *Sens Actuators B Chem* **1992,** *6*, 315-318.

(246) Chen, Y.; Tan, C.; Zhang, H.; Wang, L., Two-dimensional graphene analogues for biomedical applications. *Chem. Soc. Rev.* **2015,** *44*, 2681-2701.

(247) Ping, J.; Fan, Z.; Sindoro, M.; Ying, Y.; Zhang, H., Recent Advances in Sensing Applications of Two-Dimensional Transition Metal Dichalcogenide Nanosheets and Their Composites. *Adv. Funct. Mater.* **2017,** *27*, 1605817-n/a.

(248) Kolobov, A. V.; Tominaga, J., Emerging Applications of 2D TMDCs. In *Two-Dimensional Transition-Metal Dichalcogenides*, Springer International Publishing: Cham, 2016; pp 473-512.

(249) Late, D. J.; Huang, Y.-K.; Liu, B.; Acharya, J.; Shirodkar, S. N.; Luo, J.; Yan, A.; Charles, D.; Waghmare, U. V.; Dravid, V. P.; Rao, C. N. R., Sensing Behavior of Atomically Thin-Layered MoS2 Transistors. *ACS Nano* **2013,** *7*, 4879-4891.

(250) Lin, M.-W.; Liu, L.; Lan, Q.; Tan, X.; Dhindsa, K. S.; Zeng, P.; Naik, V. M.; Cheng, M. M.-C.; Zhou, Z., Mobility Enhancement and Highly Efficient Gating of Monolayer MoS_2 Transistors with Polymer Electrolyte. *J. Phys. D: Appl. Phys.* **2012,** *45*, 345102.

(251) Lee, K.; Gatensby, R.; McEvoy, N.; Hallam, T.; Duesberg, G. S., High-Performance Sensors Based on Molybdenum Disulfide Thin Films. *Adv. Mater.* **2013,** *25*, 6699-6702.

(252) Liu, B.; Chen, L.; Liu, G.; Abbas, A. N.; Fathi, M.; Zhou, C., High-Performance Chemical Sensing Using Schottky-Contacted Chemical Vapor Deposition Grown Monolayer MoS_2 Transistors. *ACS Nano* **2014,** *8*, 5304-5314.

(253) Late, D. J.; Huang, Y.-K.; Liu, B.; Acharya, J.; Shirodkar, S. N.; Luo, J.; Yan, A.; Charles, D.; Waghmare, U. V.; Dravid, V. P.; Rao, C. N. R., Sensing Behavior of Atomically Thin-Layered MoS_2 Transistors. *ACS Nano* **2013,** *7*, 4879-4891.

(254) Jiang, S.; Cheng, R.; Ng, R.; Huang, Y.; Duan, X., Highly sensitive detection of mercury(II) ions with few-layer molybdenum disulfide. *Nano Res.* **2015,** *8*, 257-262.

(255) Ang, P. K.; Chen, W.; Wee, A. T. S.; Loh, K. P., Solution-Gated Epitaxial Graphene as pH Sensor. *J. Am. Chem. Soc.* **2008,** *130*, 14392-14393.

(256) Fu, W.; Nef, C.; Knopfmacher, O.; Tarasov, A.; Weiss, M.; Calame, M.; Schönenberger, C., Graphene transistors are insensitive to pH changes in solution. *Nano Lett.* **2011,** *11*, 3597-3600.

(257) Lee, J.; Dak, P.; Lee, Y.; Park, H.; Choi, W.; Alam, M. A.; Kim, S., Two-dimensional Layered MoS_2 Biosensors Enable Highly Sensitive Detection of Biomolecules. *Sci. Rep.* **2014,** *4*, 7352.

(258) Wang, L.; Wang, Y.; Wong, J. I.; Palacios, T.; Kong, J.; Yang, H. Y., Functionalized MoS_2 Nanosheet-Based Field-Effect Biosensor for Label-Free Sensitive Detection of Cancer Marker Proteins in Solution. *Small* **2014,** *10*, 1101-1105.

(259) Zhu, C.; Zeng, Z.; Li, H.; Li, F.; Fan, C.; Zhang, H., Single-Layer MoS_2-Based Nanoprobes for Homogeneous Detection of Biomolecules. *J. Am. Chem. Soc.* **2013,** *135*, 5998-6001.

(260) Ge, J.; Tang, L.-J.; Xi, Q.; Li, X.-P.; Yu, R.-Q.; Jiang, J.-H.; Chu, X., A WS_2 nanosheet based sensing platform for highly sensitive detection of T4 polynucleotide kinase and its inhibitors. *Nanoscale* **2014,** *6*, 6866-6872.

(261) Zhang, Y.; Zheng, B.; Zhu, C.; Zhang, X.; Tan, C.; Li, H.; Chen, B.; Yang, J.; Chen, J.; Huang, Y.; Wang, L.; Zhang, H., Single-Layer Transition Metal Dichalcogenide Nanosheet-Based Nanosensors for Rapid, Sensitive, and Multiplexed Detection of DNA. *Adv. Mater.* **2015,** *27*, 935-939.

(262) Kong, R.-M.; Ding, L.; Wang, Z.; You, J.; Qu, F., A novel aptamer-functionalized MoS_2 nanosheet fluorescent biosensor for sensitive detection of prostate specific antigen. *Analytical and Bioanalytical Chemistry* **2015,** *407*, 369-377.

(263) Chen, X.; McDonald, A. R., Functionalization of Two-Dimensional Transition-Metal Dichalcogenides. *Adv. Mater.* **2016,** *28*, 5738-5746.

(264) Lu, C.-H.; Li, J.; Zhang, X.-L.; Zheng, A.-X.; Yang, H.-H.; Chen, X.; Chen, G.-N., General Approach for Monitoring Peptide–Protein Interactions Based on Graphene–Peptide Complex. *Anal. Chem.* **2011,** *83*, 7276-7282.

(265) Backes, C.; Berner, N. C.; Chen, X.; Lafargue, P.; LaPlace, P.; Freeley, M.; Duesberg, G. S.; Coleman, J. N.; McDonald, A. R., Functionalization of Liquid-Exfoliated Two-Dimensional 2H-MoS_2. *Angew. Chem. Int. Ed.* **2015,** *54*, 2638-2642.

(266) Yu, Z.; Pan, Y.; Shen, Y.; Wang, Z.; Ong, Z.-Y.; Xu, T.; Xin, R.; Pan, L.; Wang, B.; Sun, L.; Wang, J.; Zhang, G.; Zhang, Y. W.; Shi, Y.; Wang, X., Towards intrinsic charge transport in monolayer molybdenum disulfide by defect and interface engineering. *Nat. Commun.* **2014,** *5*, 5290.

(267) Wang, T.; Zhu, R.; Zhuo, J.; Zhu, Z.; Shao, Y.; Li, M., Direct Detection of DNA below ppb Level Based on Thionin-Functionalized Layered MoS_2 Electrochemical Sensors. *Anal. Chem.* **2014,** *86*, 12064-12069.

(268) Tuxen, A.; Kibsgaard, J.; Gøbel, H.; Lægsgaard, E.; Topsøe, H.; Lauritsen, J. V.; Besenbacher, F., Size Threshold in the Dibenzothiophene Adsorption on MoS_2 Nanoclusters. *ACS Nano* **2010,** *4*, 4677-4682.

(269) Nguyen, E. P.; Carey, B. J.; Ou, J. Z.; van Embden, J.; Gaspera, E. D.; Chrimes, A. F.; Spencer, M. J. S.; Zhuiykov, S.; Kalantar-zadeh, K.; Daeneke, T., Electronic Tuning of 2D MoS_2 through Surface Functionalization. *Adv. Mater.* **2015,** *27*, 6225-6229.

(270) Kim, J.-S.; Yoo, H.-W.; Choi, H. O.; Jung, H.-T., Tunable Volatile Organic Compounds Sensor by Using Thiolated Ligand Conjugation on MoS_2. *Nano Lett.* **2014,** *14*, 5941-5947.

(271) Yu, S.; Eshun, K.; Zhu, H.; Li, Q., Novel Two-Dimensional Mechano-Electric Generators and Sensors Based on Transition Metal Dichalcogenides. *Sci. Rep.* **2015,** *5*, 12854.

(272) Tsai, M.-Y.; Tarasov, A.; Hesabi, Z. R.; Taghinejad, H.; Campbell, P. M.; Joiner, C. A.; Adibi, A.; Vogel, E. M., Flexible MoS_2 Field-Effect Transistors for Gate-Tunable Piezoresistive Strain Sensors. *ACS Appl. Mater. Interfaces* **2015,** *7*, 12850-12855.

(273) Joiner, C. A.; Campbell, P. M.; Tarasov, A. A.; Beatty, B. R.; Perini, C. J.; Tsai, M.-Y.; Ready, W. J.; Vogel, E. M., Graphene-Molybdenum Disulfide-Graphene Tunneling Junctions with Large-Area Synthesized Materials. *ACS Appl. Mater. Interfaces* **2016,** *8*, 8702-8709.

(274) Tarasov, A.; Tsai, M.-Y.; Flynn, E. M.; Joiner, C. A.; Taylor, R. C.; Vogel, E. M., Gold-coated graphene field-effect transistors for quantitative analysis of protein–antibody interactions. *2D Mater.* **2015,** *2*, 044008.

(275) Taghinejad, H.; Taghinejad, M.; Tarasov, A.; Tsai, M.-Y.; Hosseinnia, A. H.; Moradinejad, H.; Campbell, P. M.; Eftekhar, A. A.; Vogel, E. M.; Adibi, A., Resonant Light-Induced Heating in Hybrid Cavity-Coupled 2D Transition-Metal Dichalcogenides. *ACS Photonics* **2016,** *3*, 700-707.

(276) Mak, K. F.; Shan, J., Photonics and optoelectronics of 2D semiconductor transition metal dichalcogenides. *Nat. Photon.* **2016,** *10*, 216-226.

(277) Fang, H.; Tosun, M.; Seol, G.; Chang, T. C.; Takei, K.; Guo, J.; Javey, A., Degenerate n-Doping of Few-Layer Transition Metal Dichalcogenides by Potassium. *Nano Lett.* **2013,** *13*, 1991-1995.

(278) Davison, A.; Holm, R.; Benson, R.; Mahler, W., Metal Complexes Derived from cis-1, 2-dicyano-1, 2-ethylenedithiolate and Bis (Trifluoromethyl)-1, 2-dithiete. *Inorg. Syn.* **1967,** *10*, 8-26.

(279) Gusev, O. V.; Denisovich, L. I.; Peterleitner, M. G.; Rubezhov, A. Z.; Ustynyuk, N. A.; Maitlis, P. M., Electrochemical generation of 19-and 20-electron rhodocenium complexes and their properties. *J. Organomet. Chem.* **1993,** *452*, 219-222.

(280) Guo, S.; Kim, S. B.; Mohapatra, S. K.; Qi, Y.; Sajoto, T.; Kahn, A.; Marder, S. R.; Barlow, S., n-Doping of Organic Electronic Materials using Air-Stable Organometallics. *Adv. Mater.* **2012,** *24*, 699-703.

(281) Naab, B. D.; Zhang, S.; Vandewal, K.; Salleo, A.; Barlow, S.; Marder, S. R.; Bao, Z., Effective Solution- and Vacuum-Processed n-Doping by Dimers of Benzimidazoline Radicals. *Adv. Mater.* **2014,** *26*, 4268-4272.

(282) Paniagua, S. A.; Baltazar, J.; Sojoudi, H.; Mohapatra, S. K.; Zhang, S.; Henderson, C. L.; Graham, S.; Barlow, S.; Marder, S. R., Production of heavily n-and p-doped CVD graphene with solution-processed redox-active metal–organic species. *Mater. Horiz.* **2014,** *1*, 111-115.

(283) Wei, P.; Liu, N.; Lee, H. R.; Adijanto, E.; Ci, L.; Naab, B. D.; Zhong, J. Q.; Park, J.; Chen, W.; Cui, Y.; Bao, Z., Tuning the Dirac Point in CVD-Grown Graphene through Solution Processed n-Type Doping with 2-(2-Methoxyphenyl)-1,3-dimethyl-2,3-dihydro-1H-benzoimidazole. *Nano Lett.* **2013,** *13*, 1890-1897.

(284) Connelly, N. G.; Geiger, W. E., Chemical Redox Agents for Organometallic Chemistry. *Chem. Rev.* **1996,** *96*, 877-910.

(285) Kiriya, D.; Tosun, M.; Zhao, P.; Kang, J. S.; Javey, A., Air-stable surface charge transfer doping of MoS2 by benzyl viologen. *J. Am. Chem. Soc.* **2014,** *136*, 7853-7856.

(286) Mak, K. F.; Lee, C.; Hone, J.; Shan, J.; Heinz, T. F., Atomically Thin MoS_2: A New Direct-Gap Semiconductor. *Phys. Rev. Lett.* **2010,** *105*, 136805.

(287) Ellis, J. K.; Lucero, M. J.; Scuseria, G. E., The indirect to direct band gap transition in multilayered MoS_2 as predicted by screened hybrid density functional theory. *Appl. Phys. Lett.* **2011,** *99*, 261908.

(288) Liu, K.; Zhang, L.; Cao, T.; Jin, C.; Qiu, D.; Zhou, Q.; Zettl, A.; Yang, P.; Louie, S. G.; Wang, F., Evolution of interlayer coupling in twisted molybdenum disulfide bilayers. *Nat. Commun.* **2014,** *5*, 4966.

(289) Huang, S.; Ling, X.; Liang, L.; Kong, J.; Terrones, H.; Meunier, V.; Dresselhaus, M. S., Probing the Interlayer Coupling of Twisted Bilayer MoS_2 Using Photoluminescence Spectroscopy. *Nano Lett.* **2014**, DOI: 10.1021/nl5014597.

(290) Sup Choi, M.; Lee, G.-H.; Yu, Y.-J.; Lee, D.-Y.; Hwan Lee, S.; Kim, P.; Hone, J.; Jong Yoo, W., Controlled charge trapping by molybdenum disulphide and graphene in ultrathin heterostructured memory devices. *Nat. Commun.* **2013,** *4*, 1624.

(291) Amani, M.; Chin, M. L.; Birdwell, A. G.; ORegan, T. P.; Najmaei, S.; Liu, Z.; Ajayan, P. M.; Lou, J.; Dubey, M., Electrical Performance of Monolayer MoS$_2$ Field-Effect Transistors Prepared by Chemical Vapor Deposition. *Appl. Phys. Lett.* **2013,** *102*, 193107-193107.

(292) Chuang, S.; Battaglia, C.; Azcatl, A.; McDonnell, S.; Kang, J. S.; Yin, X.; Tosun, M.; Kapadia, R.; Fang, H.; Wallace, R. M., MoS2 P-type Transistors and Diodes Enabled by High Work Function MoO x Contacts. *Nano Lett.* **2014,** *14*, 1337-1342.

(293) Qiu, H.; Xu, T.; Wang, Z.; Ren, W.; Nan, H.; Ni, Z.; Chen, Q.; Yuan, S.; Miao, F.; Song, F.; Long, G.; Shi, Y.; Sun, L.; Wang, J.; Wang, X., Hopping transport through defect-induced localized states in molybdenum disulphide. *Nat. Commun.* **2013,** *4*, 2642.

(294) Santosh, K.; Longo, R. C.; Addou, R.; Wallace, R. M.; Cho, K., Impact of intrinsic atomic defects on the electronic structure of MoS_2 monolayers. *Nanotechnology* **2014,** *25*, 375703.

(295) Lu, C.-P.; Li, G.; Mao, J.; Wang, L.-M.; Andrei, E. Y., Bandgap, Mid-Gap States, and Gating Effects in MoS_2. *Nano Lett.* **2014,** *14*, 4628-4633.

(296) Tarasov, A.; Zhang, S.; Tsai, M.-Y.; Campbell, P. M.; Graham, S.; Barlow, S.; Marder, S. R.; Vogel, E. M., Controlled Doping of Large-Area Trilayer MoS_2 with Molecular Reductants and Oxidants. *Adv. Mater.* **2015,** *27*, 1175-1181.

(297) Tarasov, A.; Campbell, P.; Tsai, M.-Y.; Hesabi, Z.; Feirer, J.; Graham, S.; Ready, W.; Vogel, E., Highly Uniform Trilayer Molybdenum Disulfide for Wafer-Scale Device Fabrication. *Adv. Funct. Mater.* **2014**, DOI: 10.1002/adfm.201401389.

(298) Chakraborty, B.; Bera, A.; Muthu, D. V. S.; Bhowmick, S.; Waghmare, U. V.; Sood, A. K., Symmetry-dependent phonon renormalization in monolayer MoS 2 transistor. *Phys. Rev. B* **2012,** *85*, 161403.

(299) Bera, A.; Sood, A. K., Insights into Vibrational and Electronic Properties of MoS_2 Using Raman, Photoluminescence, and Transport Studies. In *MoS_2*, Wang, Z. M., Ed. Springer: 2014; p p. 155.

(300) Upadhyayula, L. C.; Loferski, J. J.; Wold, A.; Giriat, W.; Kershaw, R., Semiconducting Properties of Single Crystals of n- and p-Type Tungsten Diselenide (WSe_2). *J. Appl. Phys.* **1968,** *39*, 4736-4740.

(301) Tarasov, A.; Zhang, S.; Tsai, M. Y.; Campbell, P. M.; Graham, S.; Barlow, S.; Marder, S. R.; Vogel, E. M., Controlled doping of large-area trilayer MoS_2 with molecular reductants and oxidants. *Adv. Mater.* **2015,** *27*, 1175-1181.

(302) Basu, P.; Nigam, A.; Mogesa, B.; Denti, S.; Nemykin, V. N., Synthesis, characterization, spectroscopy, electronic and redox properties of a new nickel dithiolene system. *Inorg. Chim. Acta.* **2010,** *363*, 2857-2864.

(303) Akaike, K.; Nardi, M. V.; Oehzelt, M.; Frisch, J.; Opitz, A.; Christodoulou, C.; Ligorio, G.; Beyer, P.; Timpel, M.; Pis, I.; Bondino, F.; Moudgil, K.; Barlow, S.; Marder, S. R.; Koch, N., Effective Work Function Reduction of Practical Electrodes Using an Organometallic Dimer. *Adv. Funct. Mater.* **2016,** *26*, 2493-2502.

(304) Mohapatra, S. K.; Fonari, A.; Risko, C.; Yesudas, K.; Moudgil, K.; Delcamp, J. H.; Timofeeva, T. V.; Brédas, J.-L.; Marder, S. R.; Barlow, S., Dimers of Nineteen-Electron Sandwich Compounds: Crystal and Electronic Structures, and Comparison of Reducing Strengths. *Chem. Eur. J.* **2014,** *20*, 15385-15394.

(305) Moudgil, K.; Mann, M. A.; Risko, C.; Bottomley, L. A.; Marder, S. R.; Barlow, S., Dimers of Nineteen-Electron Sandwich Compounds: An Electrochemical Study of the Kinetics of Their Formation. *Organometallics* **2015,** *34*, 3706-3712.

(306) Tsai, M.-Y.; Zhang, S.; Campbell, P. M.; Dasari, R. R.; Ba, X.; Tarasov, A.; Graham, S.; Barlow, S.; Marder, S. R.; Vogel, E. M., Solution-Processed Doping of Trilayer WSe_2 with Redox-Active Molecules. *Chemistry of Materials* **2017**. DOI: 10.1021/acs.chemmater.7b01998

(307) Zeng, H.; Liu, G.-B.; Dai, J.; Yan, Y.; Zhu, B.; He, R.; Xie, L.; Xu, S.; Chen, X.; Yao, W., Optical signature of symmetry variations and spin-valley coupling in atomically thin tungsten dichalcogenides. *Sci. Rep.* **2013,** *3*.

(308) Zhou, H.; Wang, C.; Shaw, J. C.; Cheng, R.; Chen, Y.; Huang, X.; Liu, Y.; Weiss, N. O.; Lin, Z.; Huang, Y.; Duan, X., Large Area Growth and Electrical Properties of p-Type WSe_2 Atomic Layers. *Nano Lett.* **2015,** *15*, 709-713.

(309) Wang, W.; Liu, Y.; Tang, L.; Jin, Y.; Zhao, T.; Xiu, F., Controllable Schottky Barriers between MoS_2 and Permalloy. *Sci. Rep.* **2014,** *4*, 6928.

(310) Liu, W.; Cao, W.; Kang, J.; Banerjee, K., High-Performance Field-Effect-Transistors on Monolayer-WSe_2. *ECS Trans.* **2013,** *58*, 281-285.

(311) Anwar, A.; Nabet, B.; Culp, J.; Castro, F., Effects of electron confinement on thermionic emission current in a modulation doped heterostructure. *J. Appl. Phys.* **1999,** *85*, 2663-2666.

(312) Cheng, R.; Jiang, S.; Chen, Y.; Liu, Y.; Weiss, N.; Cheng, H.-C.; Wu, H.; Huang, Y.; Duan, X., Few-layer molybdenum disulfide transistors and circuits for high-speed flexible electronics. *Nat. Commun.* **2014,** *5*, 5143.

(313) Amani, M.; Chin, M. L.; Mazzoni, A. L.; Burke, R. A.; Najmaei, S.; Ajayan, P. M.; Lou, J.; Dubey, M., Growth-substrate induced performance degradation in chemically synthesized monolayer MoS_2 field effect transistors. *Appl. Phys. Lett.* **2014,** *104*, 203506.

(314) Pu, J.; Yomogida, Y.; Liu, K.-K.; Li, L.-J.; Iwasa, Y.; Takenobu, T., Highly Flexible MoS_2 Thin-film Transistors with Ion Gel Dielectrics. *Nano Lett.* **2012,** *12*, 4013-4017.

(315) Chang, H.-Y.; Yang, S.; Lee, J.; Tao, L.; Hwang, W.-S.; Jena, D.; Lu, N.; Akinwande, D., High-Performance, Highly Bendable MoS_2 Transistors with High-K Dielectrics for Flexible Low-Power Systems. *ACS Nano* **2013,** *7*, 5446-5452.

(316) Lee, G.-H.; Yu, Y.-J.; Cui, X.; Petrone, N.; Lee, C.-H.; Choi, M. S.; Lee, D.-Y.; Lee, C.; Yoo, W. J.; Watanabe, K.; Taniguchi, T.; Nuckolls, C.; Kim, P.; Hone, J., Flexible and Transparent MoS_2 Field-Effect Transistors on Hexagonal Boron Nitride-Graphene Heterostructures. *ACS Nano* **2013,** *7*, 7931-7936.

(317) Tarasov, A.; Campbell, P. M.; Tsai, M.-Y.; Hesabi, Z. R.; Feirer, J.; Graham, S.; Ready, W. J.; Vogel, E. M., Highly Uniform Trilayer Molybdenum Disulfide for Wafer-Scale Device Fabrication. *Adv. Funct. Mater.* **2014,** *24*, 6389-6400.

(318) Salvatore, G. A.; Münzenrieder, N.; Barraud, C.; Petti, L.; Zysset, C.; Büthe, L.; Ensslin, K.; Tröster, G., Fabrication and Transfer of Flexible Few-Layers MoS2 Thin Film Transistors to Any Arbitrary Substrate. *ACS Nano* **2013,** *7*, 8809-8815.

(319) Yoon, J.; Park, W.; Bae, G.-Y.; Kim, Y.; Jang, H. S.; Hyun, Y.; Lim, S. K.; Kahng, Y. H.; Hong, W.-K.; Lee, B. H.; Ko, H. C., Highly Flexible and Transparent Multilayer MoS2 Transistors with Graphene Electrodes. *Small* **2013,** *9*, 3295-3300.

(320) Carvalho, A.; Neto, A. H. C., Donor and acceptor levels in semiconducting transition-metal dichalcogenides. *Phys. Rev. B* **2014,** *89*, 081406.

(321) Feenstra, R. M.; Jena, D.; Gu, G., Single-particle tunneling in doped graphene-insulator-graphene junctions. *J. Appl. Phys.* **2012,** *111*, 043711.

(322) Barlian, A. A.; Woo-Tae, P.; Mallon, J. R.; Rastegar, A. J.; Pruitt, B. L., Review: Semiconductor Piezoresistance for Microsystems. *Proc. IEEE* **2009,** *97*, 513-552.

(323) Beeby, S., *MEMS mechanical sensors*. Artech House: Boston, 2004.

(324) Kang, T.-K., Evidence for giant piezoresistance effect in n-type silicon nanowire field-effect transistors. *Appl. Phys. Lett.* **2012,** *100*, 163501.

(325) Pushpapraj, S.; Jianmin, M.; Woo-Tae, P.; Dim-Lee, K., Gate-bias-controlled sensitivity and SNR enhancement in a nanowire FET pressure sensor. *J. Micromech. Microeng.* **2011,** *21*, 105007.

(326) Helbling, T.; Roman, C.; Durrer, L.; Stampfer, C.; Hierold, C., Gauge Factor Tuning, Long-Term Stability, and Miniaturization of Nanoelectromechanical Carbon-Nanotube Sensors. *IEEE Trans. Electron Dev.* **2011,** *58*, 4053-4060.

(327) Liu, H.; Si, M.; Deng, Y.; Neal, A. T.; Du, Y.; Najmaei, S.; Ajayan, P. M.; Lou, J.; Ye, P. D., Switching Mechanism in Single-Layer Molybdenum Disulfide Transistors: An Insight into Current Flow across Schottky Barriers. *ACS Nano* **2014,** *8*, 1031-1038.

(328) Bergveld, P., Thirty years of ISFETOLOGY: What happened in the past 30 years and what may happen in the next 30 years. *Sens. Actuators B* **2003,** *88*, 1-20.

(329) Salieb-Beugelaar, G. B.; Hunziker, P. R., Towards nano-diagnostics for rapid diagnosis of infectious diseases–current technological state. *Eur. J. Nanomed.* **2014,** *6*, 11-28.

(330) Makowski, M. S.; Ivanisevic, A., Molecular Analysis of Blood with Micro-/Nanoscale Field-Effect-Transistor Biosensors. *Small* **2011,** *7*, 1863-1875.

(331) Duarte-Guevara, C.; Lai, F.-L.; Cheng, C.-W.; Reddy, B.; Salm, E.; Swaminathan, V.; Tsui, Y.-K.; Tuan, H. C.; Kalnitsky, A.; Liu, Y.-S.; Bashir, R., Enhanced Biosensing Resolution with Foundry Fabricated Individually Addressable Dual-Gated ISFETs. *Anal. Chem.* **2014,** *86*, 8359-8367.

(332) Fernandes, P. G.; Seitz, O.; Chapman, R. A.; Stiegler, H. J.; Wen, H.-C.; Chabal, Y. J.; Vogel, E. M., Effect of mobile ions on ultrathin silicon-on-insulator-based sensors. *Appl. Phys. Lett.* **2010,** *97*, 034103.

(333) Tarasov, A.; Wipf, M.; Stoop, R. L.; Bedner, K.; Fu, W.; Guzenko, V. A.; Knopfmacher, O.; Calame, M.; Schönenberger, C., Understanding the electrolyte

background for biochemical sensing with ion-sensitive field-effect transistors. *ACS Nano* **2012,** *6*, 9291-9298.

(334) Guan, W.; Duan, X.; Reed, M. A., Highly specific and sensitive non-enzymatic determination of uric acid in serum and urine by extended gate field effect transistor sensors. *Biosens. Bioelectron.* **2014,** *51*, 225-231.

(335) Goda, T.; Miyahara, Y., Label-free and reagent-less protein biosensing using aptamer-modified extended-gate field-effect transistors. *Biosens. Bioelectron.* **2013,** *45*, 89-94.

(336) Kim, D.-S.; Park, J.-E.; Shin, J.-K.; Kim, P. K.; Lim, G.; Shoji, S., An extended gate FET-based biosensor integrated with a Si microfluidic channel for detection of protein complexes. *Sens. Actuators B* **2006,** *117*, 488-494.

(337) Chen, J.-C.; Chou, J.-C.; Sun, T.-P.; Hsiung, S.-K., Portable urea biosensor based on the extended-gate field effect transistor. *Sens. Actuators B* **2003,** *91*, 180-186.

(338) Minami, T.; Minamiki, T.; Hashima, Y.; Yokoyama, D.; Sekine, T.; Fukuda, K.; Kumaki, D.; Tokito, S., An extended-gate type organic field effect transistor functionalised by phenylboronic acid for saccharide detection in water. *Chem. Commun.* **2014,** *50*, 15613-15615.

(339) Chen, C.-P.; Ganguly, A.; Lu, C.-Y.; Chen, T.-Y.; Kuo, C.-C.; Chen, R.-S.; Tu, W.-H.; Fischer, W. B.; Chen, K.-H.; Chen, L.-C., Ultrasensitive in situ label-free DNA detection using a GaN nanowire-based extended-gate field-effect-transistor sensor. *Anal. Chem.* **2011,** *83*, 1938-1943.

(340) Minamiki, T.; Minami, T.; Kurita, R.; Niwa, O.; Wakida, S.-i.; Fukuda, K.; Kumaki, D.; Tokito, S., Accurate and reproducible detection of proteins in water using an extended-gate type organic transistor biosensor. *Appl. Phys. Lett.* **2014,** *104*, 243703.

(341) Ishige, Y.; Shimoda, M.; Kamahori, M., Extended-gate FET-based enzyme sensor with ferrocenyl-alkanethiol modified gold sensing electrode. *Biosens. Bioelectron.* **2009,** *24*, 1096-1102.

(342) Lyu, H.-K.; Choi, Y.-S.; Shin, J.-K.; Kim, J.-H. In *A commercial MOSFET-based biosensor with a gold extended gate electrode*, SPIE Defense, Security, and Sensing, International Society for Optics and Photonics: 2009; p 73130S.

(343) Dak, P.; Nair, P.; Go, J.; Alam, M. A. In *Extended-gate biosensors achieve fluid stability with no loss in charge sensitivity*, Device Research Conference (DRC), 2013 71st Annual, 23-26 June 2013; IEEE: 2013; pp 105-106.

(344) Snowder, G. D.; Van Vleck, L. D.; Cundiff, L. V.; Bennett, G. L.; Koohmaraie, M.; Dikeman, M. E., Bovine respiratory disease in feedlot cattle: Phenotypic, environmental, and genetic correlations with growth, carcass, and longissimus muscle palatability traits. *Journal of Animal Science* **2007,** *85*, 1885-1892.

(345) Scott, P. R. In *Factors of Respiratory Disease: Review of Management Factors*, Bovine Respiratory Disease: Total Health Management, Edinburgh, Scotland, Anthony, F. J., Ed. Schering-Plough Animal Health: Edinburgh, Scotland, 1994; pp 17-24.

(346) Thompson, P. N.; Stone, A.; Schultheiss, W. A., Use of treatment records and lung lesion scoring to estimate the effect of respiratory disease on growth during early and late finishing periods in South African feedlot cattle. *Journal of Animal Science* **2006,** *84*, 488-498.

(347) Ellis, J. A., Update on viral parthenogenesis in BRD. *Animal Health Research Reviews* **2009,** *10*, 149-153.

(348) Confer, A. W., Update on bacterial pathogenesis in BRD. *Animal health research reviews / Conference of Research Workers in Animal Diseases* **2009,** *10*, 145-8.

(349) Giovannini, S.; Zanoni, M. G.; Salogni, C.; Cinotti, S.; Alborali, G. L., Mycoplasma bovis infection in respiratory disease of dairy calves less than one month old. *Research in Veterinary Science* **2013,** *95*, 576-579.

(350) Raaperi, K.; Orro, T.; Viltrop, A., Epidemiology and control of bovine herpesvirus 1 infection in Europe. *Veterinary Journal* **2014,** *201*, 249-256.

(351) Strube, W.; Auer, S.; Block, W.; Heinen, E.; Kretzdorn, D.; Rodenbach, C.; Schmeer, N., A gE deleted infectious bovine rhinotracheitis marker vaccine for use in improved bovine herpesvirus 1 control programs. *Vet Microbiol* **1996,** *53*, 181-9.

(352) Wellenberg, G. J.; Verstraten, E. R.; Mars, M. H.; Van Oirschot, J. T., Detection of bovine herpesvirus 1 glycoprotein E antibodies in individual milk samples by enzyme-linked immunosorbent assays. *J. Clin. Microbiol.* **1998,** *36*, 409-13.

(353) Thiry, E.; Saliki, J.; Bublot, M.; Pastoret, P. P., Reactivation of infectious bovine rhinotracheitis virus by transport. *Comp Immunol Microbiol Infect Dis* **1987,** *10*, 59-63.

(354) El-Kholy, A. A.; Abdou, E. R.; Rady, D. I.; Elseafy, M. M., Baculovirus expression and diagnostic utility of the glycoprotein E of bovine herpesvirus-1.1 Egyptian strain "Abu-Hammad". *Journal of Virological Methods* **2013,** *191*, 33-40.

(355) Anderson, S.; Wakeley, P.; Wibberley, G.; Webster, K.; Sawyer, J., Development and evaluation of a Luminex multiplex serology assay to detect antibodies to bovine herpes virus 1, parainfluenza 3 virus, bovine viral diarrhoea virus, and bovine respiratory syncytial virus, with comparison to existing ELISA detection methods. *Journal of Immunological Methods* **2011,** *366*, 79-88.

(356) Chan, J.; Venugopal, A.; Pirkle, A.; McDonnell, S.; Hinojos, D.; Magnuson, C. W.; Ruoff, R. S.; Colombo, L.; Wallace, R. M.; Vogel, E. M., Reducing extrinsic performance-limiting factors in graphene grown by chemical vapor deposition. *ACS Nano* **2012,** *6*, 3224-3229.

(357) Fu, W.; Nef, C.; Tarasov, A.; Wipf, M.; Stoop, R.; Knopfmacher, O.; Weiss, M.; Calame, M.; Schoenenberger, C., High mobility graphene ion-sensitive field-effect transistors by noncovalent functionalization. *Nanoscale* **2013,** *5*, 12104-12110.

(358) Wipf, M.; Stoop, R. L.; Tarasov, A.; Bedner, K.; Fu, W.; Wright, I. A.; Martin, C. J.; Constable, E. C.; Calame, M.; Schönenberger, C., Selective sodium sensing with gold-coated silicon nanowire field-effect transistors in a differential setup. *ACS Nano* **2013,** *7*, 5978-5983.

(359) Stoop, R. L.; Wipf, M.; Müller, S.; Bedner, K.; Wright, I. A.; Martin, C. J.; Constable, E. C.; Fu, W.; Tarasov, A.; Calame, M., Competing surface reactions limiting the performance of ion-sensitive field-effect transistors. *Sens. Actuators B* **2015,** *220*, 500-507.

(360) Wang, C.; Wang, J.; Deng, L., Evaluating interaction forces between BSA and rabbit anti-BSA in sulphathiazole sodium, tylosin and levofloxacin solution by AFM. *Nanoscale Res. Lett.* **2011,** *6*, 1-9.

(361) Laidler, K. J., Chemical kinetics. In *Chemical kinetics*, McGraw-Hill: 1977.

(362) Zhu, A. Y.; Yi, F.; Reed, J. C.; Zhu, H.; Cubukcu, E., Optoelectromechanical Multimodal Biosensor with Graphene Active Region. *Nano Lett.* **2014,** *14*, 5641-5649.

(363) Wang, C.; Wang, J.; Deng, L., Evaluating interaction forces between BSA and rabbit anti-BSA in sulphathiazole sodium, tylosin and levofloxacin solution by AFM. *Nanoscale Res. Lett.* **2011,** *6*, 579.

(364) Fernandes, P. G.; Stiegler, H. J.; Zhao, M.; Cantley, K. D.; Obradovic, B.; Chapman, R. A.; Wen, H.-C.; Mahmud, G.; Vogel, E. M., SPICE macromodel of silicon-on-insulator-field-effect-transistor-based biological sensors. *Sens. Actuators B* **2012,** *161*, 163-170.

(365) Tarasov, A.; Wipf, M.; Bedner, K.; Kurz, J.; Fu, W.; Guzenko, V.; Knopfmacher, O.; Stoop, R.; Calame, M.; Schönenberger, C., True reference nanosensor realized with silicon nanowires. *Langmuir* **2012,** *28*, 9899-9905.

(366) Chen, S.; Bomer, J. G.; Carlen, E. T.; van den Berg, A., Al_2O_3/silicon nanoISFET with near ideal Nernstian response. *Nano Lett.* **2011,** *11*, 2334-2341.

(367) Yates, D. E.; Levine, S.; Healy, T. W., Site-binding model of the electrical double layer at the oxide/water interface. *J. Chem. Soc., Faraday Trans.* **1974,** *70*, 1807-1818.

(368) Hammock, M. L.; Knopfmacher, O.; Naab, B. D.; Tok, J. B.-H.; Bao, Z., Investigation of protein detection parameters using nanofunctionalized organic field-effect transistors. *ACS Nano* **2013,** *7*, 3970-3980.

(369) Lehman, D. J.; Roof, L. L.; Brideau, R. J.; Aeed, P. A.; Thomsen, D. R.; Elhammer, A. P.; Wathen, M. W.; Homa, F. L., Comparison of soluble and secreted

forms of human parainfluenza virus type 3 glycoproteins expressed from mammalian and insect cells as subunit vaccines. *Journal of General Virology* **1993,** *74*, 459-469.

(370) Donofrio, G.; Bottarelli, E.; Sandro, C.; Flammini, C. F., Expression of bovine viral diarrhea virus glycoprotein E2 as a soluble secreted form in a Mammalian cell line. *Clin Vaccine Immunol* **2006,** *13*, 698-701.

(371) Chua, J. H.; Chee, R. E.; Agarwal, A.; Wong, S. M.; Zhang, G. J., Label-free electrical detection of cardiac biomarker with complementary metal-oxide semiconductor-compatible silicon nanowire sensor arrays. *Anal. Chem.* **2009,** *81*, 6266-71.

(372) Tarasov, A.; Fu, W.; Knopfmacher, O.; Brunner, J.; Calame, M.; Schönenberger, C., Signal-to-noise ratio in dual-gated silicon nanoribbon field-effect sensors. *Appl. Phys. Lett.* **2011,** *98*, 012114-012114-3.

(373) Bedner, K.; Guzenko, V. A.; Tarasov, A.; Wipf, M.; Stoop, R. L.; Rigante, S.; Brunner, J.; Fu, W.; David, C.; Calame, M., Investigation of the dominant 1/f noise source in silicon nanowire sensors. *Sens. Actuators B* **2014,** *191*, 270-275.

(374) Tsai, M.-Y.; Creedon, N.; Brightbill, E.; Pavlidis, S.; Brown, B.; Gray, D. W.; Shields, N.; Sayers, R.; Mooney, M. H.; O'Riordan, A.; Vogel, E. M., Direct correlation between potentiometric and impedance biosensing of antibody-antigen interactions using an integrated system. *Appl. Phys. Lett.* **2017,** *111*, 073701.

(375) Sin, M. L. Y.; Mach, K. E.; Wong, P. K.; Liao, J. C., Advances and challenges in biosensor-based diagnosis of infectious diseases. *Expert Rev. Mol. Diagn.* **2014,** *14*, 225-244.

(376) Singh, P., SPR Biosensors: Historical Perspectives and Current Challenges. *Sens Actuators B Chem* **2016,** *229*, 110-130.

(377) Ozdemir, M. S.; Marczak, M.; Bohets, H.; Bonroy, K.; Roymans, D.; Stuyver, L.; Vanhoutte, K.; Pawlak, M.; Bakker, E., A Label-Free Potentiometric Sensor Principle for the Detection of Antibody–Antigen Interactions. *Anal. Chem.* **2013,** *85*, 4770-4776.

(378) Tarasov, A.; Gray, D. W.; Tsai, M.-Y.; Shields, N.; Montrose, A.; Creedon, N.; Lovera, P.; O'Riordan, A.; Mooney, M. H.; Vogel, E. M., A potentiometric biosensor for rapid on-site disease diagnostics. *Biosens. Bioelectron.* **2016,** *79*, 669-678.

(379) Prodromidis, M. I., Impedimetric immunosensors—A review. *Electrochim. Acta* **2010,** *55*, 4227-4233.

(380) Daniels, J. S.; Pourmand, N., Label-Free Impedance Biosensors: Opportunities and Challenges. *Electroanalysis* **2007,** *19*, 1239-1257.

(381) Katz, E.; Willner, I., Probing Biomolecular Interactions at Conductive and Semiconductive Surfaces by Impedance Spectroscopy: Routes to Impedimetric

Immunosensors, DNA-Sensors, and Enzyme Biosensors. *Electroanalysis* **2003,** *15*, 913-947.

(382) Montrose, A.; Creedon, N.; Sayers, R.; Barry, S.; O'Riordan, A., Novel Single Gold Nanowire-based Electrochemical Immunosensor for Rapid Detection of Bovine Viral Diarrhoea Antibodies in Serum. *Journal of Biosensors & Bioelectronics* **2015,** *6*, 174.

(383) Wahl, A.; O'Riordan, A., Chapter 6 Nanoelectrodes in Electrochemical Analysis. In *Electrochemical Strategies in Detection Science*, The Royal Society of Chemistry: 2016; pp 205-228.

(384) Wahl, A.; Barry, S.; Dawson, K.; MacHale, J.; Quinn, A. J.; O'Riordan, A., Electroanalysis at Ultramicro and Nanoscale Electrodes: A Comparative Study. *J. Electrochem. Soc.* **2014,** *161*, B3055-B3060.

(385) Madou, M. J.; Cubicciotti, R., Scaling issues in chemical and biological sensors. *Proc. IEEE* **2003,** *91*, 830-838.

(386) Franks, W.; Schenker, I.; Schmutz, P.; Hierlemann, A., Impedance characterization and modeling of electrodes for biomedical applications. *IEEE Trans. Biomed. Eng* **2005,** *52*, 1295-1302.

(387) Radhakrishnan, R.; Suni, I. I.; Bever, C. S.; Hammock, B. D., Impedance Biosensors: Applications to Sustainability and Remaining Technical Challenges. *ACS Sustain Chem Eng* **2014,** *2*, 1649-1655.

(388) Bard, A. J.; Faulkner, L. R., *Electrochemical Methods: Fundamentals and Applications*. 2 ed.; John Wiley & Sons, Inc.: 2001.

(389) ter Heijne, A.; Schaetzle, O.; Gimenez, S.; Navarro, L.; Hamelers, B.; Fabregat-Santiago, F., Analysis of bio-anode performance through electrochemical impedance spectroscopy. *Bioelectrochemistry* **2015,** *106, Part A*, 64-72.

(390) Hamelers, H. V. M.; ter Heijne, A.; Stein, N.; Rozendal, R. A.; Buisman, C. J. N., Butler–Volmer–Monod model for describing bio-anode polarization curves. *Bioresour. Technol.* **2011,** *102*, 381-387.

(391) Finklea, H. O.; Liu, L.; Ravenscroft, M. S.; Punturi, S., Multiple Electron Tunneling Paths across Self-Assembled Monolayers of Alkanethiols with Attached Ruthenium(II/III) Redox Centers. *J. Phys. Chem.* **1996,** *100*, 18852-18858.

(392) Gray, D. W.; Welsh, M. D.; Doherty, S.; Mansoor, F.; Chevallier, O. P.; Elliott, C. T.; Mooney, M. H., Identification of systemic immune response markers through metabolomic profiling of plasma from calves given an intra-nasally delivered respiratory vaccine. *Vet Res.* **2015,** *46*, 7.

(393) Lasia, A., *Electrochemical Impedance Spectroscopy and its Applications*. Springer-Verlag New York: 2014; p 367.

(394) Cañas, N. A.; Hirose, K.; Pascucci, B.; Wagner, N.; Friedrich, K. A.; Hiesgen, R., Investigations of lithium–sulfur batteries using electrochemical impedance spectroscopy. *Electrochim. Acta* **2013,** *97*, 42-51.

(395) Mansfeld, F., Use of electrochemical impedance spectroscopy for the study of corrosion protection by polymer coatings. *J. Appl. Electrochem.* **1995,** *25*, 187-202.

(396) Tsai, M.-Y.; Cheng, W.-H.; Jeng, J.-S.; Chen, J.-S., Improving performance of inverted organic solar cells using ZTO nanoparticles as cathode buffer layer. *Solid-State Electron.* **2016,** *120*, 56-62.

(397) Cheng, W.-H.; Chiou, J.-W.; Tsai, M.-Y.; Jeng, J.-S.; Chen, J.-S.; Hsu, S. L.-C.; Chou, W.-Y., Lithium-Induced Defect Levels in ZnO Nanoparticles To Facilitate Electron Transport in Inverted Organic Photovoltaics. *J. Phys. Chem. C* **2016,** *120*, 15035-15041.